JOURNAL OF GEOGRAGHY AND CARTOGRAPHY

EnPress Publisher

Journal of Geography and Cartography

Journal of Geography and Cartography

Contents

Original Research Articles

Review Articles

ORIGINAL RESEARCH ARTICLE

Study the bio-potential parameter for the detection of seismic and environmental changes in Indian region

Rudraksh Tiwari[1], Vijay S Katta[1], Vinod Kumar Kushwah[1*], Mulayam Singh Gaur[1], Priti Dimri[2]

[1]*Department of Physics, Hindustan College of Science & Technology, Farah, Mathura, India; Affiliated to Dr. A.P.J. Abdul Kalam Technical University, Lucknow, U.P. India; E-mail: twrrudraksh1@gmail.com;*

[2]*Department of Computer Science and Applications, G.B. Pant Engineering College, Ghurdauri, Pauri 246194, Uttarakhand, India*

ABSTRACT

The changes the magnetic flux generated (electric, magnetic and electromagnetic waves) on the surface of earth due to sudden changes is a matter of discussion. These emissions occur along the fault line generated due to geological and tectonic processes. When sudden changes occur in the environment due to seismic and atmospheric variations, these sensing was observed by creatures and human bodies because the animals and trees adopt the abnormal signals and change the behavior. We have analyzed the changing behavior of recorded signal by live sensors (i.e., banyan tree). So we use the deep-rooted and long-aged banyan tree. The root of banyan tree (long-aged) has been working as a live sensor to record the geological and environmental changes. We record the low frequency signals propagated through solar-terrestrial environment which directly affect the root system of the banyan tree and changes that have been observed by live sensors. Then, very low frequency (VLF) signal may propagate to the earth-ionosphere waveguide. We have also analyzed the different parameters of live cells which is inbuilt in latex of the tree, so we record the dielectric parameters of green stem latex and found some parameters i.e., dielectric constant (ε) and dielectric loss (ε') of various trees to verify these natural hazards and found good correlation. Therefore, we can say by regularly monitoring the bio-potential signal and dielectric properties of banyan tree and we are able to find the precursory signature of seismic hazards and environmental changes.

Keywords: Dielectric Constant; Dielectric Loss; Earthquake; Latex; Seismo-electromagnetics

ARTICLE INFO

COPYRIGHT

1. Introduction

Earthquake is a very devastating phenomenon occurred in earth surface due to sudden moment of plate tectonic theory. Earthquake prediction is a new area of research at present, which serves as a promising tool in finding the natural hazard and minimizing loss of life and property. It is nevertheless not that easy to identify the seismic signals when a terrible earthquake is about to come. When rocks collided with each other, low level electromagnetic waves were generated in the vicinity of prone area. If we have access to detect such waves, it will help us to predict the precursory signature of earthquake, thus enabling us to define the time, place and magnitude of earthquake. However, scientists still have difficulty in predicting and analyzing such low level electromagnetic waves, because these abnormal signals may originate before every natural hazard, for instance, before the initiation of active volcanoes, landslides, earthquakes, hurricane, tsun-

ami and so forth. Here, we focus on seismic electric signals or activities, which consist of series of waves originated before the commencement of earthquakes in several areas in the country. Certain green plants, such as mimosa pudica, venus flytraps and banyan trees, with deep root and long age, are very sensitive to electric signals. These trees can sensibly perceive the environmental changes which we use as the indication of seismic activity. Therefore, we require a system, and with the help of such system, we are able to define the precursory signature of any seismic activity. It has been reported in previous research that ground-based observations of ultra-low frequency signals and very low frequency signals (0.01-10 Hz) may show the precursory signature of earthquakes[1,2]. Many researchers have reported earthquake precursors from ground-based observations of ultra-low frequency (ULF) such as measured by Fraser Smith AC[1]. They reported the results of measurements of low frequency magnetic noise by two independent monitoring systems prior to the occurrence of the Ms = 7.1 Loma Prieta earthquake of 17 October 1989. Their measurements cover 25 narrow frequency bands in the more than six-decade frequency range 0.01 Hz-32 kHz, with a time resolution varying from a half hour in the ULF range (0.01-10 Hz) to one second in the extremely low frequency (ELF)/VLF range (10 Hz-32 kHz). The ULF system is located near Corralitos, around 7 km from the epicenter. The ELF/VLF system is located on the Stanford campus, about 52 km from the epicenter. However, the ULF data have some distinctive and anomalous features. First, a narrow-band signal appeared in the range (0.05-0.2) Hz around September 12 and persisted until the appearance of the second anomalous feature, which consisted of a substantial increase in the noise background starting on 5 October and covering almost the entire frequency range of the ULF system. Third, there was an anomalous dip in the noise background in the range (0.2-5) Hz, starting one day ahead of the earthquake. Finally, it is the most compelling that there was an increase to an exceptionally high level of activity in the range

(0.01-0.5) Hz starting approximately three hours before the earthquake. Further, while the systems were sensitive to motion, seismic measurements indicate that there were no significant shocks preceding the quake. Thus, the various anomalous features in our data and in particular, the large-amplitude increase in activity starting three hours before the quake may have been magnetic precursors. The results of precursory signature by electromagnetic emissions were reported by Hayakawa[3]. The electromagnetic phenomena of ground-based observations abrupt low frequency signals was measured by Varotsos P and Alexopolous K[4]. These signals have also been recorded by Gokhberg MB[5] with high frequency receivers. The propagation characteristic of low frequency signals during and before the time of seismic activities were recorded by various authors[6-8]. The characteristics of ultra-low frequency signals have less contamination, low skin depth and low attenuation propagated in seismic swarm reported by Park et al.[9] He explained mechanism with mathematical modeling and found that the low frequency signals propagating through large distance from epicenter has been received by resistivity of signal 1000 ohm meter for surrounding rock and 10 ohm meter for a 500 meter wide by 20 km deep fault and the mechanism of ultra-low frequency signals of electromagnetic field generation based on micro fracturing mechanism, whose creation and relaxation of charges at the walls of opening cracks ion from earthquake was explained by Molchanov OA and Hayakawa M[10]. This phenomenon is also verified by Benardi A, Gufeld IL, Hayakawa M, and Kopytenko Y[11-14]. They have been investigated thoroughly by different mechanisms and recording technique, and found that the ULF range is very prominent for seismic activity research. During the last couple of years, the seismic activities have generated unoccassionally, which has brought disastrous damage to human life and property. Various theories and mechanism have been produced to record the precursory signature of seismic activity by various researchers and such theories were approved by different experiential

verifications. Among them, one mechanism is adopted in this paper for precursory study of seismic activity. The mechanism of electromagnetic energy on latex involves the transport of the electrical charges by the ions present in the biomass cell wall and cellulose. Once the electromagnetic energy encountered with the latex, randomly oriented dipoles in dielectric material may align themselves in a direction opposite to applied external electric field. The molecule absorbs the energy stored as potential energy. By the mechanism of ionic conduction and dipole rotation, polar molecules vibrate and produce kinetic energy and the dielectric properties can be studied on the energy that is being reflected, transmitted through the surface and absorbed by the materials. Each type of energy is specified with its term. Dielectric constant (ε) is the ability of material to store electric energy reported by Ramasamy S and Moghtaderi B[15]. Dielectric loss (ε') is the characteristic of material to convert the electromagnetic energy into heat, which is clearly explained by Salema AA[16]. The relationship of these two values is represented by equation as follows:

$$\varepsilon^* = \varepsilon - j\varepsilon' \tag{1}$$

Where ε^* is the complex dielectric constant, while ε and ε' are the real and imaginary part of complex dielectric constant[15]. Loss tangent is the ratio of dielectric loss to dielectric constant. Omar and his group explained the attenuation of microwave power in materials resulted in heating, which has been compiled and characterized by EFB (Empty Fruit Bunch) for pyrolysis using microwaves as an alternative heating source[17]. EFB has been taken from a local oil palm mill and was subjected to fuel, chemical and dielectric property analysis. Notably, high water content is an advantage in microwave heating and gas water is a good microwave absorber, which results in fast drying. The dielectric properties of EFB were observed to be proportional to the moisture content. However, low values of both dielectric constant and loss of dried EFBs would require the addition of microwave absorbers

for pyrolysis reaction. The dipole rotation is depended on several factors such as moisture, frequency and fiber directions as discussed by Hussein I[18]. The study of dielectric properties of oil palm shell, oil palm fiber, empty fruit bunch, hardwood (Acacia mangium, Swietenia macrophylla and Maescpsis eminii) and switch grass[16-19] were reported by various authors and they have found the same type of correlation. In this paper, we will discuss the low frequency signals generated through collision of ground particles and propagated through earth medium and received by latex in the form of potential difference, which are received by (EPR-3531) Electronic Poly-recorder to determine the internal characteristics of latex i.e., the form of waves, which will give the amplitude and intensity of the signal. We also calculated dielectric properties like dielectric constant, dielectric loss of the latex, which verify and show a very good correlation with seismic activities.

2. Experimental set-up and ionospheric data

We have installed the three-channel Electronic Poly-recorder (EPR-3531) for receiving the bio-potential signals in the form of waveform. The system has been installed in rural area nearby active fault region (Mathura-Faridabad ridge) which is far away from artificial and manmade noise and characteristics of latex have been identified by LCR Hi-Tester Meter to analyze the dielectric properties like dielectric constant (ε), dielectric loss (ε') of latex material from deep-rooted trees (i.e., banyan trees of different ages) and simultaneous observation is taken by Terrestrial Antenna installed on a college building of three stories near to recording station of bio-potential signals. We have examined the real time data with different data of ionosphere, i.e., magnetic storm data and earthquake data, and found correlation between seismic and atmospheric activity simultaneously and we will discuss it later in our result section.

3
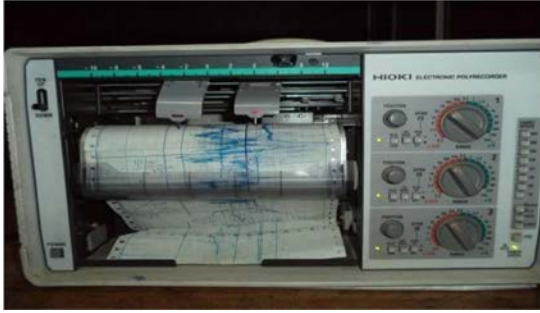
Electronic Poly-recorder (EPR-3531) Hi-Tester Meter (3235-50)

Figure 1. The Electronic Poly-recorder to measure the bio-potential and LCR Hi-Tester Meter for measuring the dielectric properties**.**

In order to measure the level of the signal strength at bio-potential antenna, we have taken the observations of the natural D.C. potential with respect to banyan tree using a digital multimeter model NO. MAS830L from 1 May, 2017 to 30 July, 2017. We found that the bio-potential increased from 10 to 50 mV from 1 May, 2017 to 30 July, 2017 on the occasion of seismic events before and after the occurrence of earthquake. The root of tree works as an antenna system to record the amplitude variation of signal generated in mV. It means that when the signal strength was larger than 200 µV/m at the antenna, the amplitude was enhanced as compared to the regular signal. We recorded the enhanced signal (around 30-45 mV) during the Rohtak earthquake. The signal at the antenna was assumed to propagate through the earth-ionosphere waveguide from the epicentral region of three earthquakes during which there was not much attenuation. These signals were observed in the form of signal bursts of varying amplitude in months which have been mentioned earlier in the paper, as observed at Farah, Mathura region, and were correlated with seismic activity data. The observations were taken in rural area and the bio-potential antenna was made by inserting silver electrodes in a banyan tree of some 100 years old. It has been found that during the days of seismic activity, the bio-potential data is dominated by the emission from a seismic source, while during non-seismic days, the data has been observed in normal potential, which is around 5-10 mV. Now we made the calculation of attenuation suffered by seismo-electromagnetic signals at a frequency of 3 KHz for a model of the earth's crust, in which the signal propagated from the source region in the middle layer to the top layer of the earth's crust, through the upper layer during the precursory surface of any seismic activity. We have analyzed the data of bio-potential, terrestrial and magnetic storm from 1 May, 2017 to 30 July, 2017 and done the statistical analysis of data and then found that the seismic activity will help us in predicting the natural hazards. In this analysis, the bio-potential signals was enhanced due to occurring of seismic activity but not more enhanced in terrestrial antenna recording signals during the precursory time. We have taken the data of earthquake from Indian Meteorological Department website to choose the data of local and regional earthquake nearby around 1000 km with low depth and high magnitude. The signal is received both by bio-potential and terrestrial antenna, and the enhancement of amplitude in terrestrial antenna is received at the same time as that of bio-potential. The more enhanced terrestrial signals is eliminated by low pass filter with MATLab software.
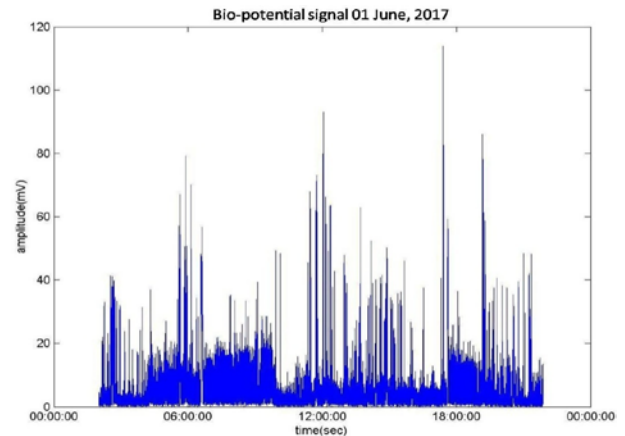
Figure 2. The signal bursts of varying amplitudes recorded by bio-potential antenna recorded at Mathura**.**

4

3. Results and discussion

When any seismic activity occurred under the ground, the emission has been responded with abrupt changes in amplitude, polarization ratio, statistical analysis at the time of event, before and after the occurrence of seismic activity and verified the atmospheric signals which is only recorded in terrestrial antenna instead of ground-based sensors. Now for more authentication, we have started the bio-potential study by electronic poly recorder and the internal characteristic has been analyzed by LCR Hi-Tester Meter, which have provided real mechanism of generation of seismic activity to be discussed later. We have analyzed the data of bio-potential by deep-rooted banyan tree and found that the abnormal amplitude signal was enhanced during and before the seismic activity, which was greater than the mean value. The amplitude variations of the transient change of potential difference (bio-potential) are shown by solid lines (blue color) in **Figure 2** and comparison with seismic activity data was discussed in **Figure 8**, which verified that the signal has been generated under the ground and give the explanation of atmospheric signals and bio-potential respectively. In **Figure 3**, we see the signal bursts of varying amplitudes recorded at monitoring station by terrestrial antenna. We have plotted the amplitude (mV) on Y-axis and real time recorded on X-axis for 24 hours on 1 June, 2017. The area shown by blue color lines are the signal and spikes are the noises. Terrestrial antenna measures the coupling of atmosphere-lithosphere-ionosphere. It is clear that the signal bursts recorded by terrestrial antenna was not the original frequency because it is a mixture of different attenuations by various sources like aeroplane noises, some building noises, reflection of bird and manmade disturbances. So we can say that the signal received by the terrestrial antenna was not desirable signal for authentication of a seismic activity in sub-continent region. Signals received by terrestrial antenna are the source for indication of environmental variation and seismic hazards.
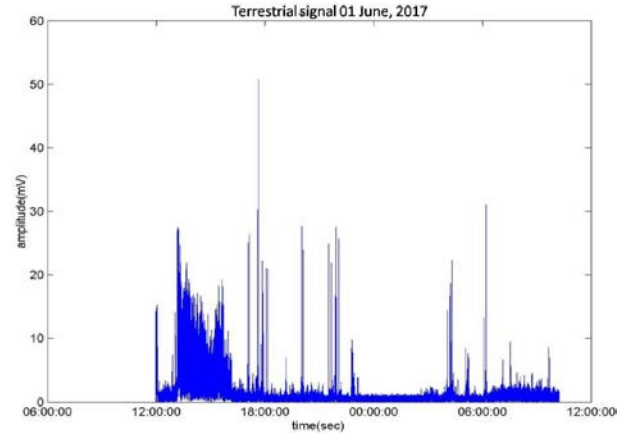
Figure 3. The signal bursts of varying amplitudes recorded by terrestrial antenna recorded at Mathura**.**

The amplitude variations of the transient change of potential difference between the two electrodes were obtained by inserting the electrodes in the tree (bio-potential) with time as shown in **Figure 2**. The signal enhancements have two possibilities. One is that the amplitudes were enhanced due to some changes in the atmosphere (i.e., seasonal variation and disturbed magnetic storm data) and the second possibility is that the amplitudes were enhanced due to the changes in potential difference between the two electrodes generated prior or during and after the earthquakes. The reason of the amplitude enhancements (bio-potential) is due to the movement of tectonic plates which create the pressure (in the form of energy) due to friction (i.e., dipping process of two plates with subduction zone and micro fracturing process). So, when any seismic activity occurred within 1000 Km region at a shallow depth, the pressure has been produced and released in the form of energy; When the energy has been come out near the root of old-aged tree, the potential has been changed abruptly. This phenomenon is responsible for the enhancement of amplitude of bio-potential data. **Figure 2** represents the signal received by Electronic Poly-recorder (EPR-3531). The signal received was further analyzed by MATLAB Software which can authentify the signal received by terrestrial antenna at the same date and time. The signal with less destruction, less noise and without attenuation of obstructs can easily be received by inserting electrodes in deep-rooted banyan tree, denoting that

5

the concentration of xylem and phloem was received in the graphical form with the help of EPR-3531. The signal received by terrestrial antenna and bio-potential antenna are verified by the study of dielectric properties of banyan tree (100 yrs), Banyan tree (50 yrs) and akkaua tree (10 yrs) respectively. We have also analyzed dielectric properties of latex of different trees to verify the terrestrial and bio-potential signal received. It is proved that when two types of latex is available from two types of trees, it is certain that one is lower-edge and shallow in depth while the other is old-aged and deep-rooted. As we all know, when the age of the tree succeeds, the latex of the tree becomes more concentrated in comparison to lower-aged tree. The similar type of analysis has been recorded on human blood by Gaur MS[20]. When electromagnetic wave energy is just near the circular radius of tree, the root absorbs electromagnetic energy, which directly affects the latex. And the loss has been increased due to increase of frequency, whose mechanism is similar to human nature of all circumstances with pressure of different ages. We have also analyzed the dielectric properties of green stem latex and found some parameters like dielectric constant (ε) and dielectric loss (ε') of various trees and found very good correlation with online seismic activities, which may be a precursory signature of hazards. As we can see in **Figure 4**, the dielectric constant (ε) of banyan tree (100 yrs.), banyan tree (50 yrs) and akkaua tree (10 yrs) is decreasing with the increase in frequency (Hz). When frequency increased from 1 to 10^5 Hz, dielectric constant was decreased. The result depicted that electric field of Hi-Tester Meter affected the interaction of latex and electromagnetic waves. When the frequency increased, a continuous varying electric field was created. This varying electric field created polarization in Latex. Dipole moment in latex gradually decreased as frequency increased. So, dipole had shorter time to realign itself according to the oscillating electric field[2,21]. Conductive effect of electromagnetic wave heating also diminished quickly in high frequency[5]. Hence, dielectric constant which indicated the ability of

material to store electric energy decreased.

Dielectric loss (ε') is the ability of material to convert the electromagnetic energy into heat. Dielectric losses of all the trees used in study were increasing when the frequency increased from 103 to 105 Hz. Beyond 104 Hz, the dielectric loss was slightly increased with the increasing of frequency. This dielectric loss trend was observed due to different electrical conductivity of long-aged banyan tree (100 yrs), banyan tree (50 yrs) and akkaua tree(10yrs) at varying frequency as reported in an earlier study of Salema *et al.*[16] When the seismic activity occurs, the dielectric loss increases because the electromagnetic waves diminish the latex of tree as reached in contact with deep-rooted trees like banyan tree. **Figure 4** deals with the study of dielectric properties of different tree roots. For more authentications of results received by both antennas, we have started the dielectric study of latex obtained from various trees like banyan tree (100 yrs), banyan tree (50 yrs) and akkaua tree (10 yrs). We have seen that dielectric constant of 100 yrs banyan tree is stronger in comparison to trees of other ages. Banyan tree is deep-rooted and the roots are reached to the faults created by movement of tectonic plates, which is the basic cause of disaster. Hence, we can say that if we regularly monitor the dielectric properties of banyan tree, we are in a position to make the statement regarding natural disaster.

We know that these variations in latex in the form of potential difference have the similar type of activity as in human's blood[20]. **Figure 5** reveals the study of dielectric loss measured by Hi-Tester Meter. We have analyzed the comparative study of dielectric loss at various frequencies. Dielectric loss of banyan tree (100 yrs) is less in comparison to other trees at same frequency under study. Dielectric properties of the latex of the banyan tree (100 yrs), banyan tree (50 yrs) and akkaua tree (10yrs) show a resemblance with the seismic activity and if we monitor the dielectric properties at regular intervals of time, they may help in giving the precursory signature of seismic hazards. Further, more studies and real time data have been required

to provide better explanation for the prediction of earthquake.
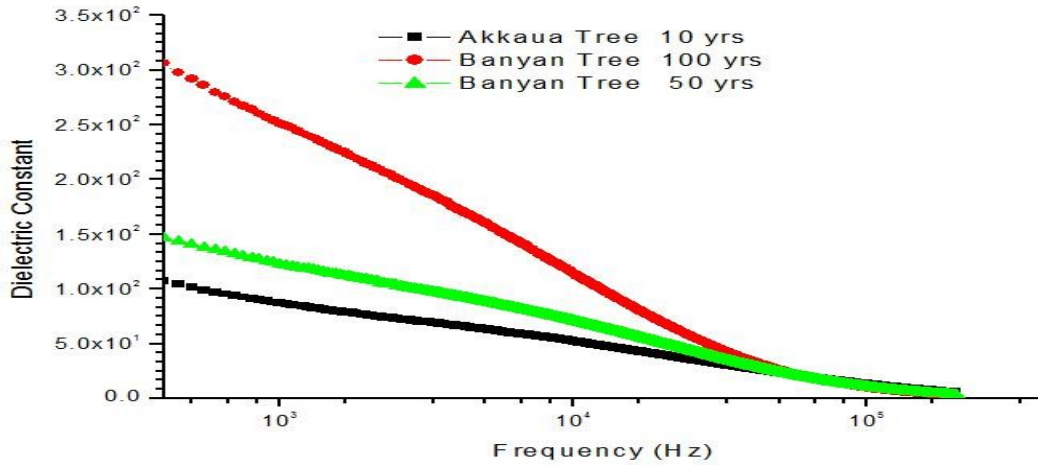
Figure 4. Dielectric constant of latex of banyan tree (100 yrs), banyan tree (50 yrs) and akkaua tree (10 yrs).
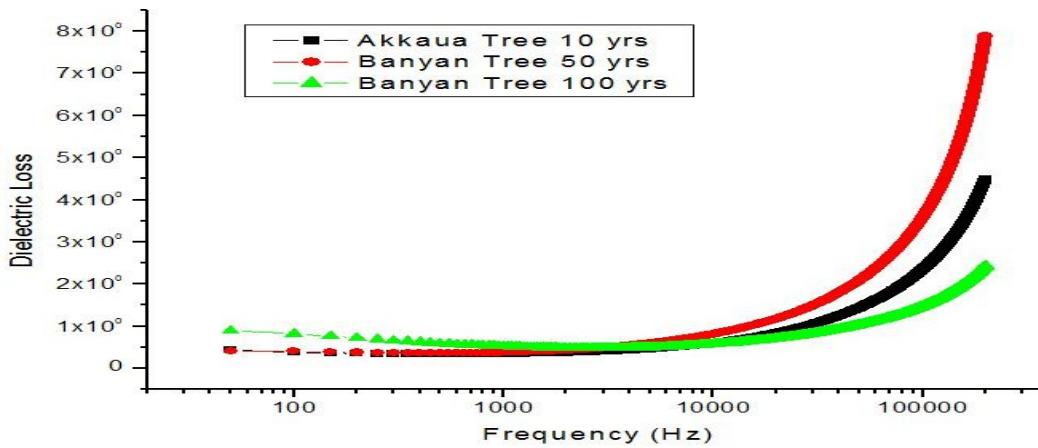
Figure 5. Dielectric loss of latex of banyan tree (100 yrs), banyan tree (50 yrs) and akkaua tree (10 yrs).

In **Figure 6**, the map shows the position of Delhi-Himalayan belt and the fault region on main boundary fault. This actual fault line created around 1880 under an impact of a big earthquake. These signals were observed in the form of signal burst of varying amplitude in recent time, whose date have been mentioned earlier in this paper, as observed at Farah, Mathura region and were correlated with seismic activity data discussed earlier case by case. The observations were taken in rural area and the bio-potential antenna was made by inserting silver electrodes in a banyan tree, around 100 yrs old. Under the guidelines of model calculation of Arora BR and Singh BP[22], we have considered two flat values of conductivities, 10^{-2} S/m for the upper layer and 10^{-4} S/m for the middle layer and calculated attenuation of magnitudes for all emissions between ultra-low frequency signals and

very low frequency signals. We have taken the conductivity model of upper layer conductivity range from Tsarev VA and Sasaki V[23]. They suggested that the range of the upper layer is 10^{-2} – 10^{-1} S/M with the lower basement conductivity around 10^{-2} S/M. They also suggested that the attenuation for ELF (extremely low frequency) range of signals is between 3 Hz and 30 kHz, but it increases steeply from ultra-low frequency to high frequency signals. The model of electromagnetic signal propagation through seismic faults activity, as a waveguide, is similar to earth-ionosphere waveguide. Since there exist a long distance fault known as MBF (main boundary fault) at the northern base of the Himalayan belt, extending between north west and north east India and the seismic activity occurred in nearby 500 km radius range. It is found that active fault of Mathura-

Faridabad total region is considered as MBF, so we have recorded the signal in very precise time.

National Center for Seismology, MoES
Preliminary Information of Significant Earthquakes

2017-06-01   22:55:56   04:25:56/02-06-2017   28.8 N   76.7 E   22   5.0   Rohtak

Figure 6. The position of Delhi-Himalayan belt and the fault region on main boundary fault**.**
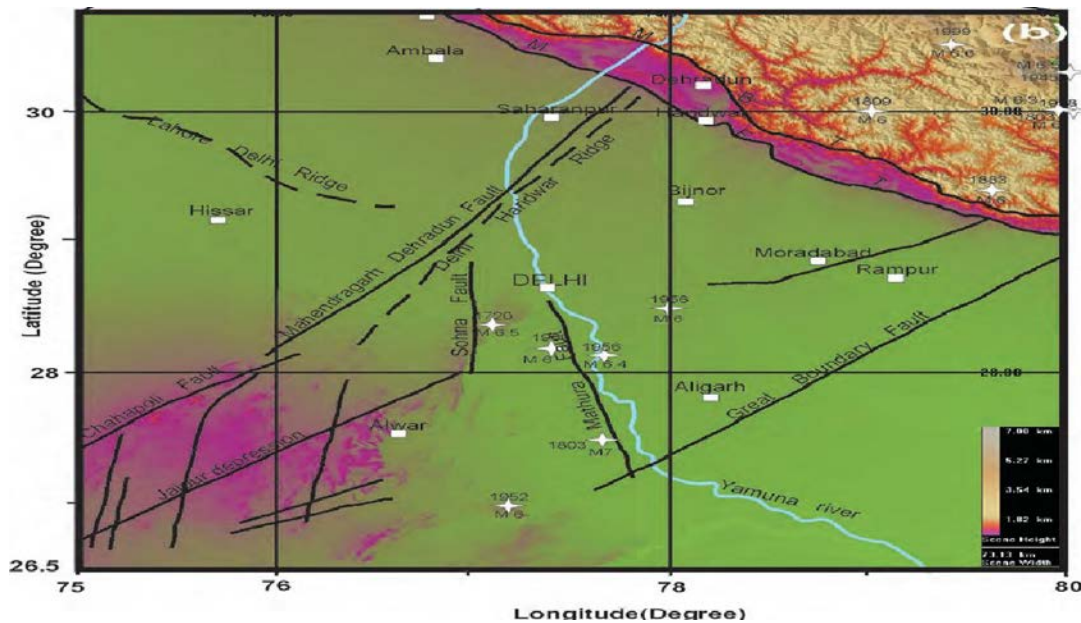
Figure 7. The earthquake of magnitude 5 richter scale taken from IMD, Delhi**.**

The information of earthquake we have taken from Indian Meteorological Department website shows that the seismic activity occurred on 1 June, 2017 at Longitude 76.7° E and Latitude 28.8° N. The map of seismic activity in Indian region is presented in **Figure 7**, showing the earthquakes with preferred latitudes and longitudes and the location of receiving station marked by an asterisk and earthquakes marked by star is also displayed in this map. The low frequency signal penetrated the earth surface and propagated the ionosphere was received by terrestrial antenna. So, many earthquakkes occurred at several regions in the above mentioned time period, but we have chosen the strong magnitude earthquake with reference of receiving enhanced signal and the signal is verified by various analysis, which gave clear indication of precursory signature of seismic activity.
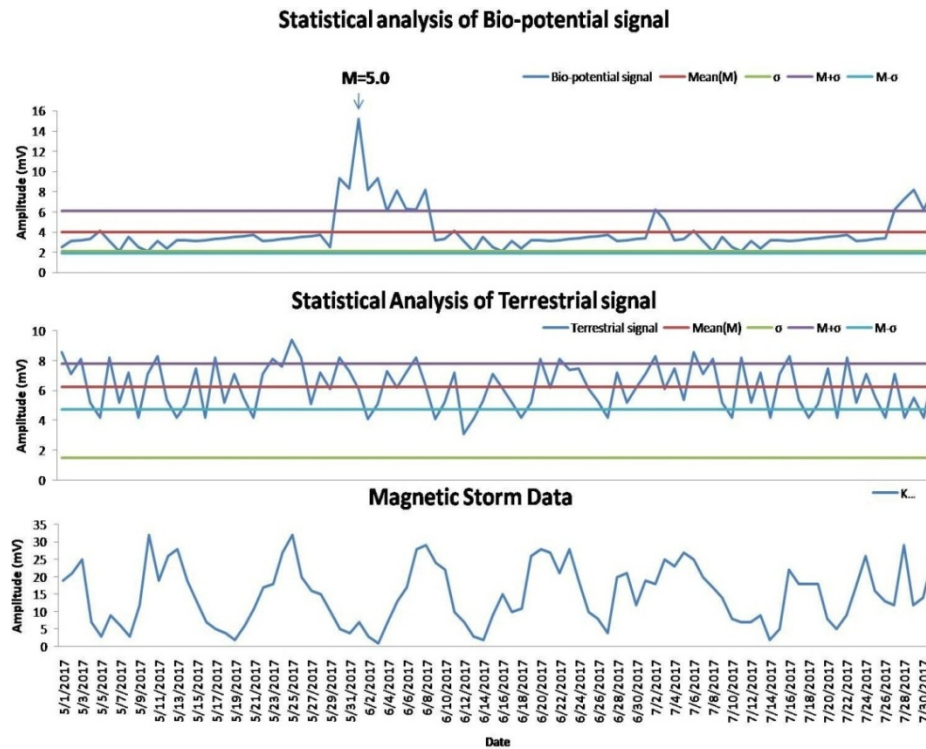
Figure 8. The statistical analysis of bio-potential signal, terrestrial signal and magnetic storm data.

4. Statistical analysis of data

In **Figure 8**, we applied statistical analysis to verify the data recorded by bio-potential sensor. We found that, there are the large enhancements in amplitudes from regular amplitude fluctuations, so we plotted graph on the same scale to view the changes in all the data observed at the same period from positive to negative fluctuations. The amplitude variations of the transient change of potential difference (bio-potential) are shown by solid lines (blue color) in the upper panel. Here, the amplitudes are passed within standard deviations during the whole period of analysis, and we found a day (1 June 2017 and 28 July 2017) when the amplitude was abnormally enhanced to search the possibilities of amplitude enhancement by rigorous analysis for this data. And the two possibilities related to amplitude enhanced signals have been found. One is that the amplitudes were enhanced due to some changes in the atmosphere. (i.e., seasonal variation and disturbed magnetic storm data) which is plotted in the bottom panel and the second possibility is that the amplitudes are enhanced due to the changes in potential difference between the two electrodes

generated prior or during and after the earthquakes. The reason of the amplitude enhancements (biopotential) is due to moment of tectonic plates which create the pressure (in the form of energy) like friction (i.e., micro fracturing process). So, when any seismic activity occurred within 1000 km region at a shallow depth, the pressure has been produced and released in the form of energy; When the energy has come and filled in previous fault line which are active, the electromagentic signals are moved in this fault and received out near the deep rooted old-age tree, which is worked as a live sensor. The precursory electromagnetic emissions have been generated before any seismic activity due to the inner particle of the earth (i.e., sand, which is associated with various element such as Na, K, S, Au, Ag, Fe, etc.) collided with each other by fracturing process, tectonic plate movement and electronic kinetic effect. And then the energy accumulated in the form of emissions and propagated in near active fault channel, so the bio-potential is enhanced due to very complex region and other enhancement recorded on 28 July, 2017. Due to the enhancement of magnetic storm data generated from sun penetrating the ground surface of the earth,

it is necessary to distinguish the enhanced bio-potential signal between earthquake and magnetic storm.

5. Conclusions

We have analyzed the data of bio-potential, terrestrial and magnetic storm from 1 May, 2017 to 30 July, 2017 and found that the study on seismic activity will also help us in predicting other natural hazards after a series of statistical analysis. In this study, we compared the dielectric properties of 100 yrs banyan tree, 50 yrs banyan tree and 10 yrs akkaua tree and found that dielectric constant of 100 yrs banyan tree is stronger in comparison to 50 yrs banyan tree and 10 yrs akkaua tree. We also compared dielectric loss of 100 yrs banyan tree, 50 yrs banyan tree and 10 yrs akkaua tree and found that dielectric loss of 100 yrs banyan tree is less in comparison to 50 yrs banyan tree and 10 yrs akkaua tree. It means the 100 yrs banyan tree has more strength to sense the electromagnetic waves originated during and before any seismic hazards. This natural disturbance causes the increase of relaxation process and produces the change in bio-potential from time to time in order to develop a clear understanding of this process. We have conducted the experiment to measure relaxation process by means of dielectric properties. Consequently, we can say dielectric properties are also helpful in verifying the precursory signature of seismic activity. We conclude that when the higher magnitude signal or high energy signal reach in contact with latex of banyan tree roots, it absorbed the energy while the latex is shrinking during the time, which is a precursory signature of seismic hazards. We identified the different parameters correlated with the mechanism of dielectric properties of materials i.e., similar to human blood[20]. We recorded the signal in terrestrial antenna and electronic poly recorder to study the dielectric properties of banyan tree, which is verified by statistical analysis, and we found that there are very good correlation between them. It means we are in a position to say that we are able to predict the precursory signature of any seismic

hazard occurred in nearby fault region save the life of the people and provide disaster forecast for the future.

Conflict of interest

The authors declare that they have no conflict of interest.

References

1. Fraser-Smith AC, Bernardi A, Mc Gill PR, *et al*. Low-frequency magnetic field measurements near the epicenter of the Ms 7.1 Loma-Prieta earthquake. Geophysical Research Letters 1990; 17(9): 1465–1468.
2. Fraser-Smith AC, Mc Gill PR, Helliwell RA, *et al*. Ultra-low frequency magnetic field measurements in southern California during the Northridge Earthquake of 17 January 1994. Geophysical Research Letters 1994; 21(20): 2195–2198.
3. Hayakawa M, Itoh T, Hattori K, *et al*. ULF electromagnetic precursors for an earthquake at Biak, Indonesia on February 17, 1996. Geophysical Research Letters 2000; 27(10): 1531–1534. doi: https://doi.org/10.1029/1999GL005432.
4. Varotsos P, Alexopolous K. Physical properties of the variations in the electric field of the earth preceding earthquakes. Tectonophysics 1987; 136 (3-4): 335–339.
5. Gokhberg MB, Gufeld IL, Rozhnoy AA, *et al*. Study of seismic influence on the ionosphere by super long-wave probing of the earth-ionosphere waveguide." Physics of the Earth and Planetary Interiors 1989; 57(1-2): 64–67.
6. Molchanov OA, Hayakawa M. On the generation mechanism of ULF seismogenic electromagnetic emissions. Physics of the Earth and Planetary Interiors 1998; 105(3-4): 201–210.
7. Galprin YI, Hayakawa M. On the magnetospheric

effects of experimental ground explosions observed from AUREOL-3. Journal of Geomagnetism and Geoelectricity 1996; 48(10): 1241–1263.

8. Parrot M, Mogilevsky MM. VLF emissions associated with earthquake observed in the ionosphere and magnetosphere. Physics of the Earth and Planetary Interiors 1989; 57(12): 86–99.

9. Park SK, Johnson MJS, Madden TR, *et al*. Electromagnetic precursors to earthquakes in ULF band: A review of observations and mechanism. Reviews of Geophysics 1993; 31(2): 117–132.

10. Molchanov OA, Hayakawa M. Generation of ULF electromagnetic emission by microfracturing. Geophysical Research Letters 1995; 22(22): 3091–3094.

11. Benardi A, Fraser-Smith AC, McGill PR, *et al*. ULF magnetic field measurements near the epicenter of the Ms 7.1 Loma Prieta earthquake. Physics of the Earth and Planetary 1991; 68(1-2): 45–63.

12. Gufeld IL, Gusev G, Pokhhotelov O. Is the prediction of earthquake data possible by VLF radio wave monitoring method? In: Electromagnetic phenomena related to earthquake prediction. Tokyo: TERRAPUB; 1994. p. 381.

13. Hayakawa M, Molchanov OA, Ondoh T, *et al*. On the precursory signature of Kobe earthquake on VLF subionospheric signal. Proceedings of International Symposium on Electromagnetic Compatibility; 1997. p. 72–75. doi: 10.1109/ELMAGC.1997.617080.

14. Kopytenko Y, Ismagilov V, Hayakawa M, *et al*. Investigation of the ULF electromagnetic phenomena related to earthquake: contemporary achievements and the perspectives. Annali Di Geophysica 2001; 44(2): 325–334.

15. Ramasamy S, Moghtaderi B. Dielectric properties of typical Australian wood-based biomass materials at microwave frequency. Journal of Energy Fuels 2010; 24(12): 4534–4548.

16. Salema AA, Yeow YK, Ishaque K, *et al*. Dielectric properties and microwave heating of oil palm biomass and biochar. Industrial Crop Production 2013; 50: 366–374.

17. Omar R, Idris A, Yunus R, *et al*. Characterization of empty fruit bunch for microwave-assisted pyrolysis. Fuel 2011; 90(4): 1536–1544.

18. Husein I, Sadiyo S, Nugroho N, *et al*. Electrical properties of Indonesian hardwood. Case study: Acacia mangium, swietenia macrophylla and maesopsis eminii. Wood Research 2014; 59(4): 695–704.

19. Motasemi F, Afzal MT, Salema AA, *et al*. Microwave dielectric characterization of switchgrass for bioenergy and biofuel. Fuel 2014; 124: 151–157.

20. Gaur MS, Tiwari RK, Shukla P, *et al*. Thermally stimulated current analysis in human blood. Trends in Biomaterials and Artificial Organs 2007; 21(1): 8–13.

21 Ahmad Z. Polymeric dielectric materials. Dielectric Material 2012; 3–26. doi: https://10.5772/50638.

22. Arora BR, Singh BP. Himalayan seismicity. In: Gupta HK, Gupta GD (editors). Bangalore: Memoir; 1992. p. 23, 223.

23. Tsarev VA, Sasaki V. Low frequency seismogenic electromagnetic radiation: How does it propagate in earth's crust and where it can be detected? In: Hayakawa M (editor). Atmospheric and ionospheric electromagnetic phenomena associated with earthquakes. Tokyo: Terra Scientific Publishing Co.; 1999. p. 383.

ORIGINAL RESEARCH ARTICLE

Analysis of shoreline changes along the coast of Tiruvallur district, Tamil Nadu, India

K. Jayakumar[*]

Centre for Remote Sensing and Geoinformatics, Sathyabama Institute of Science and Technology, Rajiv Gandhi Road, Jeppiaar Nagar, Sholinganallur, Chennai 6000119, TN, India; E-mail: jaikumar.gis@gmail.com

ABSTRACT

Shore line change is considered as one of the most dynamic processes, which were mapped along the coast of Tiruvallur district by using topographic maps of 1976 and multi-temporal satellite images. The satellite images pertaining to 1988, 1991, 2006, 2010, 2013 and 2016 were used to extract the shorelines. It is important to map and monitor the HTL (High Tide Line) at frequent time intervals as the shoreline was demarcated by using visual interpretation technique from satellite images and topographic maps. Followed by this, an overlay analysis was performed to calculate areas of erosion and accretion in the study area. The results revealed that the coast of Tiruvallur district lost 603 ha and gained 630 ha due to erosion and accretion respectively. It was confirmed after the ground truth survey carried out in the study area. The high accretion of 178 ha was found nearby Pulicat Lake and low accretion of 19 ha was seen between Pulicat Lake and Kattupali Port. The high erosion area was found along the Pulicat Lake, Kattupali and Ennore ports, and Ennore creek mouth and southern Ennore such as Periya Kuppam, Chinna Kuppam, Kasi Koil Kuppam, and Thyagarajapuram. It may be concluded that the coastal erosion and accretion in the study area were mainly caused by anthropogenic and natural factors, which altered the coastal environment.

Keywords: Erosion; Accretion; Shoreline; Multi-temporal; Overlay Analysis; Coastal Zone

1. Introduction

India has a long coastline extending over a length of 7,517 km, in which 5,423 km belongs to the mainland covering 9 states, while 2,094 km belongs to islands territories including two union territories according to India State of Forest Report in 2015. Tamil Nadu constitutes a length of coastline 1,075 km, of which 27.9 km occupied by Tiruvallur district. It is straight and also the twelfth largest coast in Tamil Nadu and falls on the Bay of Bengal. The major coastal land form features of the coast of Tiruvallur district include rivers, beaches, coastal dunes, mudflats, backwater, mangroves, saltpans, aquaculture, spits and strand features[1]. The shoreline is one of the most dynamic coastal landform features in the coastal zone and various geological processes are involving and altering the shore line, which includes deposition, erosion, sedimentation, tsunami, cyclone, storm surge, flooding, waves, winds, tides, currents, and sea level raises and so forth. On the other hand, man-made disturbances, like construction of jetties, ports, sea walls, groins, mining of the beach sand, breakwaters, urbanization, garbage dump, industrialization, discharge of domestic wastages, industrial effluent, recreational activities and reduction in sediment supply from the rivers etc. are also changing the shoreline.

These two factors are the main causes for shore line changes which lead to erosion and accretion in short-term and long-term[1-5], which play a crucial role in impacting the surrounding habitats and shore lines as well. Remote sensing technology was employed, since 1980, throughout the world to understand the shore line changes and explain their causes and quantum[6-9].

As modern scientific tools, remote sensing and GIS have benefited us a lot in mapping and monitoring the shoreline changes for long time periods, thus helping evaluate erosion and accretion[3–5,8]. In the study of Manik Mahapatra *et al.*[4], digital shoreline analysis system has been used to analyze the coast of south Gujarat, India. Saranathan *et al.*[3] have used remote sensing and GIS tools to explain how the shoreline changes in Tarangampadi village, Nagapattinam district, Tamil Nadu, India. Anil Cherian *et al.*[10] studied the assessment of coastal erosion along the southern Tamilnadu coast and carried out a risk assessment by setting indicators of coastal erosion. Jayakumar and Malarvannan[1] have developed WebGIS for managing the shoreline changes in the Northern Tamil Nadu coast. In Faik Ahmet Sesli's study[8], aerial images and digital photogrammetry data was used to monitor the coast from 1935 to 2006 in Samsun, Turkey. Another study by Bertacchini and Capra[11] provided very high resolution satellite images for two places in Italy, which was very useful for map updating and environmental monitoring. The present study is intended to use multi-temporal satellite images to record the impacts from both natural and human on the coast of Tiruvallur district and to analyze morphological differences, variations in shoreline changes, erosions and accretion. Since there were no details of shoreline changes study conducted on the coast of Tiruvallur district, it is the need of hour to address the changes in shoreline along the coast of Tiruvallur and frequently publish the reports for formulating policies, which will better improve planning and management of coastal resources. The aim of the present study is to analyze the shoreline changes along the coast of Tiruvallur and evaluate erosion and deposition over the periods of 40 years from 1976-2016.

2. Study area

Tiruvallur district is located in the Northernmost district in Tamil Nadu, India. There are two taluks consisted by the coast of Tiruvallur district, namely Ponneri and Thiruvottriyur (**Figure 1**). As per census of India 2011, the total population of Tiruvallur district is about 3,728,104, of which the total population of the Ponneri taluk is about 389,862, and the Thiruvottriyur taluk is about 596,156. The population statistics showed that these two taluks are highly populated and all people are living in the coastal area itself, which made these taluks economic centres of the district and state as well. The major economic activities of these two taluks include fishing, shipping, tourism, agriculture, aquaculture, salt pans and industrial activities. Benefited by these activities, these taluks support the overall economy of the district and state. The total number of fishing communities in the district is about 54,420, which comprises of 58 fishing villages, 17 revenue villages and 28 fish landing center. The present study area lies between 13°26′41″-12°23′25″ N latitudes and 80°19′31″-80°6′9″ E longitudes. The coastal zone of Tiruvallur district is very narrow and a few places where extensive mud flat is present because of Ennor Creek and Pulicat Lake. The coastline length of Tiruvallur district covers 27.9 km with an elevation of 5 meters. In the recent past, reports and articles highlighted the vulnerability of the coast of Tiruvallur district. The major impacts include shoreline changes and erosion due to a thropogenic and natural factors affecting the study area because it is located close to road, residency and businesses all along the shoreline. Additionally, ecological sensitive areas of Pulicat Lake, Ennore Creek, Kattupali and Ennore ports are also presented along this coastline within 100 meters distance. If there occur any natural calamities, the impact would be very high. For example, land submerged in the sea due to coastal erosion. The coast showing direct or indirect connections with shoreline changes have been selected and examined in detail with

13

respect to present shore line. The main objective of this study is to analyze the shoreline changes along the coast of Tiruvallur and evaluate erosion and deposition from 1976 to 2016.
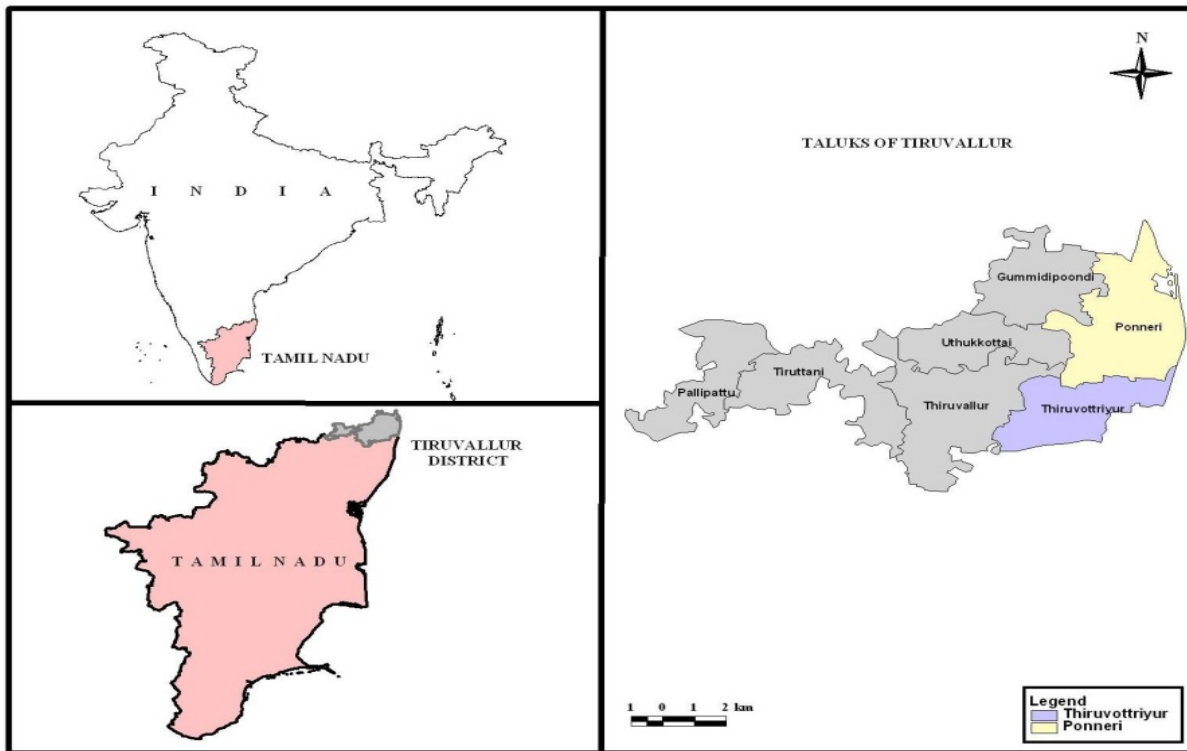
Figure 1. Study area map of taluks of Tiruvallur coast**.**

3. Materials and methodology

In this study, two types of data have been used, including topographical maps and satellite data. First, the satellite data of Landsat-5 TM (Thematic Mapper) data of 1988, 1991 and 2006 and Landsat-7 ETM+ (Enhanced Thematic Mapper Plus) data of 2010, 2013 and 2016 were downloaded from the U.S. Geological Survey (USGS) website[12]. Second, the topographic maps of the 66 C2, C6, C7 and C8 were purchased from Survey of India (SOI) at 1:50,000 for the year of 1976, which were scanned and georeferenced. The satellite images of study were imported to ERDASIMAGINE 2011 software and performed layer stacking followed by gap filling for the image of 2010 of Landsat-7 ETM+. All these images were corrected with reference to topographic maps for distortion and adjusted to the correct scale using ground control point sand rectified by using UTM projection with WGS 84 datum. Finally, visual interpretation technique was adopted to digitize the shorelines of Tiruvallur for all the different years (line of the high water level). Erosion and accretion in different shorelines along the coast of Tiruvallur were compared and calculated, as is shown by a flow chart of methodology in the **Figure 2**. The digital datasets of shore line changes were finalized after ground truth verification and Google earth images.
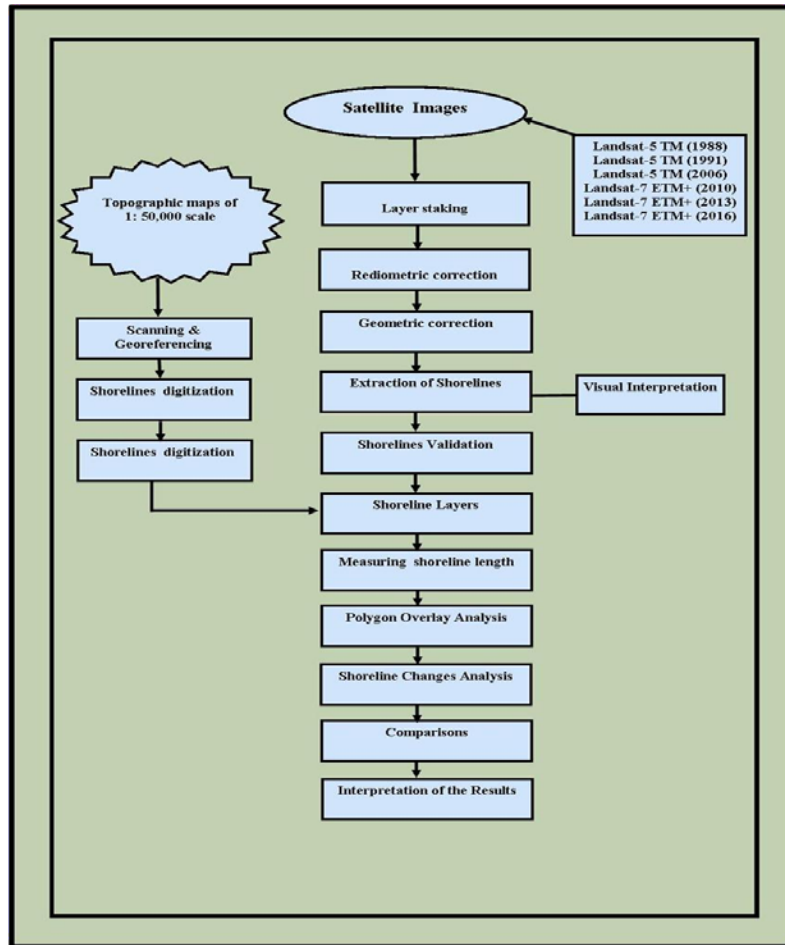
Figure 2. A flow chart of methodology**.**

4. Results and discussion

In this study, application of remote sensing and GIS technology were used, which are known as the most effective scientific tools for mapping, monitoring and analyzing shoreline changes and evaluating erosion and accretion along the coast of Tiruvallur district for the period of four decades from 1976 to 2016. The coast of Tiruvallur is shrinking and changing as it becomes increasingly vulnerable to storms, flooding and other natural disasters, which cause coastal erosion and the retreating of shore line. Apart from this, the man-made coastal erosion has reached alarming proportions in Tiruvallur, which is threatening the future of the two taluks Ponneri and Tiruvattriyur as well as the fishing villages within them. Coastal erosion, in which waves, is destroying around a half meter to one meters of shoreline every year. In some locations, up to two meters has disappeared over the same period. There is a chance to submerge of land area, when sea level is increasingly rising so as to impact infrastructures like roads, buildings, vegetation and ground water sources, coastal and terrestrial environment. A similar study by Gnanappazham[13] used remote sensing to manage shoreline changes in the Pichavaram mangrove wetland over the 76 years, in which the author highlighted that the natural and anthropogenic factors were the main causes for shrinking coastline. Another study by Jayakumar[5] was also confirmed by using remote sensing technology for the management of Godavari wetland from 1938 to 2012, in which the author highlighted that shoreline changes, erosion and accretion were occurring mainly due to anthropogenic causes, which would impact the coastal environment in the near future. The shore line for 1976, 1988, 1991, 2006, 2010, 2013 and 2016 were generated in **Figure 3**. These shore lines were overlaid one over the other in order to find out areas of erosion and accretion between 1976-

1988, 1988-1991, 1991-2006, 2006-2010, 2010-2013 and 2013-2016 (**Figure 4**). A similar study from Jayakumar and Malarvannan[1] on shore line change was carried out to find the changed and unchanged part of the shore line with overlay analysis. For example, **Figure 4** showed that the shoreline of 1976 was used as a reference line followed by an inner line and an outer line of 1988 as called erosion and accretion respectively. The erosion and accretion are represented by red and green colours respectively. It is easy to find the amount of erosion and accretion from 1976 to 2016, which will help users to predict the amount of erosion and accretion in future as well. This study can be considered as a decision support system with regard to Tiruvallur coast, as it shows spatial and temporal changes in the study area, which is priceless for the users who are working on the coastal zone managements.
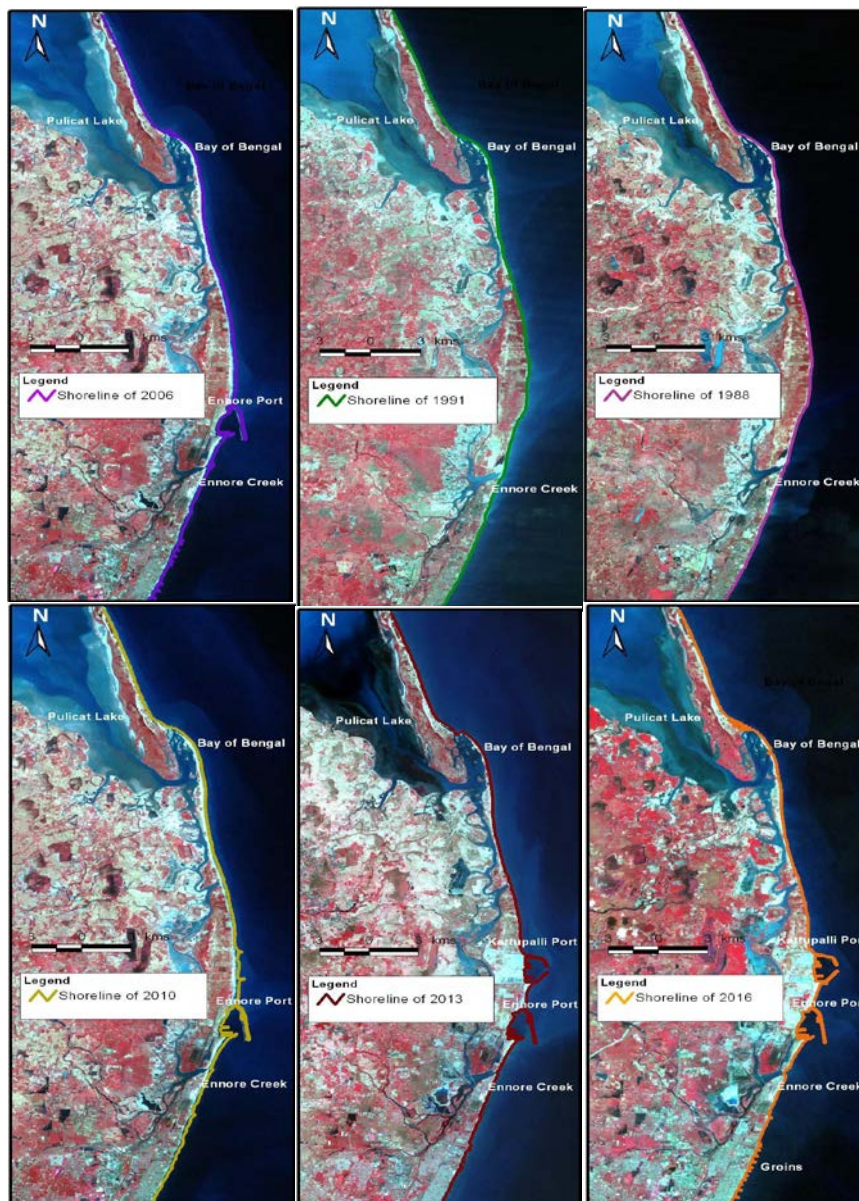
Figure 3. Shore line changes maps of Tiruvallur from 1976 to 2016**.**
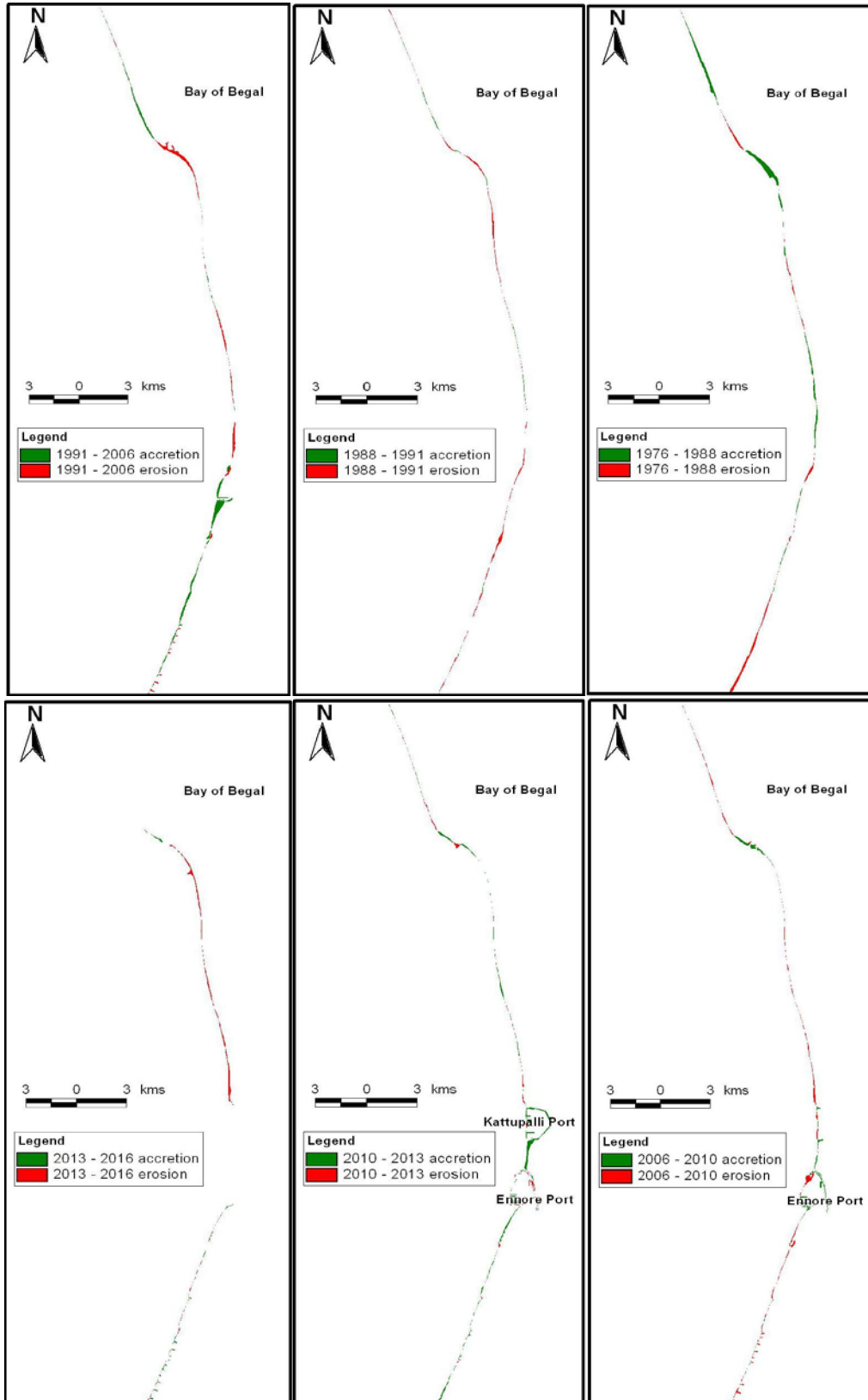
Figure 4. The maps displayed erosion and accretion variation between 1976 and 2016.

4.1 Tiruvallur coast

The total coast line length of Tiruvallur coast is 27.9 km and covers two taluks, namely Ponneri and Thiruvottiyur taluks, which have a total of 53,007 fishing communities; 58 fishing villages; 17 revenue villages; 28 fish landing centers. Within the study area, it was identified that the most hazardous zones include Kattupalli, Ennore Creek and from Ennore to Thygarajapuram. The main coastal villages of Pulicat, Minjur, Ennore and Thiruvottiyur are dominated by fishermen community and their primary occupation is also fishing. The results revealed through remote sensing about 178 ha of accretion and 126 ha of erosion were observed in the study area over a period of 40 years as shown in **Table 1**. In detail, the erosion was about 108 ha between 1988 and 1991 followed by 126 ha during 1991 to 2006, 120 ha during 2006 to 2010, 37 ha during 2010 to 2013, 100 ha during 2013 to 2016, and 112 ha during 1976 to 1988. The accretion was observed about 178 ha during 1976 to 1988, 19 ha during 2010 to 2013, 172 ha 1988 to 1991, 76 ha during 1991 to 2006, 161 ha during 2006 to 2010, and 24 ha during 2013 to 2016 (**Figure 4**).

Table1. Erosion and accretion mapped using multi-temporal remote sensing (ha)

Districts		Tiruvallur	
Sl.No.	Year	Erosion	Accretion
1	1976-1988	112	178
2	1988-1991	108	19
3	1991-2006	126	172
4	2006-2010	120	76
5	2010-2013	37	161
6	2013–2016	100	24
Total		603	630

The following satellite images of 1988, 1991, 2006, 2010, 2013, 2016 and topographic maps of 1976 were used to delineate the shoreline positions for above mentioned years and they were overlaid one by one to calculate erosion and accretion over the period of 40 years from 1976 to 2016. The coast of Tiruvallur shoreline changes was mapped and then areas of erosion and accretion were calculated as shown in **Table 1** and **Figure 5**.
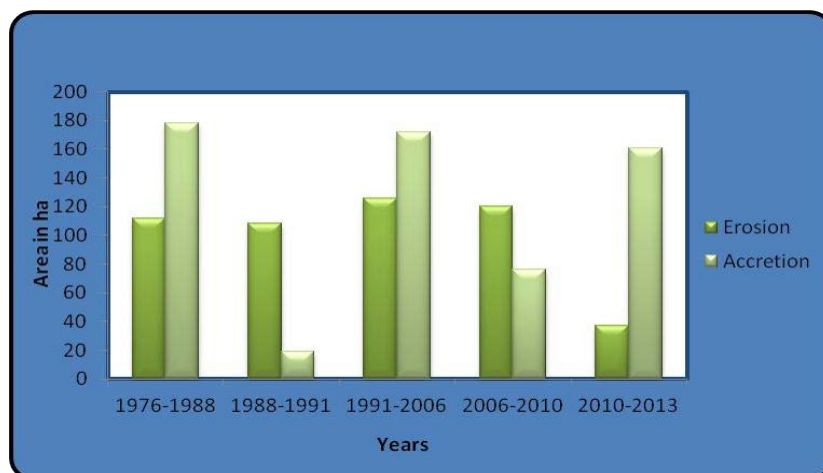
Figure 5. Changes in the area of erosion and accretion from 1976 to 2016**.**

18

4.2 Morphological changes of Tiruvallur district coast as follows

The coastline of Tiruvallur district coast is highly vulnerable under both human and natural interference, which played a crucial role over the four decades. The total length of coastline of the Tiruvallur district is about 27.9 km. The analysis of survey of India topographic maps and satellite images of Tiruvallur district indicated that the coastline is narrow and both Pulicat Lake and Ennore Creek were covered with extensive mud flat. Followed by this, man-made structures were observed in a few locations, including Ennore Thermal Power Station established in the year of 1970, Ennore Port constructed on 1st February, 2001, Kattupalli Port by 30th January, 2013 and various groins. The man-made structures coupled with dense inhabitation, industrialization, urbanization, development activities of port and fishing made shoreline more vulnerable under erosion, leaving less depositions. The analysis of shoreline changes with the support of satellite images and topographic maps showed the vulnerability zone of the Tiruvallur district coast. It may be pointed out that the construction of artificial structures such as ports, jetties, groins, beach nourishment, etc. and the presence of dense population are the main reasons for the negative effect of coastal environments. The study of Kasinatha Pandian *et al.*[14] also confirmed that the natural events such as tides, waves, currents, tsunami, coastal floods, climate changes and bathymetry effects are adding the changes in the coastal environment as well. A study from Jayakumar and Malarvannan[1] have confirmed that the reasons of shoreline changes are mainly due to development and extension activities of ports and other structures like construction, dredge, transportation, excavation, building, machinery on offshore, which induce several changes along the coast.

5. Conclusion

The coastal zone of Tiruvallur coast is highly vulnerable due to anthropogenic and natural causes. In this study, remote sensing and GIS technology were applied along the coast of Tiruvallur district for a period of 40 years from 1976 to 2016. It may be concluded that the construction of artificial structures coupled with natural events and the presence of dense population were the main reasons impacting coastal environment. The present study may benefits different stakeholders for developing policies and making decision to perform better management. It is the need of the hour to address and regularly update relevant study results on the coastal area environment, which will help the decision makers to immediately view scientific findings and addresses so as to speed up the evaluation process during the disaster periods.

Conflict of interest

No conflict of interest was reported by the author.

References

1. Jayakumar K, Malarvannan S. An assessment of shore line changes over the northern Tamil Nadu coast using open source based webGIS techniques. Journal of Coastal Conservation 2016; 20(6): 477–487.
2. To DV, Thao PTP. A Shoreline Analysis using DSAS in NarnDinh: coastal area. International Journal of Geoinformatics 2008; 4(1): 37–42.
3. Saranathan E, Chandrasekaran R, Soosai Manickaraj D, *et al*. Shoreline changes in Tharangampadi villages, Nagapattinam District, Tamil Nadu, India — A Case study. Journal of Indian Society of Remote Sensing 2011; 39(1): 107–115.
4. Mahapatra M, Ratheesh R, Rajawat AS. Shoreline change analysis along the coast of south Gujarat, India, using digital shore line analysis system. Journal of Indian Society of Remote Sensing 2014; 42(4): 869–876.
5. Jayakumar K. Remote sensing and GIS application in the management of Godavari mangrove wetland, Andhra Pradesh, South India. Thesis submitted to University of Madras; 2014. p. 150.
6. Marfai MA, Almohammad H, Dey S, *et al*. Coastal dynamic and shore line mapping: Multi-sources spatial data analysis in Semarang Indonesia. Environmental Monitoring and Assessment 2008; 142: 297–308. doi: https://doi.org/10.1007/s 10661-007-9929-2.
7. Zhang J, Wang Y, Wang Z. Change analysis of land surface temperature based on robust statistics in the estuarine area of Pearl River (China) from 1990 to 2000 by Landsat TM/ETM+ data.

International Journal of Remote Sensing 2007; 28(10): 2383–2390.

8. Sesli FA. Mapping and monitoring temporal changes for coastline and coastal area by using aerial data images and digital photogrammetry: A case study from Samsun, Turkey. International Journal of the Physical Sciences 2010; 5(10): 1567–1575.

9. Ramsay D. Coastal erosion and inundation due to climate change in the Pacific and East Timor. Synthesis report prepared by Department of Climate Change and Energy Efficiency, Government of Australia, 2011.

10. Cherian A, Chandrasekar N, Gujar AR, *et al*. Coastal erosion assessment along the southern Tamil Nadu Coast, India. International Journal of Earth Science and Engineering 2012; 5(2): 352–357.

11. Bertacchini E, Capra A. Map updating and coastline control with very high resolution satellite images: Application to Molise and Puglia coasts (Italy). Italian Journal of Remote Sensing 2010;

42(2): 103–115.

12. U.S. Geological Survey (USGS) website. Available from: https://www.usgs.gov/.

13. Gnanappazham L. A remote sensing and GIS based decision support system for effective management of Pichavaram mangrove wetland, South India. Thesis submitted to University of Madras; 2007. p. 170.

14. Pandian K, Ramesh P, Ramanamurthy S, *et al*. Shore line changes and near shore processes along Ennore Coast, East Coast of South India. Journal of Coastal Research 2004; 20: 828–845.

15. To DV, Thao PTP. A Shoreline analysis using DSAS in NarnDinh: Coastal area. International Journal of Geoinformatics 2008; 4(1): 37–42.

16. Zhang J, Wang Y, Wang Z. Change analysis of land surface temperature based on robust statistics in the estuarine area of Pearl River (China) from 1990 to 2000 by Landsat TM/ETM+ data. International Journal of Remote Sensing 2007; 28(10): 2383–2390.

ORIGINAL RESEARCH ARTICLE

Lead concentration in dust fall in Zahedan, Sistan and Baluchistan Province, Iran

Sara Abdollahi[1], Akram Karimi[2], Meysam Madadi[3], Saeid Eslamian[4], Kaveh Ostad-Ali-Askari[5*], Vijay P. Singh[6]

[1]*MSc in Environmental Sciences, Department of Environmental Sciences, Yazd University, Yazd, Iran.*

[2]*MSc of Environmental Sciences, College of Environment, Department of Environment, Karaj, Iran.*

[3]*MSc of Environmental Sciences, Department of Environmental Sciences, Gorgan University of Agricultural Sciences and Natural Resources, Gorgan, Iran.*

[4]*Department of Water Engineering, Isfahan University of Technology, Isfahan, Iran.*

[5]*Department of Civil Engineering, Isfahan (Khorasgan) Branch, Islamic Azad University, University Blvd, Arqavanieh, Jey Street, P.O. Box:81595-158, Isfahan, Iran. E-mails: koa.askari@khuisf.ac.ir; kaveh.oaa2000@gmail.com*

[6]*Department of Biological and Agricultural Engineering & Zachry Department of Civil Engineering, Texas A and M University, 321 Scoates Hall, 2117 TAMU, College Station, Texas 77843-2117, U.S.A.*

ABSTRACT

Dust is one of the atmospheric pollutants that have adverse environmental effects and consequences. Dust fall contains particles of 100 microns or even smaller ones, which fall from the atmosphere onto the earth surface. The aim of this study is to determine the concentration of lead in dust fall samples in order to study the pollution level of this element in Zahedan, Sistan and Baluchistan Province, Iran. Therefore, sampling was carried out using 30 marble dust collectors (MDCO) for 3 months in the spring of 2015 to investigate the quantitative variation and spatial analysis of lead content in dust fall. These dust collectors were placed at 30 stations on the building roofs with a height of approximately 1.5 meters across the city. According to the results, the mean lead concentration in the spring was 90.16 mg/kg. In addition, the zoning map of lead content shows that the lowest level of lead was measured at Imam Khomeini station while the highest amount of lead appeared in Mostafa Khomeini station.

Keywords: Dust Fall; Lead Content; Pollution; Zahedan

1. Introduction

Rabid urbanization and continued demand for infrastructure development in urban areas have led to disturbances and as a result, a significant decrease in the quality of urban environments[1]. Transportation development and associated environmental issues are important concerns for all countries throughout the world. Such development has many benefits, but it also contributes to enormous adverse impacts on the environment. The environmental problems caused by traffic are mainly due to highway toxic emissions, which will inevitably lead to air pollution. Traffic is responsible for the intense emission of a wide range of pollutants, especially heavy metals[2]. The phenomenon of dust storms is one of the serious problems in various regions in the world, including Iran[3]. This is while the largest part of dust in the atmosphere occurs with the origin of fine-grain particles. These particles are more prevalent in arid and

semi-arid regions of the world. In fact, the creation of dust can be a response to the change in the land cover. However, the role of human activities along with the natural conditions of the geographic environments should not be ignored[4]. The aim of this study is to determine the concentration of lead content in dust fall samples to investigate urban pollution of this element. Today, there are two theoretical and experimental methods to measure the dust fall. In the experimental method, dust collectors are used to collect horizontal and vertical dust. Comparison of horizontal and vertical collectors shows that the marble dust collector (MDCO) has the highest efficiency for collecting dust particles[5].

The marble dust collector designed by Gunner in 1975 is widely used in many researches. This device consists of a plastic container and one or two rows of glass balls, which can be mounted on the ground or attached to a vertical base. The plastic container is used in many different types, among which circular containers are better than rectangular ones, since the effects of wind on rectangular containers are more pronounced. The diameter of the marble used is 1.6 centimeters[6]. Glass marbles are suitable for depositing dust applications as standard equipment due to their convenience to use, accessibility, and maintenance-free characteristics[7].

In addition, dust is considered as one of the most important atmospheric phenomena and natural disasters, and has received significant attention from many scholars and researchers in different fields of atmospheric science. The origin and mechanism of formation, transfer, diffusion and the consequences of this phenomenon are studied by various techniques and methods[8]. In recent years, it seems that there has been a change in the frequency of occurrence of this climatic hazardous phenomenon, which has caused problems in some parts of our country. The frequency of dust at a point depends on the size and diameter of the particles, in addition to the wind intensity, speed and dryness of the soil particles[9]. Studies on the abundance of dusty days in the country indicate that Iran Central basins have the highest frequency of dusty days[10]. Major sources of dust in the Middle East and Southwest Asia are the Arabian Peninsula with deserts surrounding it, most of which are active during the period from April to July[11]. Generally, the soils of arid regions are vulnerable to erosion due to the lack of organic and colloidal matter. Therefore, dust is the most important natural source of air pollution in most cities located in arid and semi-arid regions of Iran[12].

Dust fall refers to the dust that falls from the atmosphere onto the surface of the earth. By studying the dust fall, we can indirectly examine the contamination of total suspended particles[13]. Heavy metals are classified as one of the most hazardous groups of anthropogenic pollutants due to their toxicity and persistence in the environment[14]. In general, two types of pollutants were detected in dust: the first one consisting of CO, NO_2, SO_2, heavy metals, especially lead and cadmium, and the second group containing chemical, physical and biochemical components[15]. Human activities lead to increased levels of heavy metals in the environment. These metals accumulate in street dust, soil and surface water and affect the global ecosystem[16,17]. Heavy metals formed as fine and light compounds suspend in the atmosphere, dissolve during precipitation events and fall onto the surface of the earth. However, the coarse and heave portion of metal compounds settled down on the ground surface over time. In general, the presence of heavy metals in the atmosphere or in airborne dust increases the concentration of these elements in the body of inhabitants in the infected areas[8].

Lead is one of the heavy metals that are introduced to the environment by human in different ways. Activities such as ammunition manufacturing, casting, dyeing, leaded petrol production, sealing the pipes, cable coating production, lead melting and fusion, lead arsenate used in agricultural, battery production, brass alloys production, the combustion of leaded petrol in motor vehicles, etc. are the introducers of this hazardous substance into the environment[18]. In recent years, because of the elimination of lead from petrol, its emission into the urban environment has decreased significantly; however, the accumula-

tion of its previous uses has remained in the environment[19].

2. Literature review

Salamatian studied the quantitative variation of the dust fall and determined some of its physical and chemical properties in Isfahan, Iran. Sampling was done using a marble dust collector during a six-month period. The results showed that the average dust fall weight in Isfahan was 12 gr/m^2 and 17 gr/m^2 in winter and spring, respectively[8].

Akbari *et al.* studied the dust fall of Behbahan, Iran, using a marble dust collector during September and October. They concluded that the amount of dust fall in September is higher than in October. Also, some factors such as changes in Urban cover, roughness of the city, the streets orientation to the dominant winds and the level of traffic were considered effective in urban dust fall level[3].

Jia *et al.* examined the characteristics of dust fall and the identified the source of dust in arid and semi-arid parts of northern China. They studied 29 sites and identified 26 elements in the dust. Spatial and temporal changes were observed in these particles, and they found that these elements were in the highest level in spring, since the most dust storms occur in this season[6].

3. Materials and methods

3.1 Study area

The present study is conducted in Zahedan City (Sistan and Baluchistan Province), with an area of about 557 km² and a population of 574,000. The height of this city from the sea level is 1385 m with a longitude of 60º51′25″ E and latitude of 29º30′45″ N.

3.2 Sampling of dust fall and determining the lead content

Systematic random sampling method was used to determine the sampling points so that 30 stations were selected across the city. Marble dust collector was used to investigate the dust fall. The sampler was placed at a height of 1.5 meters from the roof surface. **Figure 1** shows the location of sampling stations. Sampling was carried out for three months from April to June 2015. At the end of each month, trapped dust was carefully collected. The concentration of lead content in dust samples was measured using a flame atomic absorption spectrometer Model Analytic jena-350.
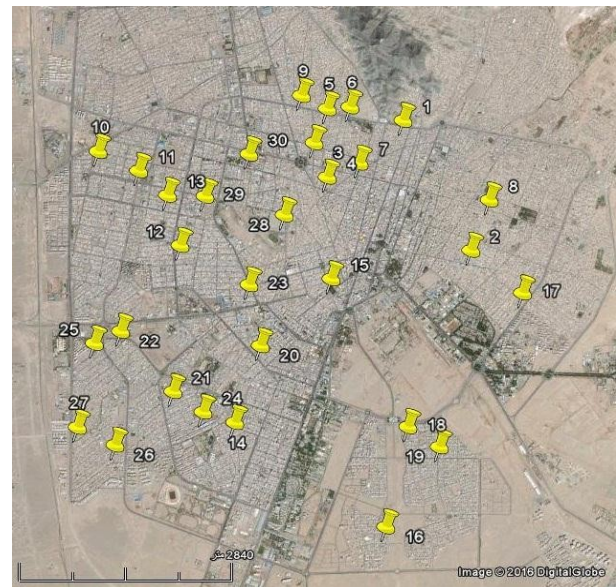
Figure 1. The location of sampling stations on Google Earth.

3.3 Isolation and spatial distribution of lead content in dust fall

Pollination index (*PI*) and ecological risk (*Er*) were used to determine the status of lead contamination (Equations 1 and 2).

$$PI = Cn/Bn \tag{1}$$
$$E\ r = Tr.PI \tag{2}$$

Where, *Cn* is lead concentration in each sample; *Bn* is the background level of this metal in the soil, and the *Tr* is the toxic response factor. According to Hakanson, the value of *Tr* for lead is 5. **Table 1** shows how these indicators are categorized.

According to the results obtained from different stations, the zoning map of the study area was prepared by Kriging method using Arc GIS 9.3 (**Figure 2**), so as to investigate the spatial distribution and frequency of lead across the city.

23

Table 1. Indices and the environmental potential pollution degree for heavy metals[8,20,21]

Air quality index	PI index	Environmental potential pollution risk	RI index	Environmental pollution risk for each metal	Er index
Low	$PI < 1$	Low risk	$RI < 150$	Low risk	$Er < 40$
Moderate	$1 < PI < 3$	Moderate risk	$150 < RI < 300$	Moderate risk	$40 < Er < 80$
High	$PI > 3$	High risk	$300 < RI < 600$	High risk	$80 < Er < 160$
-	-	Very high risk	$RI > 600$	Very high risk	$160 < Er < 320$

4. Results and discussion

4.1 The amount of lead content in the dust fall

Table 2 shows descriptive statistics of lead content, and **Table 3** shows the pollution index and the ecological risk associated with lead content in spring.

Table 2. Descriptive statistics of lead content in different months in spring season (mg/kg)

	Arithmetic mean (mg/kg)	Standard deviation	Minimum	Maximum	Skewness	Kurtosis	k-s (p-value)
April	99.13	11.74	74.70	116.10	-0.226	-0.686	0.51
May	85.10	12.30	37.73	103.25	-2.368	7.695	0.05
June	86.27	12.98	50.75	99.85	-1.598	2.092	0.20

Table 3. Indices of lead content in dust fall in spring 2015 (mg/kg)

Average lead content in spring	Pollution index in spring	Ecological risk in spring
90.16	1.11	5.55

As shown in **Table 3**, the value of *PI* in spring is greater than 1, so it is classified as the moderate pollution. According to the figure, the lead content in the dust fall in spring in the range of Mustafa Khomeini, Enghelab and Badr stations is higher th-an that in the rest stations. While the lowest amount of lead content in dust fall was measured at Imam Khomeini, University and Jam-e-Jam stations (**Figure 2**).
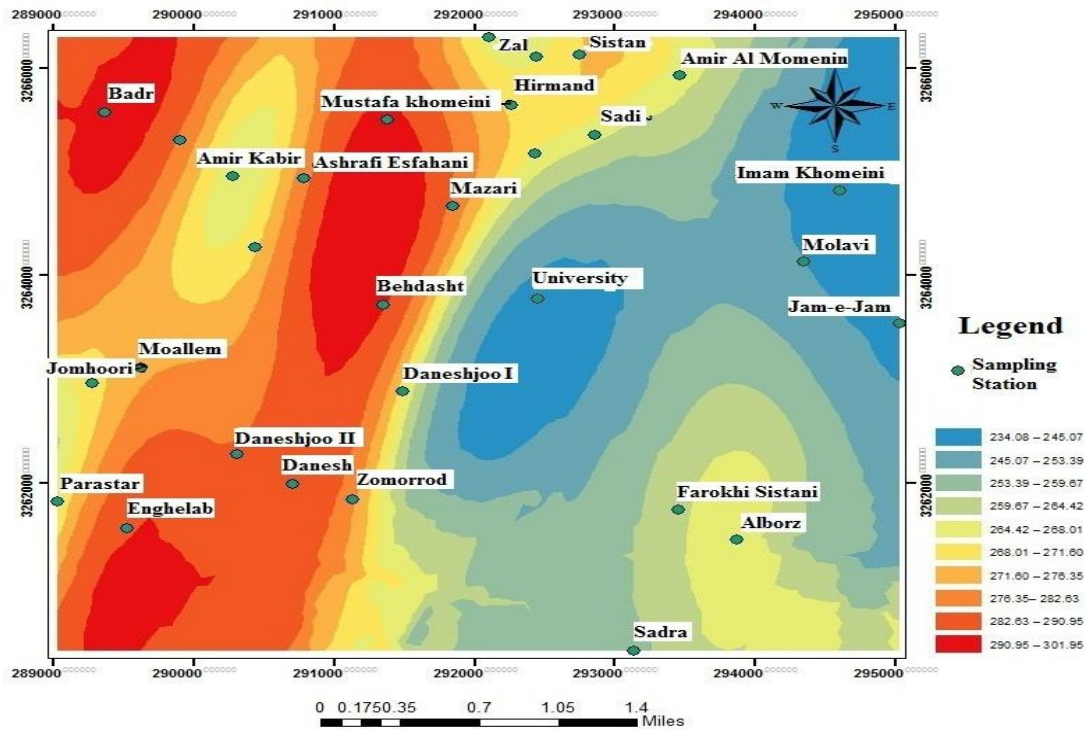
Figure 2. Zoning map of lead in the dust fall in spring.

24

5. Conclusion

As mentioned above, in most cities in arid and semi-arid regions of Iran, the main cause of air pollution is dust. Lead is one of the most harmful metals for human health. The results of this study show that the concentration of lead in Zahedan dust exceeds the values previously measured in Yazd and Behbahan[3]. The results of zoning of lead content in dust fall showed that the highest concentration of lead was measured in Mostafa Khomeini station while the lowest concentration was recorded in Imam Khomeini station. Studies indicate that the main source of lead pollution in air is additive matter of vehicle fuel. Therefore, high traffic of motor vehicle can be a cause of increased concentration of heavy metals.

6. Suggestions

In this study, we tried to calculate the amount of lead content the dust falls in Zahedan City. It is suggested that other heavy metals such as zinc, nickel, and copper in the dust of Zahedan City in Sistan and Baluchistan Province be investigated in order to obtain information on their pollution potential and environmental hazards. Also, exposure of citizens to these elements can be addressed. In addition, the transmission trend of these elements could be found by comparing the results with the research carried out in other border cities of Iran. Considering that in some of the studied stations the concentration of heavy metals exceeds the standard, it is suggested that the origin and emission source of these elements should be determined in future researches and solutions for controlling, reducing and preventing their effects could be provided.

Conflict of interest

The authors declare that they have no conflict of interest.

References

1. Joshi UM, Vijayaraghavan K, Balasubramanian R. Elemental composition of urban street dusts and their dissolution characteristics in various aqueous media. Chemosphere 2009; 77(4): 526–533.
2. Wu S, Zhou S, Li X, *et al.* An approach to partition the anthropogenic and natural components of heavy metal accumulations in roadside agricultural soil. Environmental Monitoring and Assessment 2011; 173: 871–881.
3. Akbari A, Azimzadeh HR, Ekhtesasi, MR. Quantitative examination of dust falls (Case study: Behbahan — September and October, 2011). 1st National Conference on the Desert; 2012.
4. Raeispour K. Statistical analysis and isometropia of dust in Khuzestan Province (MSc thesis). University of Sistan and Baluchestan; 2008. p. 189.
5. Sow M, Goossens D, Rajot JL. Calibration of the MDCO dust collector and of four versions of the inverted frisbee dust deposition sampler. Geomorphology 2006; 82(3-4): 360–375.
6. Jia Q, Huang Y. Coarse dust around mining areas: A study of available dust collectors and their efficiency. Lule Tekniska Universitet; 2008.
7. Goossens D, Offer ZY. An evaluation of the efficiency of some eolian dust collectors. Soil Technology 1994; 7: 25–35.
8. Salamatan S. Quantitative variations of dust fall and some of its physical and chemical properties from January 2012 to June 2013 (Case study: Isfahan City) (MSc thesis). Yazd University; 2013. p. 3–4.
9. Azizi G, Shamsipour A, Miri M, *et al.* Statistic and synoptic analysis of dust phenomena in West of Iran. Journal of Environmental Studies 2012; 38(63): 123–134.
10. Alijani B. Climate of Iran (in Persian). Tehran: Payame Nour University Press; 2006.
11. Gossens D, Rajort JL. Techniques to measure the dry aeolian deposition of dust in arid and semi-arid landscapes: A comparative study in West Niger. Erath Surface Processes and Landforms 2008; 33(2): 178–195.
12. Soltani, Bahram, Mabani, *et al.* The basics of urban green space architecture; Did Press; 2005.
13. Hai C, Yuan C, Liu G, *et al.* Research on the components of dust fall in Hohhot in comparison with surface soil components in different lands of Inner Mongolia Plateau. Water, Air and Soil Pollution 2008; 190: 27–34.
14. Csavina J, Field J, Taylor MP, *et al.* A review on the importance of metals and metalloids in atmospheric dust and aerosol from mining operations. Science of the Total Environment 2012; 433: 58–73.
15. Rodrıguez I, Galí S, Marcos C. Atmospheric inorganic aerosol of a non-industrial city in the centre of an industrial region of the North of Spain, and its possible influence on the climate on a regional scale. Environmental Geology 2009; 56(8): 1551–1561.
16. Jorkesh S, Salehi M, Hassan E, *et al.* Concentration of some heavy metals in atmospheric dust in the Lenjanat district of Isfahan. National Conference on Air Flow and Pollution. Tehran; November 2012.
17. Sharrett AR, Orheim RM, Carter AP, *et al.* Components of variation in lead, cadmium, copper, and zinc concentration in home drinking water: The

seattle study of trace metal exposure. Environmental Research 1982; 28(2): 476–498.

18. Hosseini E, Azimzadeh, Hamid Reza, *et al*. Lead concentration in the dust fall in Yazd City. 3rd national conference on wind erosion anddust storms. January 2013; Yazd: Yazd University.

19. Moayedi, Mohajerani, Hamidreza, *et al*. Coexistence of blood lead levels in residents of Arak city with clinical syndromes. Journal of the Faculty of Medicine 2008; 32(1): 75–79.

20. Saeedi M, Lily, Salmanzadeh M. Heavy metals and polycyclic aromatic hydrocarbons: Pollution and ecological risk assessment in street dust of Tehran. Journal of Hazardous Materials 2012; 227-228: 9–17.

21. Wei B, Jiang F, Li X, *et al.* Heavy metal induced ecological risk in the city of Urumqi, NW China. Environmental Monitoring and Assessment 2008; 160: 33–45.

ORIGINAL RESEARCH ARTICLE

Use of earth observation images and GIS techniques for groundwater exploration in hard rock terrain

P. Mohana[1*], S. Muthusamy[2]

[1] *Centre for Remote Sensing & Geoinformatics, Sathyabama University, Chennai - 119, India. E-mail: mohanaperumal@yahoo.com*

[2] *Department of Geology, V.O.C College, Tuticorin, Tamil Nadu, India.*

ABSTRACT

It increased the demands on ground-water supplies that prolonged drought and improper maintenance of water resources. So it is necessary to evaluate ground-water resources in the hard rock terrain. In recent years, Remote-Sensing methods have been increasingly recognized as a means of obtaining crucial geoscientific data for both regional and site-specific investigations. This work aims to develop and apply integrated methods combining the information obtained by geo-hydrological field mapping and those obtained by analyzing multi-source remotely sensed data in a GIS environment for better understanding the Groundwater condition in hard rock terrain. In this study, digitally enhanced Landsat ETM+ data was used to extract information on geology, geomorphology. The Hill-Shading techniques are applied to SRTM DEM data to enhance terrain perspective views, and extract Geomorphological features and morphologically defined structures through the means of lineament analysis. A combination of Spectral information from Landsat ETM+ data plus spatial information from SRTM-DEM data is used to address the groundwater potential of alluvium, colluvium, and fractured crystalline rocks in the study area. The spatial distribution of groundwater potential zones shows regional patterns related to lithologies, lineaments, drainage systems, and landforms. High-yielding wells and springs are often related to large lineaments and corresponding structural features such as dykes. The results show that the combination of remote sensing, GIS, traditional fieldwork, and models provide a powerful tool for water resources assessment and management, and groundwater exploration planning.

Keywords: Remote Sensing; GIS; ETM+; SRTM; Groundwater Potential Zones

ARTICLE INFO

COPYRIGHT

1. Introduction

In recent years, remote-sensing methods have been increasingly recognized as a means of obtaining crucial geoscientific data for both regional and site-specific investigations. In the field of Groundwater exploration, various methods were followed but this study focuses on groundwater detection in hard rock terrain[1,2]. The remote sensing data should be acquired and integrated into the early stages of an investigation and used in conjunction with traditional mapping techniques. Hard rock terrain normally creates complex hydrogeology over a long period. Groundwater in hard rock terrain is present or stored in the confined fractures zones and weathered horizons. It is mainly due to the porosity nature of the rock and the fracturing zones, which causes the movement of the water into the hard rock. In India, about 65% of the country is underlined by hard rocks[3].

In this study various image processing techniques, DEM to derive the hard rock characteristics and various structures, to delineate the po-
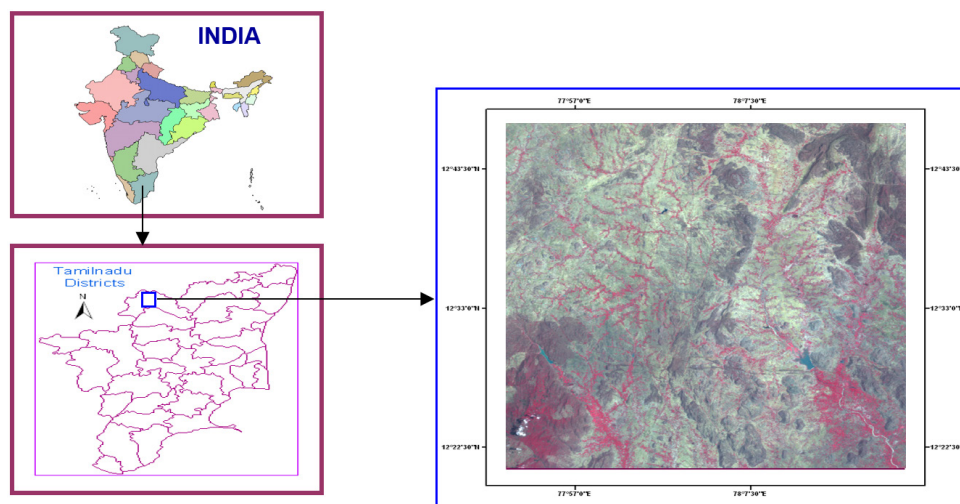
Figure 1. Location Map of the Study area**.**

tential zones of groundwater.

2. Aim and objectives

The overall objective of this study is to contribute to systematic groundwater studies utilizing Digital Image Processing, Digital Elevation Models (DEM) and Geographic Information Systems (GIS) in the assessment of groundwater resources.

The specific objectives of the study are:

➢ To identify and suggest suitable digital enhancement techniques for extraction of groundwater controlling features, which is characteristic of hard rock crystalline formation, such as regional geology, geological structures and landforms.

➢ To prepare thematic maps of the area such as lithology, lineaments, landforms and geomorphology from remotely sensed data and other data sources like DEM.

➢ To assess groundwater controlling features by combining remote sensing, field studies and DEM.

➢ To identify and delineate groundwater potential zones through the integration of various thematic maps with GIS techniques.

➢ To make recommendations for future work and provide guidelines for groundwater prospecting.

2.1 Study area

The study area is situated to the north part of Dharmapuri district (upper Ponnaiyar Basin) and lies between Latitudes 12o 20" – 12o 45" N and Longi-

tudes 77o 50" – 780 15" E and extends over an area of about 182 km2 covering 24 villages (**Figure 1**). The study area lies in hard rock terrain. Groundwater is available only in weathered and fractured zones. In this area assured surface water supplies are nominal and most of the farmers depend on groundwater for drinking and irrigation purposes.

2.2 Data used

In this study, a variety of data including satellite images, digital elevation models, geological maps, standard 1:50.000 scale topographic maps, and various thematic maps obtained from various sources have been used as data sources together with ground truth studies that have also been carried out. Different sets of data were used for the study like Landsat ETM+ 2015 data and SRTM data.

2.3 Methodology

The methodology employed is summarized in the flow chart in **Figure 2**. It involves digital Enhancement of Lansat ETM+ data for the extraction of lithological, structural and Geomorphological features and evaluation of digital elevation model (DEM) as well as field studies. The field studies are comprised of hydrogeological and structural investigations. The SRTM-DEM was used to extract lineaments and to map drainage systems and landforms. All data were integrated with a Geographic Information System (GIS) and analyzed to assess the groundwater controlling features. Finally, groundwa-

28
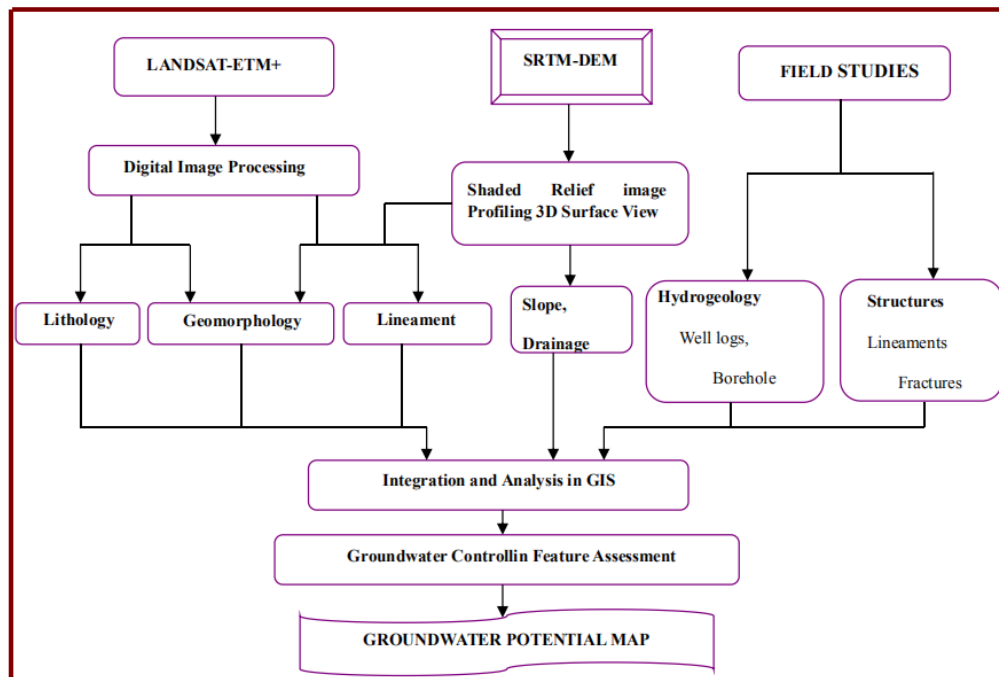
Figure 2. A flow chart depict the methodology adopted for preparation of Groundwater Potential Mapping**.**

ter potential maps were prepared based on the GIS analysis. The image processing software ERDAS (Earth Resources Data Analysis System) was used for the remote sensing data enhancements. ArcGIS 10.1 were utilized for GIS analysis. The geological, lineament maps and other collateral data were also made use of for the preparation of hydro geomorphological map. The hydro geomorphical map of the area was finalized after field checks with GPS at selected locations for verifying the doubtful units.

3. Integrating remote sensing and GIS in groundwater studies

3.1 Digital image processing and image interpretation

Image enhancement techniques are used in this study utilized the procedures that made the georeferenced images clearer and more interpretable for hydrogeological analysis. To extract the Lithological, Structural and Geomorphological features and from satellite images that cannot be clearly detected in a single band, the spectral information of the lithological and structural features recorded in multiple bands are utilized. The geological structures, especially the fractures that are considered to be one of the high

ratings of groundwater controlling parameters, have been clearly brought out during the digital image enhancement techniques. The integration of Landsat ETM+ images with high-resolution PAN data provides complementary information with respect to the discrimination of major geological features and allows lineament extraction in detail. The selection procedure using the statistical techniques was applied in ETM+ data that covers the most prominent rock types in the study area. Principal component analysis (PCA) was performed with the six reflective bands of ETM+ and a number of different three-band PC color composite combinations were created and analyzed for their content (**Figure 3B**). The Decorrelation stretch (DS) conducted on ETM+ bands 4, 5 and 2 is shown in (**Figures 3C & D**) better lithological and geomorphological contrast was obtained when compared, for instance, with the standard band combination of PCA and FCC images. Moreover, most of the lithological units in the study area are discernible in the image. In general, the decorrelation stretch proved to be the most effective in accentuating colors, thus facilitating visual discrimination of various hydrogeological features. This is because the technique removes the high correlation common-

ly found in multispectral data sets and thus produces more colorful composite images[4-5].

3.2 Evaluations of SRTM Data

The evaluation of digital topographic data is of great importance as it contributes to the detection of the specific geomorphologic/ topographic settings in rougher terrain. Data of the Shuttle Radar Topography Mission (SRTM) are used to provide digital elevation information (90 m spatial resolution). SRTM DEM data are used for lineament analysis. The primary method used for the interpretation of the SRTM DEMs was to extract lineaments through the creation of hill-shading DEMs. Hill-shading DEMs with different azimuth directions and sun angles are used in this study (**Figure 4. A & B**). This technique is effective in creating images that enhance geomorphic features. The result shows that the shaded relief image can provide good enough geological information. Subsurface structures such as fault zones can be derived by geomorphologic analysis (drainage pattern) and the identification of linear tonal anomalies on the imageries. Linear morphologic features (lineaments) as visible on hillside maps and LANDSAT imageries are often related to traces of faults and fractures in the subsurface influencing groundwater permeability (**Figure 4C**).
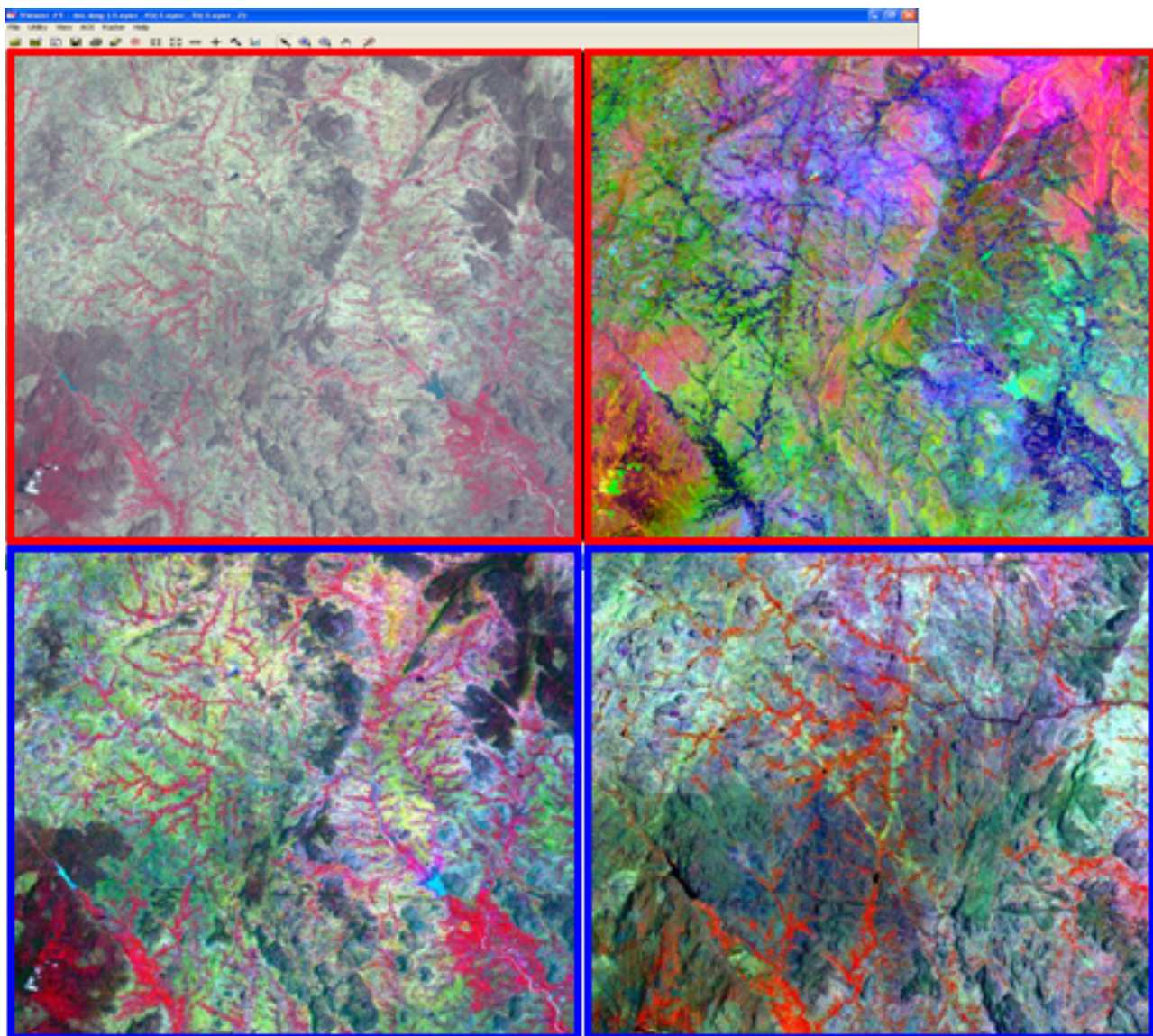
Figure 3. Enhanced Landsat-ETM+ images. A. FCC (4-3-2). B. PCA (4-3-2). C. Decorrelation Stretched (4-3-2). D. Subset image highlight the various hydrogeological features.

30
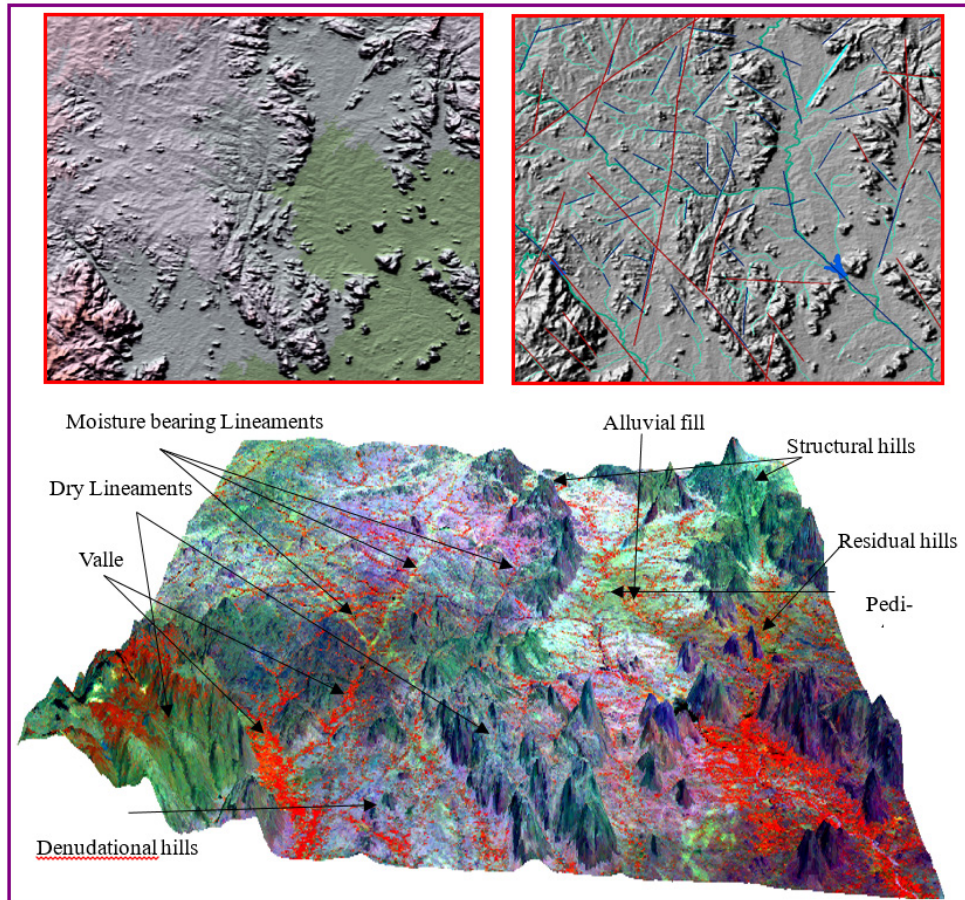
Figure 4. A. Shaded relief image with varying sun azimuth and angle that can enhance the structural features in the study area. B. Shaded relief image with overlay in drainage and lineaments. C. 3D perspective view of the study area created from SRTM hill-shading DEM along with the Hydrogeological interpretation.

3.3 Spatial analysis

Spatial analysis was performed in GIS to assess terrain features, e.g., water bodies, stream networks, faults, rock type, elevation, land-use classes and vegetation cover. GIS-RS spatial analysis was used to generate land surface statistics and to assist in the study of spatial relationships between terrain elements for image enhancements.

4. Result and discussion

4.1 Geology

Igneous and metamorphic rocks are closely interspersed throughout most of the Region. Igneous rocks are predominantly granite; subordinate amounts of dolerite are widespread. Metamorphic rocks, chiefly Charnockite, Migmatite, gneiss and schist are common and tend to be folded and faulted extensively. The rocks are broken and displaced by numerous faults and zones of shearing, some of which are many miles long. Fortunately, indirect evidence of the degree of fracturing of a particular rock may be derived from terrain analysis, chiefly soil thickness and topographic expression. In most places, massive granite and gabbro have thin soils and are poorly fractured, whereas gneiss and schist have thicker soils and moderate to relatively high fracture densities.

4.2 Structure

The geological structure normally encountered in hard rock areas of places such as India is granite or granite gneiss overlain by a variable thickness of weathered material[6]. Since identification and demarcation of moisture-laden fractures in the crystalline rock formation will aid quick exploration of groundwater, a detailed analysis has been done (**Figures 5 & 6**). The analysis of pre-monsoon data through the

digital enhancement technique offered a differenti-ation of moisture-bearing lineament with dry linea-ment based on land use/land cover along the fracture zones. While the moisture-bearing lineaments in this terrain signify a promising groundwater occurrence at a shallow depth, the dry lineament signifies an unpromising shallow groundwater occurrence[7]. It is generally accepted that lineaments analysis alone cannot be used for borehole siting. Remotely sensed data along with hydrogeological data, when integrat-ed with statistics and GIS techniques, may provide a valuable tool to help in the selection of successful borehole sites in areas that consist of crystalline rocks and have a semi-arid terrain[8,9].

4.3 Drainage

According to El-Baz, the coincidence of drain-age with structural features, as well as the channels that drain into fractures, provides the ideal fluvi-al-structural configuration for groundwater accumu-lation. So, these features are valuable for ground-water exploration in the study area. Intersecting drainage patterns, indicative of subsurface structures suitable for groundwater occurrences.

4.4 Geomorphology

The geomorphology of an area is highly influ-enced by the lithology and structure of the underly-ing formations[10]. So hydro geomorphological units have a direct relation to groundwater. Hydrogeomor-phologically, the study area is classified into different zones covered by Denudostructural hills; Denuda-tional hills, Residual hills, Alluvial plain, Pediment, peneplain and Valley fill (**Table 2**). The delineation of hydrogeomorphic zones aims at demarcating ar-eas of groundwater recharge/discharge and potential zones for development.

4.5 Groundwater Potential zones

By integrating both hydrogeological and hy-drogeomorphological details derived through the visual onscreen interpretation of different enhanced products, a groundwater prospective zone map of the study area was prepared **Figure 7**. The groundwater conditions of the study area have been arrived at by incorporating the details obtained through ground surveys with a groundwater prospective zone map **Table 2**. The various geomorphic units are classified as favorable, moderately favorable and poor zones of groundwater[11,12].

Groundwater development is promising in the floodplains, alluvial plains and valley fills that are associated with thick alluvium and weathered mate-rial that has high porosity and permeability charac-

Table 2. Geomorphic Units for Hydrogeomorphological Mapping in the Study area

S.No	Geomorphic units	Structures	Lithology	Groundwater Conditions
1.	Structural hills	Lineaments, Joints, Fractures etc.	Charnockites, Kon-dalites etc.	Mainly act as a run-off zone, not suitable for groundwater prospecting.
2.	Residual hills	Joints, Fractures etc.	Charnockites, Gran-ites etc.	Mainly act as a run-off zone. Fractures and intersection of fractures are promising zones for groundwater extraction.
3.	Pediment	Fracture controlled	Gneisses, Granite, Charnockite etc.	Sporadically distributed in the study area. Moder-ate to poor groundwater prospective zones.
4.	Pediplain	-	Gneisses, Granite etc.	Mainly covered by red soil. The weathered thickness range from 1–7 m. The occurrence of groundwater is in unconfined condition within weathered and fractured layer. Moderate ground-water prospective zone.
5.	Valley fills	Fracture controlled	Recent alluvium, colluvium, clay, sand, silt etc.	Fine/medium grain unconsolidated sediments with thickness of 1–5 m. Most of the wells drilled in this zone are high yielding. Good/excellent groundwater prospective zone.
6.	Alluvial plain	-	Recent alluvium, colluvium, clay, sand, silt etc.	Fine/medium grain unconsolidated sediments with thickness of 1–10 m. Most of the wells and dug wells drilled in this zone are high yielding. Excel-lent groundwater prospective zone.

teristics. Only a small area is occupied by these landforms, and hence favorable zones of groundwater are very limited in the basin area. A large part of the area is occupied by pediments, peneplains, structural hills, which do not favor much infiltration and hence are generally not favorable for groundwater exploration. The study reveals that a large part of the area has good to moderate groundwater producing potential.
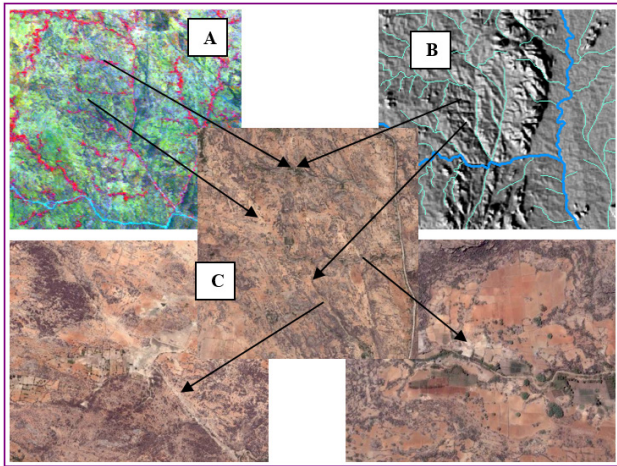
Figure 5. A. A lineament detected on contrast-stretched DS image. B. The same lineament detected on a Shaded relief image. C. Field photographs of an NW-SE trending fault trace that corresponds to the lineament.
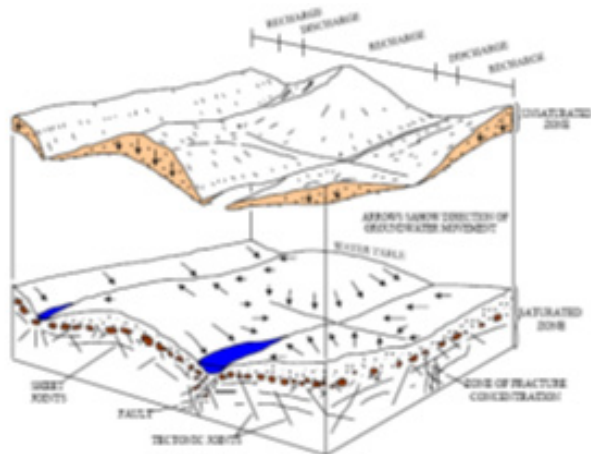
Figure 6. Block diagram of fracture zones and groundwater movements associated with surface fracture traces.

4.6 Conclusion and recommendations

The different types of digital enhancement techniques, such as linear stretching, band combination, PCA and filtering, hill shading techniques using DEM are found to be useful for extracting the various groundwater controlling features in typical hard rock terrain. The integration of the details derived from digitally enhanced ETM+ and DEM products with GIS has helped in the preparation of a groundwater potential zone map. The occurrence of groundwater is controlled by rock type, structures and landforms as revealed from GIS analyses and field investigations. High-yielding wells and springs are often related to large lineaments, lineament intersections and corresponding structural features.

In metamorphic and igneous intrusive rocks with rugged landforms, groundwater occurs mainly in drainage channels with valley-fill deposits. Zones of very good groundwater potential are characteristic for alluvial/colluvial layers overlying crystalline rocks, flat topography with dense lineaments and structurally controlled drainage channels with valley-fill deposits. The overall results demonstrate that the use of Digital Image Processing, DEM and GIS provide potentially powerful tools to study groundwater resources and design a suitable exploration plan.
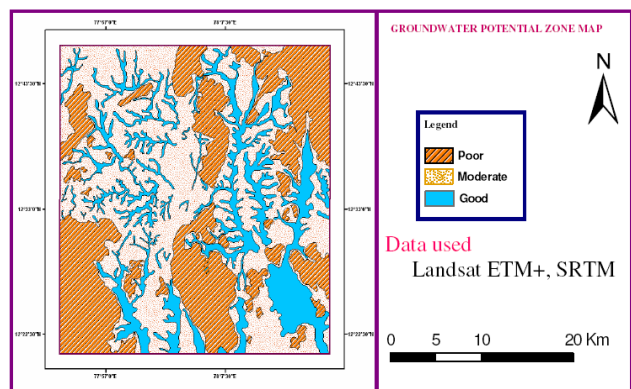
Figure 7. Groundwater potential map of the study area.

5. Recommendations

Several approaches were applied to understand the hydrogeological conditions of the hard rock aquifers in parts of Tamilnadu. Because of the inhomogeneous nature of hard rock aquifers, it is crucial to use investigation techniques that maximize the information from various sources. An attempt was made to optimize the available data using methods that have proved to be successful in hydrogeological studies in other parts of the world. The following recommendations are given.

33

➢ Geospatial data are powerful tools to improve our understanding of groundwater systems. While not directly measuring hydrogeological properties, they provide continuous detailed terrain information and allow the mapping of features significant to groundwater development. Various satellite data with different spectral and spatial resolutions coupled with digital image processing techniques help to accurately produce detailed maps. Ground verification is crucial to increase the accuracy of the interpretation results.

➢ Geographic Information Systems are very time and cost-effective once the database is created and provide many advantages over traditional approaches. Integration of different data layers such as remote sensing, geomorphology and field data in a GIS environment provides means to unravel the nature of hard rock aquifers. Spatial and statistical analysis allows understanding the correlation between different parameters. This integrated approach of groundwater potential assessment in a GIS is highly recommended.

➢ Structures are assessed at the outcrop scale to decipher the nature of lineaments interpreted from remote sensing data. Field investigations of well sites in relation to location, topography and structures as well as subsurface information such as pumping test and lithological log data are most valuable to improve our understanding of the hydrogeological conditions (**Figure 8**).
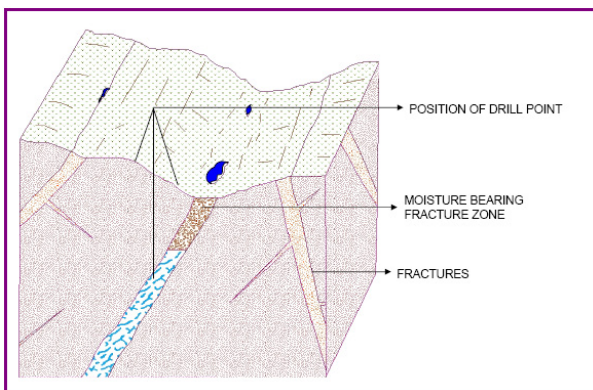
Figure 8. Correct positioning of rig**.**

Conflict of interest

The authors declare that they have no conflict of interest.

References

1. Nag SK, Kundu A. Delineation of groundwater potential zones in hard rock terrain in Kashipur block, Purulia District, west Bengal using geospatial techniques. International Journal of Waste Resources 2016; 6(1): 1000201.

2. Kavitha M, Naidu, Mohana P. Delinational of groundwater potential zones of Thurinjapuram watershed using geospatial technology. Indian Journal of Science and Technology 2011; 4(11): 1470–1476.

3. Saraf AK, Choudhury PR. Integrated remote sensing and GIS for groundwater exploration and identification of artificial recharge sites. International Journal of Remote Sensing 1998; 19(10):1825–1841.

4. Tahir AG, Garba ML, Hassan C. Lineaments analysis to identify favourable areas for groundwater in Kano City, Northwestern Nigeria. Journal of Environment and Earth Science 2015; 5(2): 1–6.

5. Mondal MS, Pandey AC, Garg RD. Groundwater prospect evaluation based on hydrogeomorphological mapping using high resolution satellite images: A case study in Uttarakahand. Journal of the Indian Society of Remote Sensing 2007; 36(1): 69–76.

6. Drury SA, Peart RJ, Deller MEA. Hydrogeological potential of major fractures in Eritrea. Journal of African Earth Sciences 2001; 32(2): 163–177.

7. Mogaji KA, Aboyehi OS, Omosuyi GO. Mapping of lineaments for groundwater targeting in the basement complex region of Ondo State, Nigeria, using remote sensing and GIS Techniques. International Journal of Water Resources and Environemental Engineering 2011; 3(7): 150–160.

8. Murugesan B, Thirunavukkarasu R, Senapathi V, *et al*. Application of remote sensing and GIS analysis for groundwater potential zone in kodaikanal Taluka, South India. Earth Science 2012; 7(1): 65–75.

9. Waikar ML, Nilawar AP. Identification of groundwater potential zone using remote sensing and GIS technique. International Journal of Innovative Research in Science, Engineering and Technology 2014; 3(5): 66–75.

10. Ravindran KV, Jeyaram A. Groundwater prospects of shahbad tehsil, baran district, eastern rajasthan: A re-

34

mote sensing approach. Journal of the Indian Society of Remote Sensing 1997; 25: 239–246.

11. Sameena M, Ranganna G, Krishnamurtty J, *et al*. Targeting Groundwater Zones and Artificial Recharge sets using Remote Sensing and GIS techniques. Abs. 12th Convention IGC 2000. p. 113–114.

12. Solomon S. Applications for groundwater potential assessment in Eritrea. Remote Sensing and GIS 2003.

ORIGINAL RESEARCH ARTICLE

Using of remote sensing and aeromagnetic data for predicting potential areas of hydrothermal mineral deposits in the Central Eastern Desert of Egypt

Mohamed Abdelkareem[1*], Abdelhady Akrby[1], Mousa Fakhry[1], Mohamed Mostafa[2]

[1] Geology Department, South Valley University, Qena 83523, Egypt. E-mail: mohamed.abdelkareem@sci.svu.edu.eg
[2] Egyptian Mineral Resources Authority, Cairo, Egypt.

ABSTRACT

This article explored mineral resources and their relation to structural settings in the Central Eastern Desert (CED) of Egypt. Integration of remote sensing (RS) with aeromagnetic (AMG) data was conducted to generate a mineral predictive map. Several image transformation and enhancement techniques were performed to Landsat Operational Land Imager (OLI) and Shuttle Radar Topography Mission (SRTM) data. Using band ratios and oriented principal component analysis (PCA) on OLI data allowed delineating hydrothermal alteration zones (HAZs) and highlighted structural discontinuity. Moreover, processing of the AMG using Standard Euler deconvolution and residual magnetic anomalies successfully revealed the subsurface structural features. Zones of hydrothermal alteration and surface/subsurface geologic structural density maps were combined through GIS technique. The results showed a mineral predictive map that ranked from very low to very high probability. Field validation allowed verifying the prepared map and revealed several mineralized sites including talc, talc-schist, gold mines and quartz veins associated with hematite. Overall, integration of RS and AMG data is a powerful technique in revealing areas of potential mineralization involved with hydrothermal processes.

Keywords: Remote Sensing; Aeromagnetic Data; Hydrothermal Alteration; Egypt

1. Introduction

Remote sensing technique commonly applied in reconnaissance studies. It represents an important way in deciphering several features such as geological, geomorphic, structural and mineral resources. NASA has launched several generations of unmanned Landsat satellites (1 to 8) that have acquired valuable RS data for mineral resources, structural features and land-use/cover information. Several studies used RS data for lithologic mapping[1–7], detecting HAZs[8–12], and characterizing the geologic and the geomorphic features[13,14]. Ratio images were performed for enhancing the spectral variations among the bands. This approach has been used in remote sensing to mark the spectral differences[15], to map lithology and HAZs[16]. This is because such transformation process can display a high contrast range of spectral characteristics than do individual bands.

Aeromagnetic data represent a significant factor in identifying subsurface structures based on the variation of the geomagnetic field, which results from the differences in the magnetite content of the associated rock units. Such geologic structures represented the conduit of

the mineral deposits associated with hydrothermal solutions. Therefore, integration of RS images and AMG data would complement the surface and subsurface view of the present study, where we can understand the surface/subsurface geologic structures, characterize the lithologic features, and highlight the probable areas of mineralization.

Several studies were conducted in the Central Eastern Desert (CED) of Egypt using RS data[17–22]. Landsat data were utilized for lithologic mapping and mineral exploration in arid regions[1–4,8,23]. O'Connor and McDonald (1988) used Landsat Thematic Mapper (TM) and applied color composite of band ratios 5/7, 5/1 and 4 in R, G, and B, respectively, to distinguish volcanic, serpentinite-mélange and late to post-tectonic molasse sedimentary units in the Central Eastern Desert of Egypt[18]. Sultan *et al.* (1988) integrated field and observations of Landsat data in the CED and revealed elongated NW-SE deformation associated with faulting and ductile shear zones, NW trending related to left-lateral faults, and some lithologic contacts related to faulting[19]. They related these features to the Najd fault systems and were not the results of obduction/accretion tectonics.

The main aim of the present study is to explore the optimum area of mineral resources based on combining surface/subsurface structural elements and zones of hydrothermal processes. So as to accomplish this objective the HAZs and areas of structural complexity will be delineated using SRTM, OLI and aeromagnetic data. Field and metalogenic data will validate the mineral predictive map.

2. Study area

The study area is situated in the eastern part of the CED of Egypt, extending between Longitudes 33o 52' 50' E and 34o 15' 00'' E, and Latitudes 25o 54' 00'' N and 26o 15' 00'' N. It occupies about 11980 sq km. It represents an important part of the proposed "Golden Triangle" project area that extending in the CED of Egypt, between Qena, Safaga and Quseir (**Figure 1**). It occupies the area west of the Quseir city in the Red Sea that well known by G. Duwi (Quseir) area (**Figure 1**). Lithologically, the exposed rock units in the study area vary from Precambrian to recent. The Precambrian rock units are represented by igneous and metamorphic rocks. The eastern part of the basement exposure is overlain by younger sedimentary formation ranging in age from late Mesozoic to Quaternary.
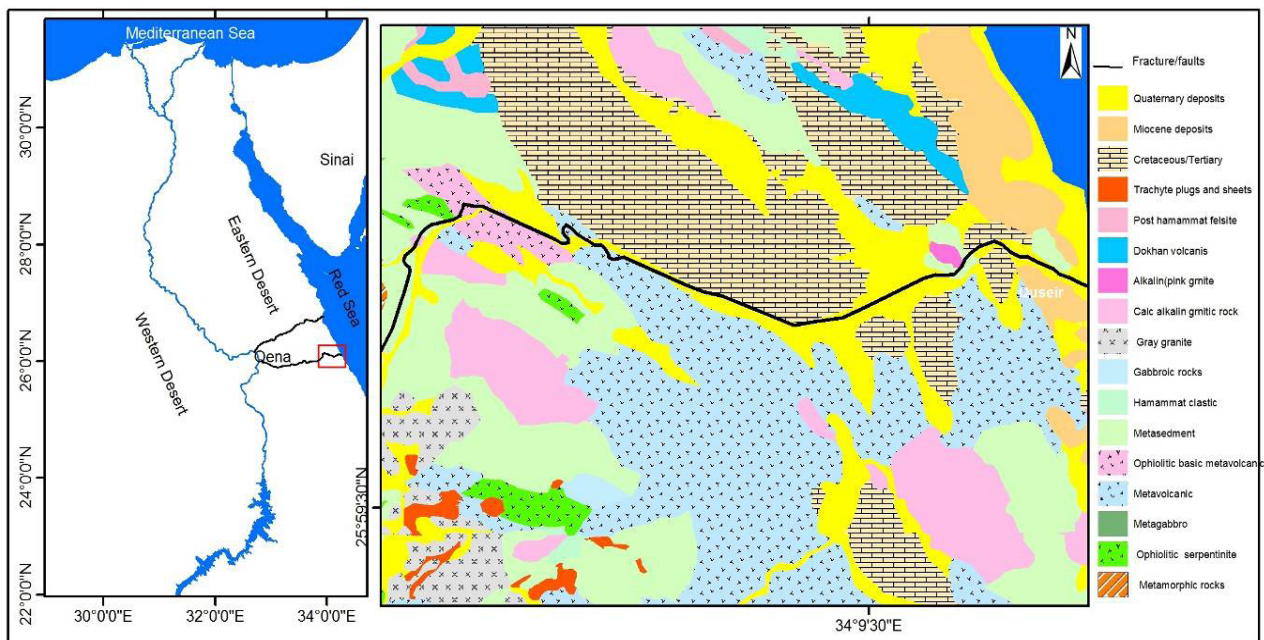
Figure 1. (a) Location map of the study area marked in red polygon nearness to the Red Sea zone. (b) Landsat ETM+ mosaic image showing the locality of the study area west of Quseir city and the accessible roads from Nile Valley to the Red Sea. (c) Geologic map of study (modified after Conoco, 1987)[24].

The study area occupied by Precambrian basement complex and Phanerozoic sedimentary rocks[25,26]. The basement complex, considered a part of the ANS which formed contemporaneously with the Late Proterozoic to Early Paleozoic time. During the Tertiary, the Arabian-Nubian Shield (ANS) was rifted apart by the Red Sea. The ANS of northeast Africa was cratonized during the late Pan-African Orogeny due to the collision of East and West Gondwana[27]. The basement complex in the ED of Egypt built up of island-arc/back-arc systems, consisting of metavolcanic, metasediments and associated ophiolitic rock assemblages[28,29]. These assemblages then, deformed and intruded by granitic masses of Syn- Late- and Post-tectonic during the Pan-African Orogeny.

3. Data used and methods

The available datasets such as a geological map, airborne total magnetic field survey, remote sensing, and field data were integrated in the present study using different spatial analysis techniques. Several studies were conducted to integrate aeromagnetic and RS data integration[7,30,31]. These studies have successfully displayed approaches to link the occurrence of mineral resources and understanding the surface and subsurface features.

3.1 Remote sensing data

In this article we utilized OLI data launched on February 11, 2013 from Vandenberg Air Force Base in California. OLI presents data from nine spectral bands (visible, near and shortwave infrared bands and two thermal long-wave bands). One image (path 174, raw 42) of Landsat data that acquired from USGS was processed using ENVI and ArcGIS software packages to extract the lithologic and HAZs.

Image transformation approaches like band ratios and PCA were utilized. In band ratios, dividing process of the digital numbers (DNs) of two spatially consistent bands are applied[5,32,33]. This technique clearly highlights the spectral variations of the mapped materials. Moreover, the PCA technique was performed. The statistical parameters are computed to characterize which component is significant based on the eigenvectors values to delineate the plausible area of hydrothermal alteration.

3.2 Aeromagnetic data

The utilized AMG data were compiled from the surveys that have been conducted in 1984 by the Western Geophysical Company of America (Aero Service Division), the Egyptian General Petroleum Corporation (EGPC) in conjunction with the Egyptian Geological Survey and Mining Authority (EGS-MA).

The Aeromagnetic magnetic anomaly (TMI) data were processed to be reduced to the pole (RTP). This technique was done by subtracting the International Geomagnetic Reference Field (IGRF). The residual and Euler methods also were applied. Euler deconvolution technique applies potential field derivatives to reveal subsurface depth of a magnetic or gravity source[34]. It represents a valuable method for delineating contacts and depth estimation. The eminence of depth estimation depends on the selection of the structural index (SI) value and appropriate sampling of the data. It has become a tool to determine the source location of the potential field anomalies[35,36], and provides automatic estimates of source location and depth. To conduct this, the SI was applied to characterize many source types. The SI can be interpreted as the exponent in a power law expressing the decreasing of field strength versus distance from the source.

4. Results and discussion

4.1 Optical remote sensing data

Utilizing Landsat data allowed highlighting areas of hydrothermal alteration. This was based on the spectral signatures of the rock units. Utilizing band ratio composites 6/7, 6/5, 5 in R, G, and B, areas of HAZs that marked in yellow and pinkish colors were highlighted[37,38] (**Figure 2a, Figure 2b**).

The PCA of selected bands is applied in the selected study area. Selected bands of 2, 4, 5, and 6 of OLI sensor were developed to show iron oxide image (**Table 1**). The results showed that the eigenvalue represents 96.64% of total variance and the first
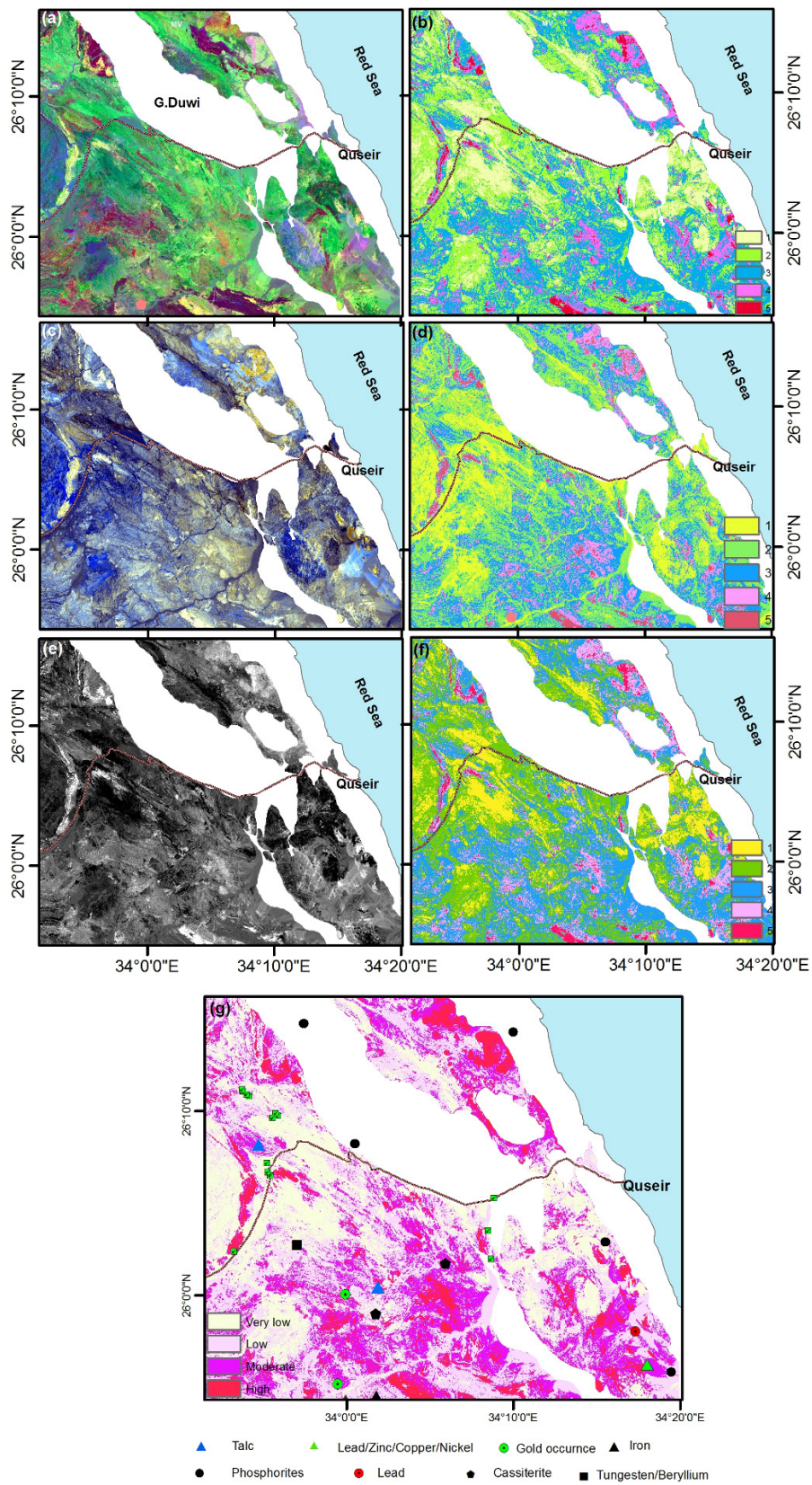
Figure 2. Alteration zones (a) band ratio 6/7, 6/5, 5; (b) classified band ratios of Ramadan *et al*.[40]; (c) Crosta technique, F, H+F, H in R, G, and B; (d) classified Crosta technique; (e) band ratios 6/7; (f) classified band ratios 6/7)alteration zones compiled from band ratios and PCA.; (g) alteration zone map of the study area**.**

39

component PC1 represents a positive loading from all bands. The PC4 displays positive loading from band 2 (0.70) versus band 4 (-0.66). Therefore, the PC4 was negated to display the iron-rich minerals in bright pixels.

In order to highlight areas of OH-bearing minerals, bands of 2, 5, 6, and 7 of Landsat-8 (image H) were used[10,39]. The results displayed that in PC3, there is a contrast between eigenvector loading from band 6 (-0.66) and band 7 (0.59). Therefore, the darkest pixels represent the OH-bearing minerals. After negation of the PC3, the hydrothermal altered areas appear in bright tone.

In order to generate Crosta's alteration image (**Figure 2c**), the F, H+F, H images are displayed in R, G, and B, respectively. This showed the suggested alteration zones in brighter whitish-yellowish hues. Higher DN defines the optimum areas of the alteration zones. The resulted map was classified into many classes depending on the grade of the alteration. Undesirable similar hues resulted from the sediments are masked by white polygon. Noteworthy, displaying band ratio 6/7 also highlighted the OH-bearing minerals (**Figure 2e, Figure 2f**) much more similar to Crosta technique. Accordingly, the HAZs are clearly highlighted in bright tone that graded into five zones (**Figure 2f**).

The extent of alteration zones is considered here for exploring areas of mineral resources which connected to hydrothermal activities. The Landsat data allowed highlighting the HAZs (**Figure 2g**). Combining data from band ratios and PCA well defined the rock alteration resulting from the hydrothermal activities. These zones can distinguish areas rich in hydroxyl and iron-oxide alterations. Therefore, this image was graded into five ranks after assigning weight factor for each class. The higher weight (numeric number) represents a higher grade of mineral favorability (**Figure 2g**).

4.2 Radar remote sensing for lineament extraction

Analysis of SRTM DEM (**Figure 3a**) revealed that the variations in topography range from 0 to 876 m (a.s.l). Moreover, it provided information on the geometry that was not identifiable by other RS techniques. The most elevated areas encountered in G. Duwi (elongated ridge trends NW–SE; ~550 m), G. Hamrawein (~650 m), G. Umm Himeiyir (~580 m), G. Murr (~715 m), and G. Umm Shagir (~600 m). The geological interpretation of the Landsat imagery and SRTM data (**Figure 3a**) revealed structural discontinuity that represented in lineaments. The results of lineaments analysis including density map (**Figure 3d**) and the distribution of lineaments using rose diagram reveal that the basement rocks (e.g. granites, metavolcanics, metasediments) and Cretacious/Tertiary sedimentary succession in the investigated area are highly fractured, while the area of sedimentary rocks displays less density. The lineaments density map also reveals discontinuous distribution on the area which revealing a major tectonics. Plotting lineaments on Rose diagram of Rock ware software packages (**Figure 3c**) reveals that the study areas are dominated by trends of N 30° W, and N 40° W, N 35° E, N 45° E; however, N-S and E-W respectively, according to decreasing of abundance. The NW-SE lineaments have longer and abundant in number than the NE-SW, N-S, and E-W trends.

5. Aeromagnetic data

5.1 Aeromagnetic anomalies

The study area reveals a magnetic anomaly ranging between -181.5 and 33.2 nT. The high magnetic anomalies, which characterized by short wavelengths, are observed in the southeastern, northwestern and western parts. However, the lowest magnetic anomalies (along wavelengths) are located in the southern part of the study area (**Figure 4a**). These anomalies are characteristic for the areas of the basement rocks outcrops and that covered by sedimentary cover, respectively. The sedimentary cover areas of Gabel Duwi area and its surroundings and the coastal area are manifested with the areas of low magnetic anomalies. The magnetic anomaly map revealed that the study area is structurally controlled and the predominant trends of the anomalies are NW-SE, NE – SW, N-S, and E-W.

The magnetic variation map (**Figure 4a**) was

Table 1. PCA of selected bands 2, 4, 5 and 6

Eigenvector	Band 2	Band 4	Band 5	Band 6	Eignvalue %
PC1	0.15022	0.441575	0.609239	0.641306	96.64965
PC2	0.221567	0.369174	0.481423	-0.763447	2.71183
PC3	0.660352	0.479502	-0.574698	0.061116	0.517105
PC4	0.701624	-0.66242	0.258423	0.046263	0.121419

Table 2. PCA of selected bands 2, 5, 6 and 7

Eigenvector	Band 2	Band 5	Band 6	Band 7	Eigenvalue %
PC1	-0.120062	-0.49843	-0.67361	-0.53236	97.5627
PC2	-0.2805	-0.75513	0.157252	0.571283	1.627296
PC3	0.425616	0.155359	-0.66236	0.596655	0.616379
PC4	0.851913	-0.3965	0.287758	-0.18502	0.193578
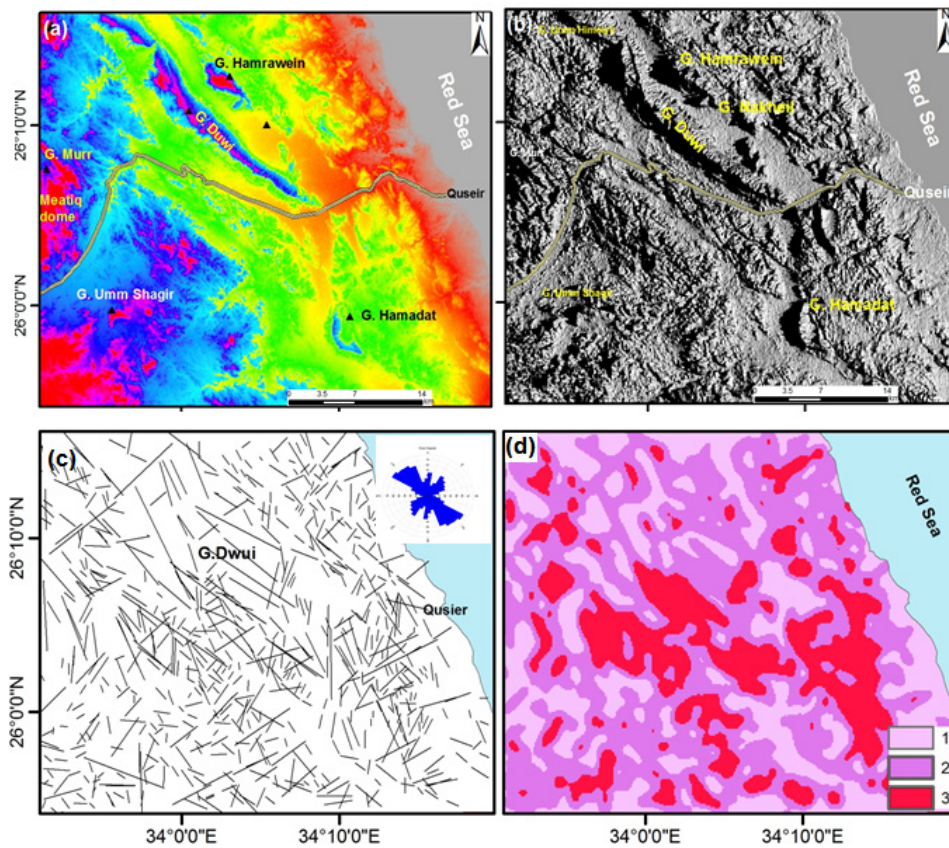
Figure 3. (a) SRTM-DEM m; (b) hill shade relief; (c) lineaments derived from remote sensing data; (d) lineament density of remote sensing data**.**

41

transformed into reduction to the pole (RTP) grid using the 2D – FFT (Fast Fourier Transform) filter (**Figure 4b**). The parameters which used for the transformation include an inclination of 39.5 and declination of 2, representing the mean values.

The resulted RTP map of the study area (**Figure 4b**) shows the presence of many magnetic zones with maximum amplitude values of about 115 nT. They are observed in southeastern and southwestern parts of the study area that associated with a metavolcanics, metasediments, metagabbros and younger granites above G. Umm Shagier, G. Muweilih, G. Umm Khurs and north G. Hamadat. Similar observations are detected in the western part related to metamorphic complexes of G. Umm Baanib and also in the northern part. The magnetic anomalies of this zone are defined by a broad high magnetic anomaly with an elongated to semicircular shape. These anomalies trend in the NE-SW, NW-SE, N-S and E-W directions. On the other hand, the magnetic anomalies with a low amplitude value of -228.95 nT are observed at the southwestern part of the study area and they are related to metasediments and Quaternary deposits above G. Umm Hombose. These areas also marked by the elongated shapes that trend in NE-SW and NW-SE directions.

5.2 Residual magnetic anomalies

In areas of basement exposures, the aeromagnetic anomalies reflect the magnetic mineral contents of the rock units[30]. Magnetic variations in areas of fracture/fault zones represent the favorable sites of mineralization. In the residual map, there are chains of small circular peaks magnetic anomaly closures, associated with volcanic and granitoid intrusions (**Figure 4c**). Porphyry deposits are often around the intrusive masses[41]. For example, tin (Sn) deposits most likely occur in the outer zone of the granitic body and tin also associated with magnetite mineralization. Therefore, these areas shown in **Figure 4c** reveal high grade of magnetic intensity. Many magmatic intrusions and quartz veins are involved with the hydrothermal activities. According to Rigol-Sanchez *et al.*[30], the high residual magnetic values pointed out zones of plausible ore-bearing

buried anomalous bodies. Therefore, zones of elevated magnetic anomalies highlight areas of higher magnetic content. In addition to the aforementioned information, the image clearly highlighted the NE-SW zone that probably intersected and dislocated the NW-SE basin.

5.3 Euler deconvolution

The Euler deconvolution method was performed using the RTP grid with structural indexes of (0) and with a moving window of 10 x 10 and Euler solution was accepted on the criterion of errors 10%. The resulted map obtained in this case (**Figure 4d**) shows depth solutions ranges from 0 to 2000 m and most of these solutions are fall in the range of 0 to 500 m represented the shallow sources. These causative sources are extended in the NW-SE, NE-SW, and N-S.

5.4 Lineaments derived from aeromagnetic data

Subsurface linear structures identified in the study area from regional and residual magnetic maps (**Figure 5a** and **Figure 5b**) revealed lineations with trend directions in NW-SE, NE-SW, NNW-SSE, and NNE-SSW, with minor directions in ENE-WSW and WNW-ENE. Lineament density map obtained from sub-surface aeromagnetic data revealed the majority of elongated NW-SE zones and their intersected NE-SW trends (**Figure 5b**).

The lineaments that were deduced from aeromagnetic data are compiled from RS to produce an integrated lineament map (**Figure 6a**) which represents the major surface and sub-surface structures (faults/fractures). Analysis of lineament of both RS and AMG data revealing that the NW-SE and NE-SW lineaments are predominant trends in the present study. The extracted lineaments from these data were interpreted to density map (**Figure 6b**). This map revealed a high density of fracture/fault zones around Umm Had, Duwi area, Wadi Kareim, and in the middle section of the study area. Moreover, the density map reveals a predominant NW-SE trend that intersects by the NE-SW trend.

The detected linear trends have played a major
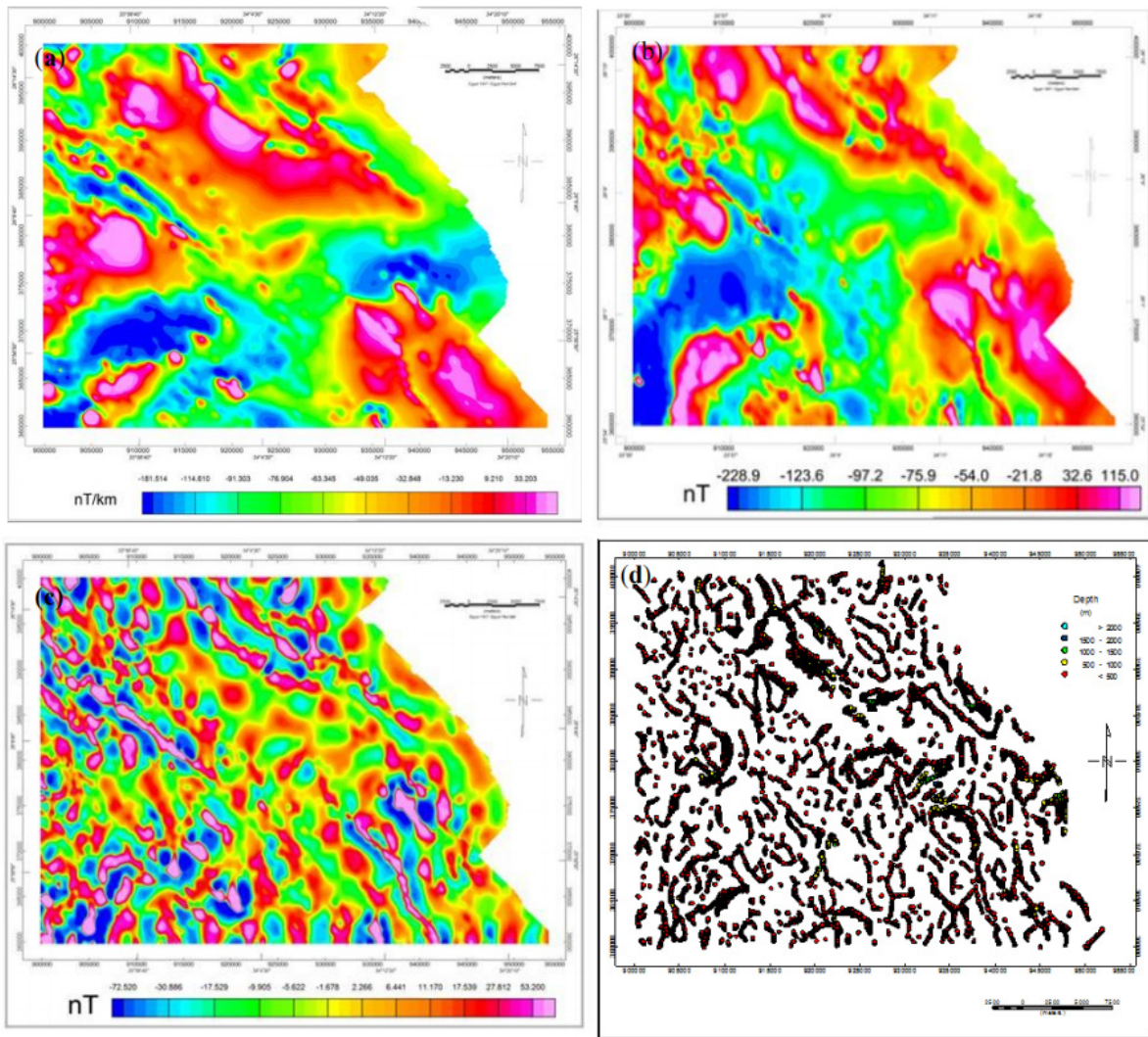
Figure 4. (a) Total magnetic intensity map of the study area; (b) reduction to the pole map of the study area; (c) residual magnetic anomaly map; (d) standard Euler deconvolution applied to RTP magnetic intensity map with structural index (SI) = 0.
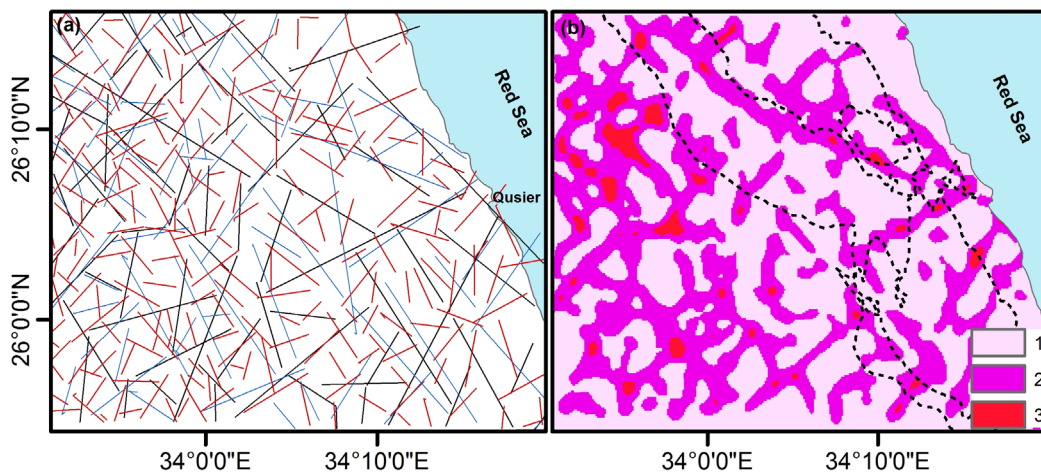
Figure 5. (a) Lineaments derived from magnetic anomaly maps; (b) lineament density map from magnetic maps revealing linear anomalies of deep seated structures of regional extent.

43
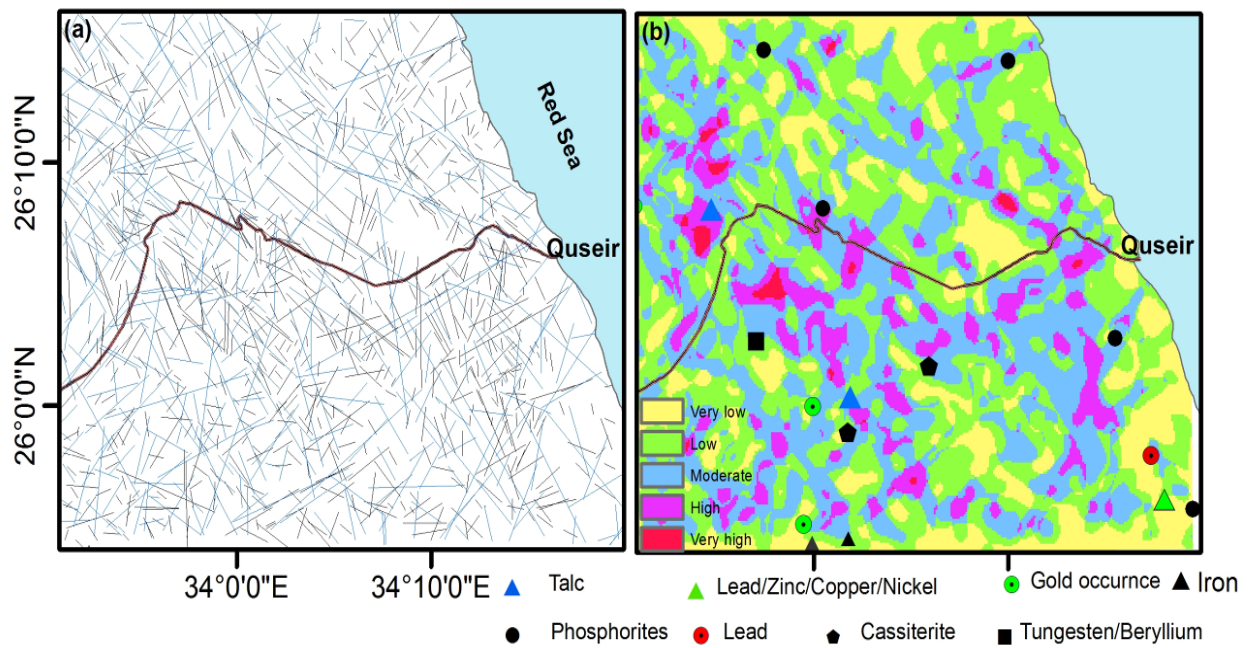
Figure 6. (a) An integrated lineaments from remote sensing (black) and magnetic data (blue); (b) lineament density map from remote sensing and magnetic data.
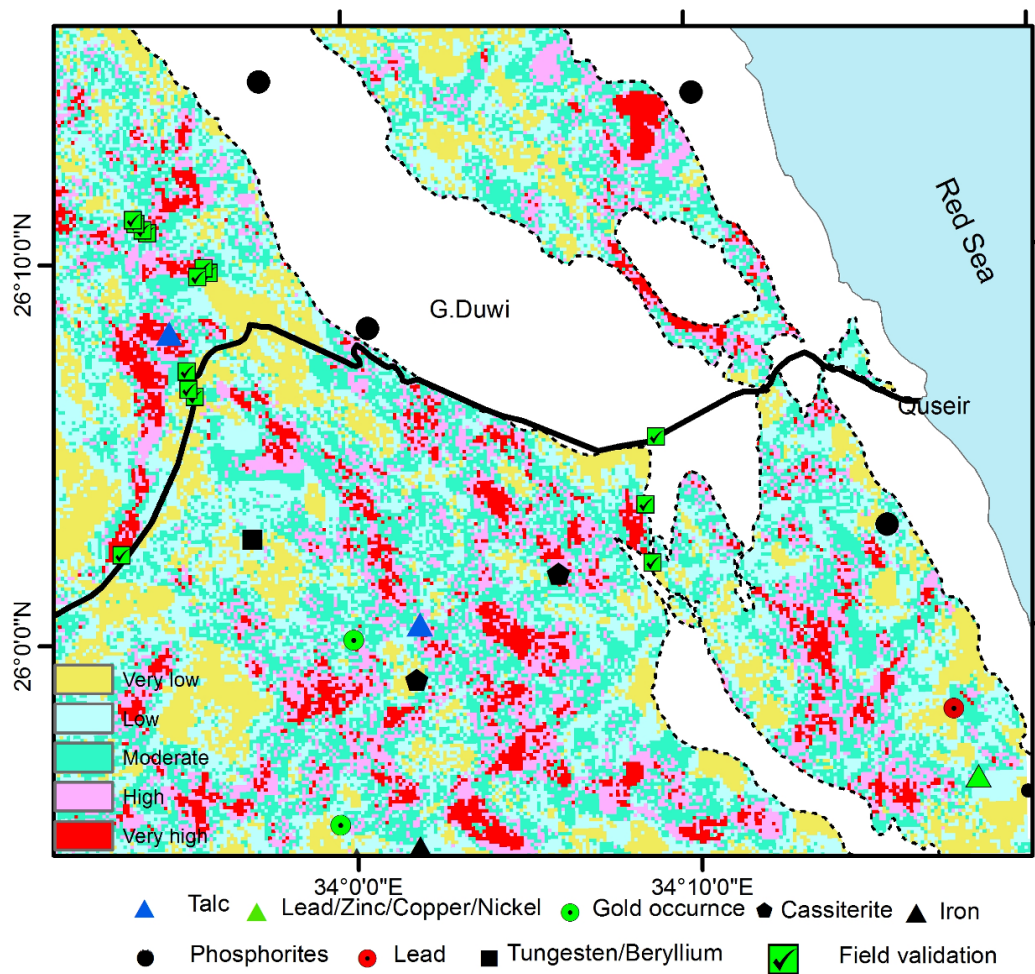
Figure 7. The mineral predictive map obtained by combining alteration zone and lineaments.

44

role in controlling the geodynamic evolution of the study area. Also it is shown that there are several strike slip faults were detected in NE-SW and NW-SE directions that have sub-surface continuation (**Figure 5a, Figure 5b**). This explains a probable dislocation of G. Duwi area north of Qift-Quseir Road from its counterpart of the sedimentary succession in the south. Landsat data validated these trends which controlled the rock units and also represent the favorable sites of the hydrothermal solutions.

In order to prepare the lineament map for further combination, we classified it into five classes after assigning weigh factors represented by numeric numbers 1, 2, and 3 (**Figure 6b**). The high value represents the higher density and the favorable site of mineral resources. Since several mineral deposits are related to hydrothermal solutions that ascending through fractures/fault zones. Therefore, zones of higher lineament density which related to tectonic/ structural deformation of the lithosphere[31] represent a prone area of mineral resources. After converting the lineament density map into a weighted map, we superimposed the existing mines on this map. This results in **Figure 6b** revealed a positive correlation between the primary mineral-occurrences such as talc, iron, cassiterite, and Cu-Au-Pb-Zn mineralizations.

6. Integrated maps for predicting areas of mineral resources

The method of combining several data in a geospatial analysis technique is significant in mineral potential mapping[30]. To determine the probable area of mineral resources in the form of weighted map, an integrated approach has been adopted for characterizing the areas of mineral occurrences[42]. These data were adapted in raster to allow comparing and integrating peer-pixels in the image array. In this section, the lineaments and alternation zones that generated from RS and AMG data are integrated. They represent the appropriate indicators of mineralization and are effective reconnaissance approach in mineral exploration.

This process of hydrothermal activities commonly occurs along the faults and fracture zones. In addition, radar remote sensing data allowed detecting fracture and fault zones (lineaments). Thus, integration of optical and radar RS data can help in detecting mineral resources associated with hydrothermal solutions. Therefore, when considering the optimal location for a new mineral prospect, there are many factors need to be considered, including, for example, the fracture/fault zones and alteration zones.

Applying a spatial dimension of these factors using geographic information system (GIS) could be a useful tool to find the suitable location for new mineral prospect. Find the high lineament density area by applying spatial analysis technique allowed detecting the most area of fracture/fault zones. Such areas represent the favorable sites for mineral occurrences; therefore, we classified the lineament density map into several classes, the highest class represents in red color, while the lower represents in light magneta (**Figure 6b**).

The high areas of alteration appear with a red color, followed by magenta, cyan, and yellow colors. In order to achieve the optimal result, we combined the altered areas which obtained from multi-sources and the lineament density map. The results revealed that the most suitable areas predicted by GIS tool are consistent with areas of high alteration and high lineament density. Moreover, these areas display good correlation with the well-known area of the existing mines (**Figure 7**). These combined data from remote sensing including lineaments and alteration zones (**Figure 2g, Figure 6b**) can be employed in predicting areas of probable mineral resources.

6.1 Mineral predictive map

The collected data were digitally superimposed in a GIS and combined using spatial analysis techniques. The final map after combining lineaments (from aeromagnetic data, and remote sensing) magnetic residual anomalies, and HAZs allowed delineating the probable sites of mineral resources. This map was distinguished into five zones including very high, high, moderate, low, and very low areas of mineral occurrences. Overlay the existing sites of mineralization on the final map revealed that talc, cassiterite, gold, and copper/lead mineralization dis-

played positive correlation with areas of very high to high favorability (**Figure 7**). However, some mineralizations are difficult to be predicted that aren't correlated with lineaments or alteration zones such as phosphorites.

6.2 Field validation

In order to validate the extracted lineaments, predicted areas of alteration zones, and verify the mineral potential map, we have used existing mines and conducted field trip in November 2016. Based on field observations, the NW lineaments were predominant over the other trends. Most of these features include fractures/fault zones that are filled by quartz veins, sills, and dykes mostly of felsic composition (**Figure 8**). Five field stops were checked, most of these sites revealed minerals involved with hydrothermal activities such as talc, gold, and areas rich in muscovite and talc-schist. However, some areas were related to altered metavolcanics and associated metapyroclastics in the right hand of Qift-Quseir road. Some trends that were extracted from the aforementioned data are clearly observed in the field e.g. strike slip faults along the major trends of NW-SE, and some of them allowed formation of the sedimentery basins. These trends may control the rock units and mineralizations. They are mostly shears and fractures that vary from centimeters to meters in width, mostly occupied by quartz veins. Foliations and alterations are common in these rocks that represented by multi-deformation.

Evidences of alteration processes include
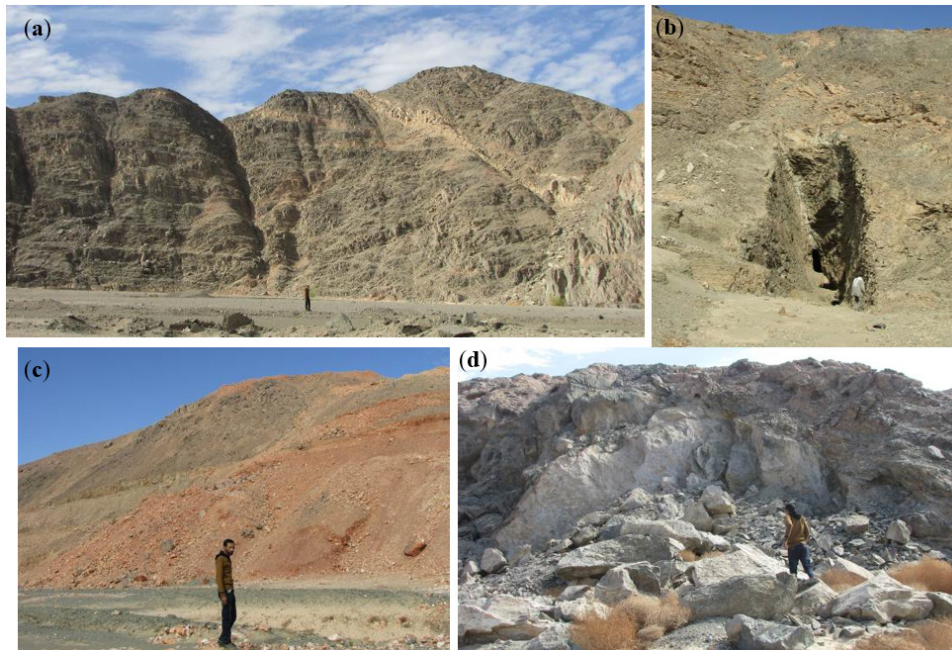
Figure 8. Field photographs (a) NW-SE joints, swarms of dykes and faults that cutting the metavolcanic rocks; (b) NW-SE quartz vein and alteration zones in gold mineralization; (c) site of hematite and quartz veins; (d) talc associated with serpentinites.

multi-colored rocks, silicification, iron-oxides, and carbonization that varies in thickness. The host rocks of the metavolcanics were sheared and altered to talc-carbonates. It pervasively altered to carbonates and micaceous minerals. Field investigations revealed that the tested areas characterized by alteration zones enriched in talc, calcite and secondary amphiboles. It is found that the HAZs are more consistent with the lineaments extracted from the magnetic intensity map (**Figure 7** and **Figure 8**). This indicated that alteration zones usually connected to deep lineaments. This integration shows that the approaches of RS and AMG maps are effective techniques for exploring iron- and OH bearing minerals. Moreover, they presented a positive relationship between the primary mineral occurrences and areas of high lineaments and alteration zones.

7. Conclusions

The study area is located west of the Quseir city, Red Sea, Egypt. Integration of RS and AMG data allowed detecting structural discontinuity and HAZs in the present study area. Image transformation techniques including band ratios and PCA were performed to Landsat OLI to reveal area of HAZs. The resulting image was discriminated into five zones characterizing the degree of the alteration. SRTM data was used to extract lineaments. Subsurface lineaments were delineated using the AMG data with several tools. In order to maximize area of probable mineral resources, HAZs and lineament density were combined to prepare the mineral prospect map. Field validation allowed verifying the prepared map and revealed several mineralized zones including talc, gold mines and quartz veins-bearing hematite.

Conflict of interest

The authors declare that they have no conflict of interest.

Acknowledgments

References

1. Sultan M, Arvidson RE, Sturchio NC. Mapping of serpentinites in the Eastern Desert of Egypt by using Landsat thematic mapper data. Journal of Geology 1986; 14(12): 995–999.

2. Abdelsalam MG, Stern RJ, Berhane WG. Mapping gossans in arid regions with Landsat TM and SIR-C images: The Beddaho Alteration Zone in northern Eritrea. Journal of African Earth Sciences 2000; 30(4): 903–916.

3. Madani A, Abdel Rahman EM, Fawzy KM, *et al.* Mapping of the hydrothermal alteration zones at Haimur Gold Mine Area, South Eastern Desert, Egypt using remote sensing techniques. The Egyptian Journal Remote Sensing Space Science 2003; 6: 47–60.

4. Ramadan TM, Kontny A. Mineralogical and structural characterization of alteration zones detected by orbital remote sensing at Shalate in District, South Eastern Desert, Egypt. Journal of African Earth Sciences 2004; 40: 89–99.

5. Abdelkareem M, El-Baz F. Characterizing hydrothermal alteration zones in Hamama area in the central Eastern Desert of Egypt by remotely sensed data. Journal of Geocarto International 2018; 33: 1307–1325.

6. Ahmed A, Abdelkareem M, Asran AM, *et al.* Geomorphic and lithologic characteristics of Wadi Feiran basin, Southern Sinai, Egypt, using remote sensing and field investigations. Earth System Science Journal 2017; 126(85): 1–25.

7. Abdelkareem M, El-Din GMK, Osman I. An integrated approach for mapping mineral resources in the Eastern Desert of Egypt. International Journal of Applied Earth Observation and Geoinformation 2018; 73: 682–696.

8. Sabins F. Remote sensing principles and interpretation. 3rd ed. W.H. Freeman Company; 1997. p. 494.

9. Sabins F. Remote sensing for mineral exploration. Ore Geology Review 1999; 14: 157–183.

10. El Khidir SO, Babikir IA. Digital image processing and geospatial analysis of landsat 7 ETM+ for mineral exploration, Abidiya area, North Sudan. International Journal of Geomatics and Geosciences 2013; 3(3): 645–658.

11. Amuda OS, Adebisi S, Jimoda L, *et al.* Challenges and possible panacea to the municipal solid wastes management in Nigeria. Journal of Sustainable Development Studies 2014; 6(1): 64–70.

12. Poormirzaee R, Oskouei MM. Use of spectral analysis for detection of alterations in ETM data, Yazd, Iran. Applied Geomatics Journal 2010; 4: 147–154.

13. El-Din GK, Abdelkareem M. Integration of remote sensing, geochemical and field data in the Qena-Safaga shear zone: Implications for structural evolution of the Eastern Desert, Egypt. Journal of African Earth Sciences 2018; 141: 179–193.

14. Abdelkareem M, El-Baz F. Mode of formation of the Nile Gorge in northern Egypt: A study by DEM-SRTM data and GIS analysis. Geological Journal 2015; 51: 760–778.

15. Goetz AFH, Rock BN, Rowan LC. Remote sensing for exploration, an overview. Economic Geology

1983; 78: 573–590.

16. Segal DB. Use of landsat multispectral scanner data for definition of limonitic exposures in heavily vegetated areas. Economic Geology 1983; 78: 711–722.

17. El-Etr HA, Yousef MSM, Dardir AA. Utilization of Landsat images and conventional aerial photographs in the delineation of some aspects of the geology of the Central Eastern Desert, Egypt. Annals of Geological Survey of Egypt 1979; 9: 136–162.

18. O'Connor EA, McDonald AJW. Application of remote sensing for geological mapping in Eastern Desert, Egypt. Proceeding of IGARSS' 88 symposium, Edimburg, Scotland; 1988. p. 631–632.

19. Sultan M, Arvidson RE, Duncan IJ, *et al.* Extension of the Najd shear system from Saudi Arabia to the Central Eastern Desert of Egypt based on integrated field and Landsat observations. Tectonics 1988; 7: 1291–1306.

20. El-Rakaiby ML. The use of enhanced Landsat-TM image in the characterization of uraniferous granite rocks in the central Eastern Desert, Egypt. International Journal of Remote sensing 1995; 16(6): 1063–1074.

21. Farghaly AMA. Structural framework of the Central-Eastern Desert of Egypt, using remote sensing techniques and ground data [PhD thesis]. Sohag: South Valley University; 1999.

22. Gad S, Kusky T. Lithological mapping in the Eastern Desert of Egypt, the Barramiya area, using Landsat thematic mapper (TM). Journal of African Earth Sciences 2006; 44(2): 196–202.

23. Sultan M, Arvidson RE, Sturchio NC, *et al.* Lithologic mapping in arid regions with Landsat thematic mapper data: Meatiq Dome, Egypt. GSA Bulletin 1987; 99(6): 748–762.

24. Conoco. Geological map of Egypt, scale 1:500,000, sheet NG 36 NW Quseir-NG 36 NW Asyut, Egypt. The Egyptian General Petroleum Corporation, Cairo, Egypt; 1987.

25. Said R. Tectonic framework of Egypt and its influence on distribution of Foraminifera. AAPG Bulletin 1962; 45: 198–218.

26. Said R (editor). The geology of Egypt. Rotterdam, Brookfield: A. A. Balkema; 1990.

27. Ghebreab W. Tectonics of the Red Sea region reassessed. Earth-Science Review 1998; 45: 1–44.

28. Gass IG. The evolution of the Pan African crystalline basement in NE Africa and Saudi Arabia. Journal of the Geological Society 1977; 134: 129–138.

29. Kröner A. Ophiolites and the evolution of tectonic boundaries in the Late Proterozoic Arabian-Nubian Shield of Northeastern Africa and Arabia. Precambrian Research 1985; 27(1-3): 277–300.

30. Rigol-Sanchez JP, Chica-Olma M, Abarca-Hernandez F. Artificial neutral networks as a tool for mineral potential mapping with GIS. International Journal of Remote Sensing 2003; 24(5): 1151–1156.

31. Alexander Io, Samuel OO, Esther CM, *et al.* Integrating Landsat-ETM and Aeromagnetic data for enhanced structural interpretation over Naragwata area, North-Central Nigeria. International Journal for Science and Engineering Research 2015; 6(9): 2229–5518.

32. Gerck E, Hurtak JJ. Laser remote sensing of forest and crops in genetic-rich tropical areas. International Archives of Photogrammetry and Remote Sensing 1992; 436–438.

33. Cappaccioni B, Vaselli O, Moretti E, *et al.* The origin of thermal water from the eastern flank of the Dead Rift Valley. Terra Nova 2003; 15(3): 145.

34. Hsu SK. Imaging magnetic sources using Euler's equation. Geophysical prospecting 2002; 50: 15–25.

35. Thompson DT. EULDPH: A new technique for making computer-assisted depth estimates from magnetic data. Geophysics 1982; 47: 31–37.

36. Reid AB, Allsop JM, Granser H, *et al.* Magnetic interpretation in three dimensions using Euler deconvolution. Geophysics 1990; 55: 80–91.

37. Ramadan TM, Abdelsalam MG, Stern RJ. Mapping gold-bearing massive sulfide deposits in the neoproterozoic Allaqi Suture, Southeast Egypt with Landsat TM and SIR-C/X SAR images. Photogrammetric Engineering & Remote Sensing 2001; 67(4): 491–497.

38. Ramadan TM, Sultan SA. Integration of Remote Sensing, Geological and Geophysical Data for the Identification of Massive Sulphide Zones at Wadi Allaqi Area, South Eastern Desert, Egypt. M.E.R.C. Ain Shams University Earth Science Series 2004; 18: 165–174.

39. Eldosouky AM, Abdelkareem M, Elkhateeb SO. Inte-

gration of remote sensing and aeromagnetic data for mapping structural features and hydrothermal alteration zones in Wadi Allaqi area, South Eastern Desert of Egypt. Journal of African Earth Sciences 2017; 130: 28–37.

40. Ramadan E, Feng X, Cheng Z. Satellite remote sensing for urban growth assessment in Shaoxing City, Zhejiang Province. Journal of Zhejiang University Science 2004; 5(9): 1095–1101.

41. Shahi H, Kamkar-Rouhani A. A GIS-based weights-of-evidence model for mineral potential mapping of hydrothermal gold deposits in Torbat-e-Heydarieh area. Journal of Mining & Environment 2004; 5(2): 79–89.

42. Woldai T, Pistocchi A, Master M. Validation and sensitivity analysis of a mineral potential model using favourability functions. Applied GIS 2006; 2(1): 19.

ORIGINAL RESEARCH ARTICLE

Advances in flash flood research based on dendrogeomorpholog

Jiazhi Qie[1,2], Yong Qie[1*]

[1] *Key Laboratory of Land Surface Pattern and Simulation, Institute of Geographic Sciences and Natural Resources Research, CAS, Beijing 100101, China. E-mail: zhangyong@igsnrr.ac.cn*
[2] *University of Chinese Academy of Sciences, Beijing 100049, China.*

ABSTRACT

Flash flood is one of the major natural hazards in China. It seriously threatens the lives of people and property in mountainous areas. Various methods have been developed for flash flood study, but most of them focused on the past few decades. As one of the effective methods of historical flash flood events reconstruction, dendrogeomorphology has been used worldwide. It can provide hazard information with long temporal scale and high temporal resolution, sometimes at the seasonal level. By comparing tree ring width and other growth characteristics between disturbed and undisturbed trees, growth disturbance signals can be found in the disturbed trees. Using the growth disturbance in tree rings, flash flood events can be dated, and then the frequency, size, and spatial distribution characteristics of flash floods that have no or little documentary records can be reconstructed. The discharge of flash flood can be reconstructed quantitatively according to the height of scars or by using hydraulic models. With the development of dendrogeomorphology, research tends to probe into the meteorological driving mechanism of flash floods and the pattern of flash floods on a larger spatial scale. In the practical application of dendrogeomorphology, more instrumental data and historical records are applied in the studies. This makes the method increasingly more widely used around the world. But work based on dendrogeomorphology has not been reported in China. In this article, we reviewed the development of the study on flash floods based on tree ring, briefly summarized the research progress, and discussed the advantages, limitations, and potential of this approach, so as to provide some reference information for relevant work in China.

Keywords: Flash Floods; Tree Ring; Dendrogemorpholog

1.Introduction

Flash floods in mountainous areas occur in a short time and are hard to prevent, usually with heavy precipitation events or infrastructure damage in most cases[1,2]. China has a mountainous terrain and the mountainous area accounts for about 2/3 of the national land area. Rainstorms occur frequently in the eastern monsoon area. Besides, the snow melts into water in the western mountains brings abundant water sources, and the height difference between the three steps is huge. These factors make flash floods occur frequently and affect a wide range in China[3]. At present, China has carried out a lot of systematic research on flash flood disasters, including analysis of flash flood causes[4–6], characteristics of temporal and spatial distribution[7–9], application of early warning indicators[10–12], the risk analysis and prediction of flash flood disaster[13–17] and so on. From the previous field survey to the application of "3S" technology, from the analysis based on historical records and measured data to the combination with mete-

orological forecast data, the research on flash flood disaster has been gradually deepened. However, most of these studies need to rely on historical flash flood data or instrumental measurement data. These data have a short recording period, especially in mountainous areas, which are limited by terrain and sparsely populated, and often lack historical data such as precipitation and flow, so it is difficult to find the historical law of flood. In recent years, dendrogemorpholog has been widely used in the dating and characteristic analysis of flash floods on a long time scale. Trees with clear annual rings will retain growth interference signals in the tree rings after being affected by flash floods. With the support of large sample size, such growth interference events can be dated with the help of cross-dating technology, so as to determine the year of flash floods. According to the number and intensity of growth disturbance, the number and spatial distribution of trees affected by flash floods, we can explore the temporal and spatial characteristics of flash floods and reconstruct the history of flash floods in areas with no or little data[18]. This method can provide alternative or supplementary data for flash flood event dating[19]. Compared with other alternative indicators, this method has accurate dating, high resolution and even up to seasonal scale[20]. A lot of work has been carried out all over the world and the research prospects are very broad. Flash floods occur frequently in China, especially in recent years, extreme precipitation events occur frequently[21–23]. Therefore, it is necessary to strengthen the research on the temporal and spatial characteristics and causes of flash floods under the background of longer time scale, so as to provide necessary background information for the prediction and prevention of flash floods in the region. Unfortunately, the relevant work has not been carried out in China. Therefore, this paper systematically introduces the development history, research methods and the latest progress of flash flood research based on dendrogemorpholog, and further discusses the problems and potential of this new research direction in China.

2. History and methods of flash flood research with using tree rings

2.1 The history of flash flood research

The study of historical dendrochronology of flash floods is a science that studies the annual growth layer of tree xylem and uses the annual growth layer for dating. It was founded by American astronomer Douglas in the early 20th century[24]. With the development of the discipline, many branches of the dendrochronological school have emerged, and dendrogemorpholog is one of them. Alestalo systematically expounded dendrogemorpholog and defined it as a discipline that uses tree rings to study geomorphic processes in historical periods and predict geomorphic processes in the future. Later, tree rings played an important role in the study of geomorphic processes such as avalanche, debris flow and rockfall[25–28].

In the early 20th century, Hardman realized the great potential of using tree rings for hydrological research[29]. However, it was not until Sigafoos studied the tree differences before and after the Potomac flood event in 1961 that he preliminarily pointed out the relationship between riparian vegetation and flood frequency[30]. Sigafoos then put forward the theoretical basis of using tree rings to study floods. His research has played a great role in the field of paleohydrology[31]. The great potential of flood botanical evidence in paleohydrology proposed by him has been repeatedly demonstrated[32] and widely used. In recent years, the study of flash flood events under the background of long-time scale by using tree rings has been widely carried out in Northern America, Eastern Europe and Mediterranean mountain basin and other areas[18,33–38]. The relevant research gradually starts from the dating of flood events and the analysis of their cycle, frequency and intensity to analyze the driving mechanism of flash floods and the changes of tree ring anatomical characteristics after being affected by flash floods.

2.2 Sampling and recognition of growth disturbance signals

Growth disturbance signals, such as scars or

bent branches of trees should be captured when doing wide sampling. Generally speaking, priority is given to disturbed trees at the exposed location of the river bank or on the inner side of the river[39,40]. For the disturbed tree, the growth sample core can be collected, and the sampling position can be as close to the scar as possible, or the wedge wood can be collected directly at the injured position[41]. For European conifers, growth cores are generally collected at the upper part of the injured position, because the radial extension of the traumatic resin channel generated by the tree response after interference is the largest above the wound[42,43]. In addition, dead tree discs or branches and exposed roots can also be collected to make cross-sectional samples. For curved trees, growth cores are collected at the curved position. For trees with damaged crown or abnormal stem morphology, growth cores shall be collected at the lower part of the injured area. When sampling, pay attention not to collect samples at other positions of the stem or in the area where scars are formed due to other factors (surrounding tree dumping, etc.)[37]. Besides these, we also should record the sampling height, DBH and the growth of surrounding trees, and take photos of the sampling trees. In addition, it is necessary to collect cores of healthy growth of the same tree species not affected by flash floods around the study area, and take one growth core on both sides of a tree to establish a local reference chronology, so as to provide basis for cross-dating. After the samples are collected back to the laboratory, the sample core is fixed on the sample slot with glue, and then the sample core or tree disc is dried and polished until the tree ring is clearly visible. The tree ring width is measured by the ring width meter. Before establishing the reference chronology, COFE-CHA program can be used to control the accuracy of dating and measurement[44].

Flood will hinder the normal radial growth of trees in the affected area and induce growth interference that can indicate the geomorphological process, including growth inhibition or release, deformed trees, abnormal growth, callus, scar or traumatic resin channel.

Among them, scar is the most widely used be-

cause it has a strong ability to provide flood time and water level information in historical periods[45,46]. **Figure 1** shows a variety of growth interference response types. During the flood, the water flow and its carriers may break the crown of shorter trees, which will cause a sudden slow-down of tree ring growth[31]. After the broken trees died, they will no longer compete with the surrounding trees, and the wheel width of the remaining trees will become wider, which is manifested as sudden growth and release. If the trees are bent due to the flood, the tree rings will show abnormal growth, and the wheel width on one side will be narrowed and the wheel width on the other side will be relatively widened. If the damage suffered by the tree is not enough to make it die, the tree will form scars in the next few years[34]. When the river bank is eroded by flood, the roots of trees beside the river bank will be exposed[47], which will not only change the wheel width, but also lead to significant changes in the anatomical structure of trees, usually including the reduction of early wood tracheid size and the increase of late wood cells[48,49], the reduction of lumen area and the increase of cell wall thickness resulting in the increase of the proportion of cell wall in early wood tracheids. The increase of cell wall thickness also leads to the decrease of radial length and tangential width of tracheids in early wood, and the increase of the number of wound resin channels in early wood and late wood[36]. However, when Pinusdensi-floraSieb is eroded by flood for a long time, the lumen size of plant cells will not change[50]. Moreover, the changes of anatomical characteristics of different tree species are different, and there are obvious tree species differences. For example, when analyzing the changes of anatomical characteristics of Almsglutinosal, Fraxinus Angustifolia Vahl and Quercus Pyrenaica Willd in the Mediterranean region after flash floods, it is found that the lumen area of the three tree species decreases after flash floods and the results of nonparametric test are significant, but the area changes of early wood fibers and parenchyma cells vary with different tree species, and the degree of change is not obvious. Therefore, flash floods cannot be identified only based on this[37].

In short, by comparing the ring width and other

characteristics of disturbed and undisturbed trees, we can find the sudden growth change of disturbed trees[51], so as to determine the occurrence time of growth disturbance, and then provide the flash flood event sequence with annual resolution and even seasonal resolution on a long time scale, and provide basic information for flood model simulation in small watersheds.
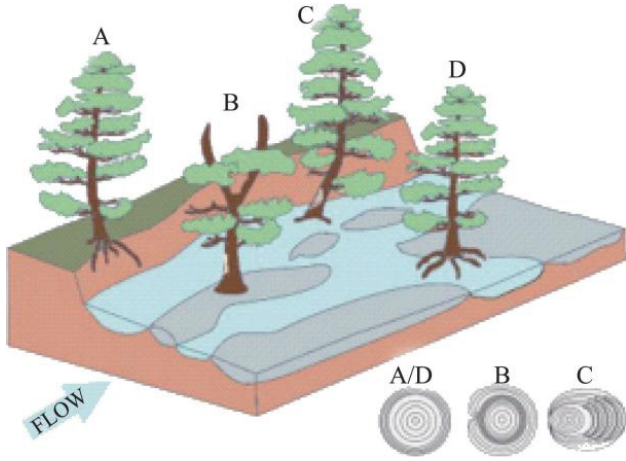
Figure 1. Predominant dendrogeomorphic macro-evidence in trees affected by flash floods and associated responses in tree-ring width and cell structure.

2.3 Dating and analysis of flash floods

The dating of flash floods often depends on the number of samples showing growth interference in the same year, the signal intensity of growth interference[52,53] and the spatial distribution of damaged trees in the river area[54]. When growth interference signals appear in tree rings for many years, only the first year of growth interference is often considered as the exact year of flash floods[55]. In practical application, it is generally necessary to define the index to determine the flash flood event. In individual years, the strength of flash flood signal can be expressed by the index I_t[56,57]. At first, the index was applied to the determination of avalanche disaster events. Afterwards, Šilhán[58] cited this index in the analysis of flash floods:

$$I_t = (\sum R_t / \sum A_t) \times 100\% \qquad (1)$$

In this formula: R_t is the number of trees showing growth disturbance affected by flash floods in year t, and A_t is the number of all live trees collected in year t.

When the index is applied, a large number of samples need to be collected to avoid overestimation of recent interference events. The weight index W_t defined by Kogelnig Mayer *et al.*, comprehensively considers the type, quantity and intensity of growth interference and the sample size that can be used for reconstruction[52]. This index was first used to analyze avalanche and debris flow events, and then cited in the analysis of flash floods:

$$W_t = [(\sum T_i \times 7) + (\sum T_s \times 5) + (\sum T_m \times 3) + \sum T_w] \times (\sum R_t / \sum A_t) \qquad (2)$$

In this formula: T_i represents the number of trees with scars, and T_s, T_m and T_w represent the number of trees with strong, medium and weak growth interference respectively. Compared with index I_t, W_t takes into account the difference of growth interference intensity in tree rings. There may be many types of growth interference in trees, and the intensity is $T_i > T_s > T_m > T_w$. The strongest interference type should be selected for calculation during analysis. The application of this index has different standards in different study areas. Ballesteros-c á novas *et al.*, reconstructed the flash floods in Guadalama Mountains of Spain[19]. When the weight index $W_t > 1$, it can be considered that a flash flood event occurred in that year. Ruiz Villanueva *et al.*, also graded the weight of growth disturbance when reconstructing flash floods on the Perayo River in Spain and defined the weight index (WGD: weights of growth disturbances) with a value of 0.1 ~ 1 to distinguish the growth disturbance caused by flash floods to trees in different degrees[35]. In the end, they comprehensively considered the weight value of growth disturbance WGD, the ratio of the number of damaged trees to the analyzed trees in the same year (%DT: the percentage of damaged trees) and the spatial distribution of damaged trees in the river area (SD: spatial distribution of affected trees). The year of occurrence of flash floods is determined by the product of these three parameters (WGD×% DT×SD).

3 Advances in flash floods research based on tree rings

3.1 Single point and regional flash flood event reconstruction

Flash flood reconstruction can be divided into single point reconstruction and regional reconstruction, and most of the early work was single point reconstruction. Ballesteros-Cáno-Vas *et al*., collected 287 tree ring cores from 178 Scotch pine trees disturbed by flash floods, obtained 212 growth disturbance information related to flash floods, and reconstructed twenty-five flash floods in guadalama mountains of Spain from 1748 to 2011[19].

Ruiz-Villanueva *et al*., comprehensively used archival records, instrumental survey data and dendrogemorpholog methods to reconstruct 41 flash floods in Iron Tale River Basin in Spain since the end of the 19th century, and analyzed the frequency, intensity, seasonality and driving factors of flash floods. Among them, 60% of the 36 reliable flash floods occurred in autumn and winter, while the remaining 40% occurred in spring and summer Season[59].

Casteller *et al*., collected tree samples of Chilean Austrocedrus chilensis, Pseudotsuga menziesii and Nothofagus dombeyi with interference characteristics when analyzing flash floods in the Andes[55]. Disturbance features include scars, exposed roots, sloping, broken or buried stems. According to the characteristics of scar, eccentricity, sudden growth inhibition and release of reaction wood and tree rings, and tangential wound resin channels in tree rings, 21 flash floods in this area from 1890 to 2009 were reconstructed. It was found that the average recurrence cycle of flash floods was 37.4 years. Further analysis showed that 58.2% of flash floods occurred in dormant period, 29.1% and 12.7% of the events occurred in the growth period of early wood and late wood. It can be seen that using dendrogemorpholog can reconstruct the historical flash flood event information on a seasonal scale, and the occurrence of flash flood events has certain commonalities in the region. For example, the flash flood event in 1936 was found in many study areas in Spain.

With the development and deepening of flash floods reconstruction in a single watershed, the research tends to a larger spatial scale, that is, the flash floods in multiple watershed historical periods in a region. For example, Ballesteros-Cá novas *et al*., collected the sample cores of more than 1,100 injured trees affected by flash floods on the north slope of Tatra mountain in Poland and reconstructed the flash flood activities in the past 148 years with the method of dendrogemorpholog, and then discussed the temporal and spatial patterns of floods in the historical period of four rivers on the north slope of Tatra mountain[60]. He also analyzed the hydro meteorological driving factors of flash floods, including the indicators of total precipitation in 1, 3 and 5 days from April to October. By calculating the difference coefficient of effective precipitation data in the study area, he found that when the total precipitation in 3 days exceeds 100 mm, the water level will be higher than the usual 150%. Rodri-Guez morata *et al*., reconstructed 8 flash floods that were not recorded by historical data in the 20th century and early 21st century by analyzing 117 samples of 63 European Pinus sylvestris Linn affected by flash floods, so as to fill the gap of flash floods in seven rivers on the north slope of guadalama in central Spain in the past 200 years[61]. And Š ILHán collected 446 sections of injured tree roots and 192 sample cores in 10 watersheds around the highest peak of lishola mountain in the eastern Czech Republic, reconstructed the local historical flood, and obtained 64 flood events in 28 flood years from 1883 to 2012, and pointed out that most watersheds (90%) were affected by the flood in 1997[58].

3.2 Assessment of flash flood flow

The method of dendromorpholog can be used to evaluate the flow of flash floods, and the scar height is often used. The scar height can represent the lowest water level of the flood in that year[62]. When the flood inundates the trunk, it does not necessarily cause scars, but the existence of scars proves that the flood must have reached this height in that year. Some scholars hold different views on this. For ex-

ample, McCord and Gottesfeld believe that the scar height represents the maximum water level of the river when flash floods occur[45,63]. Using Manning's equation, the height of scars in trees can be transformed into flood peak flow in the field[64].

Ballesteros-Cánovas et al., measured the slope of main rivers and the maximum height of scars in sampling trees in Gulu District, Himachal Pradesh, northwest India, and reconstructed the flood peak discharge in this area by using Manning equation[65].

When studying the flash flood situation of a river without historical records on the North slope of Tagus River Basin in Spain, Ballesteros-Cánovas et al., reconstructed a flash flood event on December 17, 1997 by using the information of the height and size of scars in trees a2ffected by flash flood, combined with two-dimensional hydraulic model and ground laser scanning technology[39]. The reconstructed peak flow was 79 ± 14 m^3/s, and the average deviation between flood level and scar height is -0.09 $\pm$ 0.53 M. Through further analysis, it is found that the geographical location of trees is the main factor to control the error, and the trees growing in exposed locations such as bedrock have the smallest evaluation error.

There is a certain error in evaluating flood peak discharge with scar height. When transported by flood, some materials such as wood debris forming scars can be located below the water surface, which can explain the reason for the error[66]. Of course, if the scar is formed before or after the flood peak, rather than when the flood peak comes, the flood peak flow assessed by the scar height may be smaller than the actual value. The possible reasons why the scar is higher than the actual water level are: when the flood breaks out and the local ultra-high water level exists, the material around the stem is deposited to form the scar[67,68]; the longitudinal propagation of cambium tissue and fiber damage can make the scar longer, so that the scar exceeds the position corresponding to the actual peak flow.

The flood peak discharge is reconstructed by scar height. The uncertainty of scar caused by debris carried by flood will increase with the increase of flood volume. Roughness can be used to quantita-tively describe the uncertainty. In addition, sampling should be as far away from the bottom of the river as possible. And selecting scarred trees that can indicate large flash flood events can minimize the uncertainty[69].

In addition to the peak discharge analysis based on scar height, other methods can be used to analyze the flood size. Ballesteros-Cánovas et al., analyzed the relationship between stem inclination and flood size of trees affected by flood, and also tried to analyze the feasibility of using stem inclination to reconstruct flood size in historical period. They established a conceptual model of tree inclination[70]. Then they parameterized the model and compared the difference between observation data and simulation data. In the end, they analyzed that the inclination of tree stem base was correlated with flood size, which proved that the method was reliable.

3.3 Study on flash flood driving mechanism

The research on the driving mechanism of flash floods based on tree rings has also been carried out gradually in recent years. Casteller et al., reconstructed the temporal and spatial pattern of flash floods in a small watershed in the Andes mountains of Patagonia in the historical period with the method of dendromorpholog[55]. They also analyzed the possible flood driving factors in combination with climate data, and found that flash floods will occur when there is a large amount of precipitation in 1–3 days and the temperature of the whole watershed exceeds the rain / snow threshold (2 ℃). Ballesteros-Cánovas et al., reconstructed the spatio-temporal pattern of flood in a river on guadalama mountains in central Spain from 1748 to 2011, analyzed the meteorological driving factors of flood in this region. Finally they found that there are great differences in rainfall thresholds of 1, 3 and 5 days during flood occurrence in different seasons, and flash flood events often occur in wet season (autumn and winter)[19].

Rodriguez-Morata et al., reconstructed the flash flood data of 7 rivers on the north slope of guadalama mountains in central Spain in the past 200 years based on scars and abnormal growth[61]. Through analysis, it was found that the total rainfall in 1, 3

and 5 days may be the factor driving the occurrence of flash floods. Ferrio *et al.*, used isotopes in tree rings for the first time to analyze flash floods in the Tagus River Basin in Spain[38]. They collected samples of four tree species in the forest area affected by flash floods and obtained their data α Cellulose, and then the oxygen isotopic composition in tree rings and meteorological data, as well as the oxygen isotopic composition in rainfall $\delta^{18}O$ comparison to investigate the possible meteorological drivers of flash floods. After removing the spring signal of oxygen isotope in tree ring cellulose, it was found that the late wood $\delta^{18}O$ is related to heavy rainfall events, but the correlation between $\delta^{18}O$ in tree rings of different tree species and the meteorological elements will be different.

A series of studies on the driving factors of flash floods show that there is a great correlation between continuous heavy precipitation and flash floods. However, flash floods are often not driven by a single factor, and their occurrence is usually the result of the comprehensive action of a variety of meteorological elements. It can be seen that the tree ring dendrogemorpholog method provides more valuable information for understanding the driving mechanism of flash floods in the context of longer time scale, and is of great significance to the early warning and protection of flash floods.

4. Advantages, limitations and potential of flash flood research based on tree wheel

Compared with other flash flood research data, tree ring index has the advantages of accurate dating, high spatial resolution, sometimes time-resolved over seasonal resolution, long recording age and easy access to copies. In a typical flash flood prone area with large trees, trees can record multiple flash floods, recover the frequency and size of flash floods in the basin, and provide more data for exploring the climate driving mechanism of flash floods and also provide more background information for the prediction and prevention of flash floods.

In addition, the method is easy to implement and there are many available tree species. And analyzable samples are also easy to find. We can not only use single point tree samples to restore flash flood history, but also use regional multi-point samples for integrated analysis. Therefore, it has great advantages in obtaining the temporal and spatial variation characteristics of flash flood events under the background of long-time scale. Of course, this method also has some limitations. First of all, flash flood prone areas are often areas with high incidence of disasters such as landslide, debris flow and rockfall, which leads to the mixing of different types of disaster signals.

In addition, the scars of the trees affected by the flood can indicate the flood event, but the period without scars in the tree rings does not mean that they are not affected by the flood. The flood may have occurred, but its size is not enough to form scars. When trees are affected by floods for a long time, scars may not form in tree rings.

In addition, most of the scarred trees are distributed in or around the river. When a strong flood occurs, it is likely to cause the scarred trees to be cut off and die, and carry the tree stumps to the downstream area, which means that the reconstructed flood time series may not be complete, that is, it is difficult to reconstruct flash floods with a long time scale by dendrogemorpholog. The years with a large number of scars can indicate high-intensity flood, but the flood intensity of the remaining years with scars is difficult to define.

There may be flash flood events after the last flash flood event covered up. For example, it is often difficult to distinguish the events that occur continuously in one year or the next year, resulting in signal loss. The limitations listed above often vary with different regions. Therefore, in different regions, targeted sampling schemes need to be designed to minimize the impact of adverse conditions in order to obtain the most flash flood information. A large number of flash flood reconstruction work based on dendrogemorpholog has been carried out abroad, but there is no report of relevant work in China. China's Qinghai Tibet Plateau Sichuan Basin transition zone, the border between Sichuan and Yunnan, the Loess Plateau, the eastern coastal area and North China are prone to flash floods, and most areas are covered

with forests. Therefore, using tree ring geomorphology to carry out flash floods research has great potential, opportunities and challenges[71].

(1) The development of dendrogemorpholog in China is relatively late, and the existing work is mainly concentrated in the field of dendroclimatology and dendroecology[72–76]. In recent years, the method of dendrogemorpholog has been slowly carried out in China, starting from a few early studies on ancient earthquakes using tree ring analysis to specific mountain disasters[77–80].

For example, Hong Ting et al., studied the years of landslide activity in Jiufang mountain in southern Gansu, the disaster assessment work carried out by Tie Yongbo et al., and Malik et al., in Moxi River Basin, Sichuan, and a series of research work on glacier activity in Southeast Tibet and along the Himalayas by means of dendrogemorpholog[81–87]. And Zhang et al., used the abnormal growth characteristics of Sabina przewalskii and It and Wt indexes to reconstruct the historical landslide work in the past 300 years for the first time in the Qilian Mountains[88]. These works show the great potential of dendrogemorpholog in domestic mountain disaster research, but the domestic flash flood reconstruction has not been carried out, which is a new research direction with great potential.

(2) Flash floods occur frequently in China. When using dendrogemorpholog to study flash floods, first of all, it is necessary to determine suitable tree species even though coniferous trees are widely used in dendrochronology. To carry out flash floods research, we must also start from the foundation, explore the appropriate sampling location of conifers and identify their response characteristics to disaster events. In fact, at present, most of the vegetations in flash flood prone areas in China are trees or shrubs, which need to be sampled and evaluated to explore the potential of disaster research. Therefore, the response characteristics of different shrubs and trees to mountain disasters are one of the important directions that need to be broken through in the future. In addition, due to regional differences, there are many means to define flash floods, but there is a lack of reliable standards, which need to be verified with the help of historical data or instrumental records. When I_t and W_t indexes are introduced into domestic research, including the definition of the intensity of flash flood events and so on, the appropriate threshold range should be determined according to the actual situation. In the end, when analyzing the characteristics of flash floods, according to the evaluation of peak discharge we need to build a small watershed flood model and determine the reasonable value of parameters in the conversion equation. It is also an important direction in the future to systematically build a flash flood event definition method suitable for domestic conditions and a small watershed flood simulation system.

In short, using dendrogemorpholog to study flash floods in China has a long way to go. We need to combine international experience and base on China's actual situation, start from the foundation and systematically carry out relevant research work.

Conflict of interest

The authors declare that they have no conflict of interest.

Acknowledgements

References

1. Collier CG. Flash flood forecasting: What are the limits of predictability? Quarterly Journal of the Royal Meteorological Society 2007; 133: 3–23.

2. Georgakokoskp. On the design of a national real-time early warning system with site-specific lightning flood forecasting capability. Bulletin of the American Meteorological Society 1986; 67(10): 1233–1239.

3. Zhao S. Preliminary study on the overall characteristics and risk zoning of flash flood disaster system in China. Journal of Natural Disasters 1996; 5(3): 93–99.

4. Gao Y, Xing J, Wang C, et al. Cause and forecast of flash flood from rainstorm. Journal of Natural Disasters 2006; 15(4): 65–70.

5. Zhou C, Jin S. Damage cause and control measures

of flash flood hazard in Henan Province. Journal of Natural Disasters 2008; 17(3): 148–151.

6. Liu C, Miao T, Chen H, *et al*. Basic feature and origin of the"8·8" flash flood- debris flow disaster happened in Zhouqu County, Gansu, China, Aug. 8, 2010. Geological Bulletin of China 2011; 30(1): 141–150.

7. Zhang P, Ren H, Hu W, *et al*. An elementary study on Chinese flash floods disaster prevention regionalization. Journal of Soil and Water Conservation 2006; 20(6): 196–200.

8. Li Z, Yang D W, Hong Y, *et al*. Characterizing spatiotemporal variations of hourly rainfall by gauge and radar in the mountainous three gorges region. Journal of Applied Meteorology and Climatology 2014; 53(4): 873–889.

9. Liu Y S, Yuan X M, Guo L, *et al*. Driving force analysis of the temporal and spatial distribution of flash floods in Sichuan Province. Sustainability 2017; 9: 1527. doi: 10.3390/su9091527.

10. Jiang J, Shao L. Standard of flash flood warning based on the precipitation observation data. Journal of Hydraulic Engineering 2010; 41(4): 458–463.

11. Cheng W. A review of rainfall thresholds for triggering flash floods. Advances in Water Science 2013; 24(6): 901–908.

12. Li Q, Wang Y, Li H, *et al*. Rainfall threshold for flash flood early warning based on flood peak modulus. Journal of Geo-information Science 2017; 19(12): 1643–1652.

13. Tang C, Shi Y. Approach to mutil-objectives assessment for urban torrent hazard. Progress in Geography 2006; 25(4): 13–21.

14. Tang C, Zhu J. A GIS based regional torrent risk zonation. Acta Geographica Sinica 2005; 60(1): 87–94.

15. Chen H, Yang D W, Hong Y, *et al*. Hydrological data assimilation with the ensemble square-root-filter: Use of streamflow observations to update model states for real-time flash flood forecasting. Advances in Water Resources 2013; 59: 209–220.

16. Huang W, Cao Z, Qi W J, *et al*. Full 2D hydrodynamic modelling of rainfall-induced flash floods. Journal of Mountain Science 2015; 12(5): 1203–1218.

17. Cui P, Zou Q. Theory and method of risk assessment and risk management of debris flows and flash floods. Progress in Geography 2016; 35(2): 137–147.

18. George S, Nielsen E. Palaeoflood records for the Red River, Manitoba, Canada, derived from anatomical tree ring signatures. The Holocene 2003; 13(4): 547–555.

19. Ballesteros-Cánovas JA, Rodríguez-Morata C, GarófanoGómez V, *et al*. Unravelling past flash flood activity in a forested mountain catchment of the Spanish Central System. Journal of Hydrology 2014; 529: 468–479.

20. Stoffel M. Dating past geomorphic processes with tan-gential rows of traumatic resin ducts. Dendrochronologia 2008; 26(1): 53–60.

21. Wang Z, Qian Y. Frequency and intensity of extreme precipitation events in China. Advances in Water Science 2009; 20(1): 1–9.

22. She D, Xia J, Zhang Y, *et al*. The trend analysis and statistical distribution of extreme rainfall events in the Huaihe River Basin in the past 50 years. Acta Geographica Sinica 2011; 66(9): 1200–1210.

23. Ren Z, Zhang M, Wang S, *et al*. Changes in precipitation extremes in South China during 1961–2011. Acta Geographica Sinica 2014; 69(5): 640–649.

24. Fritts HC. Tree rings and climate. London, UK: Academic Press; 1976.

25. Alestalo J. Dendrochronological interpretation of geomorphic processes. Fennia 1971; 105: 1–139.

26. Butler DR. Snow avalanche path terrain and vegetation, Glacier National Park, Montana. Arctic and Alpine Research 1979; 11(1): 17–32.

27. Hupp CR. Dendrogeomorphic evidence of debris flow frequency and magnitude at Mount Shasta, California. Environmental Geology and Water Sciences 1984; 6(2): 121–128.

28. Stoffel M. A review of studies dealing with tree rings and rockfall activity: The role of dendrogeomorphology in natural hazard research. Natural Hazards 2006; 39(1): 51–70.

29. Hardman G. The relationship between tree growth and stream runoff in the Truckee River Basin, California-Nevada. Transactions, American Geophysical Union 1936; 17(2): 491–493.

30. Sigafoos RS. Vegetation in relation to flood frequency near. Washington DC, USA: United States Government Printing Office; 1961.

31. Sigafoos RS. Botanical evidence of floods and flood-plain deposition. Washington DC, USA: United States Government Printing Office; 1964.

32. Baker VR. Palaeoflood hydrology and extraordinary flood events. Journal of Hydrology 1987; 96: 79–99.

33. Bégin Y. Tree-ring dating of extreme lake levels at the subarcticboreal interface. Quaternary Research 2001; 55(2): 133–139.

34. Zielonka T, Holeksa J, Ciapala S. A reconstruction of flood events using scarred trees in the Tatra Mountains, Poland. Dendrochronologia 2008; 26(3): 173–183.

35. Ruiz-Villanueva V, Díez-Herrero A, Stoffel M, *et al*. Dendrogeomorphic analysis of flash floods in a small ungauged mountain catchment (Central Spain). Geomorphology 2010; 118(3-4): 383–392.

36. Ballesteros JA, Stoffel M, Bodoque JM, *et al*. Changes in wood anatomy in tree rings of Pinus pinaster Ait following wounding by flash floods. Tree-Ring Research 2010; 66(2): 93–103.

37. Ballesteros JA, Stoffel M, Bollschweiler M, *et al*. Flash flood impacts cause changes in wood anatomy of Alnus glutinosa, Fraxinus angustifolia and Quercus pyrenaica. Tree Physiology 2010; 30(6): 773–781.

38. Ferrio JP, Díez-Herrero A, Tarrés D, *et al*. Using stable isotopes of oxygen from tree-rings to study the origin of past flood events: First results from the Iberian Peninsula. Quaternaire 2015; 26(1): 67–80.

39. Ballesteros-Cánovas JA, Eguibar M, Bodoque JM, *et al*. Estimating flash flood discharge in an ungauged mountain catchment with 2D hydraulic models and dendrogeomorphic palaeostage indicators. Hydrological Processes 2011; 25(6): 970–979.

40. Ballesteros-Cánovas JA, Stoffel M, Guardiola-Albert C.XRCT images and variograms reveal 3D changes in wood density of riparian trees affected by floods. Trees 2015; 29(4): 1115–1126.

41. Grissino-Mayer HD. A manual and tutorial for the proper use of an increment borer. Tree-Ring Research 2003; 59(2): 63–79.

42. Schneuwly DM, Stoffel M, Dorren LK, *et al*. Three-dimensional analysis of the anatomical growth response of European conifers to mechanical disturbance. Tree Physiology 2009; 29(10): 1247–1257.

43. Schneuwly DM, Stoffel M, Bollschweiler M. Formation and spread of callus tissue and tangential rows of resin ducts in Larix decidua and Picea abies following rockfall impacts. Tree Physiology 2009; 29(2): 281–289.

44. Grissino-Mayer HD. Evaluating crossdating accuracy: Amanual and tutorial for the computer program cofecha. Tree-Ring Research 2001; 57: 205–221.

45. Gottesfeld AS. British Columbia flood scars: Maximum flood-stage indicator. Geomorphology 1996; 14: 319–325.

46. George SS. Tree rings as paleoflood and paleostage indicators. Tree Rings and Natural Hazards 2010; 41: 233–239.

47. Stoffel M, Wilford DJ. Hydrogeomorphic processes and vegetation: Disturbance, process histories, dependencies and interactions. Earth Surface Processes and Landforms 2012; 37: 9–22.

48. Stoffel M, Casteller A, Luckman B H, *et al*. Spatio-temporal analysis of channel wall erosion in ephemeral torrents using tree roots: An example from the Patagonian Andes. Geology 2012; 40(3): 247–250.

49. Stoffel M, Butler DR, Corona C. Mass movements and tree rings: A guide to dendrogeomorphic field sampling and dating. Geomorphology 2013; 200: 106–120.

50. Yamamoto F, Kozlowski TT. Effects of flooding, tilting of stems, and ethrel application on growth, stem anatomy and ethylene production of pinus densiflora seedlings. Journal of Experimental Botany 1987; 38: 293–310.

51. Friedman JM, Vincent KR, Shafroth PB. Dating floodplain sediments using tree-ring response to burial. Earth Surface Processes and Landforms 2005; 30(9): 1077–1091.

52. Kogelnig-Mayer B, Stoffel M, Schneuwly-Bollschweiler M, *et al*. Possibilities and limitations of dendrogeomorphic time-series reconstructions on sites influenced by debris flows and frequent snow avalanche activity. Arctic, Antarctic, and Alpine Research 2011; 43(4): 649–658.

53. Stoffel M, Corona C. Dendroecological dating of geomorphic disturbance in trees. Tree-Ring Research 2014; 70(1): 3–20.

54. Schneuwly-Bollschweiler M, Corona C, Stoffel M.

Howto improve dating quality and reduce noise in tree-ring based debris-flow reconstructions. Quaternary Geochronology 2013; 18: 110–118.

55. Casteller A, Stoffel M, Crespo S, *et al*. Dendrogeomorphic reconstruction of flash floods in the Patagonian Andes. Geomorphology 2015; 228: 116–123.

56. Shroder JF. Dendro-geomorphological analysis of mass movement on Table Cliffs Plateau, Utah. Quaternary Research 1978; 9(2): 168–185.

57. Butler DR, Malanson GP. A reconstruction of snow-avalanche characteristics in Montana, USA using vegetative indicators. Journal of Glaciology 1985; 31: 185–187.

58. Šilhán K. Frequency, predisposition, and triggers of floods in flysch Carpathians: Regional study using dendrogeomorphic methods. Geomorphology 2015; 234: 243–253.

59. Ruiz-Villanueva V, Diez-Herrero A, Bodoque J M, *et al*. Characterisation of flash floods in small ungauged mountain basins of Central Spain using an integrated approach. Catena 2013; 110: 32–43.

60. Ballesteros-Cánovas JA, Czajka B, Janecka K, *et al*. Flash floods in the Tatra Mountain streams: Frequency and triggers. Science of the Total Environment 2015; 511: 639–648.

61. Rodriguez-Morata C, Ballesteros-Cánovas JA, Trappmann D, *et al*. Regional reconstruction of flash flood history in the Guadarrama range (Central System, Spain). Science of the Total Environment 2016; 550: 406–417.

62. Harrison SS, Reid JR. A flood-frequency graph based on tree-scar data. Proceedings of the Northern Dakota Academy of Sciences 1967; 21: 23–33.

63. McCord VA. Fluvial process dendrogeomorphology: Reconstructions of flood events from the southwestern United States using flood-scarred trees. Dean JS, MekoDM, Swetnam TW. Tree rings, environment and humanity. Tucson, USA: University of Arizona; 1996. p. 689–699.

64. Jarrett RD, England J. Reliability of paleostage indicators for pale of lood studies. House PK, Webb RH, Baker VR, *et al*. Ancient floods, modern hazards: Principles and applications of paleoflood hydrology. Water science and application Vol. 5.Washington DC, USA: American Geophysical Union; 2002. p.

91–109.

65. Ballesteros-Cánovas JA, Trappmann D, Shekhar M, *et al*. Regional flood-frequency reconstruction for Kullu district, Western Indian Himalayas. Journal of Hydrology 2017; 546: 140–149.

66. Webb RH, Jarrett RD. One-dimensional estimation techniques for discharges of paleofloods and historical floods. House PK, Webb RH, Baker VR, *et al*. Ancient floods, modern hazards: Principles and applications of paleoflood hydrology. Water Science and Application, vol. 5. Washington D C, USA: American Geophysical Union; 2002. p. 111–125.

67. Darby S. Effect of riparian vegetation on flow resistence and flood potential. Journal of Hydraulic Engineering 1999; 125(5): 443–454.

68. Carling PA, Hoffman M, Blatter AS. Initial motion of boulders in bedrock channel. House PK, Webb RH, Baker VR, *et al*. (editors). Ancient floods, modern hazards: Principles and applications of pale of lood hydrology. Water Science and Application, vol. 5. Washington D C, USA: American Geophysical Union; 2002. p. 147–160.

69. Ballesteros JA, Bodoque JM, Díez-Herrero A, *et al*. Calibration of floodplain roughness and estimation of flood discharge based on tree-ring evidence and hydraulic modelling. Journal of Hydrology 2011; 403(1-2): 103–115.

70. Ballesteros-Cánovas JA, Márquez-Peñaranda JF, SánchezSilva M, *et al*. Can tree tilting be used for pale of flood discharge estimations? Journal of Hydrology 2015; 529: 480–489.

71. Guo L, Zhang X, Liu R, *et al*. Achievements and preliminary analysis on China national flash flood disasters investigation and evaluation. Journal of Geoinformation Science 2017; 19(12): 1548–1556.

72. Shao XM, Xu Y, Yin ZY, *et al*. Climatic implications ofa 3585-year tree-ring width chronology from the northeastern Qinghai-Tibetan Plateau. Quaternary Science Reviews 2010; 29: 2111–2122.

73. Yang B, Qin C, Wang JL, *et al*. A 3,500-year tree-ring record of annual precipitation on the northeastern Tibetan Plateau. PNAS 2014; 111(8); 2903–2908.

74. Zhang QB, Evans MN, Lyu LX. Moisture dipole over the Tibetan Plateau during the past five and a half centuries. Nature Communications 2015; 6:

8062. doi: 10.1038/ncomms9062.

75. Liang EY, Wang YF, Piao SL. Species interactions slow warming-induced upward shifts of treelines on the Tibetan Plateau. PNAS 2016; 113(16): 4380–4385.

76. Liu Y, Cobb KM, Song HM, *et al*. Recent enhancement of central Pacific EI Niño variability relative to last eight centuries. Nature Communications 2017; 8: 15386. doi: 10. 1038/ncomms15386.

77. Han T. The dendrochronological method: A new method for determining the ages of seismic deformational belts in Damxung of Xizang (Tibet). Journal of the Chinese Academy of Geological Sciences 1983; (6): 95–110.

78. Han T. Discussion on epicentral locations for the Tibet M=8 earthquake on 29, September 1411. Seismology and Geology 1984; 6(4): 6–12.

79. Yang B, Liu B, Zhou J. Tree seismological study of active Gulang and Jingtai fault in Gansu Province. Seismology and Geology 1995; 17(2): 139–147.

80. Lin AM, Lin SJ. Tree damage and surface displacement: The 1931 M 8.0 Fuyun earthquake. The Journal of Geology 1998; 106: 751–757.

81. Hong T, Bai S, Wang J, *et al*. Reconstruct the activity years of Jiufangshan landslide by means of tree-rings. Journal of Mountain Science 2012; 30(1): 57–64.

82. Tie Y, Malik I, Owczarek P. Dendrochronological dating of debris flow historical events in high mountain area: Take Daozao debris flow as an example. Mountain Research 2014; 32(2): 226–232.

83. Malik I, Wistuba M, Tie YB, *et al*. Mass movements of differing magnitude and frequency in a developing highmountain area of the Moxi Basin, Hengduan Mts, China: A hazard assessment. Applied Geography 2017; 87: 54–65.

84. Yang B, Bräuning A, Dong ZB, *et al*. Late Holocene monsoonal temperate glacier fluctuations on the Tibetan Plateau. Global and Planetary Change 2008; 60: 126–140.

85. Xu P, Zhu H, Shao X, *et al*. Tree ring-dated fluctuation history of Midui glacier since the Little Ice Age in the southeastern Tibetan Plateau. Science China: Earth Sciences 2012; 42(3): 380–389.

86. Zhu HF, Shao XM, Zhang H, *et al*. Trees record changes of the temperate glaciers on the Tibetan Plateau: Potential and uncertainty. Global and Planetary Change 2019; 173: 15–23.

87. Zhu HF, Xu P, Shao XM, *et al*. Little Ice Age glacier fluctuations reconstructed for the southeastern Tibetan Plateau using tree rings. Quaternary International 2013; 283: 134–138.

88. Zhang Y, Stoffel M, Liang E Y, *et al*. Centennial-scale process activity in a complex landslide body in the Qilian Mountains, northeast Tibetan Plateau, China. Catena 2019; 179: 29–38.

ORIGINAL RESEARCH ARTICLE

Geologic and geomorphologic study of the Terra Murata and Centane-Panoramica Sites (Island of Procida, Naples Bay, Southern Tyrrhenian Sea) aimed at solving some applied geological and geotechnical problems

Gemma Aiello[*]

*Istituto di Scienze Marine (ISMAR), Consiglio Nazionale delle Ricerche (CNR), Sede di Napoli, Naples 80133, Italy.
E-mail: gemma.aiello@iamc.cnr.it*

ABSTRACT

A geologic and geomorphologic study aimed at solving some geological and geotechnical problems, regarding the massive seepage of meteoric waters in the coastal cliffs of the Island of Procida (Naples Bay, Southern Italy) composed of both tuffs and loose pyroclastic deposits, has been carried out in the geosites of Terra Murata (Middle Ages village and coastal cliff towards the Corricella Bay) and Centane-Panoramica (coastal cliff facing on the Tyrrhenian Sea).

A detailed geologic and geomorphologic survey has allowed to suggest solutions to the applied geological and geotechnical problems related to the occurrence of massive seepages of waters at the physical interface between pyroclastic rocks and loose pyroclastic deposits, characterized by different density, permeability and porosity and also controlled by a dense network of fractures, involving the pyroclastic deposits cropping out in the selected areas.

Field sampling and geotechnical laboratory analyses have been carried out to calculate the values of main geotechnical parameters of the yellow tuffs cropping out at the Terra Murata Promontory. At the same time, a detailed monitoring of the seepages of waters has been carried out through a detailed geological survey of the tuff outcrops of the promontory. The obtained results have suggested a strong control from both the geomorphologic instability of the coastal cliff and tectonic setting. At the Centane-Panoramica geosite, the geological survey, coupled with geotechnical analyses and standard penetrometric tests, has accordingly evidenced that the geomorphologic instability was mainly concentrated in the sectors of the tuff coastal cliffs facing seawards towards the Tyrrhenian Sea.

Keywords: Geology; Geomorphology; Pyroclastic Rocks; Seepages of Water; Island of Procida; Naples Bay

1. Introduction

In this paper, a geomorphologic study of instability processes in two selected areas of the Island of Procida, located in the Naples Bay (Southern Tyrrhenian Sea), has been carried out. These areas are respectively located in the historical center of Procida (Middle Ages village of Terra Murata; **Figure 1**) and in correspondence of the coastal cliff joining the Pizzaco and Solchiaro promontories, herein named the Centane-Panoramica geosite.

One aim of this paper is to outline the geologic framework of the two study areas, which are characterized by a different geologic setting. In the Terra Murata quarter, abundant seepages of waters have been detected both in the highest zone of the Middle Ages village (place after the walls) and on the coastal cliff facing the Corricella Bay (Salita Castello; **Figure 2**). They involve the volcanic successions and are located, in particular, between the volcanic tuffs and the loose pyroclas-

tic deposits, widely outcropping at the Terra Murata promontory. Since the seepages involve several edifices, it is necessary to address a geomorphological and geotechnical study aimed at individuating their control factors in order to purpose technical solutions to these geological problems.

In this paper, a geologic framework of the Terra Murata quarter will be delineated, referring to the stratigraphic relationships between the volcaniclastic rocks and deposits and to the hydrogeologic factors, which have probably controlled the seepages of waters. Some possible technical solutions will be individuated to study and solve this problem, which was probably also controlled by the occurrence in the subsurface of ancient Borbonic sewers/old tanks/cavities.

Terra Murata represents the historical center of the Island of Procida and is an ancient Middle Age village located on a tuff coastal cliff high 90 m a.s.l. Terra Murata can be accessed only through a steep street, traveling along which the village of Marina Corricella may be seen. There are some ancient doors to access the Middle Age village of Terra Murata ("Porta di Ferro" & "Porta di Mezz'Omo"), representing old points of admittance. The important structures of the village are represented by the S. Michele Arcangelo Abbey, the old village of Terra Murata, the viewpoint of Borgo street, the Place of the Arms, the Prison Complex, the old doors, the viewpoint of the Two Guns and the S. Margherita Convent (**Figure 3**).

Figure 1. View of the Middle Ages village of Terra Murata (Island of Procida), overlying a tuff coastal cliff facing on the Tyrrhenian Sea (Naples Bay)**.**

Figure 2. The tuff coastal cliff of Terra Murata towards the Corricella Bay (Island of Procida, Naples Bay)**.**

Figure 3. Sketch representation of the structures of the Middle Age village of Terra Murata**.**

The Centane-Panoramica geosite, characterized by the coastal street joining the promontories of Pizzaco and Solchiaro, where the Solchiaro yellow tuffs widely outcrop, offers many examples of geomorphologic instability. They have been observed in outcrops of the coastal cliffs facing seawards towards the Tyrrhenian Sea. These sectors have been used as the dumps of undifferentiated deposits. The present-day flat morphology of some areas may deceive on their condition of stability, which may result in precarious conditions, if these areas should be submitted to loads not proportional to the geotechnical parameters of stability of the undifferentiated Quaternary deposits or in conditions of water flooding, also considering the lacking of a drainage system of meteoric waters.

The coastal cliffs of the Island of Procida are incised in yellow tuffs and/or pyroclastic deposits and include the Terra Murata coastal cliff, facing towards the Corricella Bay and the coastal cliff of

63

the Centane-Panoramica geosite. These cliffs show a geomorphologic instability consisting of erosional lineaments and landslides, which were controlled by different factors. These factors include the marine erosion at the toe-of-slope, the wind action on the sub-vertical walls of cliffs and the instability of the superficial strata cropping out at the top of the coastal cliffs, composed of loose pyroclastic deposits alternating with paleosoils. Other factors are represented by the occurrence of undrained absorption waters and by the uncontrolled flow of superficial waters.

A sketch geologic map of the Island of Procida has been constructed (**Figure 4**), showing the occurrence of volcanic deposits having a different lithology and age. They can be placed in the general geologic setting of the formation of the whole Neapolitan and Phlegrean areas. The formation of the Vivara, Terra Murata and Punta Serra volcanoes has been ascribed to an age older than 75 ky B.P. through radiometric absolute dating[1]. The emplacement of the Campanian Ignimbrite and its proximal facies ("Breccia Museo") has been dated back to 37 ky B.P.
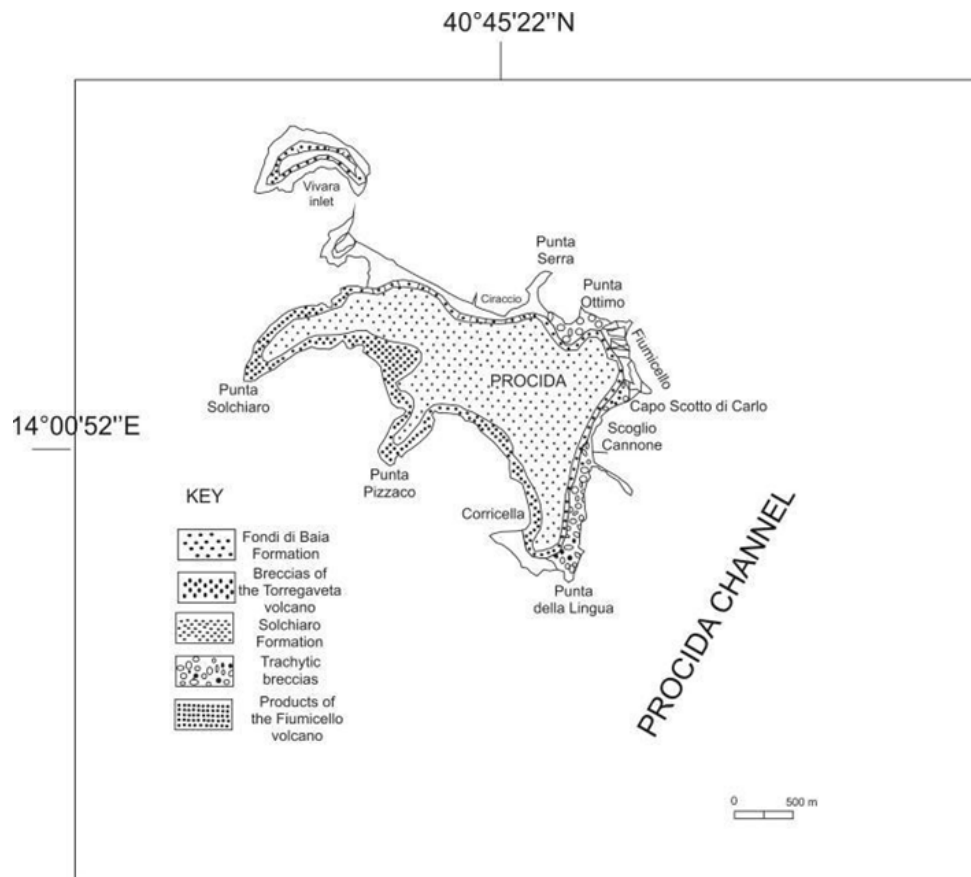
Figure 4. Sketch geological map of the Island of Procida (Naples Bay)**.**

During the time interval ranging between 30 and 10 ky B.P., a volcanic activity having a great intensity and area diffusion has led to the formation of the Solchiaro Volcano (average age 22 ky B.P.) and the emplacement of the stratified white tuffs cropping out at Soccavo and in the Naples town. During this period, other main events are represented by the formation of the Torregaveta Volcano and the emplacement of the Neapolitan Yellow Tuff about 15 ky ago[2].

During the time interval younger than 10 ky B.P., the formation of lava domes, scoria cones and monogenetic pyroclastic volcanoes took place (e.g. Monte Nuovo, Astroni, Agnano, Capo Miseno, Bacoli, Montagna Spaccata, Monte Ruscello)[3-7].

2. Materials and methods

The key methods of this paper are represented by the geological and geomorphological survey carried out on volcanic rocks and deposits. The volcanic rocks of Campania have been deeply studied by different authors through different method-

ologies, including volcanology, geochemistry, age dating and applied geological aspects[2,3,8-16]. Relevant geological surveys in volcanic deposits have been recently carried out also in the Etna Volcano, Sicily. For example, Branca *et al.* and Groppelli & Goette have addressed to the construction of significant geological maps of volcanic areas[17,18].

The geotechnical analysis of collected samples have also been performed in order to calculate such significant geotechnical parameters as the angle of inner friction (FI), the wet weight-volume ratio (GA), the dynamic resistance at the point (Rd), the un-drained cohesion (Cu) and the compression strength (σ).

The technical characteristics of the undifferentiated deposits located at the top of coastal cliffs have been determined on disturbed samples collected during standard penetrometric tests (SPT). As explained in the results, some samples of undifferentiated deposits have been collected during the SPT tests (wells 1, 2 and 5). Some geotechnical analyses have been performed in order to calculate the general technical characteristics of the deposits, while sedimentological analyses have been performed to evaluate their grain-size.

The standard penetrometric tests (SPT) have allowed for the thickness calculation of the undifferentiated deposits overlying the rocky substratum in the coastal cliffs and for the determination of the physical-chemical characteristics of the crossed grounds. The calculation has been based on algorithms correlating the significant geotechnical parameters with the number of blows of the standard penetrometer (Nspt).

3. Results

3.1 Stratigraphy of the Procida volcanic deposits

Several volcanic units having a different nature and age, crop out in the Procida Island. The lithology and the stratigraphy of these deposits are herein described. They come from localized monogenetic volcanic edifices, also if intercalations of volcanic materials having a Phlegrean and Ischian provenance are present. The age of the volcanic centers is reported from Fedele *et al.*[1]

3.1.1 Vivara volcano (age about 75 ky)

The Vivara Volcano includes the Vivara Inlet and the S. Margherita Promontory. It is represented by a well-stratified ring of yellow and grey tuffs, having a circular shape (**Figure 5**). The lower part of the Vivara tuffs is formed by massive metric banks of yellow tuffs, constituted by a yellow cineritic matrix, completely lithified and by shardy dark grey lapilli having a trachybasaltic composition. They grade upwards to grey stratified tuffs, slightly lithified. The transition among the two units crops out at Punta Capitello and in the coastal cliff between Punta Mezzogiorno and Punta Alaca, while the culmination of the crateric rim may be seen northwards of Punta Mezzogiorno and S. Margherita vecchia.

Figure 5. The Vivara volcano.

3.1.2 Pozzo Vecchio Volcano (age about 75 ky)

It is characterized by a succession starting with hydromagmatic yellow tuffs forming a ring-shaped volcano, whose crateric rim is well visible in the bay between Punta Serra and Punta Ottimo (**Figure 6**).

Figure 6. The tuff coastal cliff between the Corricella Bay and the Pozzo Vecchio beach ("Spiaggia del Postino").

The edifice of the Pozzo Vecchio Volcano is composed of thinly stratified tuffs, grading upwards into fall deposits having a coarser grain-size, poorly sorted, with intercalations of thin cineritic levels. A scoria cone, formed by banks having a reddish colour, is superimposed on the northern flank of the volcanic edifice. The scoria deposits are overlain by a lava flow having an alkali-trachytic composition.

3.1.3 Terra Murata Volcano (age about 75 ky)

It is formed by stratified yellow tuffs. The lower part of the volcanic edifice is composed of zeolitized yellow tuff, thinly stratified and well lithified. In the upper part of the sequence, a transition to less lithified tuffs including pumice levels may be observed. The Terra Murata tuffs are covered by levels of Plinian pumices, which cannot be reached in outcrop and by the distal deposits of the Fiumicello Volcano. On the eastern coastal cliff of Terra Murata, the superimposition and the thinning upwards of the Fiumicello grey tuffs on the Terra Murata yellow tuffs may be observed.

3.1.4 Fiumicello Volcano (age ranging between 75-60 ky)

It is composed of lithified hydromagmatic deposits of an eruptive center located in the northern sector of the Island of Procida. The distal deposits of this eruptive center show a wide area dispersal, being used as a marker horizon in the stratigraphic correlations between Procida and Monte di Procida[9]. The Fiumicello tuffs crop out along the coastal cliff between Punta del Pioppeto and Capo Bove, while the distal facies crop out at Punta della Lingua.

At Punta del Pioppeto and Punta della Lingua, the deposits of the Fiumicello unit are unconformably overlain by the Campanian Ignimbrite. In the proximal sections the deposits are composed of yellow and grey tuffs, having a trachybasaltic composition, hialoclastitic and thinly stratified. Scattered dome-shaped structures and impact prints in correspondence with lava blocks and yellow tuffs occur. The deposits of the distal facies are characterized by alternating grey ashes, ashes with lapilli and banks of scoria and lapilli derived from pyroclastic fall-out.

3.1.5 Campanian Ignimbrite (age 37 ky)

The Island of Procida represents an area where several volcanic units genetically related to the Campanian Ignimbrite crop out. They are interlayered between sequences of massive ashes, separating them from the Solchiaro tuffs at the top and from the Epomeo Green Tuffs at the base. These units are (from the base to the top):

(1) Pyroclastic ash flows

Massive cineritic banks rich in pumices showing at their base a characteristic level formed by pumices. Couple of levels of welded grey and pink ashes.

Levels having a decimeter thickness up to one meter (Scotto di Carlo outcrop) and corresponding to the distal facies of the Campanian Ignimbrite.

(2) Piperno bank

It is formed by scorias and lavas, rich in matrix, grading upwards into the Breccia Museo. A cineritic facies occurs at their base, eroding the underlying deposits and cropping out at Punta della Lingua, Scotto di Carlo and Cimitero.

(3) Breccia Museo

It is represented by the proximal facies of the Campanian Ignimbrite, showing a pumice pyroclastic flow at their top.

(4) Pumice flow

Level of gray and green pumices rich in degassing structures. In the section of Spiaggia del Postino, it is characterized by a layer rich in blocks.

3.1.6 Solchiaro volcano (age 22 ky)

The deposits forming this unit are genetically related to the eruptive activity of the Solchiaro tuff ring, representing the youngest eruptive activity of the Island of Procida. The crateric rim has been identified in the south-eastern sector of the Island of Procida, between the Pizzaco promontory (**Figure 7**) and the Solchiaro promontory (**Figure 8**). The deposits of the Solchiaro volcano widely occur in the upper part of the stratigraphic sequences cropping out in many coastal cliffs of the Island of Procida. They crop out also at Vivara, to the north of Punta Mezzogiorno and around Punta Capitello. Next to the volcanic vent, outcropping along the coastal street bounding the Pizzaco and the Solchiaro promontories (Panoramica Street), a transition from

stratified yellow tuffs to stratified grey tuffs has been observed, suggesting a deposition in a mostly subaerial environment.

Figure 7. The Pizzaco promontory (Island of Procida, Naples Bay)**.**

Figure 8. The Solchiaro Promontory (Island of Procida, Naples Bay)**.**

3.2 The Terra Murata coastal cliff towards the Corricella Bay

3.2.1 State of the geosite

One of the selected geosites is located in the north-western sector of the Island of Procida. In fact, the S. Michele church and the "Conservatorio delle Orfane" palace are located next to a sub-vertical slope, separating the Terra Murata village from the sea.

The subsurface lithostratigraphic reconstruction has been simplified from the occurrence of this slope. In fact, the slope allows for the direct observation of the rocky strata underlying the church for an overall thickness of 90 meters. The subsurface is constituted by a stratified tuffaceous formation, probably latitic in nature. This formation shows two different facies, having distinct lithotechnical characteristics (**Figures 9, 10, 11** and **12**).

Figure 9. The Terra Murata coastal cliff towards the Corricella Bay, where the superimposition of two facies with different lithotechnical characteristics may be seen**.**

Figure 10. Detail of the Terra Murata coastal cliff, showing the stratigraphy of the pyroclastic successions having different technical characteristics**.**

Figure 11. Detail of the Terra Murata coastal cliff whose outcrop shows the stratigraphy of the pyroclastic successions and a deep cave incised in tuffs**.**

67

Figure 12. The upper part of the Terra Murata coastal cliff, showing the superimposition of the grey facies (to the top) on the yellow facies (to the base).

The first facies, yellow in colour, is completely lithified. The second facies, grey in colour, is semi-coherent. The two facies are not separated by an abrupt lithostratigraphic boundary. In fact, the lithified yellow facies grades upwards or laterally to the semi-coherent grey facies. This is probably due to the mechanisms controlling the individuation of the two facies, such as the processes of post-depositional zeolitization, realized after an incipient hydrothermal activity and involving the most part of the tuffaceous products of the Island of Procida.

The hydrothermal activity, realized from the base to the top of the succession and proceeding along radial directions has provoked the neoformation of zeolitic minerals in the basal and central parts of the formation, which has consequently reached a lithoid consistency, assuming a yellow colour. The gradual decreasing of the hydrothermal action in the peripheral areas of the formation has determined the differentiation of a residual facies, having a grey colour and a semi-coherent consistency (**Figure 9** and **10**). Moreover, the dipping of the strata has clearly indicated that the emission centre of the tuff pyroclastic products was located next to the coast, in front of the S. Michele church.

From a mineralogic and petrographic point of view, the Terra Murata tuffs are formed by abundant glassy pumices and shales, together with trachytic inclusions and by sanidine and biotite crystals, coupled with minerals of neoformation pertaining to the group of zeolites (e.g. cabasite and phillipsite)[1].

The coastal cliffs of the Island of Procida show in outcrop the lithostratigraphic and geometric rela-tionships between the described formations. Proceeding from the Terra Murata promontory towards north, a gradual thickness increase of the grey facies with respect to the yellow one may be observed. Below the S. Michele church, the semi-coherent grey facies is lacking, while it reaches a thickness of about 30 m some tens of meters to the north.

Above the described tuffs heterogeneous breccias crop out ("Breccia di Punta della Lingua"). Above these breccias, genetically related to the Campanian Ignimbrite, the volcanic succession is composed of one or more paleosols, overlain by pyroclastites genetically related to the Solchiaro volcano and by pumice products genetically related to the Phlegrean Fields ("Fondi di Baia Formation")[19].

The geomorphology of the Terra Murata coastal cliff is herein discussed. The cliff is high about 92 m a.s.l., representing the highest part of the Island of Procida. The outcrops surrounding the S. Michele Abbey and the "Conservatorio delle Orfane" palace have not been strongly involved by erosional processes, while the coastal cliff between the promontories of Punta dei Monaci and Punta della Lingua has undergone a strong erosional action due to the sea. The coastal cliff retreated in consequence of erosional processes. The waves, bumping with the base of slope, have provoked its erosional retreatment through a physical and chemical action with the formation of deep furrows. Deep fractures have been observed downthrowing the coastal cliff at several places, which have isolated some packages, making unstable the slope. Moreover, the action of the atmospheric agents, particularly of the rain, tends to deepen the fractures, progressively widening them and triggering the occurrence of rock falls.

Table 1. Geotechnical parameters of yellow tuffs at the Terra Murata coastal cliff (Island of Procida)

Volume weight	1.3-1.5 g/cm^3
Load of compression rupture	30-70 kg/cm^2
Angle of inner friction (FI)	15°-20°
Cohesion	20-30 kg/cm^2

The volcanic deposits cropping out along the Terra Murata coastal cliff have shown technical characteristics similar to those ones of the Neapolitan Yellow Tuff (NYT) deposits[20]. Some samples

have been collected to perform the geotechnical analyses, allowing for the calculation of the geotechnical parameters resumed in **Table 1**.

3.2.2 Seepages of waters and their possible nature

At the Terra Murata geosite, the monitoring of the seepage of waters has been carried out through a detailed geologic and geomorphologic survey coupled with technical consideration. In particular, a first survey has been carried out in the place located after the door marking the beginning of the Middle Ages village. This survey has been carried out aimed at reconstructing the relationships between the seepages of water documented in this area by one hundred year (next to the door) and the similar phenomena of seepages of water documented below the street, namely Salita Castello.

At the Terra Murata place, dry and wet tuffs crop out to a few distance. Here the seepages of waters are very consistent. A first outcrop is characterized by grey tuffs, very lithified, including a coarse-grained fraction, composed of scoriaceous lapilli and dark pumice levels. At lower heights, other wet outcrops have been observed, characterized by grey-yellow tuffs, similar to those ones observed in the first outcrop. Proceeding towards lower heights, another outcrop has been surveyed, composed of dry tuffs.

The occurrence of both cavities in the subsurface (ancient pools) and the system of the old sewer, Borbonic in age, serving again some houses, should be pointed out. Recently, after the cleaning of the old sewer, the seepage of waters tended to decrease. The tuff outcrops located in the place, now appearing dry, underlie the houses linked to the modern sewer. Accordingly to the testimonies of the indoor people, some houses located in the upper part of the Terra Murata historical village are not linked to the modern sewer. In these cases, the waters should be drained towards the valley, finding preferential pathways in the joints layering and following the gradient of the tuff formations.

A second survey has been carried out on the tuff coastal cliff below the Salita Castello Street (Terra Murata) in a private house located on the coastal cliff facing towards the Marina Corricella.

Here the seepages of waters are very abundant, forcing the house's inhabitants to carry out works of ordinary maintenance. After the partial consolidation of a sector of the coastal cliff, located laterally to the house, realized through cement injections and the waterproofing of fractures, the seepage of waters were reduced. After a short time, the seepages abundantly re-started, producing a water sheet continuously falling, such as a small cascade.

The obtained results have evidenced some elements of interest. The first element is represented by the high geomorphologic instability of the Terra Murata coastal cliff towards the Marina Corricella. The coastal cliff has been arranged through some holding walls. One of them is disposed longitudinally to the houses, while other ones are disposed in a punctual way. Other interventions consist of metallic wire nettings put on single parts of the coastal cliff and of cement injections. The high geomorphologic instability has been favored by selective erosion of grey tuffs, representing the upper terms of the stratigraphic succession forming the coastal cliff. This erosion was probably controlled by the stratification of the tuffs, which are composed of lithified levels (holding out) and semi-coherent levels (coming back).

The second element is represented by the occurrence of fractures and small vertical faults, allowing for a block down throwing of the tuffs. Together with the joint layering, showing a general seaward immersion, they represent preferential drainage pathways for the inshore waters. The permeability of the upper grey tuffs should be primary, due to the scarce lithification of the deposits, rich of inter-granular spaces and secondary, due to the strong fracturing, favoring the water circulation.

3.3 The Centane-Panoramica geosite (coastal cliffs between the Pizzaco and Solchiaro Promontories)

3.3.1 State of the geosite

The area bounded by the Pizzaco and Solchiaro coastal cliffs is constituted by a degrading tuff cliff, on which deposits coming from authorized excavations have been spilled. The incongruence and the quantity of the deposits have make necessary interventions finalized to the re-development of the

area, depending on the performed geologic analysis, aimed at determining the subsurface lithology and the height trending of the area.

The geologic analysis, properly integrated by geological and technical tests for the determination of the stratigraphy and of the technical characteristics of the tuffs, representing the acoustic substratum and of the overlying undifferentiated deposits, has been carried out on the seawards sectors of the coastal cliffs. The A area was analyzed, used as a dump up to recent times.

The coastal cliff morphology has been strongly modified since they have been used as dumps of recent undifferentiated deposits. They constitute a wedge having a kilometric extension, overlying the yellow tuffs of the Solchiaro Formation along the coastal cliff between the Pizzaco and Solchiaro Promontories.

The technical characteristics of these deposits have been determined on disturbed samples, previously collected during standard penetrometric tests (SPT) through geotechnical and grain-size analysis. The results obtained from the SPT tests have allowed calculating the thickness of the undifferentiated deposits, overlying the rocky substratum of the Solchiaro tuffs and the physical and chemical characteristics of the crossed grounds. They have been calculated through algorithms of correlation, relating the geotechnical parameters with the number of blows (Nspt). The calculated geotechnical parameters are listed in **Table 2** (Solchiaro tuffs).

Table 2. Geotechnical parameters of Solchiaro yellow tuffs at the Pizzaco coastal cliff (Island of Procida) calculated through the correlation of Standard Penetrometric Tests (SPT)

Angle of inner friction (FI)	37°-40°
Wet weight-volume ratio (GA)	1.65 t/m^3
Dynamic strength at the point (Rd)	50.94 kg/cm^2
Un-drained cohesion (Cu)	0
Compression strength (σ)	1.5-2 kg/cm^2

The SPT tests have evidenced the following technical and mechanical characteristics of the undifferentiated deposits along the coastal area, namely the A area, located in the Centane-Panoramica geosite. The drill site S1 is reported as an example.

3.3.1.1 Geotechnical parameters at the drill site S1

The SPT tests have been carried out at a depth of 3.6 m, occurring at the top of the rocky substratum composed by tuffs. Between the field plan and the depth of 3.6 m, alternating strata of grounds having a variable consistency, ranging between very dense and loose, have been found.

The general characteristics have been determined in laboratory on a disturbed sample drilled at a depth of 3.4 m from the field plan during the SPT test at the drill site S1 (**Table 3**). The grain-size analysis has shown slightly muddy gravelly sand.

Table 3. General characteristics of the undifferentiated deposits at the drill site S1

Specific weight of the granules	2.36 g/cm^3
Volume weight	1.50 g/cm^3
Water content	35.70 %
Void ratio	1.67
Porosity	62.53 %
Saturation degree	100%

The state of the geosite is relatively different in the areas located onshore of the coastal street (B and D areas) with respects to the areas located seawards of the coastal street (A area). While the first ones are characterized by outcropping lithoid pyroclastic rocks (Solchiaro yellow tuff) along steep coastal cliffs, the second ones show undifferentiated deposits on flat morphological surfaces, overlying at depth the rocky substratum composed of tuffs.

3.3.2 Geomorphologic instability

The high geomorphologic instability of the coastal cliff surrounding the Chiaia beach (Island of Procida) has been recently evidenced from frequent landslides coupled with strong erosion. The accommodation of the coastal cliff has been recently carried out in the frame of the FESR project through the emplacement of containing walls, adopted in order to contain the erosional phenomena and to make sure the public baths.

The two areas located inwards of the De Gasperi Street (Centane-Panoramica geosite), namely the D and B areas, now used as recreation places for children do not have a significant geomorphologic instability if compared with the areas of the coastal cliff located seawards, also due to their lithology, mainly tuffaceous.

The Solchiaro tuffs crop out along a sub-vertical rocky slope in the first area, located landwards

and form a slope having a low gradient in the second area, located towards the valley. At a first analysis, these areas may be considered as more stable with respect to the areas located seawards, being characterized by outcropping lithoid grounds.

It must be singled out the occurrence of small fractures, involving the tuff coastal cliff. At the present-day state of geosites, these fractures do not cause problems of stability. In the future, they need to be monitored and controlled in order to forecast, with the onset of the erosion, the rock falls of the blocks isolated from these fractures.

Moreover, it is worth noting the occurrence of undifferentiated deposits at the base of the tuff coastal cliff, which should be removed to realize the environmental re-development of the area[21].

4. Discussion

Selected areas of the Island of Procida, whose geologic history is strictly related with the eruptive centers of the Phlegrean Fields and the Island of Ischia, have been studied. Procida and Vivara are two volcanic islands, located in an intermediate position between the active calderas of the Phlegrean Fields and the Island of Ischia. A deep knowledge on the stratigraphy and the volcanological evolution of the Phlegrean Fields and of Ischia has been produced by volcanological studies[3,14,22,23].

The stratigraphy and volcanology of Procida and Vivara have been deeply studied by many scholars[1,8,24-28]. The volcanic deposits cropping out in the Island of Procida have been generally explained as the result of eruptions coming from local eruptive centers. Moreover, these studies have indicated the occurrence of several pyroclastic units, linked to the eruptive activity of the Ischian and Phlegrean volcanic complexes, inter-layered in the volcanic successions erupted from the local volcanic centers of Procida and Vivara.

In the pyroclastic sequences of the two islands, the occurrence of several regional markers and their stratigraphic correlation[1,25] allows for the volcanological reconstruction and the stratigraphic framework of the volcanic products of Ischia and Procida islands in the frame of the volcanic successions of Ischia and Phlegrean Fields.

The Phlegrean Fields, with the Ischia and Pro-cida islands, represent a complex volcanic system formed by a set of small monogenetic volcanoes, disposed along a E-W trend and fed by a potassic magmatism. Recent studies on the area including the Phlegrean Fields and the Procida and Vivara islands have evidenced the existing correlation between the phases of volcanic activity for the comprehension of the volcanic processes older than the eruption of the Neapolitan Yellow Tuff[3,14,29].

The volcanic breccias cropping out at Marina di Vita Fumo (Monte di Procida) and the Procida island (Punta della Lingua, Scotto di Carlo and Pozzo Vecchio) are genetically related to a main phase of volcanic activity, whose eruptive center was probably located in the Procida Channel. Other six eruptive centers have been recognized in the Procida and Vivara islands, including the Vivara volcano, the Fiumicello volcano, the Terra Murata volcano, the Punta Serra volcano and the Solchiaro volcano. Moreover, the study of the marine area between Procida and Ischia has revealed two distinct volcanic morphologies, namely "La Catena" and "Le Formiche di Vivara", having a basaltic chemistry, similar to that one of the Procida volcanic products[8,30-32].

The volcanological evolution of the Island of Procida and Vivara is herein outlined based on the geological data. According to the stratigraphic reconstructions of Rosi et al.[11] and Fedele et al.[1], Procida and Vivara have been formed by the accumulation of volcanic products of pyroclastic fall and pyroclastic flux, coming from the surrounding volcanic complexes of Ischia and Phlegrean Fields.

The oldest volcanic deposits detected in outcrop are represented by the products of the volcanic centers, respectively trachybasaltic and trachytic, of Vivara, Pozzo Vecchio and Terra Murata. In all the three vents, eruptive centers formed by stratified yellow tuffs occur. In the Pozzo Vecchio Volcano, the growth of the tuff cone has been followed by a scoria eruption and by the final emission of a lava flow, having a trachytic composition. The depositional environment was probably submarine for the base of the volcanic edifices and subaerial for the middle and upper part of the tuff cones.

The eruptive scenario was represented by an explosive activity in a shallow water environment

(yellow tuffs of Vivara, Terra Murata and Pozzo Vecchio), followed by a progressive isolation of the eruptive conduits from the sea with the eruption of wet hydromagmatic products, represented by the grey and white tuffs forming the upper parts of the Vivara and Terra Murata tuffaceous successions and by volcanic products, which do not show any evidence of magma-water interaction (Pozzo Vecchio scorias followed by the final lavas). All the three edifices have allowed for the construction of an emerged volcanic field.

Starting from this period, the deposition of products erupted from the surrounding areas started. Among them, the first ones are represented by the deposits linked to the explosive activity in a subaerial environment, happened in the Ischia Channel in correspondence to the "Formiche di Vivara" saddle (Procida Channel). Coarse-grained breccias and pyroclastic surge deposits erupted from the center overlie part of Vivara and the north-western sectors of Procida. No available radiometric data exist on these deposits.

During the next period, ranging between 74 and 55 My, Vivara and the emerged centers of Pozzo Vecchio and Terra Murata have been overlain by neritic banks of Plinian pumices, coming from the Ischia Island. In this period, the volcanic activity newly starts with the trachybasaltic eruptive center of Fiumicello, whose hydromagmatic deposits are interlayered between the B and C Plinian pumices of the Pignatiello Formation.

The Fiumicello eruption has deeply modified the morphology of the north-eastern sector of the Island of Procida, with a thick deposit of stratified yellow tuffs and thinly stratified grey tuffs, overlying the eruptive centre of Pozzo Vecchio, from Punta di Pioppeto to Punta Ottimo and the northern sector of the Terra Murata eruptive cone.

Plinian fall deposits of the Island of Ischia are overlain by the trachybasaltic products of a second hydromagmatic eruption, coming from the Ischia Channel ("Canale d'Ischia superiore")[11]. It is represented by breccias levels, fall lapilli and pyroclastic surges, cropping out in the Vivara inlet and the sector from Ciraccio and Pozzo Vecchio.

The second trachybasaltic eruption of the Ischia Channel is followed by the eruption of the Epomeo Green Tuffs of the Island of Ischia (55 ky)[23,33-39] and of the Campanian Ignimbrite of the Phlegrean Fields (37 ky)[12,40-47].

A main modification of the morphology of the Island of Procida realized after the eruption of the Epomeo Green Tuffs of Ischia due to the infilling of the lows located between previous eruptive vents. Another phase of infilling happened after the eruption of the volcanic products related to the Campanian Ignimbrite, 37 ky ago. The present-day flat morphology of the Island of Procida has been controlled by these volcanic events.

A next morphological change happened about 19 ky ago after the eruption of the Solchiaro yellow tuffs, representing the last local event tested based on volcanic stratigraphy. The Solchiaro volcano is a cone of stratified yellow tuffs linked to a hydromagmatic explosive activity in a shallow water environment. The corresponding pyroclastic surge deposits overlie the most part of the Island of Procida and subordinately, Vivara and S. Margherita. After the products of the Solchiaro volcano, there is the deposition of distal fall ashes (loose pyroclastites) produced by the Phlegrean eruptions ("Fondi di Baia Formation"[19] or "Unità dei Tefra superiori"[11]). These deposits widely crop out in the upper terms of the Procida and Vivara successions, having an average thickness of 3-4 m. They have been deposited during the old post-caldera activity of the Phlegrean Fields (Phase A of Rosi and Sbrana[3]) and during prehistorical eruptions (Bronze Age) of the Ischia Island.

The tracts of high-relief coasts of the Island of Procida represent erosional surfaces, developed during the geological time as a consequence of the interactions between volcanism, tectonics, eustasy and climate. Perhaps, they represent transitional landforms controlled by geomorphological and geomechanical processes coupled with the anthropic activity. Therefore, they represent landforms varying during the geological time and unstable, also if the velocity of variations of the landforms may be variable.

One of the most relevant phenomena controlling the variation in shape of the high-relief coasts is represented by the coastal landslides, whose peculiarity is due to be controlled by the sea actions, if

compared with the continental landslides[48-59].

The tracts of the high-relief coasts of the Island of Procida show a notable articulation due to the complex volcano-tectonic and geomorphologic evolution of the island, during which several landslides realized[60]. They are mainly represented by rock falls and topples (WP/WPLI, 1994), whose triggering has been controlled by lithostratigraphic and structural setting. In fact, the alternating lithoid and loose levels have caused a differential erosion of the coastal cliff, with the formation of brackets, respectively holding out and coming back, having an unstable equilibrium and triggering landslides.

The tectonic setting of the coastal cliffs of the Island of Procida is characterized by fractures, both vertical and parallel to the slopes. At several places, the coastal cliffs show a more articulated profile, consisting of a sub-vertical basal slope, on which another slope develops, ranging in gradient from 35° to 45° in loose pyroclastites (Fiumicello, Solchiaro Promontory, and Vivara Inlet) and joining with an upper flat surface. In these cases, apart from rock falls involving the tuff deposits of the basal slope, slides and flows involving the loose pyroclastites of the upper slope have been observed.

In this study, both in the Terra Murata coastal cliff facing the Marina Corricella towards the Tyrrhenian sea and the Pizzaco and Solchiaro coastal cliffs (Centane-Panoramica geosite) have been analyzed. Geological survey coupled with SPT, geotechnical and grain-size analyses has revealed a high geomorphologic instability of these coastal cliffs. This instability is accompanied, in the Terra Murata coastal cliff, by important seepages of water at the contact between the tuffaceous formations, characterized by different permeability and lithology.

5. Conclusion

The tracts of high-relief coasts of the Island of Procida show a strong articulation and complexity due to the volcano-tectonic and geomorphologic evolution of the island. This geological and geotechnical study has evidenced that the seepages of waters mainly occur in the tuff outcrops located in the place signing the admittance to the Terra Murata Middle Ages village and on the slopes below the "Salita Castello" street, pertaining to the tuff coastal cliff facing towards the Corricella Bay (Tyrrhenian Sea).

The coastal cliffs are distinguished from seawards dipping rocky walls, whose evolution is mainly controlled by the erosional action of the sea at the foot of slope through the undermining of the cliff foot and by the consequent phenomena of deformation, fracturing, rupture and mass gravitational movements, with individuation of coastal landslides[57,58].

The geologic and geomorphologic study of some tuff outcrops located in the Middle Ages village of Terra Murata, representing the historical centre of the Island of Procida, has evidenced the occurrence of main water seepages, located in correspondence with pyroclastic formations having different technical characteristics and also controlled by a dense network of fractures. In some way, these water seepages have also been controlled by the occurrence of the ancient Borbonic siewer, with tanks or cavities now occurring in the subsurface. They are particularly abundant in the tuff outcrops located in the place apart from the door marking the entrance to the Middle Ages village of Terra Murata and below the Salita Castello street. The involved lithologies are represented by lithified grey tuffs, including an abundant coarse-grained fraction, composed of scoriaceous lapilli and dark pumices and subordinately, by grey-yellow tuffs.

The geologic and geomorphologic study of the Centane-Panoramica geosite has been involved in a project of environmental redevelopment and has been carried out through SPT tests and geotechnical analyses. Detailed results have been reported by Aiello[21].

The obtained results have evidenced a higher security of the areas located landwards of the coastal street joining the Pizzaco and the Solchiaro promontories (D and B areas), not showing a high geomorphologic instability and being characterized by outcrops of lithoid and coherent deposits (Solchiaro tuffs). On the contrary, the seawards areas (A and C areas), located towards valley from the street and at the top of the coastal cliff show a higher geomorphologic instability, mainly relatively to

the upper part of the slope, quite unstable, since these areas have been used as dumps up to recent times.

Some detailed conclusions are herein reported, relatively to the single areas.

B area: this area, previously used as a recreation park for children, is generally adapted to its use. The flat surface, located at the top of the coastal cliff, laterally joins a rocky sub-vertical slope incised in the Solchiaro tuffs. These grounds, being lithoid and coherent, do not show problems of geomorphologic instability. The geologic setting of this area should be controlled relatively to the future state of the geosites. In fact, the occurrence of longitudinal fractures having a random distribution implies the isolation of hazardous rocky pieces and their rock fall due to increasing erosion.

D area: this area, previously used as a recreation park for children, is generally adapted to its use. Next to this area the Solchiaro tuffs crop out along a slope having a low gradient, showing a general immersion of the strata towards the street.

A area: the flat morphology of the seawards slopes on the coastal street joining the Pizzaco and the Solchiaro coastal cliffs may be misleading on their stability conditions, which may result in precarious conditions. This may happen if these areas should be undertaken to loads not proportional to geotechnical parameters of stability of the undifferentiated deposits or during channel filling.

The geomorphologic instability of the undifferentiated deposits overlying the Solchiaro tuffs is quite high on the coastal slopes facing towards the Tyrrhenian Sea, since they are represented by loose pyroclastic deposits with scarce technical characteristics. Moreover, the slopes are unstable since these deposits have been reworked up to recent times.

The SPT tests have been finalized to the calculation of density and inner angle of friction (FI), which is related to the shear strength and the depth of the underlying rocky substratum. FI has allowed evaluating the maximum loads and considering the interventions of redevelopment and consolidation, if necessary in these areas.

The SPT tests have been performed in a highly unstable area (A area), long about 100 m and locat-ed to 46 m a.s.l. Its lithostratigraphic setting is characterized by undifferentiated loose deposits overlying the yellow tuffs, which are potentially prone to slide. The tests have been carried out in drill sites located on the seawards rim of the A area next to the break in slope marking the coastal cliff top.

Some geotechnical analyses have been carried out on samples collected during the SPT tests to calculate the general technical characteristics of the undifferentiated deposits (**Table 3**). The obtained results have indicated the occurrence of a wedge of undifferentiated deposits ranging in thickness from 6.5 to 7 m and composed of slightly muddy gravelly sands with low water content.

Table 3. General characteristics of the undifferentiated deposits at the drill site S1

Specific weight of the granules	2.36 g/cm³
Volume weight	1.50 g/cm3
Water content	35.70 %
Void ratio	1.67
Porosity	62.53 %
Saturation degree	100%

Ethics statement

The author states that this manuscript abides by the ethical norm required.

Conflict of interest

No conflict of interest was reported by the author.

References

1. Fedele L, Morra V, Perrotta A, *et al.* Carta Geologica Regionale alla scala 1:10.000. Isole di Procida e Vivara (con note illustrative). Regione Campania, Settore Difesa del Suolo, Geotermia e Geotecnica, Napoli, Italy; 2012.
2. Deino AL, Orsi G, De Vita S, *et al.* The age of the Neapolitan Yellow Tuff caldera-forming eruption (Campi Flegrei caldera — Italy) assessed by 40Ar/39Ar dating method. Journal of Volcanology and Geothermal Research 2004; 133(1-4): 157–170.
3. Rosi M, Sbrana A. The Phlegrean Fields. Quaderni De La Ricerca Scientifica; 1987. p. 175.
4. De Vita S, Orsi G, Civetta L, *et al.* The Agnano–Monte Spina eruption (4100 years BP) in the restless Campi Flegrei caldera (Italy). Journal of Volcanology and Geothermal Research 1999; 91(2-4): 269–301.
5. Arienzo I, Moretti R, Civetta L, *et al.* The feeding system of Agnano–Monte Spina eruption (Campi

Flegrei, Italy): Dragging the past into present activity and future scenarios. Chemical Geology 2010; 270(1-4): 135–147.

6. Bevilacqua A. Doubly stochastic models for volcanic hazard assessment at Campi Flegrei Caldera. Springer Verlag; 2016. p. 250.

7. Iovine RS, Fedele L, Mazzeo FC, *et al.* Timescales of magmatic processes prior to the ~4.7 ka Agnano-Monte Spina eruption (Campi Flegrei caldera, Southern Italy) based on diffusion chronometry from sanidine phenocrysts. Bulletin of Volcanology 2017; 79(2): 18. doi: 10.1007/s00445-017-1101-4.

8. Di Girolamo P, Stanzione D. Lineamenti geologici e petrologici dell'Isola di Procida. Rendiconti Società Italiana Mineralogia e Petrologia 1973; 24(5): 81–126.

9. Pescatore TS, Rolandi G. Osservazioni preliminari sulla stratigrafia dei depositi vulcanoclastici nel settore SW dei Campi Flegrei. Italian Journal of Geosciences 1981; 100(2): 233–254.

10. Di Girolamo P, Ghiara MR, Lirer L, *et al.* Vulcanologia e petrologia dei Campi Flegrei. Bollettino della Società Geologica Italiana 1984; 103: 349–370.

11. Rosi M, Sbrana A, Vezzoli L. Stratigrafia delle isole di Procida e di Vivara. Bollettino GNV 1988; 4: 500–525.

12. De Vivo B, Rolandi G, Gans P, *et al.* New constraints on the pyroclastic eruptive history of the Campanian Volcanic Plain (Italy). Mineralogy and Petrology 2001; 73: 47–65. doi: https://doi.org/10.10 07/s007100170010.

13. Rolandi G, Bellucci F, Heizler MT. *et al.* Tectonic controls on the genesis of ignimbrites from the Campanian Volcanic Zone, southern Italy. Mineralogy and Petrology 2003; 79: 3–31. doi: https://doi. org/10.10 07/s00710-003-0014-4

14. De Astis G, Pappalardo L, Piochi M. Procida volcanic history: New insights in the evolution of the Phlegrean volcanic district (Campania Region, Italy). Bulletin of Volcanology 2004; 66: 622–641. doi: https://doi.org/10.1007/s00445-004-0345-y.

15. Revellino P, Hungr O, Guadagno FM, *et al.* Velocity and run-out simulation of destructive debris flows and debris avalanches in pyroclastic deposits, Campania region, Italy. Environmental Geology 2004; 45: 295–311. doi: https://doi.org/10.1007/s002 54-003-0 885-z.

16. De Vita P, Napolitano E, Godt JW, *et al.* Deterministic estimation of hydrological thresholds for shallow landslide initiation and slope stability models: Case study from the Somma-Vesuvius area of southern Italy. Landslides 2013; 10: 713–728. doi: https://doi.or g/10.1007/s10346-012-0348-2.

17. Branca S, Coltelli M, Groppelli G. Geological Evolution of Etna Volcano. In: Bonaccorso A, Calvari S, Coltelli M (editors). Geophysical Monograph Series. Blackwell Publishing Ltd; 2004. p. 49–63. doi: 10.1 029/143GM04.

18. Groppelli G, Goette LV. Stratigraphy and geology of volcanic areas. Geological Society of America; 2010. ISBN: 9780813724645.

19. Rittmann A. Origine e differenziazione del magma ischitano. Sch-weizerische Mineralogische und Petrographische Mitteilungen 1948; 28: 643–698.

20. Scarpati C, Cole P, Perrotta A. The Neapolitan Yellow Tuff — A large volume multiphase eruption from Campi Flegrei, Southern Italy. Bulletin of Volcanology 1993; 55: 343–356.

21. Aiello G. Studio geologico del comprensorio Centane-Panoramica (Isola di Procida. Golfo di Napoli). Consiglio Nazionale delle Ricerche (CNR), Monografia, Rapporto Tecnico, edito da CNR Solar (Biblioteca Centrale del Consiglio Nazionale delle Ricerche "G. Marconi"), luglio 2016.

22. Di Girolamo P, Rolandi G. Vulcanismo sottomarino latite-basaltico-latitico (serie potassica) nel canale di Ischia (Campania). Rendiconti Acc. Sc. Fis. e Mat. in Napoli 1975; 42: 561–596.

23. Vezzoli L. Island of Ischia. Roma: Quaderni De La Ricerca Scientifica; 1988. p. 230.

24. Parascandola A. I crateri dell'Isola di Procida. Bollettino Società Naturalisti in Napoli 1924; 40: 57–60.

25. Perrotta A, Scarpati C, Luongo G, *et al.* Stratigraphy and volcanological evolution of Campi Flegrei and Procida Island. In: Stratigraphy and Geology of Volcanic Areas. GSA Special Papers 2010; 464: 185–189.

26. Putignano ML, Cinque A, Lozej A, *et al.* Late Holocene ground movements in the Phlegrean Volcanic District (Southern Italy): New geoarcheological evidence from the islands of Vivara and Procida. Mediterranée 2009; 112: 43–50.

27. Putignano ML, Schiattarella M. Geomorfologia strutturale e domini di frattura dei fondali marini pericostieri dell'Isola di Procida (Campi Flegrei insulari, Italia meridionale). Italian Journal of Quaternary Sciences 2010; 23(2): 229–242.

28. Aiello G, Marsella E. Interactions between Late Quaternary volcanic and sedimentary processes in the Naples Bay, Southern Tyrrhenian Sea. Italian Journal of Geosciences 2015; 134(2): 367–382. doi: 10.3301/IJG.2014.56.

29. Aiello G, Insinga D, Iorio M, *et al.* On the occurrence of the Neapolitan Yellow Tuff tephra in the Northern Phlegraean offshore (Eastern Tyrrhenian margin, Italy). Italian Journal of Geosciences 2017; 136: 263–274.

30. De Alteriis G, Donadio C, Ferranti L. Morfologia e strutture di apparati vulcanici sommersi nel Canale d'Ischia (Mar Tirreno). Memorie Descrittive della Carta Geologica d'Italia 1994; 52: 85–96.

31. Aiello G. New insights on the Late Quaternary geologic evolution of the Ischia Island coastal belt based on high-resolution seismic profiles. Italian Journal of Geosciences 2018; 137(1): 87–106. doi: 10.3301/I JG.2017.19.

32. Aiello G, Marsella E, Passaro S. Stratigraphic and structural setting of the Ischia volcanic complex (Naples Bay, Southern Italy) revealed by submarine seismic reflection data. Rendiconti Lincei 2012; 23: 387–408.

75

33. Gillot PY, Chiesa S, Pasquarè G, *et al.* <33,000-yr K–Ar dating of the volcano–tectonic horst of the Isle of Ischia, Gulf of Naples. Nature 1982; 229: 242–245. doi: https://doi.org/10.1038/299242a0.

34. Orsi G, Gallo G, Zanchi A. Simple-shearing block resurgence in caldera depressions: A model from Pantelleria and Ischia. Journal of Volcanology and Geothermal Research 1991; 47(1-2): 1–11.

35. Mele R, Del Prete S. Fenomeni di instabilità dei versanti in Tufo Verde del Monte Epomeo (isola d'Ischia – Campania). Bollettino della Società Geologica Italiana 1998; 117(1): 93–112.

36. Tibaldi A. Vezzoli L. Late Quaternary monoclinalic folding induced by caldera resurgence at Ischia, Italy. Geological Society of London, Special Publications 2000; 169: 103–113.

37. De Vita S, Di Vito MA, Gialanella C, *et al.* The impact of the Ischia Porto Tephra eruption on the Greek colony of Pithekoussai. Quaternary International 2013; 305: 142–152. doi: https://doi.org/10.1016/j.quaint.2013.01.002.

38. Brown RJ, Orsi G, De Vita S. New insights into Late Pleistocene explosive volcanic activity and caldera formation on Ischia (Southern Italy). Bulletin of Volcanology 2008; 70: 583–603. doi: https://doi.org/10.1007/s00445-007-0155-0.

39. Della Seta M, Marotta E, Orsi G, *et al.* Slope instability induced in volcano-tectonics a san additional source of hazard in active volcanic areas: the case of Ischia Island (Italy). Bulletin of Volcanology 2012; 74(1): 79–106.

40. Barberi F, Innocenti F, Lirer L, *et al.* The Campanian Ignimbrite: A major prehistoric eruption in the Neapolitan area (Italy). Bulletin of Volcanology 1978; 41(1): 10–31.

41. Fisher RV, Orsi G, Ort M, *et al.* Mobility of large-volume pyroclastic flow — Emplacement of the Campanian Ignimbrite, Italy. Journal of Volcanology and Geothermal Research 1993; 56(3): 205–220.

42. Civetta L, Orsi G, Pappalardo L, *et al.* Geochemical zoning, mingling, eruptive dynamics and depositional processes — The Campanian Ignimbrite, Campi Flegrei Caldera, Italy. Journal of Volcanology and Geothermal Research 1997; 75(3-4): 183–219.

43. Pappalardo L, Civetta L, D'Antonio M, *et al.* Chemical and Sr-isotopical evolution of the Phlegraean magmatic system before the Campanian Ignimbrite and the Neapolitan Yellow Tuff eruptions. Journal of Volcanology and Geothermal Research 1999; 91(2-4): 141–166.

44. Giaccio B, Isaia R, Fedele FG, *et al.* The Campanian Ignimbrite and Codola tephra layers: Two temporal/stratigraphic markers for the Early Upper Palaeolithic in southern Italy and Eastern Europe. Journal of Volcanology and Geothermal Research 2006; 177(1): 208–226.

45. Pyle DM, Ricketts GD, Margari V, *et al.* Wide dispersal and deposition of distal tephra during the Pleistocene 'Campanian Ignimbrite/Y5' eruption, Italy. Quaternary Science Reviews 2006; 25(21-22): 2713–2728.

46. Costa A, Folch A, Macedonio G, *et al.* Quantifying volcanic ash dispersal and impact of the Campanian Ignimbrite super-eruption. Geophysical Research Letters 2012; 39(10): L10301. doi: 10.1029/2012GL051605.

47. Fitzsimmons KE, Hambach U, Veres D, *et al.* The Campanian Ignimbrite Eruption: New Data on Volcanic Ash Dispersal and Its Potential Impact on Human Evolution. PLoS One 2013; 8(6): e65839. doi: https://doi.org/10.1371/journal.pone.0065839.

48. Edil TB, Le Vallejo LE. Mechanics of coastal landslides and the influence of slope parameters. Engineering Geology 1980; 16(1-2): 83–96.

49. Clark AR, Moore R, Palmer JS. Slope monitoring and the early warning systems: application to coastal landslides on the south and east coast of England, UK. Trondheim: Proceedings of the International Symposium on Landslides; 1996. p. 1531–1539.

50. Cruden DM, Varnes DJ. Landslide types and processes. In: Turner AK, Schuster RL (editors). Landslides: Investigation and mitigation (Special Report). Washington DC, USA, National Research Council, Transportation and Research Board Special Report 1996; 247: 36–75.

51. Montgomery W. Groundwater hydraulics and slope stability analysis: Elements for prediction of shoreline recession (PhD thesis). Western Michigan University; 1998. Available from: https://scholarworks.wmich.edu/dissertations/1583/.

52. Hall J, Lee EM, Meadowcroft IC. Risk-based benefit assessment of coastal cliff protection. Proceeding of the Institution of Civil Engineers-Water and Maritime Engineering 2000; 142(3): 127–139.

53. Iadanza C, Trigila A, Vittori E, *et al.* Landslides in coastal areas of Italy. Geological Society of London Special Publications 2009; 322(1): 121–141.

54. Abellan A, Calvet J, Vilaplana JM, *et al.* Detection and spatial prediction of rock falls by means of terrestrial laser scanner monitoring. Geomorphology 2010; 119(3-4): 162–171.

55. Bozzano F, Mazzanti P, Prestininzi A, *et al.* Research and development of advanced technologies for landslide hazard analysis in Italy. Landslides 2010; 7(3): 381–385.

56. Thiebes B. Theoretical Background. In: Landslide Analysis and Early Warning Systems. Springer Theses (Recognizing Outstanding Ph.D. Research). Berlin, Heidelberg: Springer. 2012.

57. Matano F, Iuliano S, Somma R, *et al.* Geostructure of Coroglio tuff cliff, Naples (Italy) derived from terrestrial laser scanner data. Journal of Maps 2016; 12(3): 407–421.

58. Esposito G, Salvini R, Matano F, *et al.* Multitemporal monitoring of a coastal landslide through SfM-derived point cloud comparison. Photogrammetric Record 2017; 32(160): 459–479.

59. Leshchinsky B, Olsen MJ, Mohney C, *et al.* Mitigating coastal landslide damage. Science 2017; 357: 981–982.

60. Calcaterra D, Del Prete S, Mele R. L'influenza dei fenomeni franosi sugli insediamenti costieri del dis-

tretto flegreo (Campania, Italia). Proc. Internat. Conf. CITTAM2003. The requalification of Mediterranean coasts among tradition, development and sustainability, Naples, June 26-28, 2003. Arte Tipografica Editore, 524–534, Napoli, Italy.

ORIGINAL RESEARCH ARTICLE

Application of remote sensing and GIS in land resource management

Sathees Kumar[*], **Nazeer Khan**

Department of Civil Engineering, Mohamed Sathak Engineering College/ Anna University, Kilakarai 623806, India.
E-mail: satheeskumar@msec.org.in

ABSTRACT

Land use or land cover (LU/LC) mapping serves as a kind of basic information for land resource study. Detecting and analyzing the quantitative changes along the earth's surface has become necessary and advantageous because it can result in proper planning, which would ultimately result in improvement in infrastructure development, economic and industrial growth. The LU/LC pattern in Madurai City, Tamil Nadu, has undergone a significant change over the past two decades due to accelerated urbanization. In this study, LU/LC change dynamics were investigated by the combined use of satellite remote sensing and geographical information system. To understand the LU/LC change in Madurai City, different land use categories and their spatial as well as temporal variability have been studied over a period of seven years (1999-2006), by analyzing Landsat images for the years 1999 and 2006 respectively with the help of ArcGIS 9.3 and ERDAS Imagine 9.1 software. This results show that geospatial technology is able to effectively capture the spatio-temporal trend of the landscape patterns associated with urbanization in this region.
Keywords: GIS; LANDSAT; Land Use; Land Cover; Remote Sensing

1. Introduction

Planning and development of urban areas with well-developed infrastructure, utilities, and services has its legitimate importance and requires extensive and accurate LU/LC classification. Information on changes in land resource classes, direction, area and pattern of LU/LC classes form a basis for future planning. It is also essential that this information on LU/LC be available in the form of maps and statistical data as they are very vital for spatial planning, management and utilization of land. However, LU/LC classification is a time-consuming and expensive process. In recent years, the significance of spatial data technologies, especially the application of remotely sensed data and geographic information systems (GIS) has greatly increased. Nowadays, remote sensing technology is offering one of the quick and effective approaches to the classification and mapping of LU/LC changes over space and time. The satellite remote sensing data with their repetitive nature have proved to be quite useful in mapping LU/LC patterns and changes with time[1-4].

Quantifying the anthropogenic or human activity that governs the LU/LC changes has become a key concept in the town planning process. A major objective of planning analysis is to determine how much space and what kind of facilities a community will need for activities, in order to perform its functions. An inventory of land uses will show the kind and amount of space used by the urban system.

LU/LC study with the use of remote sensing technology is emer-

ging as a new concept and has become a crucial item of basic tasks in order to carry through a series of important works and processes such as the prediction of land use change, prevention and management of natural disaster, and protection of environment, etc. Most importantly, it is of great significance in analyzing the present development and future development scope of the nation. In the recent years, with the enhancement of more advanced remote sensing technology and geo-analysis models, monitoring the status and dynamical change of LU/LC thoroughly by using remotely sensed digital data has become one of the most rapid, credible and effectual methods.

The main aim of this paper is to assess the LU/LC changes, and to observe the growth of various urban classes over a period of seven years in Madurai City by using remote sensing and GIS technology. For this purpose, multi-spectral, multi-temporal Landsat images were downloaded from USGS Earth Resources Observation and Science (EROS) Center[5]. The classification, identification and graphical representation of the changes detected in the classes defined for the study area were performed with the help of ERDAS Imagine 9.1 software and ArcGIS 9.2 software. The paper focuses on the analyses and discussions of the results including the pattern of changes in LU/LC studied from year 1999 to 2006.

2 Study area

The study area is Madurai City, Tamil Nadu (**Figure 1**), one of the famous historical and cultural cities in India. It is located in south central Tamil Nadu, and is the second largest city after Chennai as well as the headquarters of Madurai District. In 2011, the jurisdiction of the Madurai Corporation was expanded from 72 wards to 100 wards covering area 151 km^2 and dividing into four regions Zone I, II, III, and IV. There has been rapid growth in Madurai from 1967 and it keeps developing over the years as well as its surrounding areas. However, most of the areas around Madurai are still least developed and require transforming. It extended geographically from 9°50' North latitude to 10° North latitude and 78°02' East longitude to 78°12' East

longitude, and approximately 100 m above the mean sea level (MSL). The terrain of the city is gradually sloping from the north to south and west to east.

The River Vaigai is the prominent geological feature which bisects the city into North and South zones with the north sloping towards Vaigai River and the south zone sloping away from the river. The city became municipality in 1867 and was upgraded as a corporation in 1971 after 104 years. The corporation limit was extended from 52.18 km^2 to 151 km^2 in 2011. As per 2011 census, the population of the city is 15.35 lakhs[6]. The area has been experiencing remarkable land cover changes due to urban expansion, population pressure and various economic activities in the recent years.
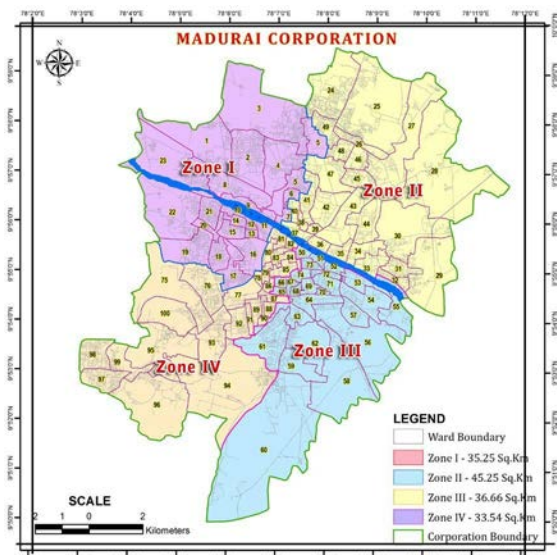
Figure 1. Location of Madurai City[7].

3. Methodology

3.1 Data

For this study, Landsat ETM+ (path 143, row 53) images were used (**Table 1**). Landsat images were downloaded from USGS Earth Resources Observation and Science (EROS) Center[5]. A base map of Madurai City was provided by Local Planning Authority of Madurai. The Landsat ETM+ image data consists of eight spectral bands, with the same spatial resolution as the first five bands of the Landsat TM image. Its 6th and 8th (panchromatic) bands have resolutions of 60 m and 15 m, respectively. All visible and infrared bands (except

the thermal infrared) were included in the analysis. Remote sensing image processing was performed using ERDAS Imagine 9.1 software. Landsat data of 1999 and 2006, as well as SOI Toposheet were selected and used to find the spatial and temporal changes in the study area during the study period.

Table 1. Landsat satellite data used in the study

Sl.No	Data product	Imagery date	Resolution (m)	Path/Row
1	Landsat	04/12/1999	30	(143 - 53)
2	ETM+	21/01/2006	30	(143 - 53)

3.2 Image classification

In this study, there are totally four LU/LC classes, that is, vegetation, built-up land, waste land, and water area. The classes in the images were decided based on the LU/LC classification system devised by National Remote Sensing Agency (NRSA) for Indian conditions[8]. The LU/LC classes are presented in **Table 2**.

Table 2. LU/LC Classification scheme of Madurai

Sl.No	LU/LC Classes
1	Vegetation
2	Built-up land
3	Waste land
4	Water area
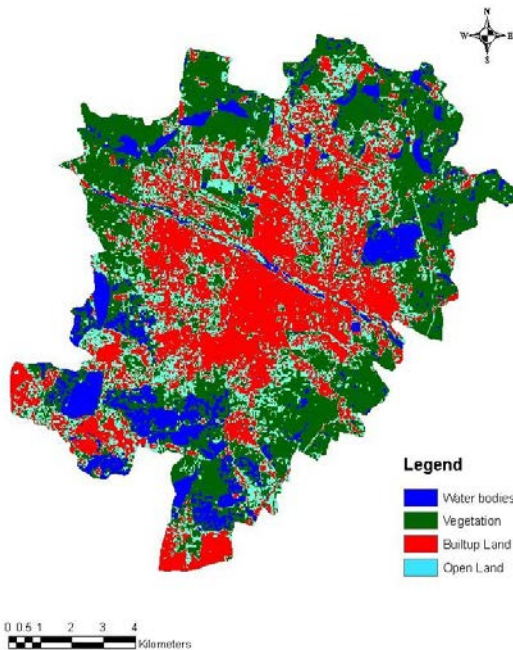
(a)
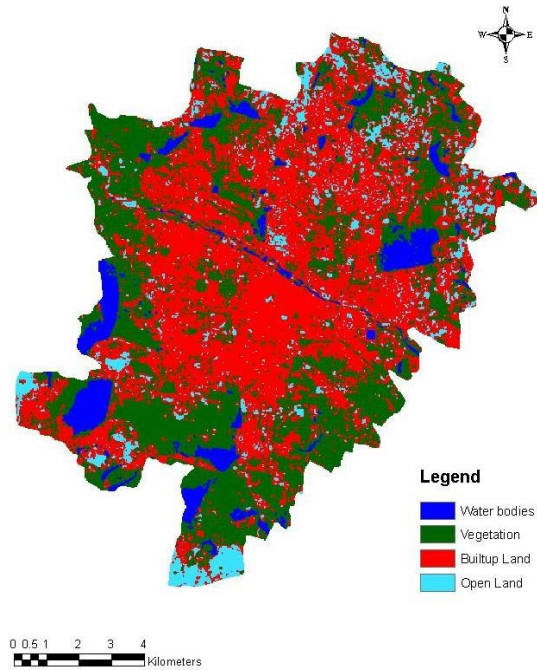
(b)

Figure 2. LU/LC classified images **(a)** 1999; **(b)** 2006**.**

In the study area, a supervised classification of the image was performed using the signature files from the unsupervised classification. For the supervised classification, a maximum likelihood rule was used as a parametric rule[9,10]. The LU/LC classified maps for 1999 and 2006 were produced from Landsat images. See in **Figure 2**.

4. Result and discussion

4.1 LU/LC change analysis

The LU/LC classification results from the year 1999 to 2006 are summarized in **Table 3**.

Table 3. Summary of areas for LU/LC classes from 1999 to 2006

LU/LC Class	Area (ha)	
	1999	2006
Built-up land	4533.57	7020.45
Open Land	2891.79	1170.45
Vegetation	5526.99	5411.79
Water bodies	1602.72	952.38
Total	14555.07	14555.07

From 1999 to 2006, built-up area increased by 17.09%. On the other hand, open land decreased by 11.82% respectively. The fluctuations were observed in vegetation and water area due to seasonal

variation found in the study area. All these land use change are closely related with the development of regional economy and the population growth in the city. The trend of LU/LC and urban change in the city is shown in the **Figure 3**.
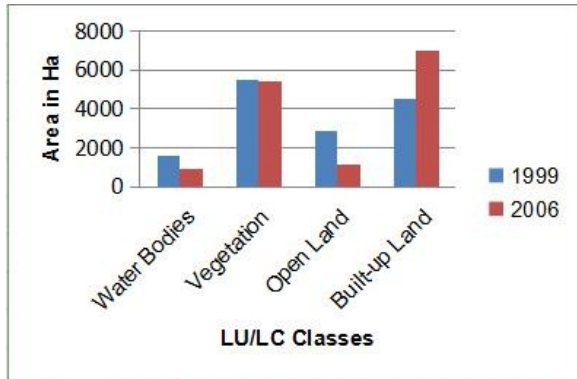
Figure 3. Comparison of LU/LC from 1999 to 2006.

5. Conclusion

This paper aims to investigate LU/LC changes occurred in Madurai City between 1999 and 2006 by using remote sensing and GIS technology. The areas of urban settlements and construction land in Madurai City increased by 17.09% from 1999 to 2006. The results of the study suggest that the analysis of sequential satellite data offers means of extraction of information on LU/LC. In fact, satellite data are very helpful for the detection of LU/LC changes due to repetitive coverage at very short intervals[11]. In this study, analysis has been done for a period of seven years. This work shows that it is feasible to analyze and monitor LU/LC change based on remote sensing images and GIS applications. The results would be of great help for the land management department to make quick quick decision in future land use planning.

Conflict of interest

The authors declare that they have no conflict of interest.

References

1. Palaniyandi M, Nagarathinam V. Land use/land cover mapping and change detection using space borne data. Journal of the Indian Society of Remote Sensing 1997; 25(1): 27–33.
2. Rahman R, Saha SK. Multi-resolution segmentation for object-based classification and accuracy assessment of land use/land cover classification using remotely sensed data. Journal of the Indian Society of Remote Sensing 2008; 36(2): 189–201.
3. Roy PS, Giriraj A. Land use and land cover analysis in Indian context. Journal of Applied Science 2008; 8(8): 1346–1353.
4. Sarma VVLN, Gurram MK, Malini BH, *et al.* Land use/land cover change detection through remote sensing and its climatic implications in the Godavari Delta Region. Journal of the Indian Society of Remote Sensing 2001; 29(1): 85–91.
5. Landsat images of Madurai City from 1999 to 2006 [Internet]. Sunrise Valley, Virgina: Earth Resources Observation and Science (EROS) Center, United States Geological Survey. Available from: https://www.usgs.gov/centers/eros
6. Ministry of Electronics & Information Technology, Government of India [Internet]. New Delhi: National Informatics Centre (NIC); 2010. Available from: http://www.madurai.tn.nic.in/distprof.htm.
7. Tamil Nadu State Centre [Internet]. New Delhi: National Informatics Centre (NIC). Available from: https://www.nic.in/state-office/.
8. Reddy MA. Text book of remote sensing and geographical information systems. Hyderabad: BS Publications; 2002. p. 450.
9. Coskun G H, Alganci U, Usta G. Analysis of land use change and urbanization in the Kucukcekmece Water Basin (Istanbul, Turkey) with temporal satellite data using remote sensing and GIS. Sensors 2008; 8(11): 7213–7223.
10. Lillesand TM, Kiefer RW, Chipman JW. Remote sensing and image interpretation. New York: John Wiley; 2003. p. 706.
11. Verbyla DL. Satellite remote sensing of natural resources. New York: Lewis Publishers; 2005. p. 198.

ORIGINAL RESEARCH ARTICLE

Genesis of Langrial Iron Ore of Hazara area, Khyber Pakhtunkhwa, Pakistan

Naghmah Haider[1*], Sajjad Khan[1], Rehanul Haq Siddiqui[2], Shahid Iqbal[3], Nazar-Ul-Haq[1]

[1]Geoscience Advance Research Laboratories, Geological Survey of Pakistan, P.O Box No. 1461, Shahzad Town, Islamabad 45600, Pakistan. E-mail: naghma.haider@gmail.com

[2]Balochistan University of Information Technology, Engineering and Management Sciences, Quetta 87300, Pakistan.

[3]Department of Earth Sciences, Quaid e Azam University, Islamabad 45600, Pakistan.

ABSTRACT

In this paper, a detailed mineralogical and genesis investigation have been carried out in the seven locations of the Iron Ore in Hazara area. Thick bedded iron ore have been observed between Kawagarh Formation and Hangu Formation i.e, Cretaceous-Paleocene boundary. At the base of Hangu Formation, variable thickness of these lateritic beds spread throughout the Hazara and Kohat-Potwar plateau. This hematite ore exists in the form of unconformity. X-ray diffraction technique (XRD), X-ray fluorescence spectrometry (XRF), detailed petroghraphic study and scanning electron microscope (SEM) techniques indicated that those iron bears minerals including hematite, chamosite and quartz, albite, clinochlore, illite-montmorillonite, kaolinite, calcite, dolomite, whereas ankerite are the impurities present in these beds. The X-ray fluorescence (XRF) results show that the total Fe_2O_3 ranges from 39 to 56%, with high silica and alumina ratio of less than one. Beneficiation requires for significant increase in ore grade. The petroghraphic study revealed the presence of ooids fragments as nuclei of other ooids with limited clastic supply, which indicate high energy shallow marine depositional setting under warm and humid climate. The overall results show that Langrial Iron Ore is a low-grade iron ore which can be upgraded up to 62% by applying modern mining techniques so as to fulfill steel requirements of the country.

Keywords: Langrial Iron Ore; Cretaceous-Paleocene Boundary; Geochemistry; Hazara Area; Hangu Formation

1. Introduction

Iron ore plays a significant role in the development of modern society, which can be used to extract iron, steel and manufacture other alloys. Iron usually occurs in a number of geological environments from deep seated basic igneous intrusion to late stage hydrothermal igneous and metamorphic and sedimentary environment[1]. Iron occurs in banded sedimentary rocks of Precambrian age as residual or replacement deposits. Iron also occurs as oolitic ironstone in Paleozoic to Cretaceous sedimentary successions of the world. The reported massive iron ores in Precambrian igneous rocks of Kirana Hills are magnetite and hematite[2]. Pyrometasomatic deposits formed due to replacement of limestone or volcanic rocks by magnetite.

Occurrences of iron ores are widespread in Pakistan. Mainly these are along unconformities, volcanogenic ores or contact metasomatic deposits. Iron ores have been reported from Indus platform zone, Foreland sedimentary belt, Himalayan crystalline belt, Ophiolitic thrust belt and Chagai magmatic arc[1]. Massive iron ore of Precam-brian

age from Kirana Hills near Sargodha consist of magnetite and hematite[2,3].

In Himalayas Foreland Fold and Thrust Belt (HFFTB) of Pakistan, ironstones of oolitic textures are mainly reported in Mesozoic to early Tertiary formations[2,4-6].

The main objective of the study is to explain the texture, mineralogy and depositional environment of the Langrial iron ore in Hazara-Abbottabad area.

2. Geological and tectonic framework

The Hazara area forms the western limb of the Hazara Kashmir Syntax (HKS) and appears as a crescent shape in the northwestern margin of the Indo-Pakistani subcontinent with a North-East to South-East trending. The crescent shaped Hazara area is bounded by Panjal Thrust and the Main Boundary Thrust (MBT) and number of local thrust faults that lie in a similar NE-SW trend (**Figure 1**).

The oldest rock unit of the area is Precambrian Hazara Formation represented by Hazara Group Slates and sedimentary rocks[7]. Hazara Formation is unconformably overlain by Abbottabad Formation of Cambrian age composed of quartzose sandstone, shale, siltstone, limestone and dolomite[8]. Overlain Mesozoic sedimentary rocks are represented by Samana Suk Formation of Jurrasic age and Cretaceous Lumshiwal and Kawagarh Formation[8,9].

The Paleocene Lockhart Formation is lying above the ironstone beds and Cretaceous Kawagarh Formation (**Table 1**) is lying below the Ironstone beds[8,10,11]. The Hangu Formation is overlain by the Lockhart Limestone[8,10,11]. Iron beds also exist at places in the cores of both limbs of anticlines of Paleocene Lockhart Limestone.
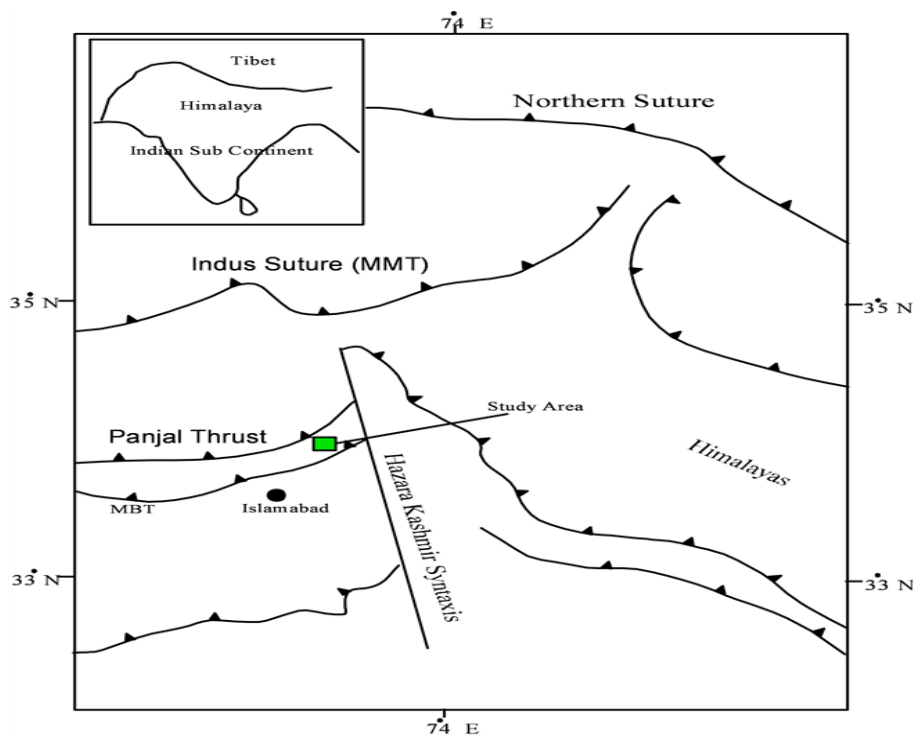
Figure 1. Tectonic sketch map of northern Pakistan[12].

Table 1. Lithostratigraphic unit of the Hazara-Abbottabad area[8]

Age	Formation	Description
Paleocene	Lockhart Limestone	Limestone dark grey to black in colour and containsintercalations of marl and shale.
Paleocene to Cretaceous	Oolitic Iron beds	Ooloitic hematite mixed with chamosite, limonite.
Upper Certaceous	Kawagarh Formation	Grey, olive grey, light grey sub-lithgraphic limestonewith subordinate with marl and calcareous shale.
Upper Certaceous	Lumshiwal Formation	Thick bedded to massive, light grey current bedded sandstone with silty, sandy, gluconitic shale towards the base.
Pre-Cambrian	Hazara Formation	Slate, phyllite and shale with minute occurrences oflimestone and graphite layers.

3. Materials and methods

During reconnaissance survey, seven stratigraphic sections, namely, Bagnotar, Bagan, Durban and Langrial, Danna Noral, Tati Maira, Najaf Pur and Jabri were selected for a detailed study. The study area spreads for about 32 kilometers to the south of Abbotabad. Sedimentary features and orientation and thickness of iron ore beds were examined and 65 samples were collected marked by Global Positioning System (GPS) for subsequent laboratory analysis (**Figure 2**). Bagnotar (Siri) area is located between 34°56'10" N and 73°20' E.
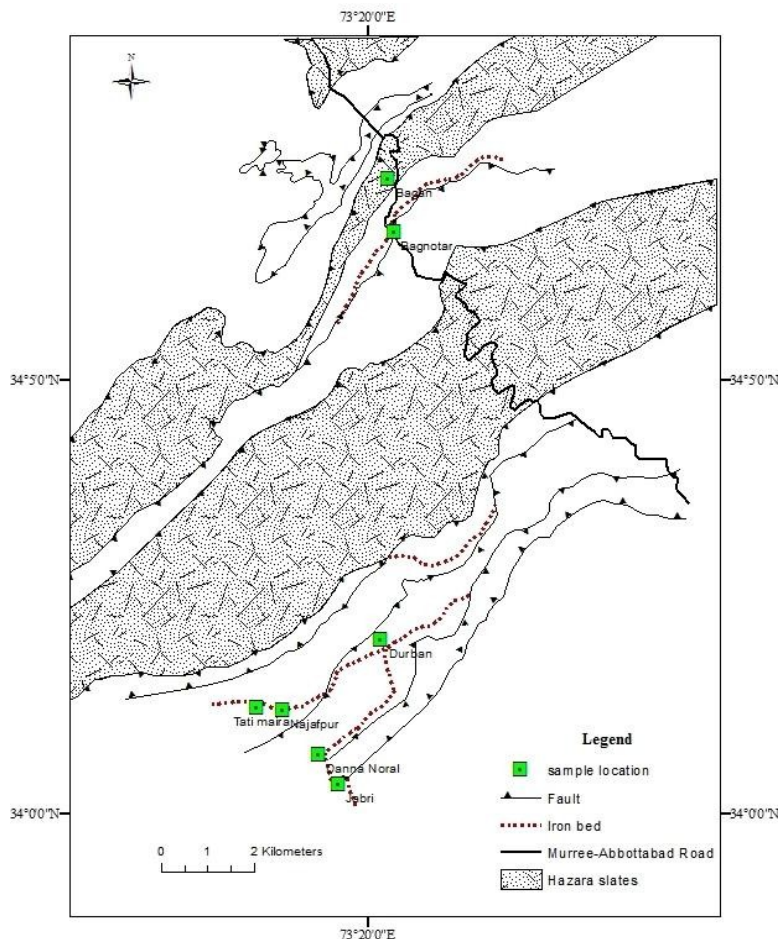
Figure 2. Location map showing geology of the study area.

The strike of the bed is N10° E with a dip varying from 32° SW to 35° SE. Iron bed of 1.5m to 2m have been reported. Iron beds exhibit oolitic to pisolitic hematitic to goethitic appearances, overlain and underlain by Lockhart Limestone due to tectonic disturbance in the area.

Bagan lies between 34°58' N and 73°20'01" E. The strike of the bed is N60° W with a dip of 20° to 45° NE. The thrusted contact between the iron ore and Lockhart formation is observed.

At Durban and Langrial area, the samples have been collected at 34°15' N and 72°17'01" E. The strike of the bed is N35° E and dip is 40° SE. Highly fractured thin to medium bedded iron ore of 2 meter thickness are noted.

Jabri area lies between 34°03'01" N and 73°17'

01" E. The strike of the bed is N60°E and dip is 30° SE. Thin to medium bedded laterite have been reported in this area.

Danna Noral is located between 34°08' N and 72°21' E. The strike and dip of the bed are N60°E, 25° SE respectively. Upper part of iron ore is Kawagarh formation with strike N45°E and 10° SW dip. The thickness of unconformity (i.e., conglomeratic beds) varies from 0.15m to 0.6m at different localities. Upper contact of iron beds is unconformable with Kawagarh formation marked by ferruginous conglomerates whereas the lower contact is sharp with greenish grey to brown flaky shale, the deposit form a synclinal structure.

Tati Maira is located between 34°06' N and 73° 19'01" E with a N30° E strike and a 25 ° NW dip

where presents lateritic beds. Najaf Pur area lies between 34°11'04" N and longitude 72°15'01" E with N60° W beds strike and dip 55° SW. The Upper part of the Iron Ore consists of nodular limestone of Lockhart Formation. At Sardhana village near Najafpur, the iron beds show anticline and syncline structure.

3.1 Petrographic techniques

Thin sections and polished slabs of selected samples are prepared at sample preparation section of the Geoscience Advance Research Laboratory, Geological Survey of Pakistan, Islamabad for the Petrographic study under camera fitted Nikon made reflected light polarizing microscope at different magnifications.

3.2 X-ray diffraction analysis

The selected samples were crushed at the crushing and powdering section of Geoscience Advance Research Laboratory of the Geological Survey of Pakistan, Islamabad. The analysis was carried out by Panalytical X'PertPRO Diffractometer (XRD) at 45 Kv and 40 mA with CuK α radiations scanning speed at 0.05°/Sec scanned by X'Pert data collector software and identified with the help of its matching peaks with the existing data base (**Figure 3**).
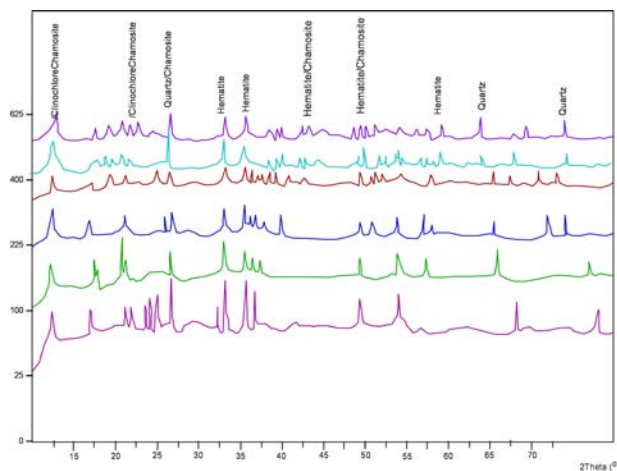
Figure 3. XRD pattern of selected powder samples, where dominant peaks are labeled.

3.3 Scanning electron microscope analysis

Thin section of selected samples was analyzed using scanning electron microscope (Model JEOL JSM 6610LV) to study microscopic structures (**Figure 4**). Compositional analyses were carried out

using EDS (OXFORD X-MAX 20mm^2). Carbon coating is well applied to the thin section to avoid charging of the particles during observation.
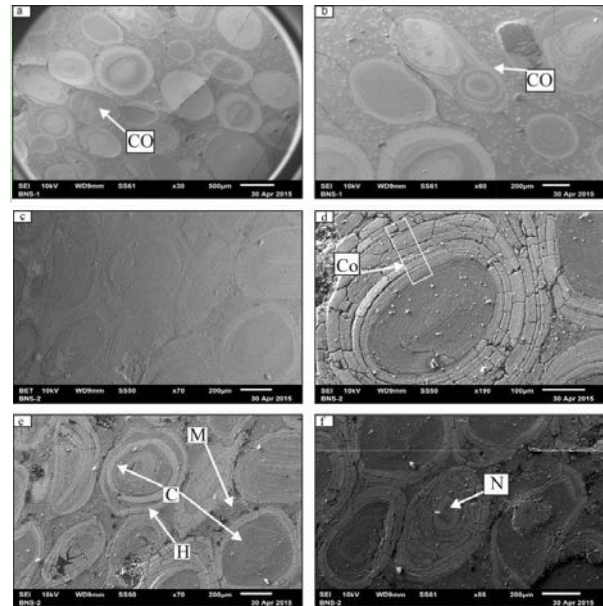
Figure 4. Scanning electron microscopic (SEM) images of the iron ore thin section. **a, c, e)** concentric and elliptical ooids; **b)** composite ooid; **d, f)** concentric lamination in cortex of the ooids. (**Note:** CO is composite ooids; Co is cortex; C is Chamosite; H is hematite; M is matrix and N is nucleus.)

3.4 X-ray fluorescence spectrometry

The chemistry of selected samples were analyzed by using Panalytical Axios WD-XRF for all major element using fundamental parameter method with the help of glass bead by taking 1:10 ratio of volatile free sample and lithium tetra borate.

4. Results and discussion

Petrographic and Mineralogical study by XRD indicates the most prominent iron minerals are hematite and chamosite (**Figure 5**). After interpretation of mineral on XRD with the help of its crystal system and d-spacing values, other minerals are quartz, albite, chamosite, clinochlore, illite-montmorillonite, kaolinite, calcite, dolomite and ankerite (**Figure 3**).

XRD study has direct influence on the commercial value of the ore and processing of the ore regarding carbon footprint and coal consumption. The study of the gangue minerals is necessary for taking steps for beneficiation of ores. According to results of X-ray diffraction analysis, it can be safely suggested that all ore samples from studied area were observed to be mainly of a hematitic nature.

Certain localites like Danna Noral and Najafpur shows hematite ores with iron content (40-50% Fe), such hematite deposits require little beneficiation.
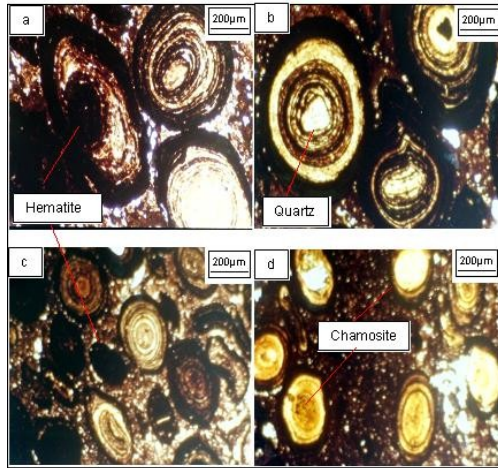
Figure 5. Photomicrographs of selected samples collected from the study area showing **a)** concentric ooids with hematite and chamosite rich concentric lamination. **a & d)** Elongated ooids due to early compaction. **b)** Nucleus of oolites consists of quartz, feldspars, hematite and rock fragments. **c & d)** ooids consist of pure hematite whereas others are comprised of entirely chamosite.

The geochemical analysis shows high silica content in the iron ore from Bagnotar area as compared to Danna Noral and Najafpur (**Tables 2** and **3**; **Figure 6**). SiO_2 ranges between 9-35% here, it is necessary to mention that three samples BNS-4, 9 and 10 belongs to Lockhart Limestone having low SiO_2 and Al_2O_3 varies between 10-18%. Beneficiation requires for reducing high alumina content. Crushing, scrubbing and washing of iron ores techniques are being adopted to reduce alumina in some extent[13].

The total Fe_2O_3 ranges from 37.2 to 72.74%. Average iron (Fe) concentration in samples from Bagnotar area is 37.89%. The trace constituents are calcium, magnesium, sodium, potassium, manganese, and phosphorus oxides. These are low-grade iron ore which can be upgraded up to 62% by applying modern mining techniques[14].

Table 2. Chemical composition of samples collected from Bagnotar area

	BNS-1	BNS-2	BNS-3	BNS-5	BNS-6	BNS-7	BNS-4	BNS-9	BNS-10
SiO_2	20.24	17.32	18.52	28.04	27.46	23.3	14.53	6.20	0.00
TiO_2	0.7	0.45	0.42	0.63	0.79	0.58	0.14	0.348	0.065
Al_2O_3	12.44	10.53	10.46	10.98	17.63	11.88	0.56	2.04	1.18
Fe_2O_3	48.25	54.21	56.31	45.06	39.45	45.24	2.81	4.40	3.68
MnO	0.04	0.1	0.08	0.13	0.03	0.03	0.26	0.04	0.189
MgO	2.58	2.31	2.28	2.27	2.0	2.01	7.42	7.77	0.62
CaO	4.12	3.06	2.62	3.07	2.98	2.96	37.3	42.13	52.5
Na_2O	0.23	0.77	0.39	0.31	0.13	0.41	0.25	0.00	0.08
K_2O	0.09	0.1	0.14	0.17	0.21	0.07	0.18	0.86	0.26
P_2O_5	1.34	1.41	1.41	1.17	0.7	1.10	0.03	0.009	0.124
SO_3	-	-	-	-	0.08	-	-	0.90	0.025
LOI	9.88	9.27	7.36	8.17	9.28	12.43	36.53	35.00	41.30
Fe	33.73	37.89	39.36	31.50	27.58	31.62	1.96	3.08	2.57
Al/Si	0.61	0.60	0.56	0.39	0.64	0.51	-	-	-

Table 3. Chemical composition of samples collected from Danna Noral, Najafpur Jabri and Tatimaira areas

	DN-29	DN-30	DN-31	NF-62	NF-63	NF-64	JB-26	JB-27	TM-33	TM-34
SiO_2	12.51	12.61	9.75	21.04	11.37	13.54	18.72	19.49	35.38	30.76
TiO_2	0.84	0.68	0.27	0.84	0.52	0.55	0.60	0.57	0.54	0.51
Al_2O_3	9.70	10.30	7.62	18.84	8.47	10.79	7.31	12.71	10.02	10.53
Fe_2O_3	63.93	59.13	72.74	37.20	69.73	57.75	52.94	50.58	38.82	46.59
MnO	0.02	0.02	0.01	0.04	0.53	0.05	0.01	0.30	0.16	0.09
MgO	1.55	1.50	1.19	4.79	2.65	3.20	1.78	3.47	1.31	1.29
CaO	2.29	5.80	1.32	1.26	3.34	3.54	1.05	1.09	1.79	2.20
Na_2O	0.48	0.25	0.38	2.11	0.00	0.18	1.94	0.0	2.12	0.0
K_2O	0.02	0.02	0.03	-	0.01	-	0.04	-	0.02	0.02
P_2O_5	1.53	1.37	0.78	0.24	0.55	2.41	0.15	0.30	1.08	1.38
LOI	7.15	8.32	5.91	13.65	8.64	7.99	15.96	13.22	8.78	9.33
Fe	44.69	41.33	50.85	26.00	48.74	40.37	37.01	35.36	27.14	32.57
Al/Si	0.77	0.82	0.78	0.89	0.74	0.79	0.39	0.65	0.28	0.34
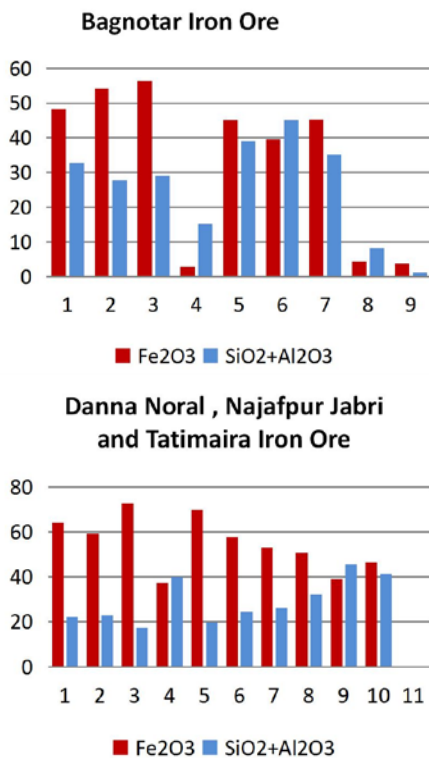
Figure 6. Iron, aluminum and silica ratios of selected samples collected from northern part, Bagnotar area and southern part including Danna Noral, Najafpur Jabri and Tati Maira areas.

Samples from Danna Noral (41-50% Fe) contain high iron content as compare to the Najafpur (26-48% Fe), Jabri (35-37% Fe) and Tati Maira (27-32% Fe). Concentration of SiO_2 and Al_2O_3 are also low as compared to Bagnotar area. The beneficiation should require gravity separation as well as magnetic separation in Langrial Iron ore deposits.

The adverse effects of high alumina to silica ratio (ideally it should be < 1) is harmful to blast furnace as well as sinter plant[13]. Aluminum silica ratio in our samples is less than 1, which is good for beneficiation (**Table 2** and **3**), while alumina raises the melting point of slag and increases fuel consumption in the furnace.

Microscopic mineralogical studies indicated that hematite is the major iron oxide mineral with quartz and chamosite. XRD studies revealed hematite as the major minerals with subordinate amounts of quartz, albite, chamosite, clinochlore, illite-montmorillonite, kaolinite, calcite, dolomite and Ankerite confirming the microscopic findings.

These oolites consist of concentric layers of the iron and iron rich clays chamosite, so these deposits contain an iron oxide hematite with iron clay (chamosite). The photo micrographs show that the

ratio between hematite and chamosite varies. Thus, some ooids consist of almost pure hematite (**Figure 5c**) whereas others are comprised of almost entirely chamosite (**Figure 5d**). The nucleus of the ooids are variable and consist of quartz, as well as feldspars, iron oxides, broken pieces of older ooids and other rock fragments (**Figure 5b**). These compositional variation are also noted through back scattered image of scanning electron microscope (**Figure 4**).

The presence of ooids fragments as nuclei of other ooids indicates that the formations of ooids are the product of a high energy shallow marine environment with limited clastic sediment supply.

5. Depositional settings

The hematite-chamositic composition of the deposits indicates intense chemical weathering under humid continental conditions[15]. Such conditions are usually common in humid equatorial settings[16]. Paleo-geographic reconstruction studies indicate that the area occupied an equatorial position during the deposition of the Langrial iron ore[10]. Ooids are generally considered to be the product of high energy shallow water and agitated environment. Such oolitic texture is the characteristic of the Phanerozoic iron deposits[17]. These ooids consist of concentric rings of iron bearing minerals and are formed by chemical process in sedimentary rocks[18]. The presence of oolitic ironstones usually shows high relative sealevel, warm and humid climate as well as favored chemical weathering[10,19,20]. In the study area, the iron ores occur in the lower part of the Palaeocene Hangu Formation. In the Salt and Surghar ranges, this lower part of the Hangu Formation is interpreted to have been deposited in terrestrial conditions, while the upper part of the formation indicates transitional settings with the overlying marine Lockhart Limestone[21]. On the contrary, recent studies have interpreted shallow marine and deltaic environment of deposition for the lower part of the Hangu Formation[16]. The present study reports abundance bioturbation and biogenic activity. Further, abundance of burrowing in the sandstone of the Hangu Formation, to go with the presence of marine fossils in the formation indicates marine deposition[22,23]. However, brackish water pollens of the palm genus Spinizonocolpites

are reported from the lower part in these areas[16]. Strong influence of subaerial exposure and lateritic palaeosol development is indicated for the Langrial iron ore[16]. A rise in relative groundwater base level may have triggered swampy/boggy land formation to spread over lateritic paleosol deposits that formed on weathered paleo-surfaces of the Cretaceous/older strata[16]. In addition, tectonic controls probably combined with eustatic and climatic controls, influenced the development of the laterites in the area[24].

The tropical, humid climatic conditions coupled with intense chemical weathering produced the initial Fe-rich material, probably as amorphous hydroxides or goethite during the lateritization processes. Marine transgression along the continental margin favored the preservation of these sediments[10]. The high PCO_2, probably associated with the Deccan Trap basalts[25] may have created a stratified ocean with reducing conditions and negative Eh. Such conditions favor Siderite ($FeCO_3$) precipitation, a phenomena also identified in modern oolitic ironstone samples, precipitating at negative Eh, (under reducing conditions) and low sulfide activity (PS2-) in sediment pore-waters[18,26,27]. However, since there are abundant dissolved sulfates dissolved in marine water, thus low sulfide activity is rarely attained in marine sediments. Further, the Deccan trap activity may also have contributed to additional amount of sulfur in the atmosphere. Hence the initial form of the iron oolite sediment appeared to have been accumulated under non-marine or brackish conditions[10].

Further, the bacterial decomposition of the organic matter, following the Cretaceous/Palaeogene mass extinction event may have created/added to the anoxic conditions that accommodate siderite precipitation[28]. The diagenetic processes, following the formation and consolidation of the initial ooids, may have then converted these into hematite-chamosite ooids[29]. The episodic basaltic volcanic activity of the Deccan Trap may have created a fluctuating oxic to anoxic conditions[28] that were favorable for the formation of chamosite (($Mg,Fe)_3$ $Fe_3(Si_3Al)O_{10}(OH)_8$), without sulfide activity as the sulfur rich aerosols settle quickly from the atmosphere[18,30]. These conditions also provided the op-portunity for the hematite precipitation as the latter is stable under moderate to strong oxidizing conditions[18,26]. These fluctuating environmental conditions must have had a strong control on the depositional and early diagenetic history of the Langrial Iron Ore.
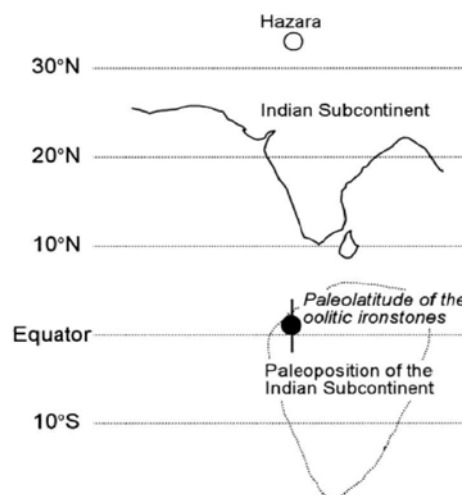
Figure 7. Fluctuating environmental conditions of Hazara area.

6. Conclusion

Langrial Iron Ore occurs in the basal part of Hangu Formation of Paleocene age mainly of hematitic nature with gangue minerals. The deposits are low grade Iron ore mostly consisting of hematite and chamosite in nature with an average Fe_2O_3 content of 52.37%. The mineralogical and petrological interpretation indicated that the deposit was formed under warm humid climate. This low grade iron ore has silica aluminum ratio of less than 1, which is good for beneficiation. Langrial Iron Ore has economic significance proved by combined petroghraphical, geochemical and mineralogical data and the value can be further increased by the application of modern metallurgical processing technologies. The oolitic layers vary in numbers and will lead to a high difficulty to separate iron from gangue minerals in the oolitic structure. It is necessary to carry out a very fine grinding to achieve the mineral separation. These deposits show potential to be economically viable in the present market.

Conflict of interest

The authors declare that they have no conflict of interest.

Acknowledgments

References

1. Kazmi AH, Abbas SG. Metallogeny and mineral deposits of Pakistan. Islamabad: Orient Petroleum Inc.; 2001. p. 88–150.
2. Maynard JB. Geochemistry of sedimentary ore deposits. New York: Springer-Verlag; 1983. p. 305.
3. Maynard JB. Geochemistry of sedimentary ore deposits. Springer Science & Business Media; 2012.
4. Ahmad Z. Directory of mineral deposits of Pakistan. Geological Survey of Pakistan (Karachi) 1969; 15: 1–220.
5. Hallam A, Maynard JB. The iron ores and associated sediments of the Chichali Formation (Oxfordian to Valanginian) of the Trans-Indus Salt Range, Pakistan. Journal of the Geological Society 1987; 144(1): 107–114.
6. Garzanti E. Himalayan ironstones, "superplumes", and the breakup of Gondwana. Geology 1993; 21(2): 105–108.
7. Middlemiss CS. The geology of Hazara and the Black mountain. Geological Survey of India, Memoirs 1896; 26: 302.
8. Shah SMI. Stratigraphy of Pakistan. Memoir of the Geological Survey of Pakistan 2009; 22: 121–132.
9. Kazmi AH, Abbasi IA. Stratigraphy & historical geology of Pakistan. Peshawar: Peshawar Publication; 2008. p. 245–263.
10. Yoshida M, Khan IH, Ahmad MN. Remanent magnetization of oolitic ironstone beds, Hazara area, Lesser Himalayan thrust zone, Northern Pakistan: Its acquisition, timing, and paleoenvironmental implications. Earth Planets Space 1998; 50: 733–744.
11. Fatmi AN. Lithostratigraphic units of the Kohat-Potwar Province, Indus Basin, Pakistan. Memoirs of the Geological Survey of Pakistan 1974; 10: 1–80.
12. Kazmi AH, Jan MQ. Geology and tectonics of Pakistan. Nazimabad: Graphic publishers; 1997. p. 77–121.
13. Rao DS, Kumar VTV, Rao SS, et al. Mineralogy and geochemistry of a low grade iron ore sample from Bellary-Hospet Sector, India and their implications on beneficiation deposits. Journal of Minerals and Materials Characterization and Engineering 2009; 8(2): 115–132.
14. Muwanguzi AJB, Karasev AV, Byaruhanga JK, et al. Characterization of chemical composition and microstructure of natural iron ore from Muko deposits. ISRN Materials Science 2012; 2012: 1–9.
15. Boggs S Jr. Petrology of sedimentary rocks. 2nd ed. Cambridge, England, Hardback: Cambridge University Press; 2009. p. 600.
16. Warwick PD, Javed S, Mashhadi STA, et al. Lithofacies and palynostratigraphy of some Cretaceous and Paleocene rocks, Surghar and Salt Range coal fields, northern Pakistan. Washington, DC: U.S. Government Publishing Office; 1995. p. 1–35.
17. Young TP. Phanerozoic ironstones: An introduction and review. Geological Society, London, Special Publications 1989; 46(1): ix-xxv.
18. Tucker ME. Sedimentary Petrology. 2nd ed. Oxford: Blackwell Science; 1991. p. 260.
19. Gilbert JM, Park CF Jr. The geology of ore deposits. New York: Waveland Press; 1986. p. 985.
20. Blatt H, Middleton G, Murray R. Origin of sedimentary rocks. 2nd ed. Englewood Cliffs: Prentice-Hall Inc.; 1980. p. 782.
21. Danilchik W, Shah SMI. Stratigraphy and coal resources of the Makarwal area, Trans-Indus Mountains, Mianwali District, Pakistan. United States Geological Survey, Professional Paper; (USA) 1987; 75 (1341): 38.
22. Davies LM, Pinfold ES. Eocene beds of the Punjab Salt Range. Memoirs of the Geological Survey of India 1935; 24(1): 79.
23. Haque AFMM. The foraminifera of the Ranikot and Laki of Nammal Gorge, Salt Range. Memoirs of the Geological Survey of Pakistan, Paleontologia Pakistanica 1956; 1: 1–300.
24. Shah SHA. Stratigraphic observations of laterites in Pakistan and oscillation and movement of the Eurasian and Indian blocks. Geological Bulletin of the University of Peshawar 1984; 17: 101–108.
25. Schoene B, Samperton KM, Eddy MP, et al. U-Pb geochronology of the Deccan Traps and relation to the end-Cretaceous mass extinction. Science 2015; 347(6218): 182–184.
26. Krauskopf KB, Bird DK. Introduction to geochemistry. New York: McGraw-Hill; 1967. p. 721.
27. Harder H. Mineral genesis in ironstones: A model based upon laboratory experiments and petrographic observation. Geological Society, London, Special Publications 1989; 46: 9–18.
28. Schulte P, Alegret L, Arenillas I, et al. The Chicxulub asteroid impact and mass extinction at the Cretaceous-Paleogene boundary. Science 2010; 327(5970): 1214–1218.
29. Crowe SA, Roberts JA, Weisener CG, et al. Alteration of iron-rich lacustrine sediments by dissimilatory iron-reducing bacteria. Geobiology 2007; 5(1): 63–73.
30. Kimberley MM. Origin of oolitic iron formations. Journal of Sedimentary Research 1979; 49(1): 111–131.

Original Research Article

Particularities of deformation processes solution with GIS application for mining landscape reclamation in East Slovakia

Sedlak Vladimír[1*], Poljakovic Peter[2]

[1] Institute of Geography, Faculty of Science, Pavol Jozef Šafárik University in Košice, Košice 04012, Slovakia. E-mail: vladimir.sedlak@upjs.sk

[2] Security and Defence Department, Armed Forces Academy of General Milan Rastislav Štefánik, Liptovský Mikuláš 03101, Slovakia. E-mail: poljakovic.peter@gmail.com

ABSTRACT

The influence of mining activity on the environment on the environment belongs to the most negative industrial influences. Mine subsidence on the surface can be a result of many deep underground mining activities. The present study offers the theory to the specific case of the deformation vectors solution in a case of disruption of the data homogeneity of the geodetic network structure in the monitoring station during periodical measurements in mine subsidence. The theory was developed for the mine subsidence at the abandoned magnesite mine of Košice-Bankov near the city of Košice in East Slovakia. The outputs from the deformation survey were implemented into geographical information system (GIS) applications to a process of gradual reclamation of whole mining landscape in the magnesite mine vicinity. After completion of the mining operations and liquidation of the mine company, it was necessary to determine the exact edges of the mine subsidence of Košice-Bankov with the zones of residual ground motion in order to implement a comprehensive reclamation of the devastated mining landscape. Requirement of knowledge about stability of the former mine subsidence was necessary for starting the reclamation work. Outputs from the present specific solutions of the deformation vectors confirmed the multi-year stability of the mine subsidence in the area of interest. Some numerical and graphical results from the deformation vectors survey in the abandoned magnesite mine of Košice-Bankov are presented. The obtained results were transformed into GIS for the needs of the municipality of Košice City to the implementation of the reclamation activities in the mining territory of Košice-Bankov.

Keywords: Mine Subsidence; Deformation Vector; Geodetic Network; GIS; Reclamation

1. Introduction

Currently, with the accretive exigencies to protect people's life and property, security has become one of the priority needs and tasks of all countries or their groupings all around the world. In terms of environment protection, since an unspoiled ecosystem is a basic condition for human living, it is necessary to protect people and its property against the negative industrial influences. The influence of mining activity on the environment belongs to the most negative industrial influences. As a result of underground mining of the mineral deposits, there resulted in land subsidence (mine subsidence[1]) in the

---

[1] Mine subsidence means lateral or vertical ground movement caused by a failure initiated at the mine level, of manmade underground mines, including but not limited to coal mines, clay mines, limestone mines, and fluorspar mines that directly damages residences or commercial buildings. Mine subsidence "does not include lateral or vertical ground movement caused by earthquake, landslide, volcanic eruption, soil conditions, soil erosion, soil freezing and thawing, improperly compacted soil, construction defects, roots of trees and shrubs or collapse of storm and sewer drains and rapid transit tunnels[7].

surface, i.e., caving zone (area), which is dangerous for the movement of people in this zone[1-6]. The underground mining of coal and other minerals creates voids which are subject to collapse. The collapse of these voids may occur at any time ranging from immediate (i.e., while the mineral is being extracted) to 100 or more years after mining. If the collapse causes sinking of the ground surface, the settlement is called mine subsidence[4,6]. Then very great danger and threat to people's lives and their property can be caused by sudden unexpected caving fall of the earth surface over the abandoned mining work[5,8,9].

According to the report of the Illinois Department of Natural Resources[10] and many current theoretical and practical knowledge and scientific studies[4,6,7], it is not possible to precisely predict how long the mine subsidence events will be finished. From the present experience, about 60 to 90 % of the total ground movement occurs within the first few weeks or months of an event. The remaining ground movement continues to develop at a continually decreasing rate and may take 3 to 5 years, or longer.

In order to protect the environment, in particular, the protection of human life and property, it is necessary to examine mine subsidence on the surface[6,11]. The most mine subsidence worldwide with their prediction by means of their modelling are examined through the coal fields[12,13].

Character and size of the subsidence on the surface depends mainly on the geotectonic ratios of rock massif above the mined out area. Knowing the extent of the subsidence trough in mining territories is determining how to prevent the entry of persons into these danger zones. Conditioning factors to establish the extent of the movement of the earth surface above the mined out territory are a geodetic way to survey deformation vectors which can be derived from the processing of measurements at monitoring stations based on these mining tangent territories. 3D (three-dimensional) deformation vectors most adequately characterize movements of ground, buildings and other engineering structures above the mined out territory. Deformation modelling is mostly based on periodic monitoring space changes of various engineering structures, buildings

or terrain surfaces by using the surveying classic terrestrial methods, i.e., measuring 3D observation data elements by using classic optic theodolites and leveling instruments in the 40's up-to 80's of the last century or universal electronic measuring instruments — total stations since the 80's of the last century, or by up-to-date progressive surveying satellite navigation technologies and systems, i.e., global positioning system (GPS) and global navigation satellite systems (GNSS) or very seldom and specific surveying technologies such as the surveying technology — interferometric synthetic aperture radar (InSAR) or using other advanced specific terrestrial and aerial and space technologies and techniques[12,14-21]. The deformation vectors are the result of such deformation investigations. The deformation vector with its value gives a global review about the deformation character of the monitored object of interest (earth surface, buildings, engineering structures, etc.) and it also can be used for modelling a future deformation development of such monitored object[4,6,7,15]. Certain specific methods (especially geophysical) for monitoring ground motion must be carried out under controlled large-scale underground work, such as destressing blasting or large-chamber mining in ore and industrial mineral deposits[22,23].

Repeating geodetic measurements in some monitoring stations under deformation investigation of engineering structures, buildings or terrain surfaces can be often complicated in the individual time (periodic) epochs. Monitoring station is presented by a geodetic network with the given structure of the geodetic points on which various geodetic/surveying measurements are realized to determine earth movements or movements of other objects of interest[3]. During the implementation of long-term periodic deformation, measurements can occur in various unpredictable obstacles, for e.g., loss or damage or building-up some established geodetic network points due to construction of new engineering structures and buildings or other construction earth work on the monitoring station zone. It means that the geodetic network with points at a monitoring station has the non-homogenous structure during all periodical geodetic measurements (during deformation survey).

All these or other unpredictable obstacles make it impossible for periodic execution of the original measurement sights realized at the geodetic network of the monitoring station in time of the first (primary or zero) measuring epoch. It means that any periodic measurements cannot be maintained equal conditions for realizing measurement sights. The data homogeneity of whole geodetic network in the monitoring station was disrupted. In these cases, neither a renewal of the destroyed points (reference and object points) at other places and neither substitution of some values in the geodetic network of the monitoring station (which are not measurable in the successive monitoring epochs) by other variables do not make possible to use a standard method in calculation of the deformation vector[4,7,24].

The analysis of time factor of the gradual subsidence development continuing with underground exploitation allows production of more exact model situations in each separate subsidence processes and especially, it provides an upper degree in the prevention of deformations in the surface. Possibility in improving polynomial modelling of the subsidence is conditioned by the knowledge to detect position of so-called "break points", i.e., the points in the surface in which the subsidence border with a zone of breaches and bursts start to develop over the mineral deposit exploitation. It means that the break-points determine a place of the subsidence, where it occurs to the expressive fracture of the continuous surface consistence. 3D deformation vectors locate the places of the break points presenting the subsidence edges[7,11,14,17].

2. Theory to the specific deformation vector solution

The geodetic network structure of a monitoring station can be expressively changed between monitoring epochs (epochs with periodic measurements of the observed geodetic data in the geodetic network) by the above-mentioned changes in an original geodetic network and interference with the geodetic points of such network. The most common and efficient way of geodetic networks processing in geodesy and engineering surveying is the network structures estimate based on Gauss-Markov mo-

del. The statistics formulation of Gauss-Markov model is as follows[20,25-28].

$$v = A(\hat{C} - C^0) - (L_{(0)} - L^0) = Ad\hat{C} - dL \quad (1)$$

$$\Sigma_L = \sigma_0^2 Q_L \quad (2)$$

Where v is the vector of corrections of the measured (observed) values L; A is the configuration (modelling) matrix of the geodetic network or also called Jacobian matrix, i.e., the matrix of partial derivatives of functions $L^0 = f(C^0)$ by the vector C^0; $\hat{C}$ is the vector of the aligned 3D coordinate values; C^0 is the vector of the approximate 3D coordinate values; $L_{(0)}$ is the vector of the approximate observation magnitude values of the observed elements in of the first measuring epoch $t_{(0)}$; L^0 is the vector of the approximate observation magnitude values of the observed elements; $d\hat{C}$ is the deformation vector; dL is the vector of the measured values supplements, Σ_L is the covariance matrix of the measured values; σ_0^2 is a priori variance; Q_L is the cofactor matrix of the cofactor matrix of the observations.

It will also be appeared in the changed structures, let us say in a size of the matrixes and vectors A, Q_L, C^0 and L^0. These matrixes and vectors enter into the presupposed model of the network adjustment following out from Gauss-Markov model[20,24-26].

2.1 Deformation vector

If between monitoring epochs, there are no changes in the geometrical and observational structure of the geodetic network, then the matrixes and vectors A, Q_L, C^0 and L^0 remain identical for each epoch. Only in such case the deformation vector $d\hat{C}$ can be determined by a conventional procedure according to the following model[6,13]:

In the basic (first) monitoring epoch $t_{(0)}$, we have the vector $\hat{C}_{(0)}$ of the adjusted 3D coordinates of the observed points which are obtained according to Gauss-Markov model:

$$\hat{C}_{(0)} = C^0 + (A^T Q_A^{-1} A)^{-1} A^T Q_L^{-1} (L_{(0)} - L^0) = C^0 + G(L_{(0)} - L^0) \quad (3)$$

In other following epochs $t_{(i)}$, we also obtain the vector $\hat{C}_{(i)}$ of the adjusted 3D coordinates of the observed points according to the equation:

$$\hat{C}_{(i)} = C^0 + (A^T Q_L^{-1} A)^{-1} A^T Q_L^{-1} (L_{(i)} - L^0) = C^0 + G(L_{(i)} - L^0) \quad (4)$$

Thus, the deformation vector $d\hat{C}$ will be valid the following equation:

$$d\hat{C} = \hat{C}_{(i)} - \hat{C}_{(0)} = G\left(L_{(i)} - L^0\right) \qquad (5)$$

Where L^0 and $L_{(i)}$ are the vectors of the observed magnitude values in the epochs $t_{(0)}$ and $t_{(i)}$.

Now we presuppose a case in which some changes in the established geodetic network structure of the monitoring station are occurred during the monitoring observation epochs, i.e., the geodetic network structure between the basic epoch $t_{(0)}$ and the epoch $t_{(i)}$ are changed. Then the origin matrixes and vectors A, Q_L, C^0 and L^0 will be transformed into the following equations:

$$\bar{A} = A + dA, \quad \bar{Q}_L = Q_L + dQ_L$$
$$\bar{Q}_L = Q_L + dQ_L, \quad L^0 = L^0 + dL \qquad (6)$$

According to Equations (6), the vectors $\bar{\hat{C}}_{(0)}$ and $\bar{C}_{(i)}$ of the adjusted 3D coordinates of the observed points in the epochs $t_{(0)}$ and $t_{(i)}$ will be determined:

$$\bar{\hat{C}}_{(0)} = \bar{C}^0 + (\bar{A}^T \bar{Q}_L^{-1} \bar{A})^{-1} \bar{A}^T \bar{Q}_L^{-1}\left(L_{(0)} - \bar{L}^0\right) = \bar{C}^0 + \bar{G}\left(L_{(0)} - \bar{L}^0\right) \qquad (7)$$

$$\bar{\hat{C}}_{(0)} = \bar{C}^0 + (\bar{A}^T \bar{Q}_L^{-1} \bar{A})^{-1} \bar{A}^T \bar{Q}_L^{-1}\left(L_{(i)} - \bar{L}^0\right) = \bar{C}^0 + \bar{G}\left(L_{(i)} - \bar{L}^0\right) \qquad (8)$$

and then the deformation vector $d\hat{C}$ is expressed according to Equation (5) in the form:

$$d\bar{\hat{C}} = \bar{\hat{C}}_{(i)} - \bar{\hat{C}}_{(0)} \qquad (9)$$

Which will not express only 3D changes of the geodetic network points between the particular epochs and the deformation vector can be distorted (biased) under the influence of the geodetic network structural changes. Then deformation vector $d\hat{C}$ will not afford the reliable testing information about the concrete deformation consequences.

The presented theory in the cases of some structural changes in the geodetic network can be likely to demonstrate by an analytical way if we compare the deformation vector structures $d\hat{C}$ and $d\bar{\hat{C}}$ expressed according to Equations (5) and (9). Then the structure of the deformation vector $d\bar{\hat{C}}$ is expressed according to Equation (9) and the further equation will be valid:

$$d\bar{\hat{C}} = \left[\bar{C}^0 + \bar{G}\left(L_{(i)} - \bar{L}^0\right)\right] - \left[C^0 + G\left(L_{(0)} - L^0\right)\right] = \bar{G}\left(L_{(i)} - \bar{L}^0\right) - G\left(L_{(0)} - \bar{L}^0\right) + \bar{C}^0 - C^0 \qquad (10)$$

and on the base of Equations (6) and the linearization of $\bar{G}$ into $\bar{G} = G + dG$, the following derivation will be valid for the deformation vector $d\bar{\hat{C}}$:

$$d\bar{\hat{C}} = (G + dG)\left(L_{(i)} - \bar{L}^0\right) - G\left(L_{(0)} - \bar{L}^0\right) + dC^0 = \bar{G}\left[L_{(i)} - (L^0 + dL^0)\right] + \mathrm{dG}\left(L_{(i)} - \bar{L}^0\right) - G\left(L_{(0)} - L^0\right) + dC^0 = G\left(L_{(i)} - L^0\right) + GdL^0 + dG\left(L_{(i)} - L^0\right) - G\left(L_{(0)} - L^0\right) + dC^0 = G\left(L_{(i)} - L^0\right) + GdL^0 + dG\left(L_{(i)} - \bar{L}^0\right) + dC^0 \qquad (11)$$

and finally the deformation vector $d\bar{\hat{C}}$ will be calculated according to the following equation:

$$d\bar{\hat{C}} = \mathrm{d}\hat{C} + \delta \mathrm{d}\hat{C} \qquad (12)$$

Equation (12) declares that the deformation vector $d\bar{\hat{C}}$ (calculated with the changed geodetic network structure) is different from its vector of the correct values $d\hat{C}$ only by the term $\delta \mathrm{d}\hat{C}$ (i.e., the correction component of the deformation vector corrections). In this case, the term $\delta \mathrm{d}\hat{C}$ is not generated by spatial movements of the geodetic network points between the individual epochs of measurements, but it is currently generated by changes in the geometric and observational network structure between the particular epochs due to implementation of changes in its point field and also due to changes in measurements in the epochs.

To prevent this problem (so that any depreciation of the deformation vector $d\bar{\hat{C}}$ is not occurred), which is frequently occurred at the deformation investigation, the following procedures are to be used:

The geodetic network must be carefully projected from the point of view of a maximum and permanent providing its reference points and the line sights between the reference and object points during whole monitoring period, especially.

If some reference points were lost or destroyed, new points should be established in enough proximity of these lost or destroyed reference points as possible. Same principle is held for the object points.

If matrixes A and Q_L are expressively changed between the monitoring epochs $t_{(0)}$ and $t_{(i)}$ (for example, in $t_{(0)}$, the geodetic network was measured by a trilateration measurement way, and in $t_{(i)}$ by traverse measurement, and it is necessary to observe more new magnitudes, etc.), then the deformation vector is determined according the following equations:

$$d\hat{C} = C^0 + (A^T Q_L^{-1} A)_{(i)}^{-1} A_{(i)}^T Q_{L_{(i)}}^{-1}\left(L_{(i)} - L^0\right) - \left[C^0 + (A^T Q_L^{-1} A)_{(0)}^{-1} A_{(0)}^T Q_{L_{(0)}}^{-1}\left(L_{(0)} - L^0\right)\right] \qquad (13)$$

And,

$$d\hat{C} = G_{(i)}L_{(i)} - G_{(0)}L_{(0)} - L^0(G_{(i)} - G_{(0)}) \qquad (14)$$

Because using the identical C^0 and L^0 is not the problem to adhere in the individual epochs. Or the deformation vector corrections $\delta d\hat{C}$ are calculated according to Equations (7), (8) and (10), so that the deformation vector $d\hat{\hat{C}}$ is then corrected according to the introduced Equation (12).

3. Study case example

3.1 Study territory description

The monitoring deformation station of Košice-Bankov covers a territory around the mine field of the magnesite mine in Košice-Bankov. Košice-Bankov is in the northern part of Košice City, where situated the popular city recreational and tourist center of Košice City. This popular urban recreational zone is located in close proximity to the mine field of the magnesite mine of Košice-Bankov (**Figure 1**).

Figure 1. Orthophoto map of Košice City with a detail view of the mine field of Košice- Bankov**.**
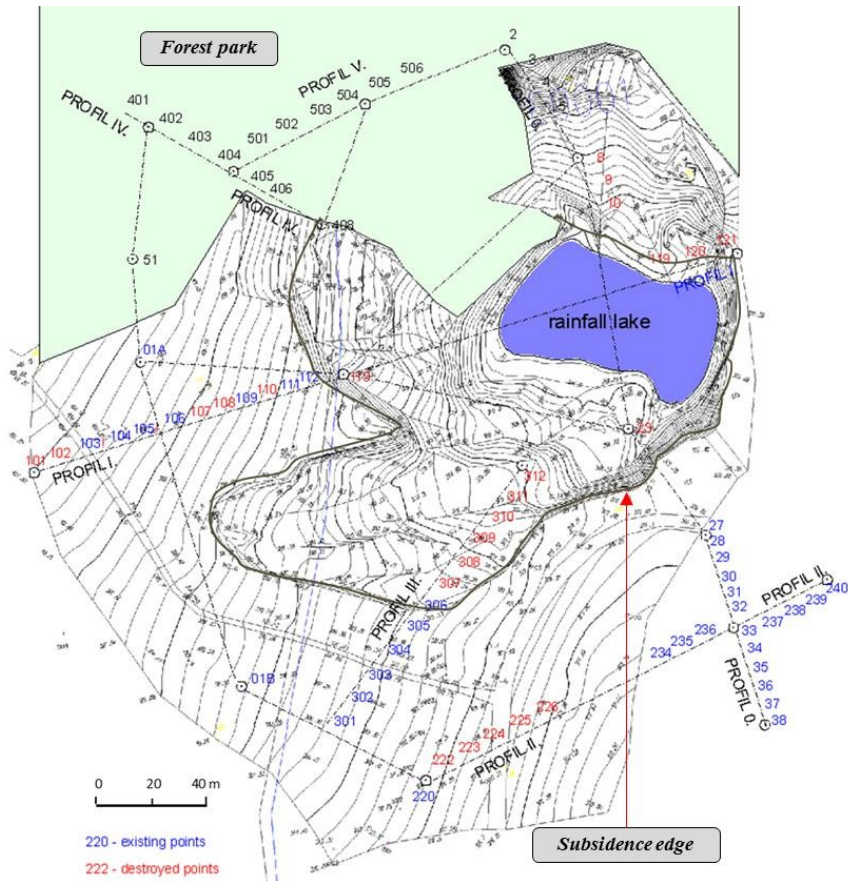

Figure 2. Monitoring station of Košice-Bankov (reference points 01C and 01D – destroyed points)**.**

94

Problems of mine damages on the surface, dependent on the underground mining at the magnesite deposit, did not receive a systematic research attention in Slovakia till 1976. After that, the requirements for a scientific motivation in the subsidence development following out from rising exploitations and from introducing progressive mine technologies were taken into consideration.

The gradual subsidence development at the Košice-Bankov mine region in the east region of Slovakia is monitored by geodetic way from the beginning (in the end of sixties of the 20th century) of the mine underground activities in the magnesite mineral deposit. The monitoring station project in the Košice-Bankov case was designed and deformation measurements were started in the spring of 1976. The first observed data were taken from this monitoring station in the same year and each year the spring and autumn geodetic terrestrial and GPS measurements were realized. The monitoring station is situated in the earth surface in the Košice-Bankov mine region near by the shaft under the name — West Shaft. The monitoring station is constructed from the geodetic network of the reference points (No.: 01A, 01B, 01C, 01D) and objective points (78 points) situated in geodetic network profiles (**Figure 2**). Some of the reference points were destroyed by the subsidence processes.

Figure 3. Mine subsidence of Košice-Bankov; panoramic view: autumn 2001**.**

Figure 4. Mine subsidence of Košice-Bankov; panoramic view: spring 2002**.**

Figure 3 and **Figure 4** present the panoramic views to the subsidence of Košice-Bankov from the south-west edge of this subsidence in 2001 and 2002 when the magnesite mine was abandoned for two up-to three years.

All surveying profiles of the monitoring station of Košice-Bankov are deployed across and along the expected movements in the subsidence (**Figure 2**). 3D data were firstly observed by 3D (positional and leveling measurements) terrestrial geodetic technology (since 1976) by using classic optical geodetic theodolites and leveling devices for very high precision leveling, later total electronic surveying devices and also devices for GPS/GNSS technology (since 1997), i.e., Trimble 3303DR Total Station, GPS: ProMark2 and GNSS: Leica Viva GS08. Periodic monitoring measurements are performed at the monitoring station of Košice-Bankov twice a year (usually in spring and autumn)[13]. In 1981, some points of this monitoring station were destroyed (defective) and again replaced in same year (points No.: 2, 3, 30, 38, 104, 105 and 227 on the profiles No.: 0, I and II), which was caused by some felling work in close forest crop. The destroyed points were replaced by very precision geodetic way according the origin coordinates.

3.2 Accuracy and quality assessment of the geodetic network

1D, 2D and 3D accuracy of the geodetic network points (the monitoring station of Košice-Bankov) in the East Slovak region was appreciated by the global and the local indices. The global indices were used for the accuracy consideration of whole network, and they were numerically expressed. We used the variance global indices: $tr(\sum_{\hat{C}})$, i.e., a track of the covariance matrix $\sum_{\hat{C}}$ and the volume global indices and $det(\sum_{\hat{C}})$, i.e., a determinant.

The local indices were as a matter of fact the point indices, which characterize a reliability of the network points:

1) mean 3D error:

$$\sigma_p = (\sigma_{\hat{X}_i}^2 + \sigma_{\hat{Y}_i}^2 + \sigma_{\hat{Z}_i}^2)^{1/2};$$

2) mean coordinate error:

$$\sigma_p = \left[\frac{1}{3}\left(\sigma_{\hat{X}_i}^2 + \sigma_{\hat{Y}_i}^2 + \sigma_{\hat{Z}_i}^2\right)\right]^{1/2};$$

3) Confidence absolute ellipses or ellipsoids, which were used for a consideration of the real 2D or 3D in the point accuracy. We need to know the ellipsis constructional elements, i.e., semi-major axis a, semi-minor axis b, bearing φ_a of the semi-major axis and ellipsoid flattening f, ($f = 1 - b/a$).

The network quality is mainly characterized by accuracy and reliability. Position accuracy of points can be expressed in addition to numerical and also graphical indicators of the network accuracy, which are the confidence curves and confidence ellipse (confidence ellipsoids in 3D case). Ellipsoids determine a random space, in which the actual location of points will be lie with a probability $1 - a$, where α is the chosen level of significance, according to which the ellipsoids are of different size. In geodetic practice, the standard confidence ellipsoids are used for 3D space. Their design parameters can be derived either from of the cofactor matrix Q_L of the adjusted coordinates, which shall be these design parameters on the main diagonal, or from the coordinate covariance matrix of the coordinate estimations $\sum_{\hat{C}}$ of the determined points, which shall be them on the main diagonal.

All calculated data according to the presented specific theory about the deformation vector estimation in a case of any accepted changes in the geodetic network of the monitoring station are presented in **Tables 1-5**. In general, **Tables 1-5** focused on the accuracy and quality assessment of the geodetic network (**Table 1**: global indices; **Table 2**: mean errors; **Table 3**: absolute confidence ellipse elements; **Table 4**: local indices; **Table 5**: values of deformation vectors[2]).

Table 1. Global indices (spring 1976 / autumn 2014)

Rank	Track	Determinant	Average mean error	Norm
$rk(\sum_{\hat{C}})$ [mm²]	$tr(\sum_{\hat{C}})$ [mm²]	$det(\sum_{\hat{C}}) \, 10^{25}$	$\sigma\hat{C}_{pr}$ [mm]	$Nor(d_{\hat{C}})$ [mm]
14/14	7041.901 / 040.879	2.869 / 2.871	22.428 / 23.051	124.218 / 25.043

Table 2. Mean errors (spring 1976/autumn 2014)

Point	m_x [mm]	m_y [mm]	m_z [mm]
2	15.7 / 17.8	32.9 / 44.6	12.5 / 70.9
3	14.8 / 31.2	27.2 / 59.0	30.5 / 69.8
30	21.1 / 27.7	26.5 / 21.9	45.5 / 31.2
38	16.6 / 21.6	16.3 / 10.3	20.1 / 19.1
104	18.2 / 40.4	34.1 / 68.7	55.4 / 79.9
105	28.2 / 34.9	17.1 / 24.2	9.9 / 20.4
227	20.0 / 19.2	8.5 / 8.5	10.9 / 12.5

Table 3. Absolute confidence ellipse elements (spring 1976 / autumn 2014; α = 0.05)

Point	a_i [mm]	b_i [mm]	φ_{a_i} [gon]	f
2	49.9 / 53.5	5.9 / 8.2	172.303 / 172.684	1.8818 / 1.1008
3	40.8 / 30.4	12.3 / 3.5	172.704 / 179.148	0.6985 / 0.8794
30	43.0 / 42.4	18.2 / 20.1	160.340 / 160.054	0.5767 / 0.7821
38	23.5 / 29.8	21.8 / 23.4	40.966 / 41.122	0.0723 / 0.2523
104	47.5 / 79.7	24.0 / 10.1	211.146 / 217.101	0.4947 / 0.8991
105	42.8 / 45.0	15.3 / 19.3	370.337 / 371.011	0.6425 / 0.5851
227	28.8 / 25.4	8.1 / 9.8	19.634 / 12.226	0.7188 / 0.6673

Table 4. Local indices (spring 1976 / autumn 2014)

Point	Mean 3D error σ_p [mm]	Mean coordinate error σ_{xyz} [mm]
2	36.4 / 39.7	25.7 / 19.2
3	30.9 / 28.7	21.8 / 24.7
30	33.9 / 32.4	23.9 / 23.5
38	23.3 / 27.2	16.5 / 12.9
104	38.6 / 17.2	27.3 / 55.4
105	32.9 / 26.2	23.3 / 21.5
227	21.7 / 23.7	15.3 / 19.1

Table 5. Deformation vector values (spring 2007[3] / autumn 2014)

$d\widehat{C}$ [mm]	Point						
	2	3	30	38	104	105	227
	2.4 / 3.1	-2.9 / -2.8	-8.0 / -9.8	6.7 / 6.9	-4.0 / -5.7	0.6 / 1.4	9.7 / 10.5

Tables 1-5 comprehend the adjusted mean errors of the individual coordinates, global and local 3D indices and their absolute confidence ellipsoid elements determining 3D accuracy of some chosen replaced points. The numbers in front of the back slash belong to year 1976 when geodetic measurements were started. The numbers after the back slash belong to the autumn of 2014[4] when all geodetic measurements were finished. In 2007, the points No.: 2, 3, 30, 38, 104, 105 and 227

---

[2] The values of the deformation vectors from the last geodetic measurement (autumn 2014) are compared to the deformation vectors from measurements in 2007 (spring 2017). In 2007, the theory of a specific deformation vector solution presented in the article was verified for the first time in the Košice-Bankov mine subsidence.

[3] 2007 — the year of verification of the theory of the presented specific solution of the deformation vector in the Košice-Bankov mine subsidence.

[4] Deformation survey on the monitoring station of Košice-Bankov without the reclamation work intervention was finished in the autumn of 2014.

were re-stabilized due to small earth construction work needed to the preparation work for a future reclamation of the mining territory of Košice-Bankov. The deformation vector values confirm possibility in the deformation vectors valuation according to the presented theory[20]. However, the deformation vector values need not mean any displacement of the points. Despite the fact that the points of the geodetic network were adjusted in a common way according to the Gauss-Mark model, the deformation vector values can be loaded by accumulating measurement errors. Therefore, for their prominence testing, it is required to carry out testing of the deformation vector by the global and localization test of the congruence (see chapter 3.3). In the last surveying during the autumn of 2014, the deformation vectors on the tested points (No.: 2, 3, 30, 38, 104, 105 and 227) of the monitoring station were ranged from +10.5 mm (point No. 227) to -9.8 mm (point No. 30) (**Table 5** and **Figure 5**).
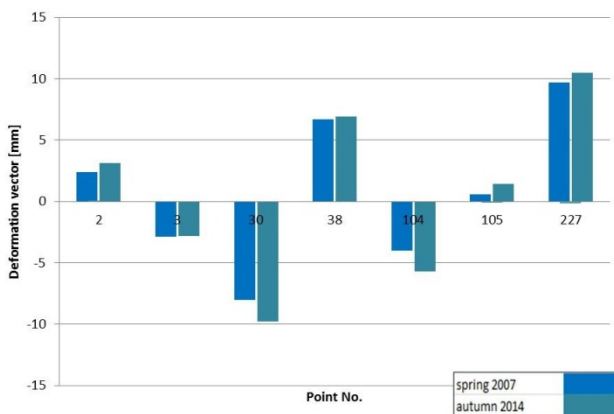
Figure 5. Graphical representation of the deformation vectors on the tested monitoring station points; years: spring 2007 and autumn 2014.

The negative values of the deformation vectors at points No. 3, 30 and 104 represent the opposite trend (direction) of the deformation vector in the space (3D) than at points No. 2, 38, 105 and 227. 3D mean errors (σ_P) were ranged from 17.2 to 39.7 mm (autumn 2014), and the mean coordinate errors (σ_{XYZ}) were from 19.1 to 55.4 mm (autumn 2014) (**Table 4**). After the last geodetic measurement in the autumn of 2014, all points of the monitoring station of Košice-Bankov were destroyed by the reclamation work, i.e., the reference points were removed and the object points were backfilled by the secondary imported soil from various land

building and excavation work in and around Košice City.

3.3 Global test of the congruence

Significant stability, respectively instability of the network points is rejected or not rejected by verifying the null-hypothesis H_0 respectively, also other alternative hypothesis[20, 29]

$$H_0 : d\hat{\hat{C}} = 0; \quad H_\alpha : d\hat{\hat{C}} \neq 0 \qquad (15)$$

Where H_0 expresses the insignificance of the coordinate differences between epochs $t_{(0)}$ and $t_{(i)}$. Test statistics T_G can be used for the global test:

$$T_G = \frac{d\hat{C}Q_{d\hat{\hat{C}}}^{-1}d\hat{C}^T}{ks_0^2} \approx F(f_1, f_2) \qquad (16)$$

Where $Q_{d\hat{C}}$ is the cofactor matrix of the final deformation vector $d\hat{\hat{C}}$; k is the coordinate numbers entering into the network adjustment ($k = 3$ for 3D coordinates) and s_0^2 is the posteriori variation factor common for both epochs $t_{(0)}$ and $t_{(i)}$.

The critical value T_{KRIT} is searched in the tables of F distribution (Fisher-Snedecor distribution) tables according to the degrees of freedom $f_1 = f_2 = n - k$ or $f_1 = f_2 = n - k + d$, where n is number of the measured values entering into the network adjustment and d is the network defect at the network free adjustment. Through the use of methods, the MINQUE is:

$$s_0^{2t(0)} = s_0^{2t(i)} = \bar{s}_0^2 = 1^{[20, 29]}$$

The test statistics T should be subjugated to a comparison with the critical test statistics T_{KRIT}. T_{KRIT} is found in the tables of F distribution according the network stages of freedom.

Table 6. Test statistics results of the geodetic network points of the Košice-Bankov monitoring station (autumn 2014)

Point	$T_{G(i)}$	$< \square \leq \quad >$	F	Notice
2	1.883	<		
3	3.011	≤		
30	3.720	<		deformation vectors are not significant
38	3.721	≤	3,724	
104	2.985	<		
105	1.873	<		
227	3.716	<		

Table 6 presents the global testing results of the geodetic network congruence.

Two occurrences can be appeared:

1. $T_G \leq T_{KRIT}$: The null-hypothesis H_0 is accepted. It means that the coordinate values differences (deformation vectors) are not significant.

2. $T_G > T_{KRIT}$: The null-hypothesis H_0 is refused. It means that the coordinate values differences (deformation vectors) are statistically significant. In this case, we can say that the deformation with the confidence level α is occurred.

4. Subsidence in GIS for mining landscape reclamation

GIS of the mining landscape of Košice-Bankov is based on the next decision points[20]: basic and easy observed geo-data presentation, basic database administration and wide information availability. The best viable solution is to execute GIS project as the Free Open Source application available on Internet. The general facility feature is free code and data source viability through the HTTP and FTP protocol located on the project web pages. Inter among others features range simple control, data and information accessibility, centralized system configuration, modular stuff and any OS platform (depends on PHP, MySQL and ArcIMS port)[20,30–32]. Network based application MySQL is in a present time the most preferred database system on Internet and it was applied also on the deformation survey outputs from the monitoring station of Košice-Bankov.

The database part of GIS for the subsidence of Košice-Bankov at any applications is running into MySQL database (**Figure 6**). 3D model of the mine subsidence of Košice-Bankov with GIS multilayers applications were delivered to the reclamation plan of the municipality of Košice City.
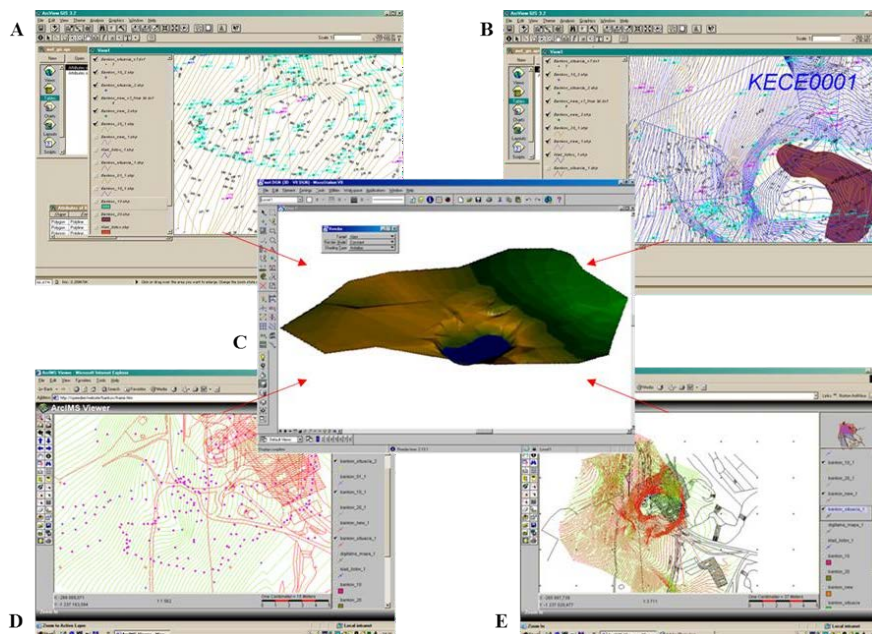
Figure 6. ArcView user interface entity visualization **(A, B)**; MicroStation V8 with Terramodeler MDL application **(C)**; Screenshot of ArcIMS—Application internet interface **(D, E).**

Given the fact that extraction of magnesite has been completed at the mine of Košice-Bankov and these mine workings are abandoned since the end of the 90-years of the last century and whole mining territory of Košice-Bankov with the huge mine subsidence on the conclusions of the deformation investigations are stable, the municipality of Košice City adopted the reclamation plan for that mine landscape. Numerical and graphical presentation of the long-term investigations on the deformation monitoring station of Košice-Bankov with their successive test analyses of the deformation vectors confirmed stability of the mine subsidence and surrounding mining territory. The mine subsidence and by mining activities devastated all surroundings around the mine plant of huge proportions (pit heaps, excavations and other mining earthworks, etc.) began gradually to backfill by a secondary imported soil. The reclamation work on the basis of the investigation geodetic deformation conclusions around the former mining territory of Košice-Bankov began at the beginning of this century. Some final reclamation work was completed in the summer of 2016.

On the territory of the former extensive mine subsidence area, the forest park of Košice-Bankov

was built as the environmental green-forest part of the urban recreation zone of Košice City. The mine subsidence began gradually to backfill by imported natural material from many construction and earthworks in Košice City and surroundings of the city. Such sporadic embankment work took too long, i.e., more than years. After completion of the embankment and other earthworks, the forest park of Košice-Bankov was built on the territory of the former mine subsidence (**Figure 7**). It was planted in particular birch trees. These trees are known by their unpretentiousness onto natural base and also by a rapid growth. Currently, birch grove is constituted by five to six year-old healthy tree.
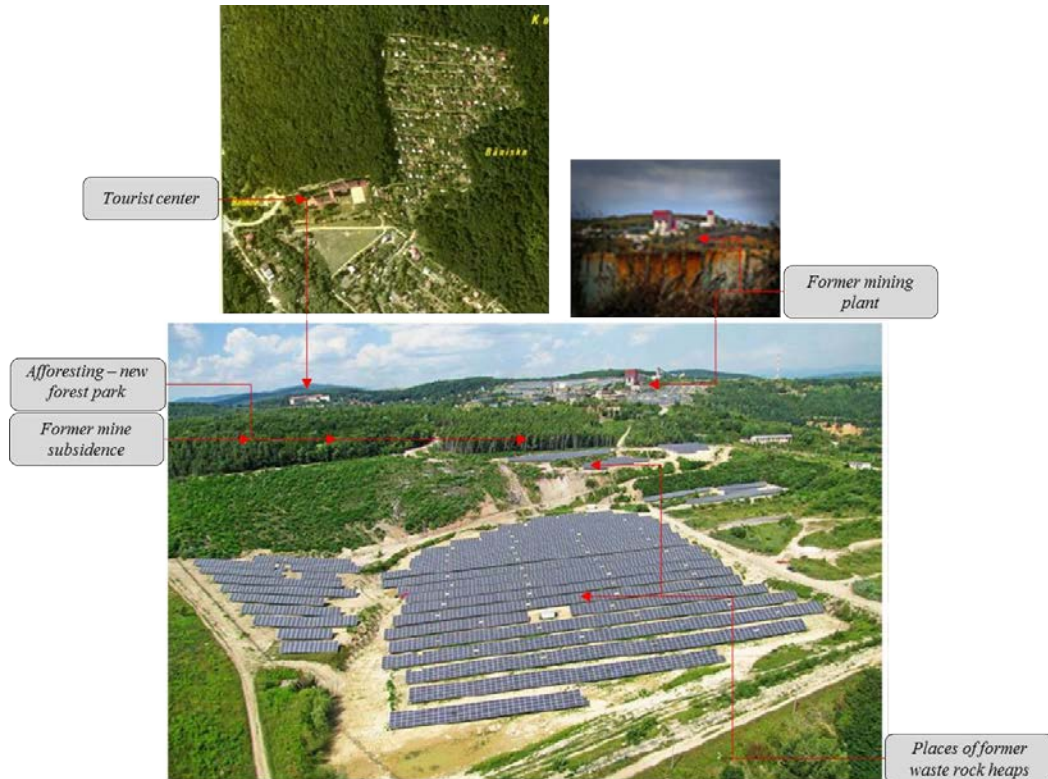
Figure 7. Subsidence and surrounding (Košice-Bankov) after reclamation (2016). Solar collectors in the places of the former waste rock heaps; afforesting (in the background) in the place of the former subsidence**.**

Finalization of the recreation zone of Košice-Bankov was completed in the autumn of 2016. Also, the old tailings piles were reclaimed as well as the devastated surroundings of the former mining plant. On the site of the former waste roc heaps, the solar collectors were built which contribute to renewable energy for Košice City (**Figure 7**).

5. Conclusions

Determination of the deformation vectors as the differences between the adjusted coordinate vectors obtained from two measured monitoring epoch in the geodetic networks is possible if the geometric observation network structure between the individual monitoring epochs is strictly saved. This research article presents the theory and practical outcomes about a possibility of the deformation vector solutions in the geodetic network of the monitoring station in case of violation of the geodetic network structure during the period of monitoring movements of the earth surface. The solved deformation vector affords unreliable image about 3D changes of the geodetic network points in a frame of some specific deformation investigation, e.g., ground movements, mine subsidence, land-slides, dams, engineering constructions, buildings, or other building objects.

The largest differences in all tested elements shown in **Tables 1–5**, especially the largest deformation vectors in **Table 5** and **Figure 5** were occurred on displacement of the point No. 30 and No. 227. Due to the fact that the tested deformation vectors on these points were not significant according to the test statistics, we can declare these points as the static ones. The study case example confirmed availability and applicability of the

99

presented theory on the deformation vector in a special occasion of deformation measurements at mine subsidence, where many violations in the geodetic structure of the monitoring station are occurred. Despite the validity of the verified presented method in solving specific deformation vector in the data, non-homogeneous geodetic network points at the monitoring station may cause a distortion of the deformation effects in the monitoring territory. Therefore, maintaining data-homogeneity of the geodetic network structure should be a priority for whole periodicity of each deformation survey.

The modelling mine subsidence in GIS from the mining territory of Košice-Bankov was delivered to the municipality of Košice city for the solution of the landscape planning to the future environmental rehabilitation of such abandoned old mining region as the magnesite mine of Košice-Bankov. Determination of the deformation vectors of the monitoring station in the undermined landscape of the abandoned magnesite mine of Košice-Bankov was important in delimitation and specification of the edges of the mine subsidence and the edge-punched zones of the subsidence with a lot of cracks and fissures. Very precise identification of the 3D position of such delimitation of the subsidence was a basic document for the plan preparation of the municipality of Košice City for the reclamation of the former mining region of Košice-Bankov as well as and the local ambient by mining activity affected landscape for a comprehensive revitalization and broadening recreational zone in the suburban zone of Košice City. The municipality of Košice City owns 3D model of the mine subsidence of Košice-Bankov in GIS with possibilities of modelling natural and industrial disasters, which largely can be helpful tools for many reclamation work in the landscape ecosystem restoration with the basic elements of safety measures against possible unforeseen and possible consequences of the former mining activities to protect the health and lives of people moving in the forest park located in the former magnesite mine of Košice-Bankov.

Ethics statement

The article was created on the basis of the long-term scientific activities of Prof. V. Sedlák in the field of geodesy and mining surveying, for the purpose of scientific research on deformations of the earth surface due to deep mining. The article presents the specific theory in solution of deformation vectors in mine subsidence. The proposed and applied method of so-called "unconditional" monitoring deformation processes in mine subsidence is verified and confirmed on samples of many geodetic measurements that was made during more than thirty-year research of prof. V. Sedlák in mining sites in Slovakia, especially in the magnesite mine of Košice-Bankov. Some partial data from the last measured geodetic values were processed by Ing. P. Poljakovič, Ph.D. student of prof. V. Sedlák. The results of my long-term research on the proposed specificity of the deformation vector solutions in the Košice-Bankov mining territory have not yet been published in such a complex form as this article presents. Until now, only partial results of the deformation research have been published in the Košice-Bankov mine subsidence.

Conflict of interest

The authors declare that they have no conflict of interest.

References

1. Cui X, Miao X, Wang J, *et al.* Improved prediction of differential subsidence caused by underground mining. International Journal of Rock Mechanics and Mining Sciences 2000; 37(4): 615–627.
2. Díaz-Fernández ME, Álvarez-Fernández MI, Álvarez-Vigil AE. Computation of influence functions for automatic mine subsidence prediction. Computational Geosciences 2010; 14(1): 83–103.

3. Djamaluddin I, Mitani Z, Esaki T. Evaluation of ground movement and damage to structures from Chinese coal mining using a new GIS coupling model. International Journal of Rock Mechanics and Mining Sciences 2011; 48(3): 380–393.

4. Knothe S. Forecasting the influence of mining (in Polish). Katowice: Śląsk Publishing House; 1984.

5. Kratzsch H. Mine subsidence engineering. Heidelberg: Springer-Verlag GmbH; 1983.

6. Reddish DJ, Whittaker BN. Subsidence: Occurrence, prediction and control. Amsterdam: Elsevier; 1989.

7. Donnelly LJ, Reddish DJ. Engineering Geology (in Polish). 1994; 34(3/4): 243–255.

8. Bauer RA, Trent BA, Dumontelle PB. Mine subsidence in Illinois: Facts for homeowners. In: Illinois state geological survey. Illinois: ISGS Publising; 2013. p. 20.

9. Colorado Geological Survey. Subsidence mine [Internet]. Colorado Geological Survey website [cit. 26 Sep. 2016]. Available from: http://Coloradogeologicalsurvey.org/geologic-hazards/subsidence-min/

10. Pinto G, et al. Subsidence [Internet]. Illinois Department of Natural Resources website, [cited 30 May 2016]. Available from: https://www.dnr.illinois.gov/mines/AML/Pages/ Subsidence.aspx.

11. Alehossein H. Back of envelope mine subsidence estimation. Australian Geomechanics: Australian Geomechanics Journal 2009; 44 (1): 29–32.

12. Jung HC, Kim SW, Jung HS, et al. Satellite observation of coal mining subsidence by persistent scatterer analysis. Engineering Geology 2007; 92(1-2): 1–13.

13. Sedlák V. Measurement and prediction of land subsidence above longwall coal mines, Slovakia. In: Borchers WJ (editor). Land subsidence/case studies and current research. Belmont: U.S. Geological Survey; 1998. p. 257–263.

14. Cai J, Wang J, Wu J, et al. Horizontal deformation rate analysis based on multiepoch GPS measurements in Shanghai. Journal of Surveying Engineering 2008; 134(4): 132–137.

15. Can E, Mekik Ç, Kuşçu Ş, et al. Computation of subsidence parameters resulting from layer movements post-operations of underground mining. Journal of Structural Geology 2013; 47: 16–24.

16. Hu L. Gradual deformation and iterative calibration of Gaussian-related stochastic models. Mathematical Geology 2000; 32(1): 87–108.

17. Lu W, Cheng S, Yang H, et al. Application of GPS technology to build a mine-subsidence observation station. Journal of China University of Mining & Technology 2008; 8(3): 377–380.

18. Marschalko M, Fuka M, Treslin L. Measurements by the method of precise inclinometry on locality affected by mining activity. Archives of Mining Sciences 2008; 53(3): 397–414.

19. Ng AHM, Ge L, Zhang K, et al. Deformation mapping in three dimensions for underground mining using InSAR—Southern highland coalfield in New South Wales, Australia. International Journal of Remote Sensing 2011; 32(22): 7227–7256.

20. Sedlák V. Possibilities of modelling surface movements in GIS in the Košice depression, Slovakia. RMZ—Materials and Geoenvironment 2004; 51(4): 2127–2133.

21. Wright P, Stow R. Detecting mine subsidence from space. International Journal of Remote Sensing 1999; 20(6): 1183–1188.

22. Konicek P, Soucek K, Stas L, et al. Long-hole destress blasting for rockburst control during deep underground coal mining. International Journal of Rock Mechanics and Mining Sciences 2013; 61: 141–153.

23. Strazalowski P, Scigala R. The example of linear discontinuous deformations caused by underground extraction. Transection of VŠB—Technical University Ostrava. Civil Engineering, Series 2005; (2): 193–198.

24. Li P, Tan Z, Deng K. Calculation of maximum ground movement and deformation caused by mining. Transactions of Nonferrous Metals Society of China 2011; 21(Sup. 3): 562–569.

25. Christensen R. General Gauss–Markov models. In: Christensen R (editor). Plane answers to complex questions: The theory of linear models. 4th ed. New York: Springer; 2011. p. 237–266.

26. Gene H, Golub CF, Van Loan. Matrix computations. Baltimore: JHU Press, 2013

27. Groß J. The general Gauss-Markov model with possibly singular dispersion matrix. Statistical Papers 2004; 45(3): 311–336.

28. Lindgren F, Ruel H, Lindström J. An explicit link between Gaussian fields and Gaussian Markov random fields: the stochastic partial differential equation approach. Journal of the Royal Statistical Society: Series B (Statistical Methodology) 2011; 73(4): 423–498.

29. Lehmann EL, Romano JP. Testing statistical hypotheses. 3rd ed. New York: Springer; 2005. p. 784.

30. Blachowski J. Application of GIS spatial regression methods in assessment of land subsidence in complicated mining conditions: Case study of the Walbrzych coal mine (SW Poland). Natural Hazards 2016; 84: 1–18.

31. Yang K, Xiao J, Duan M, et al. Geo-deformation information extraction and GIS analysis on important buildings by underground mining subsidence. In: 2009 International Conference on Information Engineering and Computer Science—ICIECS 2009. Wuhan: IEEE; 2009.

32. Yang KM, Ma JT, Pang B, et al. 3D visual technology of geo-deformation disasters induced by mining subsidence based on ArcGIS engine. Key Engineering Materials 2012; 500: 428–436.

REVIEW ARTICLE

Research progress and prospect of coastal flood disaster risk assessment against global climate change

Jiayi Fang[1,2,3], **Peijun Shi**[2,3,4,5*]

[1] *Key Laboratory of Geographic Information Science, Ministry of Education, School of Geographic Sciences, East China Normal University, Shanghai 200241, China.*

[2] *Faculty of Geographic Sciences, Beijing Normal University, Beijing 100875, China; E-mail: jyfang@geo.ecnu.edu.cn/ spj@bnu.edu.cn*

[3] *Academy of Disaster Reduction and Emergency Management, Ministry of Emergency Management & Ministry of Education, Beijing 100875, China.*

[4] *State Key Laboratory of Earth Surface Processes and Resource Ecology, Beijing Normal University, Beijing 100875, China.*

[5] *School of Geography Science, Qinghai Normal University, Xining 810016, China.*

ABSTRACT

The sea level rise under global climate change and coastal floods caused by extreme sea levels due to the high tide levels and storm surges have huge impacts on coastal society, economy, and natural environment. It has drawn great attention from global scientific researchers. This study examines the definitions and elements of coastal flooding in the general and narrow senses, and mainly focuses on the components of coastal flooding in the narrow sense. Based on the natural disaster system theory, the review systematically summarizes the progress of coastal flood research in China, and then discusses existing problems in present studies and provide future research directions with regard to this issue. It is proposed that future studies need to strengthen research on adapting to climate change in coastal areas, including studies on the risk of multi- hazards and uncertainties of hazard impacts under climate change, risk assessment of key exposure (critical infrastructure) in coastal hotspots, and cost-benefit analysis of adaptation and mitigation measures in coastal areas. Efforts to improve the resilience of coastal areas under climate change should be given more attention. The research community also should establish the mechanism of data sharing among disciplines to meet the needs of future risk assessments, so that coastal issues can be more comprehensively, systematically, and dynamically studied.

Keywords: Coastal Flood; Global Climate change; Storm Surge; Risk Assessment; Impact

1. Introduction

In the context of global warming, coastal flooding caused by sea level rise and extreme water level of high tide and storm surge has a great impact on coastal social economy and natural environment. From 1975 to 2016, 80% of the global flooding deaths happened in areas 100 km away from the coast[1]. In 2005, the Hurricane Katrina storm surge disaster chain in the United States burst the flood dike in New Orleans, causing economic losses of more than 96 billion US dollars[2]. In 2008, Cyclone Nargis swept across the delta of Myanmar, resulting in 138000 missing and dead[3]. In addition, typhoon Haiyan in the Philippines (2013), hurricane Sandy in New York (2012) and hurricane Harvey in Texas (2017) all caused huge casualties and economic loss-

es. As the important gathering places for economy and populations, China's coastal areas are prone to be influenced by extreme weather and climate. With the rapid development of urbanization, the coastal population has expanded rapidly. The high-intensity human activities, urbanization and land reclamation have made great changes in China's coastal land use and cover[4]. From 1989 to 2014, coastal floods caused by storm surges in China has led to economic losses of about US $70.6 billion and about 4354 missing and deaths[5]. Under the initiative of "The Belt and Road", coastal areas continue to develop rapidly. it can be inferred that China's coastal exposure will continue to increase in the future and the coastal areas will still be badly influenced by the natural disasters. The increasingly frequent extreme disasters in coastal areas have attracted great attention of governments, organizations and academic circles. Land-Ocean Interactions in the Coastal Zone (LOICZ) established in the "Future Earth planning" has now developed into the "Future Earth Coast" (FEC), which aims to develop and integrate multidisciplinary analysis methods (natural science + economy + society) under the background of global change, and to promote the sustainable development of coastal areas and improve their adaptability to climate change. The EU has also carried out a number of large-scale scientific research projects on this sub-

ject (**Table 1**). China has also implemented a series of major projects on the comprehensive risk research of global change in coastal zones and coastal areas. According to the major science and technology special project of the Ministry of Science and Technology of People's republic of China during the 13th Five-year Plan, it shall assess the comprehensive risk of coastal zone and coastal area change, so as to generate the distribution map of disaster-causing factors, vulnerability distribution map of disaster-bearing body and comprehensive risk map of China's coastal zone and coastal area with spatial resolution better than 1 km under the global change during 50–100 years in the future. It has been a great challenge for China as well as other countries to alleviate the risk of natural disasters in coastal areas.

To sum up, the research on coastal flood disaster risk assessment under global climate change is a frontier issue of international scientific research, which is of great significance to meet the needs of national and regional development, formulate disaster reduction strategies and implement the sustainable development of coastal zone. However, there is no widely recognized definition, genetic elements, mechanism and dynamics, as well as other relevant concepts for coastal flood risk at present, which will influence the research directions and results of coastal flood risk., Therefore, from the perspective of

Table 1. Non-exhaustive list of EU funded research projects about coastal flood under climate change

| Project and execution time	Name of Projects	Goal
DINAS-COAST (2001–2004)	Dynamic and Interactive Assessment of National, Regional and Global Vulnerability of Coastal Zones to Climate Change and Sea Level Rise	Integrating multidisciplinary knowledge (coastal geomorphology, ecology, economics, environmental geography and computer science); modeling and developing assessment models to help decision-makers analyze the impact of climate change and sea-level rise
XtremRisK (2008–2012)	Integrated Flood Risk Analysis for Extreme Storm Surges	Carrying out risk analysis for coastal flood disaster caused by extreme water level in open coastal and estuarine areas
THESEUS (2009–2013)	Innovative Technologies for Safe European Coasts in a Changing Climate	Providing a comprehensive assessment method for coastal flood and coastal erosion combined with multidisciplinary knowledge, from three specific directions: risk assessment, coping strategies and application to develop innovative adaptive measures for maintaining the sustainable development of coastal zone
RISES-AM (2013–2016)	Responses to Coastal Climate Change: Innovative Strategies for High End Scenarios — Adaptation and Mitigation	Developing innovative mitigation and adaptation measures to address extreme scenarios in coastal areas under climate change
SPP 1889 (2016–2019)	Regional Sea Level Change and Society	Carrying out cross research on climate related sea-level change through comprehensive and interdisciplinary integration means, while considering the interaction of human and environment as well as the socio-economic development of coastal areas

regional disaster, this paper summarizes the research progress and existing problems of coastal flood at home and abroad, so as to provide reference for better clarifying the research direction and refining the research problems and related research.

2. Definition of coastal flood

At present, the academic circles at home and abroad have not unified the definition for coastal flood, mainly discussing from it broad sense and narrow sense.

In the broad sense, the coastal flood refers to the flood occurring in coastal areas (**Figure 1**). In addition to influence of the extreme water level caused by sea level rise, astronomical spring tide and storm surge, it may also be affected by the comprehensive action of riverine flood and urban water logging caused by heavy precipitation. Its main disaster-causing factors may include over-fortified land-based flood, extreme precipitation and extreme seawater level. In the EU THESEUS project, Zheng *et al*.[6] and Zscheischler *et al*.[7] adopted the concept of coastal flood in broad sense. The research on coastal flood in broad sense is mostly in large estuarine urban areas, where urban waterlogging occurs frequently. Such areas will not only be threatened by marine factors, but also affected by land-based flood, coupled with extreme precipitation events and a high proportion of impermeable layer in complex urban system. Shanghai is a typical representative.
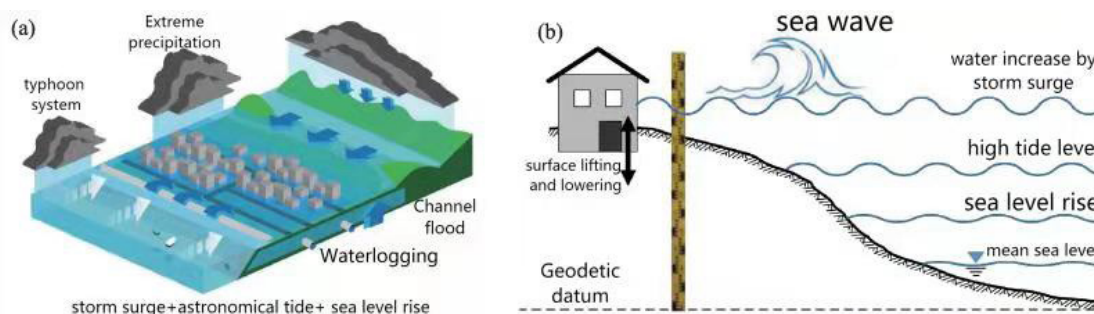
Figure 1. Coastal flooding in the broad sense (a) and the narrow sense (b).

Note: The schematic diagram of coastal flood in a broad sense is provided by Dr. Thomas Wahl of the University of Central Florida.

In the narrow sense, coastal flood generally refers to the flood caused by sea level rise, storm surge and extreme water level aroused by astronomical spring tide under climate change in coastal areas. This is also a commonly used concept in IPCC series reports. It is based on the analysis of inundation results of the extreme water level and sea level rise during the return period[8]. The study of coastal flood in broad sense involves many disaster-causing factors, and the research problem is complex. Currently, coastal flood mentioned by most international studies refers to coastal flood in a narrow sense, which is a flood disaster caused by the instability of the marine system, such as tropical cyclone storm surge, with water source coming from the ocean[9,10]. Therefore, this paper focuses on the research progress of coastal flood risk assessment in a narrow sense under climate change.

3. Analysis of disaster-causing factors of coastal flood

The disaster-causing factors of coastal flood in a narrow sense can be divided into two parts: relative sea level change representing tendency and extreme water level change representing extremity. In the 1960s, the study of extreme water level mainly considered the results of the superposition of storm surge water increase and high tide level caused by tropical cyclones, and developed a series of storm surge numerical models[11], but the consideration of sea level rise at this stage is very limited. Since the 1980s, climate change and sea level rise have attracted attention, and a series of studies have emerged to predict future sea level rise[12]. The two studies were relatively independent in the early stage. At the end of the 20th century, relevant scholars realized that compared with the inundation of static water level caused by the slow rise of sea level, the disaster

consequences caused by extreme high water level of superimposed extreme climate events will lead to more serious situations, and it is urgently necessary to carry out further research by combining the two factors[13]. Hoozemans et al.[14] and Baarse[15] preliminarily constructed the assessment method to access the impact of extreme water level during sea level rise and established the basic database, which gave the preliminary results of impact assessment on a global scale. Nicholls et al.[16], Klein et al.[17] and Nicholls[9] continuously improved the assessment method and carried out global coastal flood risk assessment research, which has become one of the main achievements cited in the Coastal Zone Chapter of the third and fourth report of IPCC. The main disaster-causing factors of coastal flood in a narrow sense can be defined by formula (1):

$$\triangle WL=\triangle SL_G+\triangle SL_{RM}+\triangle SL_{RG}+\triangle SLM_H+\triangle SLM_N+\eta_{NTR}+\eta_W \tag{1}$$

where $\triangle WL$ is the change of total water level; $\triangle SL_G$ is the global mean sea level change; $\triangle SL_{RM}$ is the regional sea level difference caused by climate and ocean factors; $\triangle SL_{RG}$ is the sea level difference caused by the change of regional earth gravity field; $\triangle SLM_N$ and $\triangle SLM_H$ respectively represent the changes of surface rise and fall caused by natural and human factors. The surface rise and fall of natural factors include neotectonic movement, glacier equilibrium adjustment and sediment compaction / integration. Most of the surface rise and fall caused by human factors are underground liquid extraction and other factors[13]. The abovementioned five factors usually change with the sea level. η_{NTR} is storm surge or surge as translated by Chinese scholars[18], but internationally it is expressed as non-tidal residual (NTR), referring to that the total water level minus the astronomical tide. Astronomical tide can obtain the part of tidal variation through harmonic analysis[19]; η_W is the increase of water by waves, but the observation device of general tide gauge station can not capture the change of sea water level caused by short-period waves. Tsunamis can also cause extreme water levels, but the extreme water level height caused by tsunamis is far beyond the measurement range of tide gauge stations, which is usually combined with seismic research. Therefore, in the current coastal flood research, most studies mainly focus on the extreme water level combination of astronomical tide and storm surge, as well as the global absolute sea level change and regional relative sea level change.

The research on extreme water level mainly focuses on its historical variation law and influencing factors, as well as the simulation and evaluation of the risk of extreme water level. Domestic and foreign scholars have studied the historical long-term variation law of extreme water level, and found that the extreme water level of most tide stations in the world shows an increasing trend, but after subtracting the average sea level change from the extreme water level, it is found that this increasing trend decreases significantly. Therefore, it is considered that most of the changes of extreme water level are caused by sea level change[20–22]. Some studies have also pointed out that the increase

The rate of extreme water level is significantly higher than the average sea level growth[23]. The extreme water level along the coast of China showed a significant growth trend, increasing at a rate of 2.0–14.1 mm/a from 1954 to 2012[24,25]. Sea level change not only plays an important role in the long-term change of extreme water level, but also leads to the increase of extreme water level frequency. Early studies have shown that the return period of extreme water level will change greatly due to slight changes in sea level[26]. Other studies at home and abroad have reached similar conclusions[27–29]. In addition to sea level changes, extreme water levels are also affected by typhoon, storm surge, wind field and atmospheric circulation index[30]. Besides studying the historical variation law of extreme water level and its influencing factors, there are also a large number of studies to evaluate the risk of extreme water level. Extreme water level risk assessment is the basis of risk assessment research. It mainly adopts two methods, namely statistical model and numerical simulation. Mature storm surge numerical models have been established internationally, such as SLOSH, ADCIRC, DELFTD, MIKE21 and GCOM-2D/3D models[31]. Dutch scholars have developed the

world's first set of storm surge and extreme water level data set based on hydrodynamic model[32]. At present, with regard to the study of extreme water level in China's coastal areas, the station data of tide gauge stations are mostly used to calculate the surge height under different return periods due to the sparse distribution of coastal stations and short time series and carried out risk assessment on this basis[33–35]. Sea level changes are often divided into absolute sea level changes caused by changes in the overall quality of marine water bodies and specific volume effects and relative sea level changes relative to a datum (such as geodetic datum or historical average sea level)[36]. The common methods for predicting the future sea level change trend are divided into two categories: one is to analyze the historical observation data by using statistical model methods such as singular spectrum analysis, grey model, Empirical Mode Decomposition (EMD), autoregressive model and wavelet analysis, and then find out their laws and extrapolate them[37]. The second is to use the global coupling model to simulate and analyze the sea level change under different greenhouse gas emission scenarios in the future[38]. Using the extrapolation of statistical model to predict future changes is greatly affected by the length and quality of data series, and assuming that the future sea level change system is in a stable state, its change law remains unchanged, so it can not reflect the actual situation of marine system changes caused by climate change. In contrast, the research on global sea level change based on large-scale numerical model is the mainstream of current research and the main method adopted in IPCC series reports[39–41]. In the IPCC AR5 report, various emission scenarios in the future are

simulated based on the CMIP5 global climate model[42]. At present, the coupled numerical model has the problems of imperfect description of the global climate change process simulation, many uncertain factors in the model and insufficient accuracy of the model. A large number of scholars around the world are trying to improve the physical mechanism of model simulation and improve the resolution of sea-level rise data products, so as to make the simulation process more reasonable and the quality and accuracy of data products higher.

Table 2 shows the relevant cases of existing (narrow sense) coastal flood risk assessment and the factors considered. Most studies consider the change of mean sea level, the superposition of astronomical spring tide and NTR, but due to the small amount of wave observation data and the great technical difficulty of simulation, it is less considered in the relevant risk assessment. Less consideration is given to regional sea level differences, more consideration is given to the ground rise and fall of natural factors, but less consideration is given to the ground rise and fall caused by human factors. It is worthy of attention that the above research is a linear superposition of sea level rise and extreme water level, without considering the coupling mechanism of the two. Lin et al.[43] made a breakthrough in the research on this issue. Based on the physical mechanism, a numerical model was used to analyze the change of storm surge water level in New York under the scenario of sea level rise. However, because the research involves a large number of numerical operations, it is difficult and requires the cooperative efforts of multiple disciplines and units, and there are few relevant research results. Therefore, the linear superposition of sea lev-

Table 2. Non-exhaustive examples of coastal flooding assessment

Literature	Content	Sea level composition					
		$\triangle SL_G$	$\triangle SL_{RM}$	$\triangle SL_{RG}$	$\triangle SL_{M^N}$	$\triangle SL_{M^H}$	$\triangle SS$
Lowe et al., 2009	National level(Britain)	√	√		√		√
Rosenzweig, 2010	City (New York)	√			√		√
Hanson et al., 2011	Global (city)	√			√	√	√
Parris et al., 2012	National level (America)	√	√		√		√
Wang et al., 2012	City (Shanghai, China)	√			√	√	√
Kebede et al., 2012	City (capital of Tanzania)	√			√		√

Note: $\triangle SS$ is the part of extreme water level relative to mean sea level.

el rise and extreme water level is still used in most of the current relevant studies.

4. Study on disaster breeding environment and disaster bearing body

Natural and human disaster breeding environments such as topography, coastal engineering and land subsidence have an important impact on the disaster formation process of coastal flood in coastal areas. With the deepening of research, in recent years, scholars have paid more and more attention to the impact of actual fortification level and land subsidence on the process of coastal flood disaster[44] the data on coastal fortification level is very limited. At present, relevant evaluation studies at home and abroad simplify the fortification level according to per capita GDP, or directly ignore fortification[45]. However, in reality, there is a certain degree of fortification in populated areas and major coastal cities. In China's coastal areas, in order to resist coastal extreme meteorological and marine disasters such as coastal erosion, coastal floods and catastrophic waves, a series of protective measures have been established to protect coastal population security and economic activities. Research shows that more than 60% of the coastlines in China have been protected by seawalls[46,47]. If fortification is not considered, the risk assessment result will be too high. In addition, there is a serious land subsidence problem in the global coastal Delta and major cities[48], which reduces the land elevation and accelerates the rise of relative sea level, thus reducing the fortification capacity. Therefore, more and more attention is paid to the impact of land rise and fall caused by natural and human factors in risk assessment[49]. Previous studies have considered this disaster breeding environment in the risk of disaster causing factors, pointing out that land subsidence changes the relative sea level rise height and amplifies the risk[50]. In China's coastal cities, land subsidence caused by human factors has been very serious[51], but the research on land subsidence in risk assessment is very limited.

In recent years, scholars at home and abroad have evaluated the impact of extreme water level on social economy and natural environment under sea level change for disaster bearing bodies such as population, economy, agriculture and wetland. Nicholls[9] and Spencer et al.[52] assessed the impact of coastal floods and wetland losses; Hanson et al.[53] assessed the population and asset risks of 136 port cities in the world under the once-in-a-century coastal flood event in the future; Jongman et al.[54] calculated the asset exposure in 2010 and 2050 under the once-in-a-century river type and coastal flood events; Hallegatte et al.[55] assessed the exposure, loss and risk of 136 major coastal cities under future coastal floods and ranked them in risk; Hinkel et al.[10] analyzed the population and asset risks under future global coastal floods and emphasized the importance of adaptive measures; Vousdoukas et al.[56] analyzed the contribution rate of various climate scenarios and socio-economic scenarios to coastal flood risk change. The disaster bearing body is not static, but dynamic. For example, the elderly population will continue to increase in the future, the floating population in coastal cities has seasonal characteristics, the land use type is changing, and the coastal exposure may continue to increase. Although there are risk assessments combining various climate scenarios and socio-economic scenarios in the future, such studies mostly focus on population and economic aggregate, such as those by Hinkel et al.[10] and Vousdoukas et al.[56], and the dynamic research of other disaster bearing bodies is very limited. In addition, there are few studies on key exposures affecting disaster losses, especially important coastal key infrastructure including power facilities, transportation hubs, shelters, material reserve bases, sluices and guard facilities[57,58]. The destruction of key infrastructure will lead to the systematic and cascade paralysis of regional infrastructure functions, and then lead to other indirect losses. At present, there are few studies on the evaluation of indirect losses and the impact evaluation of system dynamic network functions.

Vulnerability of disaster bearing body refers to the possibility of socio-economic system and ecosystem being hit by disaster-causing factors. The most common are physical vulnerability and social vulnerability[59]. The physical vulnerability of disaster bearing body focuses on the physical characteristics

of disaster causing factors and the response of disaster bearing body. Physical vulnerability analysis uses quantitative analysis to obtain the relationship between loss and disaster causing factors and give quantitative risk assessment results based on disaster data, field investigation data, insurance data, model simulation and other means[60]. By constructing the functional relationship between the inundation depth and the loss of coastal disaster bearing bodies (population, houses, seawalls, etc.), the vulnerability loss matrix or vulnerability curve can be constructed to determine the loss rate of disaster bearing bodies under different disaster intensity[61]. A large number of studies on flood disaster vulnerability curves have been carried out abroad. For example, the United States, Britain and the Netherlands have established loss curves for different building types[62,63]. Domestically, more detailed research has also been carried out in some areas such as Shanghai[64]. Due to the high requirements of physical vulnerability research on historical disaster data and the need for a large number of field research, the current disaster data are less open or of low quality and difficult access to data, and the research on vulnerability curve between water depth and loss is very limited, so it is difficult to construct a universal and practical physical vulnerability curve. This makes the current research more dependent on the international physical vulnerability curve. Social vulnerability can be understood as the sensitivity of the social system to the impact of disaster causing events and the adaptability to deal with disaster events[64]. The evaluation method usually adopts the index system method. By establishing the index evaluation system and giving weight to the factors by means of expert scoring method and factor analysis, the social vulnerability level is divided. Drawing on these methods, some progress has been made in the social vulnerability assessment of different scales and different research areas in China's coastal areas, such as the coastal municipal level[65,66] and coastal counties[67] carried out social vulnerability assessment. However, the selection and establishment of evaluation indicators and the weight giving methods are different, which are influencing and subjective. Besides, the index system method obtains

unitless scalar or relative value, which can be used to identify high vulnerability areas or vulnerability change trends, but the quantitative relationship between it and the loss is not clear, so it is difficult to be applied to quantitative risk assessment.

For the coastal zone system, a large number of scholars have also carried out research on the comprehensive vulnerability and vulnerability of coastal zone disaster bearing bodies, and established vulnerability assessment models, such as PSR model (Pressure-State-Response-Framework), DPSIR model (Driving force-Pressure-State-Impact-Response) and SPRC (Source-Pathways-Receptor-Consequence) [68,69]. Based on the above conceptual model, relevant scholars have established a comprehensive vulnerability rating model of coastal zone, which is generally the index system method[70–74], but the vulnerability obtained from the above research is also a scalar result, which is difficult to be connected with quantitative risk assessment.

5. Coastal flood risk assessment method and model

After determining the factors to be considered in coastal flood, how to determine the inundation range of coastal flood under extreme water level has become the most key problem in risk analysis[75]. At present, the means to determine the coastal flood inundation range can be summarized into two categories: one is the elevation-area method based on GIS, and the other is the numerical model based on hydrodynamic evolution.

The most commonly used method in current research is the evaluation model based on GIS, which is widely used in large-scale coastal flood Research[76–78]. However, the defect of this method is that it does not consider the duration of extreme water level and ground roughness. Not all areas under a specific water level are affected areas, so it is easy to overestimate the risk; the advantage is that it can quickly divide high-risk areas, especially for the impact under various climate scenarios in the future, and can provide global and national decision-makers with information on macro disaster risk prevention in coastal zone. Numerical models based on hydro-

dynamic evolution, such as large storm surge numerical models such as ADCIRC and DELFD 3D, can better simulate the processes of storm surge water increase and floodplain, but it is difficult to be applied to large-scale coastal flood disaster risk assessment. The main reasons are: i) The data required by the model is huge and complex; ii) The solving process is complex and time-consuming; iii) The intensity of disaster causing factors is well simulated, but other factors such as the vulnerability of disaster bearing body in risk assessment are not considered enough. With the improvement of terrain data accuracy, such as LiDAR elevation data of 5m and below, the two-dimensional flood model based on GIS grid data is more widely used, such as LisFlood[79], JFLOW[80] and Floodmap[81,82], etc. This kind of two-dimensional flood model simplifies the physical process, greatly improves the solution efficiency, and performs well in small-scale research[83]. In order to improve the extreme water level simulation, simplify the solution process and improve efficiency, some scholars use the relevant storm surge products developed by other research teams, which are generally based on the large-scale storm surge numerical model and targeted at some specific areas, such as the extreme water level height under various return periods, as the input of the flood plain process on land; then, the two-dimensional flood model based on GIS grid data is used as the evolution of flood process[84]. Howev-er, this method is also difficult to be applied to large-scale coastal flood risk assessment, mainly due to the high requirements for the accuracy of basic data, and in terms of large-scale, the amount of basic data is huge and difficult to obtain.

In conclusion, in large-scale, such as global scale or national level, the impact assessment of coastal floods on coastal areas under global climate change depends more on the elevation area method based on GIS model. In addition to the general GIS assessment models, **Table 3** summarizes the existing coastal flood impact assessment models and their main parameters. Such evaluation model integrates multi-disciplinary knowledge and considers the dynamic feedback of natural environment and socio-economic environment to a certain extent. It can provide more effective information for decision makers and stakeholders and improve the evaluation efficiency.

6. Problems in domestic related researches

Through research at home and abroad, it is found that the coastal flood disaster risk assessment in European and American developed countries under various climate scenarios has been relatively in-depth, and coastal flood risk assessment has been carried out at the national level, such as Germany[85], the United States[86], Canada[87] and the United King-

Table 3. Key attributes of coastal flood impact models

Model	Scale	Spatial resolution	Time scale	Input data	Output data	Literature
Inundation model (e.g. GIS)	Local, regional and global	Changeable	User defined	Elevation, sea level rise scenario, socio-economic data	Map of potential inundation area and affected population	Rowley *et al.*, 2007
SLAMM (Sea Level Affecting Marshes Model)	Local and regional	10–100 m	5–25 a time step	Elevation map, wetland cover, development footprint and seawall location	Map of potential inundation area and affected population	Galbraith *et al.*, 2003
DIVA (Dynamic Interactive Vulnerability Assessment)	National, regional and global	Coastline segmentation (12000 sections in the world, with an average of 70 km per section)	1–5 a, up to 100 a	Elevation, geomorphic type, coastal population, land use, administrative boundary, GDP	Coastal floods are expected to affect population, wetland change, loss and adaptation costs, and land loss	Hinkel *et al.*, 2009
LIS Coast (Large scale Integrated Sea-level and Coastal Assessment Tool)	European Region	The coastline is segmented with different lengths	Variable, user defined	Elevation, meteorological data, population, *etc*.	Expected population and economic loss, etc.	Vousdoukas *et al.*, 2018

dom[88]. However, China has not yet had relevant assessment reports at the national level. Compared with foreign countries, domestic coastal flood related research on sea-level rise and extreme water level superposition started late, and at present, most of them focus on the risk of disaster causing factors, and there are more research on the prediction of sea-level rise at the regional scale under the future climate scenario, whereas there are less disaster risk assessment in China's coastal areas under different climate scenarios in the future. Most of the existing domestic relevant studies are aimed at a certain region, such as the Pearl River Delta[18] and Shanghai[68]. It is very limited to carry out coastal flood risk assessment of sea level rise and extreme water level superposition at the national level. At the same time, there are few data products independently developed and disclosed in China, and the statistical caliber of socio-economic data and disaster data is inconsistent and of year-missing situations, which has become a major bottleneck in the current research.

(1) Lack of hazard factor coupling risk study. In most relevant studies, it is assumed that the mean sea level rise and the storm surge system leading to the extreme water level are relatively independent and of a linear superposition relation; and it is assumed that the system is stable, without considering the change resulted by global climate change to the overall storm surge system or regional volatility. Global climate change may lead to corresponding changes in the overall marine system, so it is necessary to be vigilant against the emergence of extreme scenarios (high end scenario) and "Grey Swan"[89,90], and attach importance to the inconsistency and stability process. In coastal and estuarine areas, due to the effect of nearshore topography and the superposition of multiple water sources, it is prone to the superposition of multiple disasters, which may make the disaster degree higher than the impact of only a single extreme seawater level. That is the focus of international attention[7]. Foreign countries have carried out joint probability distribution to study the nonlinear effect of superposition of various coastal flood disaster causing factors, such as combining river runoff flood with coastal flood[91], or combining coastal flood with

extreme precipitation[92]. At present, the domestic related research is relatively weak, which awaits a breakthrough in the future.

(2) Lack of interdisciplinary integration and consideration of disaster breeding environment and human factors. From the perspective of disaster system, the change of coastal flood disaster risk is affected by many factors of nature and human society, but current research involves a few factors and ignores multi-scenario and human factors. Although experts in various fields have conducted research from the perspectives of oceanography, geology and geography, there is a lack of systematic research integrating various disciplines[93]. At present, most of the relevant studies in China are carried out from the perspective of global climate change. Coastal disaster risk assessment is usually carried out based on a certain climate model or emission scenario. There is a lack of consideration of land surface system and human economic system. The consideration of coastal fortification, land subsidence control and other factors in the assessment is very limited. There are fewer studies considering both future climate scenario change and socio-economic scenario change. Although there have been simulation studies on China's future population and economy[94,95], but the two have not been combined in the current evaluation study.

(3) Lack of research on adaptive measures and resilience in coastal areas. Using quantitative cost-benefit analysis to evaluate the adaptability and mitigation measures of various coastal engineering or non-engineering to prevent, respond to or mitigate climate change and disaster risk is the current popular research trend[44,96]. In addition to fortification, there are other adaptive measures in coastal areas to deal with global climate change, which can be summarized into three categories: protection, retreat and accommodation; according to the nature of the project, it can be divided into engineering measures and non- engineering measures[97]. However, the current research on adaptive measures in China's coastal areas is in the preliminary stage[98]. Moreover, most studies began to shift from the perspective of vulnerability to the perspective of resilience, which

has increasingly attracted attention in coastal zone research[96]. Resilience research is to explore the internal stress, recovery, adaptation and transformation ability of the system under a multidisciplinary framework, emphasizing the independent resistance of the system to external interference[99]. But, the research on the resilience of China's coastal areas is also very limited.

7. Outlook

Based on the above shortcomings, this paper puts forward the following prospects to strengthen the research on coastal areas to deal with the risk of global climate change.

(1) Strengthen the research on the coupling risk and uncertainty of multiple disaster causing factors under climate change. In the future, it is necessary to strengthen the impact of global sea level rise on the tropical cyclone system and the interaction of coastal zone system. Based on the physical mechanism, a numerical model is used to simulate the changes of tropical cyclone system and extreme water level under global sea level rise. Strengthen the research on the disaster mechanism of disaster chain and disaster group, and analyze the nonlinear effect of multi disaster factor coupling with statistical model or dynamic model. Strengthen the research on the uncertainty of disaster causing factors, generate a large number of random data sets of typhoon track and intensity by random simulation, and calculate and analyze the uncertainty in the simulation by numerical model. Based on the in-depth research on the risk of coastal disaster causing factors, we will independently develop disaster causing factor products and related evaluation software for the whole coast of China, strengthen independent model research, better serve marine engineering and provide information for stakeholders.

(2) Enhance risk assessment research on key coastal areas and key exposures (key infrastructure). In the future, we should pay close attention to the investigation and hidden danger investigation of key coastal areas and key exposures, focus on the highly vulnerable population (such as the elderly population and floating population), and investigate the key infrastructure that may have a significant impact (such as dams, power facilities and transportation hubs). Typical areas can be selected to try to predict and study the disaster bearing bodies in the future, establish corresponding vulnerability curves for key exposures such as different land use types and infrastructure, and carry out comprehensive population and economic risk assessment.

(3) Improve the cost-benefit evaluation of global climate change risk adaptation and mitigation measures. At present, the research on the impact of a variety of adaptive and mitigation measures on the coastal environment is very limited, especially the measures such as embankment construction and land reclamation. In the future, deepen the research on the comprehensive impact of engineering measures such as fortification and reclamation on the coastal zone environment against global climate change. For the coastal zone system, in the face of future global climate change and extreme disaster events, how to improve the resilience of coastal areas and better adapt to global change will become increasingly important.

(4) Enlarge data openness and conduct interdisciplinary research. It is suggested that relevant departments should strengthen the openness of data required for scientific research projects, strengthen the collection and statistics of basic socio-economic data, formulate statistical norms and standards, and establish a more effective social information collection system and a more complete data database. With the rapid development of network technology, using big data for research is also a major trend in the future. Hence, it is crucial to optimize the basic data sharing mechanism among multiple disciplines, adopt interdisciplinary means, and apply the emerging means of other disciplines (such as economics, sociology and system dynamics) to the coastal areas, so as to study the coastal zone problems more comprehensively, systematically and dynamically.

Conflict of interest

The authors declare that they have no conflict of interest.

References

1. Hu P, Zhang Q, Shi P, *et al*. Flood-induced mortality across the globe: Spatiotemporal pattern and influencing factors. Science of the Total Environment 2018; 643: 171–182.

2. Townsend FF. The federal response to hurricane Katrina: Lessons learned. Bratislavské Lekárske Listy 2006; 85(4): 478–495.

3. Shibayama T. Field surveys of recent storm surge disasters. Procedia Engineering 2015; 116: 179–186.

4. Liu J, Wen J, Huang Y, *et al*. Human settlement and regional development in the context of climate change: A spatial analysis of low elevation coastal zones in China. Mitigation and Adaptation Strategies for Global Change 2015; 20(4): 527–546.

5. Fang J, Liu W, Yang S, *et al*. Spatial-temporal changes of coastal and marine disasters risks and impacts in Mainland China. Ocean & Coastal Management 2017; 139: 125–140.

6. Zheng F, Westra S, Leonard M, *et al*. Modeling dependence between extreme rainfall and storm surge to estimate coastal flooding risk. Water Resources Research 2014; 50(3): 2050–2071.

7. Zscheischler J, Westra S, Hurk BJ, *et al*. Future climate risk from compound events. Nature Climate Change 2018; 8: 469–477.

8. IPCC. Intergovernmental panel on climate change climate change 2013: Fifth assessment report (AR5). Cambridge, UK: Cambridge University Press; 2013.

9. Nicholls RJ. Coastal flooding and wetland loss in the 21st century: Changes under the SRES climate and socioeconomic scenarios. Global Environmental Change 2004; 14(1): 69–86.

10. Hinkel J, Lincke D, Vafeidis AT, *et al*. Coastal flood damage and adaptation costs under 21st century sea-level rise. PNAS 2014; 111(9): 3292–3297.

11. Feng S. Introduction to storm surge. Beijing, China: Science Press; 1982.

12. IPCC. Intergovernmental panel on climate change climate change 1990: First assessment report (AR1). Cambridge, UK: Cambridge University Press; 1990.

13. Nicholls RJ, Hanson SE, Lowe JA, *et al*. Sea-level scenarios for evaluating coastal impacts. Wiley Interdisciplinary Reviews: Climate Change 2014; 5(1): 129–150.

14. Hoozemans FMJ, Marchand M, Pennekamp HA. Sea level rise: A global vulnerability assessment: Vulnerability assessment for population, coastal wetlands and rice production on a global scale. Hague, the Netherlands: Delft Hydraulics; 1993.

15. Baarse G. Development of an operational tool for global vulnerability assessment (GVA): Update of the number of people at risk due to sea level rise and increasing flooding probability. CZM-Centre Publication No.3. Hague, the Netherlands: Ministry of Transport, Public Works and Water Management; 1995.

16. Nicholls RJ, Mimura N. Regional issues raised by sea level rise and their policy implications. Climate Research 1998; 11(1): 5–18.

17. Klein RJT, Nicholls RJ. Assessment of coastal vulnerability to climate change. AMBIO 1999; 28(2): 182–187.

18. Kang L, Ma L, Liu Y. Evaluation of farmland losses from sea level rise and storm surges in the Pearl River Delta region under global climate change. Journal of Geographical Sciences 2016; 26(4): 439–456.

19. Mawdsley RJ, Haigh ID. Spatial and temporal variability and long-term trends in skew surges globally. Frontiers in Marine Science 2016; 3: 29. doi:10.3389/fmars.2016.00029.

20. Woodworth PL, Blackman DL. Evidence for systematic changes in extreme high waters since the mid-1970s. Journal of Climate 2004; 17(6): 1190–1197.

21. Marcos M, Tsimplis MN, Shaw AGP. Sea level extremes in southern Europe. Journal of Geophysical Research: Oceans 2009; 114: C01007. doi: 10.1029/2008JC004912.

22. Menendez M, Woodworth PL. Changes in extreme high water levels based on aquasi-global tide-gauge dataset. Journal of Geophysical Research: Oceans

2010; 115: C10011. doi: 10.1029/2009JC005997.

23. Woodworth PL, Menendez M, Gehrels WR. Evidence for century-time scale acceleration in mean sea levels and for recent changes in extreme sea levels. Surveys in Geophysics 2011; 32(4-5): 603–618.

24. Feng X, Tsimplis MN. Sealevel extremes at the coasts of China. Journal of Geophysical Research: Oceans 2014; 119(3): 1593–1608.

25. Feng J, von Storch H, Jiang W, *et al*. Assessing changes in extreme sea levels along the coast of China. Journal of Geophysical Research: Oceans 2015; 120(12): 8039–8051.

26. Nicholls RJ, Hoozemans FMJ, Marchand M. Increasing flood risk and wetland losses due to global sea-level rise: Regional and global analyses. Global Environmental Change 1999; 9: S69–S87.

27. Shi Y, Yang G. Sea level rise and its impacts in China: Impacts and countermeasures of sea level rise on China's delta region. Beijing, China: Science Press; 1994.

28. ShiY, Zhu J, Xie Z, *et al*. Prediction and countermeasures of sea level rise in the Yangtze River Delta and adjacent areas. Science in China: Earth Sciences 2000; 30(3): 225–232.

29. Wu S, Feng A, Gao J, *et al*. Shortening the recurrence periods of extreme water levels under future sea-level rise. Stochastic Environmental Research and Risk Assessment 2017; 31(10): 2573–2584.

30. Wahl T, Chambers DP. Evidence for multidecadal variability in US extreme sea level records. Journal of Geophysical Research: Oceans; 120(3): 1527–1544.

31. Shi X, Tan J, Guo Z, *et al*. A review of risk assessment of storm surge disaster. Advances in Earth Science 2013; 28(8): 866–874.

32. Muis S, Verlaan M, Winsemius HC, *et al*. A global reanalysis of storm surges and extreme sea levels. Nature Communications 2016; 7: 11969. doi: 10.1038/ncomms11969.

33. Wahl T, Haigh ID, Nicholls RJ, *et al*. Understanding extreme sea levels for broad-scale coastal impact and adaptation analysis. Nature Communications 2017; 8: 16075. doi: 10.1038/ncomms16075.

34. Wu S, Feng A, Gao J, *et al*. Shortening the recurrence periods of extreme water levels under future sea-level rise. Stochastic Environmental Research and Risk As-

sessment 2017; 31(10): 2573–2584

35. Li K, Li G. Risk assessment of storm surges in the coastal area of Guangdong Province in year 2050 under climate change. Science & Technology Review 2017; 35(5): 89–95.

36. Chen M, Bai R, Zuo J, *et al*. Discussion of sea level prediction along the coastal of China. Marine Environmental Science 2013; 32(3): 451–455.

37. Duan X, Xu X, Chen M, *et al*. Methodology and case study of sea level prediction based on secular tide gauge data. Acta Scientiarum Naturalium Universitatis Pekinensis 2014; 50(6): 1065–1070.

38. Zuo J, Zuo C, Li J, *et al.* Advances in research on sea level variations in China from 2006 to 2015. Journal of Hohai University (Natural Sciences) 2015; 43(5): 442–449.

39. Church JA, Clark PU, Cazenave A, *et al*. Sea-level rise by 2100. Science 2013; 342:1445. doi:10.1126/science.342.6165.1445-a.

40. Jevrejeva S, Grinsted A, Moore JC. Upper limit for sea level projections by 2100. Environmental Research Letters 2014; 9: 104008. doi: 10.1088/1748-9326/9/10/104008.

41. Kopp RE, Horton RM, Little CM, *et al*. Probabilistic 21st and 22nd century sea-level projections at a global network of tide-gauge sites. Earth's Future 2014; 2(8): 383–406.

42. Wen J, Yuan S, Li D, *et al*. Sea level rise and its risk management. Advances in Earth Science 2018; 33(4): 350–360.

43. Lin N, Emanuel K, Oppenheimer M, *et al*. Physically based assessment of hurricane surge threat under climate change. Nature Climate Change 2012; 2(6): 462–467.

44. Ward PJ, Jongman B, Aerts JCJH, *et al*. A global framework for future costs and benefits of river-flood protection in urban areas. Nature Climate Change 2017; 7(9): 642–646.

45. Aerts JCJH, Bouwer LM, Winsemius HC, *et al*. FLOPROS: An evolving global database of flood protection standards. Natural Hazards and Earth System Sciences 2016; 16(5): 1049–1061.

46. Cai F, Su X, Liu J, *et al*. Coastal erosion in China under the condition of global climate change and measures for its prevention. Progress in Natural Science

2009; 19(4): 415–426.

47. Ma Z, Melville DS, Liu J, *et al*. Rethinking China's new great wall. Science 2014; 346: 912–914.

48. Syvitski JPM, Kettner AJ, Overeem I, *et al*. Sinking deltas due to human activities. Nature Geoscience 2009; 2(10): 681–686.

49. Woodruff JD, Irish JL, Camargo SJ. Coastal flooding by tropical cyclones and sea-level rise. Nature 2013; 504: 44–52.

50. Nicholls RJ, Cazenave A. Sea-level rise and its impact on coastal zones. Science 328: 2010; 1517–1520.

51. Zheng X, Wu Q, Ying Y, *et al*. Impacts of relative sea-level rising and strategies of control of land subsidence in coastal region of China. Bulletin of Science and Technology 2001; 17(6): 51–55.

52. Spencer T, Schuerch M, Nicholls RJ, *et al*. Global coastal wetland change under sea-level rise and related stresses: The DIVA wetland change model. Global and Planetary Change 2016; 139: 15–30.

53. Hanson S, Nicholls R, Ranger N, *et al*. A global ranking of port cities with high exposure to climate extremes. Climatic Change 2011; 104(1): 89–111.

54. Jongman B, Ward PJ, Aerts JCJH. Global exposure to river and coastal flooding: Long term trends and changes. Global Environmental Change 2012; 22(4): 823–835.

55. Hallegatte S, Green C, Nicholls RJ, *et al*. Future flood losses in major coastal cities. Nature Climate Change 2013; 3(9): 802–806.

56. Vousdoukas MI, Mentaschi L, Voukouvalas E, *et al*. Climatic and socioeconomic controls of future coastal flood risk in Europe. Nature Climate Change 2018; 8(9): 776–780.

57. Brown S, Hanson S, Nicholls RJ. Implications of sea level rise and extreme events around Europe: A review of coastal energy infrastructure. Climatic Change 2014; 122(1-2): 81–95.

58. Willis HH, Narayanan A, Fischbach JR, *et al*. Current and future exposure of infrastructure in the United States to Natural Hazards. California, CA: RAND; 2016.

59. UNISDR. Terminology on disaster risk reduction. New York, NY: UNISDR; 2009.

60. Zhou Y, Wang J. A review on development of vulnerability curve of natural disaster. Advances in Earth Science 2012; 27(4): 435–442.

61. Shi X, Guo Z, Zhang Y, *et al*. A review of research on vulnerability to storm surges. Progress in Geography 2016; 35(7): 889–897.

62. FEMA. HAZUS-MH flood model: Technical manual [EB/OL]. 2015-12-01 [2017-08-22]. https://www.fema.gov/media-library/assets/documents/24609?id=5120.

63. Jonkman SN, Vrijling JK. Loss of life due to floods. Journal of Flood Risk Management 2008; 1(1): 43–56.

64. Yin Z, Xu S. Study on risk assessment of urban natural hazards. Beijing, China: Science Press; 2012.

65. Cutter SL, Finch C. Temporal and spatial changes in social vulnerability to natural hazards. PNAS 2008; 105(7): 2301–2306.

66. Tan LR. Assessment on comprehensive vulnerability of storm surge disasters of China's coastal regions. Shanghai, China: East China Normal University; 2012.

67. Su S, Pi J, Wan C, *et al*. Categorizing social vulnerability patterns in Chinese coastal cities. Ocean & Coastal Management 2015; 116: 1–8.

68. Fang J, Chen W, Kong F, *et al*. Measuring social vulnerability to natural hazards of the coastal areas in China. Journal of Beijing Normal University (Natural Science) 2015; 51(3): 280–286.

69. Wang N, Zhang LQ, Yuan L, *et al*. Research into vulnerability assessment for coastal zones in the context of climate change. Acta Ecologica Sinica 2012; 32(7): 2248–2258.

70. Wang T, Zou X, Li B. Research progress of coastal vulnerability to varied driving factors. Marine Science Bulletin 2015; 34(4): 361–369.

71. Li H, Yang G. The advance in studies on coastal vulnerability to global change. Advance in Earth Sciences 2002; 17(1): 104–109.

72. Chu J, Gao S, Xu J. Risk and safety evaluation methodologies for coastal systems: A review. Marine Science Bulletin 2005; 24(3): 80–87.

73. Sun L, Shi C. Progress in vulnerability assessment of natural disasters in coastal cities. Journal of Catastrophology 2007; 22(1): 102–105.

74. Yin J, Yin Z, Xu S. Composite risk assessment of typhoon-induced disaster for China's coastal area.

Natural Hazards 2013; 69(3): 1423–1434.

75. Li X, Duan X, Zhang Z, *et al*. The vulnerability zoning research on the sea-level rise of Chinese coastal. Journal of Catastrophology 2016; 31(4): 103–109.

76. Mcleod E, Poulter B, Hinkel J, *et al*. Sea-level rise impact models and environmental conservation: A review of models and their applications. Ocean & Coastal Management 2010; 53(9): 507–517.

77. Hall JW, Meadowcroft IC, Sayers PB, *et al*. Integrated flood risk management in England and Wales. Natural Hazards Review 2003; 4(3): 126–135.

78. Rowley RJ, Kostelnick JC, Braaten D, *et al*. Risk of rising sea level to population and land area. Eos, Transactions, American Geophysical Union 2007; 88(9): 105–107.

79. Fang J, Sun S, Shi P, *et al*. Assessment and mapping of potential storm surge impacts on global population and economy. International Journal of Disaster Risk Science 2014; 5(4): 323–331.

80. Bates PD, De Roo APJ. A simple raster-based model for flood inundation simulation. Journal of Hydrology 2000; 236(1): 54–77.

81. Bradbrook K. JFLOW: A multi scale two-dimensional dynamic flood model. Water and Environment Journal 2006; 20(2): 79–86.

82. Yu D, Lane SN. Urban fluvial flood modelling using a two-dimensional diffusion-wave treatment, part I: Meshre solution effects. Hydrological Processes 2006; 20(7): 1541–1565.

83. Yu D, Lane SN. Urban fluvial flood modelling using a two-dimensional diffusion-wave treatment, part II: Development of a sub-grid-scale treatment. Hydrological Processes 2006; 20(7): 1567–1583.

84. Yin J, Yu D, Yin Z, *et al*. Evaluating the impact and risk of pluvial flash flood on intra-urban road network: A case study in the city center of Shanghai, China. Journal of Hydrology 2016; 537: 138–145.

85. Yin J, Yu D, Lin N, *et al*. Evaluating the cascading impacts of sea level rise and coastal flooding on emergency response spatial accessibility in Lower Manhattan, New York City. Journal of Hydrology 2017; 555: 648–658.

86. Sterr H. Assessment of vulnerability and adaptation to sea-level rise for the coastal zone of Germany. Journal of Coastal Research 2008; 24(2): 380–393.

87. Parris AS, Bromirski P, Burkett V, *et al*. Global sea level rise scenarios for the United States National Climate Assessment. NOAA Tech Memo OAR Climate Program Office; 2012.

88. Lemmen DS, Warren FJ, James TS, *et al*. Canada's marine coasts in a changing climate. Ottawa, Canada: Government of Canada; 2016.

89. Sayers PB, Horritt M, Penning-Rowsell E, *et al*. Climate change risk assessment 2017: Projections of future flood risk in the UK[R]. London, UK: Committee on Climate Change; 2017.

90. Lin N, Emanuel K. Grey swan tropical cyclones. Nature Climate Change 2016; 6(1): 106–111.

91. Rahmstorf S. Rising hazard of storm-surge flooding. PNAS 2017; 114(45): 11806–11808.

92. Lamb R, Keef C, Tawn J, *et al*. A new method to assess the risk of local and widespread flooding on rivers and coasts. Journal of Flood Risk Management 2010; 3(4): 323–336.

93. Wahl T, Jain S, Bender J, *et al*. Increasing risk of compound flooding from storm surge and rainfall for major US cities. Nature Climate Change 2015; 5(12): 1093–1097.

94. Hinkel J, Jaeger C, Nicholls RJ, *et al*. Sea-level rise scenarios and coastal risk management. Nature Climate Change 2015; 5(3): 188–190.

95. JiangT, Zhao J, Cao L, *et al*. Projection of national and provincial economy under the shared socioeconomic pathways in China. Climate Change Research 2018; 14(1): 50–58.

96. Jiang T, Zhao J, Jing C, *et al*. National and provincial population projected to 2100 under the shared socioeconomic pathways in China. Climate Change Research 2017; 13(2): 128–137.

97. Aerts JCJH, Botzen WJW, Emanuel K, *et al*. Evaluating flood resilience strategies for coastal megacities. Science 2014; 344: 473–475.

98. Linham MM, Nicholls RJ. Adaptation technologies for coastal erosion and flooding: A review. Proceedings of the ICE—Maritime Engineering 2012; 165(3): 95–112.

99. Feng AQ, Gao JB, Wu SH, *et al*. A review of storm surge disaster risk research and adaptation in China under climate change. Progress in Geography 2016; 35(11): 1411–1419.

115

100. Pelling M, Blackburn S. Megacities and the coast: Risk, resilience and transformation. London, UK: Routledge; 2014.

Review Article

Evaluating models and effective factors obtained from remote sensing (RS) and geographic information system(GIS) in the prediction of forest fire risk: A structured review

Akram Karimi[1], Sara Abdollahi[2], Kaveh Ostad-Ali-Askari[3*], Vijay P. Singh[4], Saeid Eslamian[5], Ali Heidarian[5], Mohsen Nekooei[5], Hossein Gholami[3], Sona Pazdar[6]

[1]*Graduate Degree in Environmental Education, Evaluation and Evaluation Tendency, Karaj Environmental Faculty, Karaj, Iran.*

[2]*MSc of Environmental Science, Yazd University, Yazd, Iran.*

[3]*Department of Civil Engineering, Isfahan (Khorasgan) Branch, Islamic Azad University, Isfahan, Iran. E-mail: kaveh.oaa2000@gmail.com*

[4]*Department of Biological and Agricultural Engineering &Zachry Department of Civil Engineering, Texas A and M University, 321 Scoates Hall, 2117 TAMU, College Station, Texas 77843-2117, U.S.A.*

[5]*Department of Water Engineering, College of Agriculture, Isfahan University of Technology, Isfahan, Iran.*

[6]*Civil Engineering Department, Aghigh University, Shahinshahr, Iran.*

ABSTRACT

Fire, a phenomenon occurs in most parts of the world and causes severe financial losses, even, irreparable damages. Many parameters are involved in the occurrence of a fire; some of which are constant over time (at least in a fire cycle), but the others are dynamic and vary over time. Unlike the earthquake, the disturbance of fire depends on a set of physical, chemical, and biological relations. Monitoring the changes to predict the occurrence of fire is efficient in forest management. **Method:** In this research, the Persian and English databases were structurally searched using the keywords of fire risk modeling, fire risk, fire risk prediction, remote sensing and the reviewed papers that predicted the fire risk in the field of remote sensing and geographic information system were retrieved. Then, the modeling and zoning data of fire risk prediction were extracted and analyzed in a descriptive manner. Accordingly, the study was conducted in 1995-2017. **Findings:** Fuzzy analytic hierarchy process (AHP) zoning method was more practical among the applied methods and the plant moisture stress measurement was the most efficient among the remote sensing indices. **Discussion and Conclusion:** The findings indicate that RS and GIS are effective tools in the study of fire risk prediction.
Keywords: Modeling; Risk Prediction; Fire; Fire Risk Modeling; Remote Sensing; Geographic Information System

1. Introduction

Fire is considered as one of the main causes of disturbance and change in most natural ecosystems[1]. According to the statistics provided by the organization, forests and rangelands contribute as much as 61.82%. Investigations show that the major Iranian fires occur in these areas[2]. Forest fires are one of the main concerns in many parts of the world not only from an environmental point of view but also from an economic, social, and security perspective[3]. Through the Middle East and North Africa, Iran is ranked as the fourth country in terms of forest fire[4]. Since planning before the fire requires being aware of when and where it is likely to occur, or where it has a more negative effect, the assessment of fire risk is the major component of fire control[5]. Fire ri-

sk assessment is one of the basic tasks for forest fire control and management in forest zones and the zones with forest fire risk can be a useful guide for the forest fire management, which is a very important prevention strategy[6]. The high-risk fire zones referred to as zones with the potential of fire or the zones in where the fire easily extends[7]. The most effective way to reduce the damage caused by forest fires is to prevent fire using all appropriate conservation and management measures. Various studies have been conducted to improve the early prediction of fire and detection systems to develop the response strategies during the incident time[8,9]. However, today, with the development of remote sensing technology, satellite imagery is used as the most important tool to control, prevent, and monitor zones for fire and geographic information systems to integrate remote sensing and land-based information. In recent decades, researchers have predicted fire risk zones including fire risk zoning and modeling using remote sensing and geospatial applications[10]. Due to their frequent applications, these sciences play a crucial role in environmental assessments. Numerous studies have been done so far in Iran especially in Golestan Province regarding forest fires. The present study is a structured review aimed at determining the models and effective factors obtained by RS and GIS in predicting fire risk.

2. Theoretical framework and bases

Initially, the definitions related to the issue of fire are discussed that has been mentioned frequently in various papers.

2.1 Definition of fire

Fire is one of the destruction factors causing damage to human life and properties in addition to economic damage and environmental pollution. The imposed damage rate is different depending on the types and severity of the fire, etc. that is also important in different countries and zones where the probability of fire is high, and where the management of fire control and monitoring is more important[11].

2.2 Risk assessment

The incident occurrence possibility refers to the probability of its occurrence and severity. The outcome of the risk assessment should determine whether the risk is tolerable or not[12].

Vulnerability: A combination of two words of risk and fire (the probability of its start and extend) and vulnerability due to a fire (the result of a fire)[13]. In addition, it means assessing the constant and changing factors of the fire environment (fuel, water, air, and topography), which determines the ease of combustion, the speed of expansion, the difficulty of controlling, and the effects of the fires[14].

2.3 Fire occurrence risk

The probability of fire occurrence varies in terms of time and place. Usually, the probability of fire occurrence is determined at various levels, such as low, moderate, high and very high, or with terms like improbable, possible, probable, and high probable[11]. According to the definition of Food and Agriculture Organization, the risk of fire occurrence is through the presence or activity of any effective factor. According to another definition, fire risk is the potential of combustion sources[15].

2.4 Modeling

The process of creating and choosing a model is called modeling. The transformation of a statistical concept into a mathematical language is a kind of modeling. The more math concepts are used, the more valuable the model will be established[16].

2.5 Fire risk map

A digital map is regarded to a specific zone, which is created by combining multiple and effective thematic layers in the event of a fire. To create a risk map, initially, a weight is considered for each layer depending on their effect. The greater the effect of each variable, the higher the weight for that variable will be considered[17].

So far, various models have been used to assess the fire risk, which include comparing the performance of more conventional, more accurate, and more recent models to use the best model in the future research. However, in order to achieve accurate results, it is always necessary to note that which model or method has an acceptable accuracy in generating a potential fire risk map. In order to es-

timate how and when the fire will have adverse effects, it is necessary to consider a model that will consider the fire and its potential for expansion as well as the fire vulnerability[18]. Considering the most effective factors, the proper weight allocation is very important to select the best forest fire risk model. The use of remote sensing data from satellite due to its features such as wide and integrated view, the use of large sections, the use of different parts of the electromagnetic spectrum to record the phenomena, speed and transmission and the variety of data forms, and especially their repetition, are unique. Therefore, it has been used as a suitable tool for the assessment, monitoring, control, and management of water, soil, forest, and rangeland resources. Today, such images are widely used in various studies of natural resources and the preparation of various maps. For example, Chuvieco *et al.*[19] and Haji Mohammadi & Biranoond[20] used remote sensing and geographic information systems to improve the framework for assessing the risk of fire. The risk of fire based on the probability of occurrence and potential damage can be evaluated and human and natural sources are considered as important sources of fire.

3. Research method

This research was conducted through a structured review aimed at determining the models and factors affecting the prediction of fire incidence in Iran. To this end, the SID, Google Scholar, Magiran and Iran Medex databases were searched for retrieval of internal papers and the ScienceDirect database for the retrieval of English papers during 1995-2017. The English keywords include fire risk prediction, fire risk assessment, remote sensing, and Persian keywords include modeling, risk prediction, fire, fire risk modeling, remote sensing, and geographic information system. The fire risk prediction keywords are combined using the function and once or together. The inclusion criterion is the research papers that used remote sensing and geographic information systems in the field of fire risk prediction. Then, the papers whose full text was available were reviewed. The required data such as introduction, study location, the purpose of the study, data collection sources, and the study area were extract-

ed. Most of the papers have obtained their required data from Modis images and weather stations located in the study area while other satellites including IRS-1D (and LISS-III) have also been used.
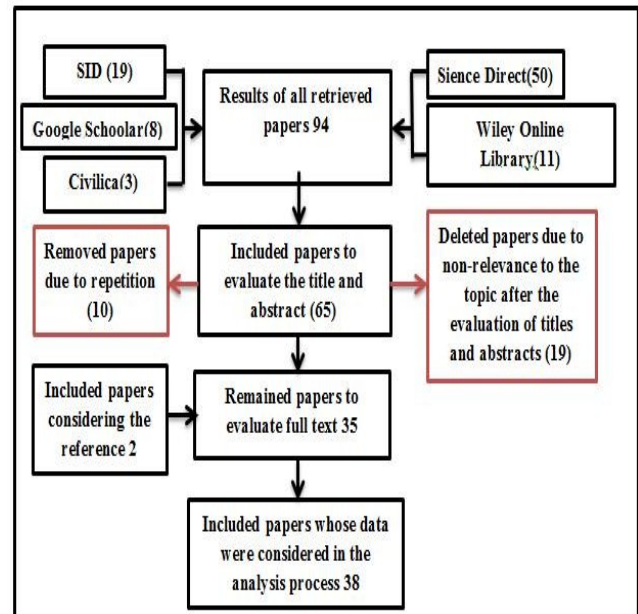

Figure 1. General steps of the method.

4. Findings and results

Following the search for the structured keywords in online databases, 50 papers were retrieved. After removing repetitive and unrelated papers, 38 eligible papers were selected for further analysis. The results show that the number of papers in the field of fire risk has increased over time. Various data sources were used to collect data. The studied papers were classified into two categories, namely zoning and modeling. One of the zoning papers such as Mosavari *et al.*'s [21] for fire risk zoning in the forests of Golestan Province has used (slope, direction, altitude, rain, climate, wind speed, moisture, temperature, plant type, plant density) and biological agents (distance from the village, distance from the road). Using the hierarchical analysis method, the factors affecting the occurrence and expansion of fire were compared in paired wise and their coefficient was determined. Eventually, a fire risk map was developed in five classes of very low, low, moderate, severe, and very severe.

Modeling studies include quantitative, qualitative or statistical models that are described below. Murta & Bozer[22], Makia *et al.*[23], Jaiswal *et al.*[7] and Adab *et al.*[4] predicted the vegetation water

situation using remote sensing and satellite imagery such as IRS, LISS-III, and MODIS. Nepstad[24] have applied drought indices to predict the risk of fire. The remote sensing data and meteorological data (temperature, relative moisture, and precipitation) and map of vegetation, slope, distance from the road and residential zones were integrated in GIS, as well as measuring the relationship between leaf water content and the normal water index, near infrared band, and confirmation of infrared short wave spectral data. They concluded that vegetation status such as Normalized difference moisture index (NDMI) and Global Vegetation Moisture Index (GVMI) in temperate zones shows the fore model better than the normalized vegetation index (NDMI). They have predicted the zones with fire risk potential with an acceptable accuracy.

Other types of research including the studies of Xu et al.[25], Beygi et al.[26], Nasiri[27], Chandra [28], Sharma et al.[29], Mohammadi et al.[30], Mosavari et al.[21], Jahdi et al.[31], Darvishi et al.[32], Behzadfar & Vahid[33], Aghajani et al.[34], Huyền & Tuân[35], and other researchers developed the map of fire risk zones by specifying weights via Analytic Hierarchy Process (AHP) or fuzzy logic for factors such as slope, direction, altitude, land use, distance from the road and distance from the canal, type of vegetation and distance from residential zones, and Canopy Coverage percentage. Finally, the fire risk map was prepared using the weight layers and weight coefficient for each of the factors and the zones were classified into four classes of very high sensitivity, high sensitivity, low sensitivity, and moderate sensitivity

Huyen and Tuna obtained the fire risk map using the following model[35]:

$$CFRISK = 0.4379 \times FUI + 0.2190 \times SLI + 0.2437 \times ASI + 0.0994 \times AC \qquad (1)$$

CFRISK is the cumulative fire risk index value; SLI is the slope index; ASI is the aspect index; ACI is the accessibility index and FUI is the fuel type index.

Adab et al. used the following model with regard to the factors affecting fire in the province[4] .

$$HFI = [100v + 50s + 25a + 10.(r + c) + 5e]/10 \qquad (2)$$

Where; v, s, a, r, c, and e indicate vegetation moisture, slope, aspect, distance from road, and

distance.

They also conducted the forest fire risk zoning in another research using Molgan's fire awareness models based on the atmospheric parameters in determining the potential and severity of forest fires as well as GIS technique. The results indicated that the applied model has a proper efficiency at spatial level annually in all seasons except for winter, which is as follows.

$$G = \sum_{n-1}^{n-m} T - D \qquad (3)$$

Table 1. G values for determining the intensity of the fire

Value of ignition index	Interpretation
G=300	No fire risk
301<G<500	Low fire risk
501<G<1000	Moderate fire risk
1001<G<4000	High fire risk
G>4000	Very high fire risk

In which, T is the air temperature (0°C), Dis saturation vapor pressure deficiency in millimeter-sis number of days since the rain has passed. The following parameters are presented in terms of the calculation of the intensity of the parameter G[36].

In another study[25], a fire risk map was developed using aerial images and the following model.

$$RC = 7 \times VT + 5 \times (S + A + E) + 3(DR + DS + DF) \qquad (4)$$

RC is the numerical index of forest fire risk where VT indicates the vegetation type; S indicates the slope, A indicates the aspect and E indicates the elevation. DR, DS, and DF indicate the distance from roads, settlements, and farmlands, respectively.

In another study, using Xu's model, the authors investigated the fire risk areas in the northern part of Iran.

Also in another study, Fire Risk Zonation Index model was applied[37]:

$$FRZI = (FTI \times 9) + (ASI \times 7) + (RDI \times 6) + (SLI \times 5) + (ELI \times 4)/10* \qquad (5)$$

Where FRZI is the fire risk zonation index; FTI is the fuel type index; SLI is the slope index; ASI is the aspect index; RDI is the road index; ELI is the elevation index.

Other researchers developed a fire risk map for Indian woodlands using aerial photos and GIS. In this research, firstly, the most important factors influencing the fire of the study area were identified. Then, by plotting vegetation map, slope, distance

from the road and residential areas, they were weighed based on the sensitivity to the potential of fire and using the index and integration in the GIS environment. The hazardous forest map of the forest area studied in the four classes of fire hazard category is very low to low. The results of this study show a high correlation with fire areas.

$$FR = 10Fi(1-11) + 2Hj(1-4) + 2Rk(1-4) + 3Sl(1-6) \qquad (6)$$

In another study, Yin et al.[38] used an index FFR for fire hazard modeling, in which the *FFR* forest fire risk index (*V*) is vegetation variable (with 9 classes), *P* near residential areas (with 4 classes), *S* tilt factor (with 5 classes), *A* direction (with 4 classes) and subcategories *i, j, k, l, m* classes.

$$FFR = 0.40Vi + 0.15pj + 0.15Ai + 0.15Hm \qquad (7)$$

Tran *et al.* used the following risk model to predict the risk of fire[39].

$$SIMap = (FR \times 0.4) + (SR \times 0.2) + (RR \times 0.2) + (SR \times 0.1) + (AR \times 0.1) \qquad (8)$$

In which, *SIMap* is susceptibility index map; *FR* is rated forest; *SR* is rated settlement; *RR* is rated road; *SR* is rated slope and *AR* is rated aspect.

Saxena *et al.*[40] identified the fire risk zones using the following models. The results of this research show a good adaptation between fire zones and high fire risk zones.

$$FRZI = 5Vi = (1-10) + 4Aj = (1-5) + 2Sk = (1-6) + 1Rl = (1-10) \qquad (9)$$

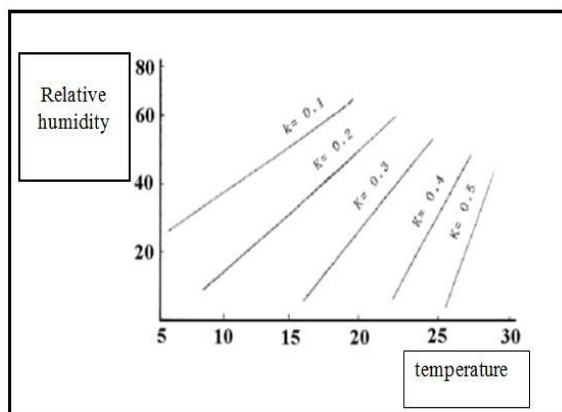$$FRZI = (5As + 4El + 5Sl + 9Ft + Dr + 7Hb + 5Rd)/10 \qquad (10)$$

Figure 2. Forest fire risk coefficient through Francilla method.

A study has been conducted, which used Francilla model and applied two main factors of the maximum temperature and the minimum relative moisture compared to the fire risk estimation and the preparation of risk map with different degrees of very severe, severe, moderate, and poor for different month separately at the studied zone[41] (See **Figure 2**).

Vadrevu *et al.*[42] used a fuzzy theory to design a fire risk map with decision-making algorithms in a GIS environment as a framework for preparing a fire risk map. The result of this study was a good demonstration of high-risk zones, which shows that using multi-criteria decision making combined with the GIS environment can be a useful tool to assess the occurrence of a fire. In another research, the use of remote sensing and geographic information systems was developed to prepare a fire risk map[43]. Remote sensing and satellite information systems are the basis of the fire models that are well suited to the risky zones. In this research, the satellite data (1989-2006) were used to survey burned zones. Different classes based on the sensitivity to fire are in the four classes of very sensitive to very low sensitivity. Mohammadinejad & Tavakoli studied the fire status in oak and wild pistachio (Pistacia atlanticaDesf) forests in Lorestan Province using GIS[44]. The results indicate that the most important cause of destruction in the forests of Zagros and west of the country is fire[44].

5. Discussion

This review study was conducted to evaluate the studies on forest fire risk prediction. A review of various studies showed that the thematic field of almost half of the risk zoning studies has been qualitative and moisture stress and temperature and moisture rate were the factors affecting the zoning of vegetation index. A high percentage of studies have used remote sensing and geographic information systems capabilities and reported the incidence of fire. Other papers also have access to information from meteorological stations. The other class of fire modeling studies has been carried out. Among the models made in various studies, three categories of fire risk models are discussed in this study[45]. The resulting map is a qualitative categorization for different zones. These types of models are provided periodically and seasonally. These models can be divided into three general categories:

5.1 Qualitative and quantitative models based on expertise

Quantitative models based on expertise classify the variables of fire using numerical scales carried out based on the weight of the ground observations of the research and expert opinions. The main advantage of this modeling is the possibility to detect the high-risk zone for decision-making and management. Also, these models show the possibility of spreading or starting a fire and identify areas with high fire potential[10,46].

5.2 Quantitative models based on multi-criteria evaluation

Multi-criteria models also use expert knowledge for modeling. This method is useful when the opinions of the experts are diverse in order to reach an agreement between experts. This can be mentioned in the study of Chen *et al.*[47].

5.3 Statistical models

Statistical models are often accurate and these models depend on the spatial properties of the studied area. Therefore, they cannot be used for extrapolation and other areas. These models include linear and nonlinear regression, logistic regression, and Poisson distribution[46,48]. When the fire model is very different or the fire variables are not very clear, the neural network is a suitable method.

Also, models are divided into two groups of long-term and short-term based on the time scale and spatial scale. Long-term models use static parameters such as topography, road networks, and vegetation types. These models show the fire risk model and they are useful for forest management and monitoring to prevent the occurrence of fire. Short-term models use meteorological data and predict the risk of fire on a daily or weekly basis. Some of these systems can be Canadian Forest Fire Danger Rating System (NFDRS) (Carla and Switzerland, 2013). Forest fires are one of the destructive factors of these ecosystems, and efforts should be made to anticipate the occurrence of a fire before it occurs. Correct information about the factors that affects fire and its continuous monitoring can help forest management to prevent this disruptive factor. Therefore, RS and GIS are good tools for zoning

high-risk zones for better management. This technology allows researchers to keep monitoring any changes in the level of vegetation indices to create a suitable and dynamic mode for each zone individually[6]. The main elements affecting the fire risk are environmental factors (slope, direction, attitude, rain, climate, wind speed, moisture, temperature, vegetation type, vegetation density) and biological factors (distance from the village, distance from the road)[21]. All of these elements have a different effect. Combining these factors together creates homogenize zones of risk rate that provide a valuable opportunity for forest management. Remote sensing and geographic information system are invaluable and useful software for integrating all factors and achieving results[32,46]. Regarding preparing the fire distribution map, Stolle *et al.*[49] investigated the relationship between the land use and the occurred fires. Vazquez and Moreno examined the distribution model of the fire points, and Juan *et al.*[51] used Cornell method to prepare the fire risk map. The results of the studies show that the vegetation indices and their integration with other factors affecting the occurrence of fire and conducting a comprehensive assessment can be easily done using remote sensing and geographic information system, which is a new method in risk assessment studies. Investigating the fire location with vegetation indices increases the awareness of researchers regarding the incidence of fire. This could give a new and profound understanding of forest management[4]. The studies that have been used to predict the risk of a fire, which have been investigated in this study, are often limited to qualitatively zoning of the maps from low risk to high risk. Due to the high capacity of remote sensing, the continuous monitoring of forests to dynamically and daily express the fire risk has been scarcely considered. Although the technology of geographic information systems is rapidly expanding, it often has the ability to integrate meteorological station and remote sensing information. Nevertheless, it is necessary to pay more attention to the capabilities of this science. This study is one of the first studies that have systematically examined the studies that have been so far carried out on the assessment of fire risk using remote sensing or GIS. Some of the limitations of this study were the

fact that some of the studies in the field of fire were aimed to find and control the fire after the occurrence and some other, while the distinction between risk prediction and fire behavior was problematic.

6. Conclusion

Forest is affected by several factors such as human factors and natural factors that are divided into two types of constant factors and variable factors over time. Controlling human factors and monitoring of variable natural factors over time can play an important role in controlling unexpected fires in the forest. The use of geographic information systems and remote sensing to monitor natural hazards is increasing in Iran. Therefore, the attention of forestry managers to the capabilities of this software and attention to the conducted studies in this regard is necessary and useful.

Conflict of interest

The authors declare that they have no conflict of interest.

Funding information

Author's contributions

In writing this article, the authors had an equal share of participation and participated in all stages, including writing, editing, arbitration, and all stages of scientific work.

Ethics

In this article, all ethical principles related to scientific-research articles such as validity and authenticity, originality, data collection in a standard manner, integrity, and accuracy of research and etc. are observed.

Acknowledgments

References

1. Fearnside PM. Deforestation in Brazilian Amazonia: History, rates, and consequences. Conservation Biology 2005; 19(3): 680–688. doi: https://doi.org/10.1111/j.1523-1739.2005.00697.x.
2. Ardakani S, Voldazoj M, Mohamadzade A, *et al.* Spectroscopic characterization of fire and field objectives for identification and separation in remote sensing data (PhD thesis). Tehran: Khaje-Naseerdin-Toosi University of Technology; 2010.
3. Miller DE, Hays CR. Missouri Drought Response Plan. Water Resource Report No. 44; 1995. p. 52.
4. Adab H, Kanniah D, Solaimani K. GIS-based probability assessment of fire risk in grassland and forested landscapes of Golestan Province, Iran. International Conference on Environmental and Computer Science IPCBEE; Singapore: IACSIT Press; 2011. Available from: http://www.ipcbee.com/vol19/33-ICECS2011R30007.pdf.
5. Chuvieco E, Aguado I, Yebra M, *et al.* Development of a framework for fire risk assessment using remote sensing and geographic information system technologies. Ecological Modelling 2010; 221(1): 46–58.
6. Mohammadi F. Preparation of forest fire hazard map using satellite imagery and GIS in a part of Paveh forest (in Persian). Kurdistan Natural Resources Faculty 2009; p. 69.
7. Jaiswal RK, Mukherjee S, Raju KD, *et al.* Forest fire risk zone mapping from satellite imagery and GIS. International Journal of Applied Earth Observation and Geoformation 2002; 4(1): 1–10. doi: https://doi.org/10.1016/S0303-2434(02)00006-5.
8. Alonso-Betanzos A, Fontenla-Romero O, Guijarro-Berdiñas B, *et al.* An intelligent system for forest fire risk prediction and firefighting management in Galicia. Expert Systems with Applications 2003; 25(4): 545–554. doi: https://doi.org/10.1016/S0957-4174(03)00095-2.
9. Bernabeu P, Vergara L, Bosh I, *et al.* A prediction/detection scheme for automatic forest fire surveillance. Digital Signal Processing 2004; 14(5): 481–507. doi: https://doi.org/10.1016/j.dsp.2004.06.003.
10. Roy PS. Forest fire and degradation assessment using satellite remote sensing and geographic information system. Satellite Remote Sensing and GIS Applications in Agricultural Meteorology 2003; 361–400. Available from: http://www.wamis.org/agm/pubs/agm8/Paper-18.pdf.
11. Canadian Forest Service [Internet]. Wildland fires, insects, and disturbances. Available from: http://www.nrcan.gc.ca/forests/fire-insects-disturbances/fire/14470.
12. Boonchut P. Decision support for hazardous material routing. Enschede: International Institute for Geo-information Science and Earth Observation (ITC) (MSc thesis); 2005. Available from: https://www.itc.nl/library/papers_2005/msc/upla/boonchut.pdf.
13. Chuvieco E, Agaudo I, Cocero D, *et al.* Design of an

empirical index to estimate fuel moisture content from NOAA-AVHRR analysis in forest fire danger studies. International Journal of Remote Sensing 2003; 24(8): 1621–1637. doi: https://doi.org/10.1080/01431160210144660b.

14. Taylor SW, Alexander ME. Science, technology, and human factors in fire danger rating: The Canadian experience. International Journal of Wildland Fire 2006; 15(1): 121–135. doi: https://doi.org/10.1071/WF05021.

15. Food and Agriculture Organization (FAO) [Internet]. International Forest Fire News. 1995. Available from: http://www.fao.org/statistics/en/.

16. SadeghiKaji H. Assessment of fire risk and probability in the natural lands of Chaharmahal-va-Bakhtiari Province (MSc thesis) (in Persian). Shahrekord: Shahrekord University; 2011; p. 86.

17. Hernandez-Leal PA, Arbelo M, Gonzalez-Calvo A. Fire risk assessment using satellite data. Advances in Space Research 2006; 37(4): 741–746. doi: 10.1016/j.asr.2004.12.053.

18. Chuvieco E, Sandow Ch, Günther KP, et al. Global burned area mapping from European satellites: The ESA FIRE-CCI project. Journal of Photogrammetry and Remote Sensing 2012; XXXIX-B8: 13–16. doi: https://doi.org/10.5194/isprsarchives-XXXIX-B8-13-2012.

19. Chuvieco E, Aguado I, Jurdao S, et al. Integrating geospatial information into fire risk assessment. International Journal of Wildland Fire 2012; 23(5): 606–619. doi: 10.1071/WF12052.

20. HajiMohammadi H, Bazajeed M, Qalahiri F, et al. The structure of the atmosphere, in the event of a fire in northern Iran (in Persian). Journal of Golestan University (Geospatial Space Magazine Quarterly) 2015; 25(7): 187–206. Available from: http://gps.gu.ac.ir/article_54249.html.

21. Mosavari A, Adhami. Fire hazard zonation using GIS, AHP case study—Caspian forests of northern Iran — Golestan Province (In Persian) 2012; p. 11.

22. Murta A, Bozer R. Estimation of the burned area in forest fires using computational intelligence techniques. Procedia Computer Science 2012; 12: 282–285. doi: https://doi.org/10.1016/j.procs.2012.09.070

23. Makia M, Ishiahra M, Tamura M. Estimation of leaf water status to monitor the risk of forest fires by using remotely sensed data. Remote Sensing of Environment 2004; 90(4): 441–450. doi: https://doi.org/10.1016/j.rse.2004.02.002.

24. Nepstad DC. 2007. The Amazon's vicious cycles: Drought and fire in the greenhouse - ecological and climatic tipping points of the world's largest tropical rainforest, and practical preventive measures. A report to the World Wide Fund for Nature (WWF). Available from: https://digital.library.unt.edu/ark:/67531/metadc226671/m2/1/high_res_d/WWFBinaryitem7658.pdf.

25. Xu D, Dai L, Shao G, et al. Forest fire risk zone mapping from 2005 satellite images and GIS for Baihe Forestry Bureau, Jilin, China. Journal of Forestry Research 2005; 16(3): 169–174. Available from: https://doi.org/10.1007/BF02856809.

26. Beygi H, Shafiei AB, Erfanian M. Evaluating the fuzzy weighted linear combination method in forest fire risk mapping (Case study: Sardasht Forests, West Azerbaijan Province, Iran). Journal of Science and Technology of Wood and Forest 2015; 22(3): 29–51.

27. Nasiri M. Investigation on wood resistance of different tree species to fire at caspian forests of Iran. Iranian Journal of Forest & Poplar Research 2012; 20(3): 505–513.

28. Chandra S. Application of remote sensing and GIS technology in forest fire risk modeling and management of forest fires: A case study in the Garhwal Himalayan region. In: Van Oosterom P, Zlatanova S, Fendel EM (editors). Geo-information for Disaster Management. Berlin, Heidelberg: Springer; 2005. Available from: https://doi.org/10.1007/3-540-27468-5_86.

29. Sharma D, Hoa V, Cuong PV, et al. Forest fire risk zonation for Jammu District forest division using remote sensing and GIS. Hanoi, Vietnam: 7th FIG Regional Conference, Spatial Data Serving People: Land Governance and the Environment—Building the Capacity. October 1-12, 2009.

30. Mohammadi F, Shabani N, Pourhashemi M, et al. Forest fire hazard mapping using AHP and GIS (In Persian). Iranian Forest and Poplar Researches Journal 2010; 18(4): 586–569.

31. Jahdi R, Darvishsefat A, Etemad V. Predicting forest fire spread using fire behavior model (Case study: Malekroud Forest-Siahkal). Iranian Journal of Forest and Poplar Research 2013; 5(4): 419–430.

32. Darvishi L, Ghods-Khah M, Gholami V. A regional model for forest fire hazard zonation in forests of Dorud city (Case study: Babahar region). Iranian Journal of Forest and Range Protection Research 2013; 11(1): 10–20. doi: http://dx.doi.org/10.22092/ijfrpr.2013.106396.

33. Behzadfar M, Vahid H. Fire risk zonation in North Khorasan Province, Iran. The first international conference on wildfire in natural resources lands; September 2011. Available from: https://www.researchgate.net/publication/236134271.

34. Aghajani H, Fallah A, Fazlollah Emadian S. Modelling and analyzing the surface fire behavior in Hyrcanian forest of Iran, Journal of Forest Science 2014; 60(9): 353–362. doi:10.17221/97/2013-JFS.

35. Huyền DTT, Tuân VA. Applying GIS and multi criteria evaluation in forest fire risk zoning in Son La Province, Vietnam. International Symposium on Geoinformatics for Spatial Infrastructure Development in Earth and Allied Sciences; 2008. Available from: http://wgrass.media.osaka-cu.ac.jp/gisid-eas10/papers/8918d883b5c5b166ca47d6733c18.pdf.

36. Zarekar A, Kazemi-Zamani B, Ghorbani S, et al. Mapping spatial distribution of forest fire using MCDM and GIS (Case study: Three forest zones in Guilan Province) Iranian Journal of Forest and Poplar Research 2013; 21(2): 218–230. doi: http://dx.doi.org/10.22092/ijfpr.2013.3854.

37. Farooq M, Malik T, Rabbani G. Forest fire risk zonation using remote sensing and GIS technology in Kansrao forest range of Rajaji National Park, Uttarakhand, India. International Journal of Advanced Remote Sensing and GIS 2013; 2: 86–95. Available from: https://www.researchgate.net/publication/2781 59215.

38. Yin H, Kong F, Li X. RS and GIS-based forest fire zone mapping in Dahinggan Mountains. Chinese Geographical Science 2004; 14(3): 251–257. doi: 10. 1007/s11769-003-0055-y.

39. Tran AT, Dinh ND, Danh T, *et al.* Forest fire risk mapping by using satellite imagery and GIS for Quang Ninh Province, Vietnam. 2008; Available from: https://www.researchgate.net/publication/2608 71777.

40. Saxena A, Chandra S, Srivastava P. Geospatial modeling for forest fire risk zonation in Himalayas and Siwaliks, India. Remote Sensing and GIS Applications to Forest Fire Management, Fire Effects Assessment 2005; 133–137.

41. Kartoolinezhad D. Wildfires risk assessment of North-East Hyrcanyan Forests of Iran by using Keetch-Byram and Mc-Arthur Indices 2016; 14(1): 48–57. doi: 10.22092/ijfrpr.2016.107641.

42. Prasad Vadrevu K, Badarinath KVS, Anuradha E. Spatial patterns in vegetation fires in the Indian region. Environmental Monitoring and Assessment 2008; 147(1-3): 1–13. doi: 10.1007/s10661-007-009 2-6.

43. Sowmya SV, Somashekar RK. Application of remote sensing and geographical information system in mapping forest fire risk zone at Bhadra wildlife sanctuary, India. Journal of Environmental Biology 2010; 31(6): 969–974.

44. Mohammadinejad M, Tavakoli M. Survey of fire status in oak and wild pistachio (Pistacia atlanticaDesf) forest zone of Lorestan Province (in Persian). The first National Conference on Oak and wild pistachio (Pistacia atlanticaDesf) in Zagros 1998; 76–77.

45. Burgan RE, Klaver RW, Klaver JM. Fuel models and fire potential from satellite and surface observations. International Journal of Wildland Fire 1998; 8: 159–170. doi: https://doi.org/10.1071/WF9980159

46. Chuvieco E, Salas J. Mapping the spatial distribution of forest fire danger using GIS. International Journal of Geographic Information Systems 1996; 10(3): 333–345. Available from: https://doi.org/10.1 080/02693799608902082.

47. Chen W, Sakai K, Moriya L, *et al.* Estimation of vegetation in semi-arid sandy land based on multivariate statistical modeling using remote sensing data. Environmental Modeling & Assessment 2013; 18(5): 547–558. doi: 10.1007/s10666-013-9359-1.

48. Lozano FJ, Suárez-Seoane S, Kelly M, *et al.* A multi-scale approach for modeling fire occurrence probability using satellite data and classification trees: A case studying a mountainous Mediterranean region. Remote Sensing of Environment 2008; 112(3): 708–719. doi: https://doi.org/10.1016/j.rse.2 007.06.006.

49. Stolle F, Chomitz KM, Lambin EF, *et al.* Land use and vegetation fires in Jambi Province, Sumatra, Indonesia. Forest Ecology and Management 2003; 179 (1-3): 277–292. doi: https://doi.org/10.1016/S0 378-1127(02)00547-9.

50. Vazquez A, Moreno JM. Spatial distribution of forest fires in Sierra de Credos (Central Spain). Forest Ecology and Management 2001; 147(1): 223–239. Available from: https://doi.org/10.1016/S0378-1127 (00)00436-9.

51. Juan de la Riva, Pérez-Cabello F, Lana-Renault N, *et al.* Mapping wildfire occurrence at regional scale. Remote Sensing of Environment 2004; 92(3): 363–369. doi: https://doi.org/10.1016/j.rse.2004.06.022.

Journal of Geography and Cartography

Focus and Scope

Journal of Geography and Cartography (JGC) is an international open-access academic journal with rigorous peer-reviewed process. We are interested in the scientific topics from all fields of geography and cartography. Our ultimate goal is to make the journal a platform of global academic sources for high-quality geo-papers.

JGC publishes original research articles, review articles, editorials, case reports, letters, brief commentaries, perspectives, methods, etc.

Examples of relevant topics include but are not limited to:

1. Human geography and urban-rural planning
2. Geography science
3. Geochemistry
4. Natural geography
5. Plant geography
6. Hydrology
7. Soil geography
8. Geophysics
9. Environment science
10. Geographic information system
11. Cartography
12. Remote sensing technique
13. Geography teaching theory
14. Man-land relationship by analyzing and mapping geographic phenomena

EnPress Publisher, LLC

EnPress Publisher, LLC, is a scholastic conduit for an assembly of professionals in the domains of science, technology, medicine, engineering, education, social sciences and many more, as a roundtable for their intellectual discourse and presentation, and as an instrument to galvanize research designs, policy implementation and commercial interests, to facilitate the prevailing over their challenges and to encourage to the full advantage of their resources and true potential.

We are the intellectual and academic home for academic, educators, scholars, clinicians, corporate researchers, who all play important roles in a wide range of national and international research organisations, and whose interests, expertise, research approaches and industry objectives from around the world coalesce together to advance significant contributions in their research and professional fields.

As an instrument of information purveyor, we seek to combine academic rigor and originality with the nuanced development of policy and practice. Via our journals, client database, online campaigns and social media presence, we offer a platform for industry professionals to interconnect, as well as opening doors towards cost-effective solutions for them to succeed, and we confidently hope to inspire a new generation of multidisciplinary researchers, think-tank experts, policymakers and business entities to innovate and advance their knowledge across fields.